Effect of Substitution at B-Site in Relaxor Barium Niobates: An Investigation on Origin of Giant Dielectric Constant

A Thesis
Submitted By

DEVANG D. SHAH

For the award of the degree of
DOCTOR OF PHILOSOPHY
IN
PHYSICS

UNDER THE GUIDANCE OF

Dr. P. K. MEHTA

DEPARTMENT OF PHYSICS
FACULTY OF SCIENCE
THE MAHARAJA SAYAJIRAO UNIVERSITY OF BARODA
VADODARA 390 002, GUJARAT INDIA

October, 2012

Effect of Substitution at B-Site in Relaxor Barium Niobates: An Investigation on Origin of Giant Dielectric Constant

A Thesis

Submitted by

DEVANG D. SHAH

For the award of the degree of

DOCTOR OF PHILOSOPHY

IN
PHYSICS

UNDER THE GUIDANCE OF

Dr. P. K. MEHTA

DEPARTMENT OF PHYSICS
FACULTY OF SCIENCE
THE MAHARAJA SAYAJIRAO UNIVERSITY OF BARODA,
VADODARA-390002, GUJARAT INDIA

OCTOBER 2012

Dedicated

to

My Three Gods...

Without their blessing, love and encouragement this could not be possible..........

मात्रु देवो भव:

(Mother is God)

Smt. Sharmisthaben D. Shah

पितृ देवो भव:

(Father is God)

Late Shri. Dineshandra K. Shah

गुरु देवो भव:

(Teacher is God)

All My Teachers

Declaration by the Candidate

I hereby declare that the work embodied in the present thesis entitled "**Effect of Substitution at B-Site in Relaxor Barium Niobates: An Investigation on Origin of Giant Dielectric Constant"** is original and carried out by me under the guidance of Dr. Prashant K. Mehta. This work has been carried out at Department of Physics, Faculty of Science, The Maharaja Sayajirao University of Baroda, Vadodara (India), approved by Council of Post – Graduate Studies and Research. This work is supported by the UGC-DAE-Consortium for Scientific Research (UDCSR) Indore centre under the collaborative research scheme.

I have put in more than two years of attendance with the supervisor at the University. I further declare that to the best of my knowledge neither the thesis nor any part there of has been submitted for the award of any degree or diploma at other University or Organization.

Date:

Devang D. Shah
Department of Physics,
Faculty of Science,
The M. S. University of Baroda,
Vadodara (India).

THE MAHARAJA SAYAJIRAO UNIVERSITY OF BARODA

Dr. Prashant K. Mehta
Associate Professor

Department of Physics
Faculty of Science
The M. S. University of Baroda
Vadodara – 390 002

Tel. **0265–2795339 (O); 2795569 (Fax);** **Email: pkmehta_phy@yahoo.co.in**

Certificate from the Thesis Supervisor

This is to certify that the thesis entitled "**Effect of Substitution at B-Site in Relaxor Barium Niobates: An Investigation on Origin of Giant Dielectric Constant**" is a piece of work done by Mr. Devang D. Shah, under my guidance and supervision for the degree of Doctor of Philosophy of The Maharaja Sayajirao University of Baroda, India and the candidate has put in an attendance of more than two years with me.

To the best of my knowledge and belief the thesis

1. embodies the work of the candidate himself,
2. has been duly completed,
3. fulfills the requirements of the ordinance relating to the Ph. D. degree of the University and
4. is up to the standard both in respect of content and language for being referred to examiner.

Date:

Dr. Prashant K. Mehta
Thesis Supervisor

Forwarded through:

Forwarded through:

Prof. A. C. Sharma

Head,
Physics Department.

Prof. Nikhil D. Desai

Dean,
Faculty of Science.

ACKNOWLEDGEMENTS

It gives me immense pleasure to acknowledge my indebtedness to my thesis supervisor **Dr. Prashant K. Mehta**, *Department of Physics, The Maharaja Sayajirao University of Baroda for his elite guidance, ceaseless encouragement and constant inspiration throughout my research work. I express my deep sense of gratitude and respectful regards to him for putting me at ease and affectionately inspiring me during my research studies.*

I would like to express my profound gratitude to **Dr. Alok Banerjee, Dr. Ram Janay Choudhary, Dr. V. Ganeshan, Dr. P. Chaddha, Prof. Ajay Gupta, Dr. N. P. Lalla, Dr. T. Sripathy, Dr. O. G. Singh, Dr. A. M. Awashti, Dr. D. M. Phase & Dr. Mukul Gupta**, *Scientists and* **Mr. Kranti Kumar, Mr. Suresh Bhardwaj, Mr. Manoj, Mr. Mohan, Mr. Anil, Aahireji, Deshpandeji and Vadekarji,** *engineers at UGC-DAE-CSR Centre Indore, for valuable discussions which led to improvement in my understanding of Physics. I thank them from the bottom of my heart for helping me for sample characterization and data analysis, despite their busy schedule. I also appreciate them for boosting my research in this field.*

I also express my indebtedness to **Dr. Ravi Kumar, Dr. K. Ashokan, Dr. Sunil Oza & Dr. D. K. Awasthi**, *Scientists and* **Mr. Vijay Patel,** *engineer, Inter University Accelerator Centre, New Delhi for their constant support and valuable suggestions at every stage of my research work. I am grateful to them for their active interest shown in my experiments and the resultant discussion motivated me to carry my research further in this direction.*

I would like to heartily thank **Dr. C. J. Panchal, & Dr. M. S. Desai**, *Department of Applied Physics, Faculty of Technology and Engineering, The M.S. University of Baroda, Vadodara, and* **Dr. Bharati Rehani,** *Department of Metallurgical and Materials Engineering, Faculty of Technology and Engineering, The M.S. University of Baroda, Vadodara. I have immensely benefited from the discussion with them and their critical evaluations for which I shall always be obliged to them.*

It is my pleasure to acknowledge the encouragement and cooperation rendered to me by **Prof. A. C. Sharma**, *Head of Physics Department, The M. S. University of Baroda, Vadodara, during the entire period of my research work. I can never forget the freedom he has given me for using all possible facilities here in the department. Thanks are also due to* **Prof. G. R. Pandya, Prof. C. F. Desai, Prof. N. L. Singh, Prof. D. K. Kanchan, Prof. J. P. Singh, Prof. P. K. Jha, Dr. D. G. Rathod, Dr. M. B. Sureshkumar, Dr. S. Mukharjee, Dr. K. R. Jotania, Dr. M. N srinivas, Dr. K. C. Sebestian, Dr. Keyur Vyas, Dr. Mitesh Sarkar, Dr. B. P. Shah, Dr. P. H. Soni & Shri N. V. Patel,** *for their co-operation .I am very much grateful to* **Prof. Nikhil D. Desai**, *Dean, Faculty of Science for his strong support and help.*

I am thankful to UGC – DAE – Consortium for Scientific Research (UDCSR) Indore Centre, India for providing me 'Research Fellowship under Collaborative Research Scheme and experimental facilities at Indore Centre. I am also thankful to Inter University Accelerator Centre (IUAC), New Delhi for providing research facilities.

I am also grateful to The Maharaja Sayajirao University of Baroda, Vadodara for providing me infrastructure and research facility.

I express my regards to all my loving teachers and other staff members of the Physics Department for their cooperation and also the entire non-teaching staff, Specifically **Mr. Rakeshbhai Parikh & Mr. Maheshbhai Panchal** *of Physics Department for providing me an affable and healthy atmosphere during my Ph.D. work at the department. I also thank* **Mr. Piyushbhai Rana** *along with his work shop staff.*

It is a pleasure to acknowledge the active cooperation and help given by my Senior research scholars, amongst whom **Dr. Ankur Pandya** *helped me a lot to clear my basic level analysis and important guidance to carry out my experiments and analysis along with the thesis writing. I also like to thank* **Nishant Barot, Keyur Patel, Jaimin Rai, Gopal & Dr. Maunik Jani,** *for their support in my research work. Moreover I cannot forget the enjoyable and fruitful time spent with* **Dr. G. Kiran Kumar, Dr. Sejal Shah, Dr. Minakshi Pant, Dr. Dolly Singh, Dr. Shyam Khambholaja, Rakesh Chauchan & Aditya Patel.**

I cannot forgot the support and amiable moments spent with my other research colleagues from Vadodara; **Dharmendra Tawde, Dhaval Modi, Nikit Deshmukh, Sagar Ambavale, Chaitali Gavade, Sangeeta Kishor, Kavita Mishra, Digish Patel, Naveen Agarwal, Manish Jayshval, Poonam Sharma, Prajkta Joge, Paresh Prajapati, P. K. Rath, Manish Patel, Nimesh Patel, Vishwanath, B.S. Bishnoi, Gaurang Patel, Purvi Patel** *and Senior colleagues* **Dr. AshimPramanik, Dr. KaustavMukharjee, Dr. Ram Prakash, Dr. Ajay Soni** *from UDCSR Indore as well as* **Dr. Dinesh Shukla and Dr. Abhinav** *from IUAC New Delhi Centre. I would also like to thank my research colleagues at different institutes* **Dr. Prashant Vachhani, Dr. Swati Pandya, Aashish, Tirthankar, Sanmukh, Venkateswarlu, Suryanarayan Das, Sarath, Dhirendra, Aamir, Aga, Yogesh** *and many others for sharing their knowledge with me.*

Above all, the credit also goes to my all relatives, my younger brother **Mr. Mitesh D. Shah** *and Didi and Jijaji,* **Niyati K. Shah & Keyur Shah**, *and my lovable nephew* **Jaival Shah**, *along with our good family friends* **Kaushal Darji, Ketul Modi, Hitesh Ka.Patel & Mayur Darji** *for their unlimited love, support and encouragement.*

Finally, I would express my deepest gratitude to my parents **Mummy and Papa**, *my loving and caring fiancée* **Chaitali, her parents** *and the hidden entity that is* **GOD**. *Without the love and blessings of all these, it would be difficult for me to travel this journey of success. Finally, I express my thanks and I apology to all those who provided help to me and I could not recall at this moment.*

DEVANG D. SHAH

CONTENTS

List of Figures

List of Tables

CHAPTER 1

Introduction

(Introduction to Research Area of Present Work and Review of Work Already been Done)

The very brief introduction to the research area, research topic, related compounds and mineral group of the compounds is presented here. Fundamental properties and specific characteristics of ferroelectric, relaxor ferroelectric and other high dielectric constant ceramics are summarized here. The mineral group perovskite and double perovskite are introduced in detail with its properties, constraints and salient features. The detailed literature survey on the available high dielectric constant materials along with the explanation for such observed results are presented. Literature survey on multiferroic nature of the compounds, thin film preparation and its characterization is also presented here.

In the past several decades, need for compact energy storage devices have engrossed much more attention. The modern energy storage devices need to have very high storage capacity to fulfill the need of increasing energy consumption. The capacitors with very high capacity and low loss can be utilized to store high electrical energy in a small volume (i.e. high energy density). At present though electric double layer capacitors (EDLC) are available with high energy storage capacity, but they can not sustain very high voltage [1]. Another category of capacitors available in the market is ceramic capacitors. Ceramic capacitors can sustain very high voltage. Advantages of ceramic capacitors are: low inductance, suitable for high frequency application etc [2]. The enhancement in energy density of such ceramic capacitors may bring a revolutionary change in the field of energy storage devices. The energy density of any capacitor depends on the dielectric material of the capacitor. The dielectric constant of the material determines the energy density of the material. The materials exhibiting high values of dielectric constant can store more electrical energy [2-5]. In the present scenario ferroelectric materials exhibit very high values of dielectric constant [3-6].

1.1 Ferroelectrics:

The ferroelectric (FE) materials are special type of dielectric materials exhibiting high values of dielectric constant. The reason for such high dielectric constant is existence of permanent dipoles. The compounds with non-cubic structural symmetry exhibit finite separation between positive charge center and negative charge center. The finite separation results in development of permanent dipole moment for these compounds. In the absence of electric field these polarizations are randomly oriented in all the directions. With the application of electrical field these dipoles get aligned in the direction of field and exhibit finite polarization at macroscopic level. The response of the polarization is not linear for these materials. They show a wide hysteresis loop on reversing the applied electrical field. The systematic development of typical hysteresis loop for a ferroelectric material is visualized through Figure 1.1(a). The value of saturation polarization determines the dielectric constant of given material. The dielectric constant does increase with increase in temperature up to a particular temperature. Above this temperature the dielectric constant suddenly drops to zero. The reason for such drop in dielectric constant is structural phase transition from non cubic symmetry to cubic symmetry. This temperature is known as ferroelectric to paraelectric transition temperature or Curie point T_c. The values of dielectric constant are highest just bellow the transition temperature. This typical nature of ferroelectric material is shown in the Figure 1.2(a). The well known ceramic oxides exhibiting ferroelectricity at room temperature are $PbTiO_3$, $BaTiO_3$, $KNbO_3$, $LiTaO_3$, etc.

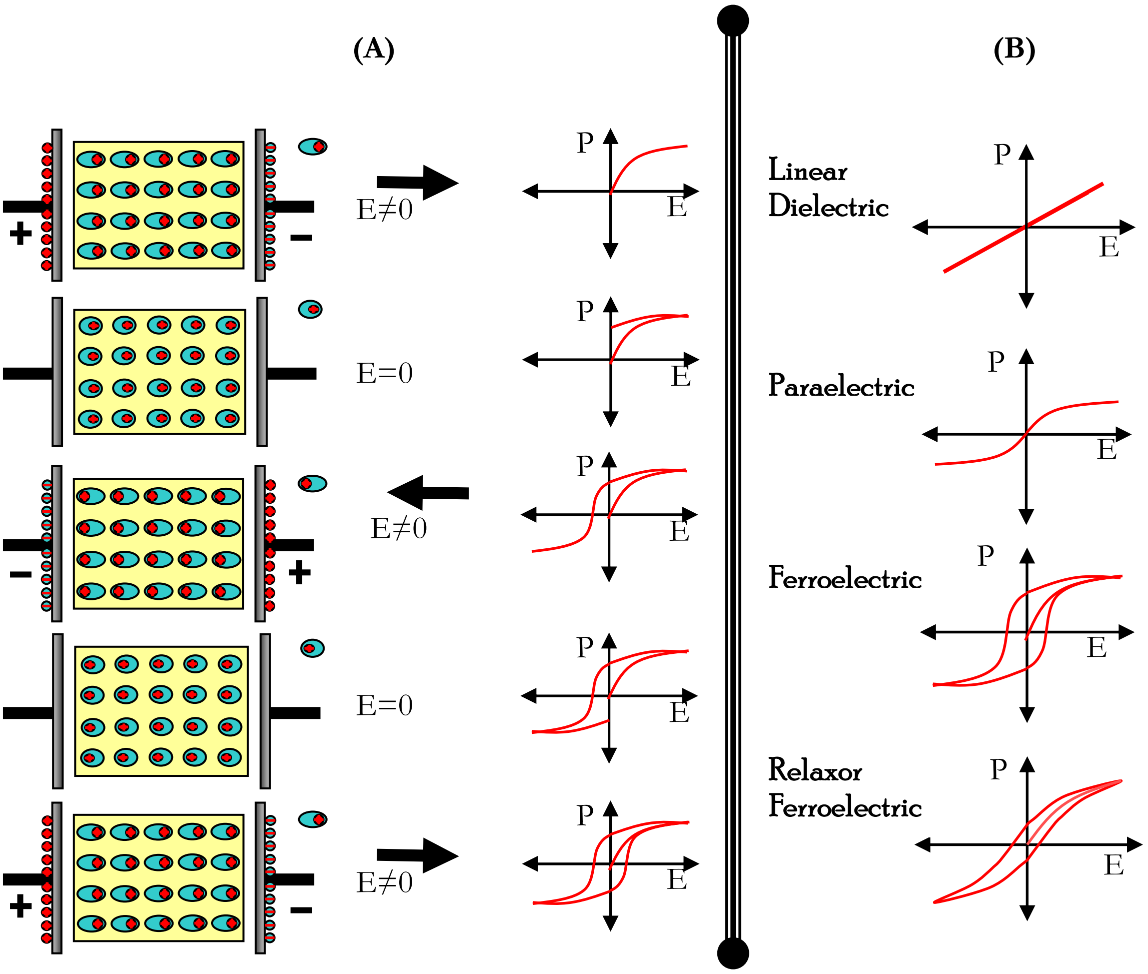

Figure 1.1: (A) The systematic development of hysteresis loop for a ferroelectric materials, (B) The hysteresis loop for different types of materials.

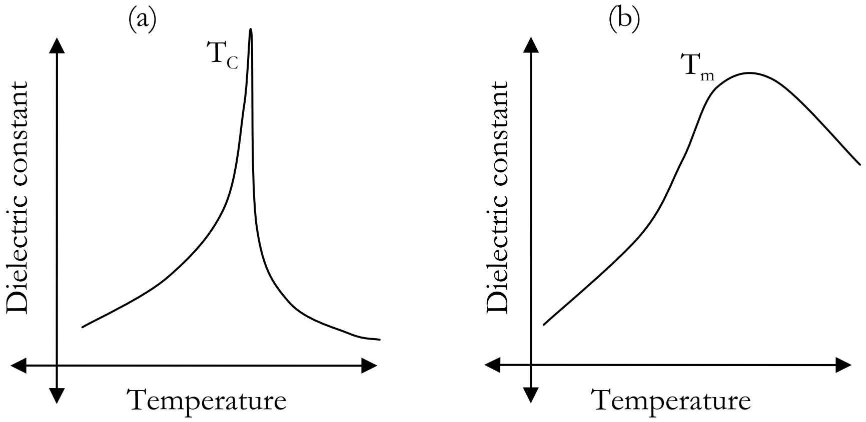

Figure 1.2: The nature of transition temperature for (a) ferroelectric and (b) relaxor ferroelectric materials.

1.2 Relaxor Ferroelectrics:

These are a special class of ferroelectric materials. These materials exhibit strong frequency as well as temperature dependent dispersion in their dielectric constant data. The dielectric constant values for relaxor ferroelectric materials show broad maxima instead of sharp peak values at phase transition temperature as shown in the Figure 1.2(b). Such a broad transition is known as Diffuse Phase Transition (DPT) [6-8]. These materials exhibit comparatively narrow hysteresis loop with high values of dielectric polarization (see Figure 1.1(b)). Relaxor ferroelectrics (RFE) strongly disobey Curie-Weiss law, which is well obeyed by ferroelectric materials. Relaxor ferroelectrics do not show any structural transitions at peak temperatures T_m. The ceramic oxides $Pb(Mg_{0.33}Nb_{0.67})O_3$ (PMN), $Pb(Sc_{0.5}Nb_{0.5})O_3$ (PSN), $Pb(Fe_{0.5}Nb_{0.5})O_3$ (PFN), $Pb(Sc_{0.5}Ta_{0.5})O_3$ (PST), etc are well known relaxor ferroelectric compounds [9-17].

1.3 High K Ceramics:

In the recent years more attention has been given to develop high dielectric constant (High K) ceramic compounds [3]. Among them ABO_3 type perovskite compounds like $CaCu_3Ti_4O_{12}$ (CCTO), $Bi_{0.67}Cu_3Ti_4O_{12}$ (BCTO), $Na_{0.5}Bi_{0.5}Cu_3Ti_4O_{12}$ (NBCTO), etc. have shown giant values of dielectric constant with cubic or nearly cubic symmetry [18-26]. The reason for such high dielectric constant demonstrated by cubic compounds is unclear. In contrast to ferroelectric and relaxor ferroelectric compounds these compounds do not show peak related to phase transition. The dielectric constant remains nearly unaffected by the temperature. Another perovskite ceramic compound $Ba(Fe_{0.5}Nb_{0.5})O_3$ (BFN) is also studied widely for exhibiting high dielectric constant and relaxor like nature [27-38].

1.4 Perovskite Structure:

The majority ceramic oxides showing relaxor ferroelectricity and/or high K values are belonging to perovskite mineral group. The perovskite group is identified by the study of naturally available mineral calcium titanate $CaTiO_3$. The compounds with general chemical formula ABO_3 are known as perovskite compounds. The unit cell with formula unit ABO_3 is shown in the Figure 1.3. The stability of perovskite structure depends on four factors:

1. Charge balance: The over all charge of the perovskite structure is balanced by suitable combination of positively charged anions and negatively charged oxygen. In general the A site ions and B site ions possess charge state 2+ and 4+ respectively in order to

balance the 6- charge exhibited by the three oxygen atoms. Thus the overall ABO3 structure remains neutral.

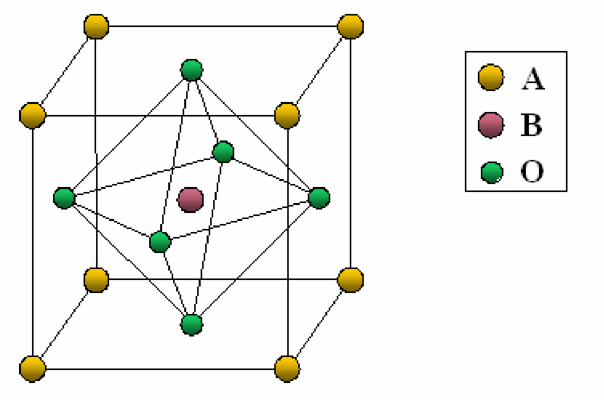

Figure 1.3: ABO_3 type single perovskite structure.

2. No of atom balance (stoichiometry): The ratio of the atoms should be maintained at proportion of 1:1:3 occupying the positions at A-site, B-site and O-site, respectively. The total number of atoms per formula unit also should also be maintained at 5.
3. Oxygen balance: A very small amount of oxygen loss from the entire compound may cause partial charge imbalance at either A-site or B-site. In order to prevent such defects the oxygen should be balanced equally.
4. Ionic radii balance (tolerance factor): The few selected anions having suitable ionic radii only can be replaced at A-site or B-site of ABO_3 structure. The tolerance factor (t) of perovskite formula does not permit all anions to be replaced at A-site or B-site. The tolerance factor for ABO_3 structure is given by [39-40];

$$t = \frac{(R_A + R_O)}{\sqrt{2}(R_B + R_O)} \qquad \text{...... (1.1)}$$

The value of t in the range 0.8 to 1.1 is only permitted for the perovskite mineral structure [6, 39, 41-42]. Therefore the A and B site anions should be selected in such a way that their ionic radii satisfy this tolerance limit.

1.5 Double Perovskite Structure:

A complex perovskite structure in which B site element is substituted by two different elements (B' and B") is generally known as double perovskite structure [40]. Here the substitution is done in such a way that the overall charge and number of atom per ABO_3 unit remains unaffected. In order to fulfill the above condition two different types of combinations based on the proportions of B' and B" elements are commonly permitted.

1. The equal proportion of B' and B" elements (1:1 system – Generally referred as double perovskite structure): here the B' and B" elements contribute equally to balance the atoms per formula unite. i.e. $AB'_{1/2}B''_{1/2}O_3$. In this view the permitted charge states for B' and B" site elements are respectively, 2+ and 6+ or 3+ and 5+ or 4+ and 4+, etc. thus the average charge becomes 4+ at B site.

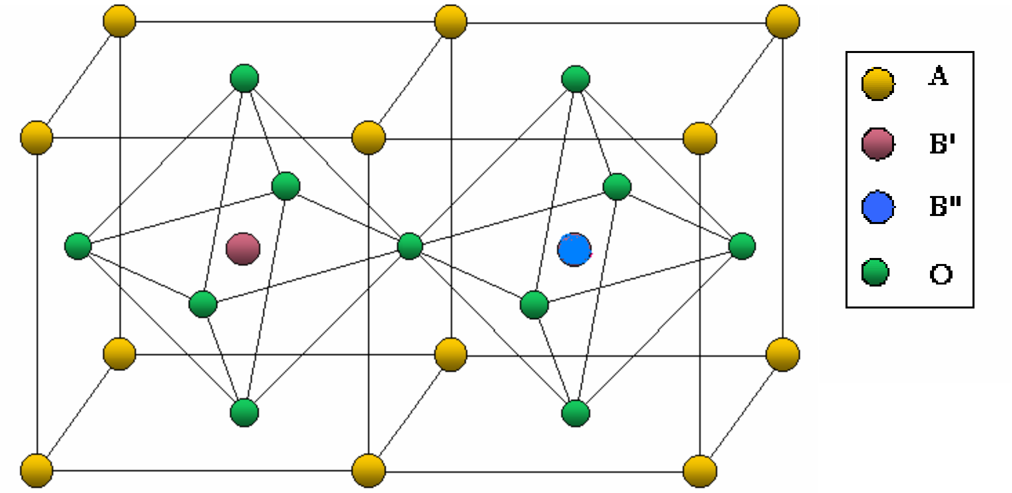

Figure 1.4: $A_2B'B''O_6$ [or $A(B'_{0.5}B''_{0.5})O_3$] type double perovskite structure.

The tolerance factor for the case of 1:1 systems is given by [40];

$$t = \frac{(R_A + R_O)}{\sqrt{2}\left(\left(\frac{R_{B'}+R_{B''}}{2}\right)+R_O\right)} \qquad \text{...... (1.2)}$$

2. The un equal proportion of B' and B" elements (1:2 system): here the contribution of B" element is double than that of the B' element to balance the number of atom per formula unit. i.e. $AB'_{1/3}B''_{2/3}O_3$. In this view the permitted charge states for B' and B" site elements are respectively, 2+ and 5+ $\left(\text{i.e. } 2+ \times {}^{1}\!/_{3} + 5+ \times {}^{2}\!/_{3} = 4+\right)$ or 4+ and 4+, etc. thus the average charge becomes 4+ at B site.

The tolerance factor for the case of 1:2 systems is given by;

$$t = \frac{(R_A + R_O)}{\sqrt{2}\left(\left(\frac{R_{B'}+2R_{B''}}{3}\right)+R_O\right)} \qquad \text{...... (1.3)}$$

1.6 Barium Niobates:

The barium niobates are barium based complex ceramic oxides in which A site is occupied by Ba and B" site is occupied by Nb. The barium based systems are environment friendly systems in comparison to well established Lead based toxic system [43-44]. The selection of Nb is done because it enhances electrical properties of compound and also cheaper than Tantalum based systems.

1.7 Literature Survey:

In the research area of high energy storage devices two types of materials are extensively studied: (1) Relaxor Ferroelectric compounds with high dielectric constant and (2) High K ceramics not exhibiting relaxor behavior [18-38, 45-47]. The relaxor ferroelectric (RFE) ceramic compounds exhibiting high dielectric constant ($\varepsilon' > 10^4$) are of enormous importance due to their wide functional properties like; ferro-electricity, magneto electric behavior, relaxor properties, multiferroic behavior, piezoelectricity etc [32, 48-51]. Bulk as well as films of such materials are useful due to their wide applications as industrial capacitors, sensors, actuators, power transmission devices, memory devices, high energy storage devices, etc [5,52]. Relaxor ferroelectrics are special type of dielectric materials with very high dielectric constant. They are generally characterized by frequency dispersion in their dielectric constant vs. temperature curves and broad maxima in the same curves. Unlike normal ferroelectric they show narrow electrical hysteresis loop (P-E loop) [7-8]. In addition relaxor ferroelectrics strongly disobey Curie-Weiss law, which is well obeyed by Ferroelectrics [6-8]. Further, relaxor ferroelectrics do not show any structural transitions at peak temperatures Tm [7-8].

The origin of its high dielectric constant and relaxor behavior has been explained on the basis of two contradicting theories. Several attempts have been made earlier to explain the high dielectric constant in $Pb(Fe_{1/2}Nb_{1/2})O_3$ (PFN), $Pb(Fe_{1/2}Ta_{1/2})O_3$ (PFT), $Pb(Mg_{1/3}Nb_{2/3})O_3$ (PMN), $Ba(Fe_{1/2}Nb_{1/2})O_3$ (BFN), $Sr(Fe_{1/2}Nb_{1/2})O_3$ (SFN), $Pb(Mg_{1/3}Nb_{2/3})O_3$-$PbTiO_3$ (PMN-PT), $Pb(Fe_{1/2}Nb_{1/2})O_3$-$PbTiO_3$ (PFN-PT), $Ba(Fe_{1/2}Nb_{1/2})O_3$-$BaTiO_3$ (BFN-BT) etc. on the basis of chemical disorder leading to a local permanent polarization induced ferroelectricity [5, 8, 18-19, 27-28, 52-58]. Alternatively, the high dielectric constant in $CaCu_3Ti_4O_{12}$ (CCTO) like compounds was linked to the extrinsic factors like the grain boundary effects, oxygen vacancies, space charge polarization, etc. [20-21, 32-33, 57-61]. It is indeed desirable to have a proper understanding of the origin of the physico-chemical behaviour in these systems for tailoring their appropriate industrial applications.

In the past Lead (Pb) based RFE compounds were extensively investigated by several groups exhibiting promising properties, but they are toxic [9-17, 62-64]. In the present era electronic device industries requires environment friendly material. The Barium (Ba), Strontium (Sr) and Bismuth (Bi) are found most prominent candidates for replacement of toxic Lead (Pb) based compounds [39, 65-66]. Among them Barium Niobate based double perovskite mixed oxide systems are useful to enhance electrical properties of compound and are cheaper than tantalum based systems [32-33, 67]. These compounds have very high dielectric constant and found exhibiting relaxor ferroelectric behavior.

The Barium Iron Niobate [$Ba(Fe_{0.5}Nb_{0.5})O_3$] – (BFN) was discovered first by Saha and Sinha [27-28] in 2003 exhibiting very high dielectric constant [27-31]. According to Saha and Sinha, BFN is a relaxor ferroelectric having a monoclinic crystal structure. The same compound was reported as a non-ferroelectric having a cubic crystal structure by Raevski et al. and Z. Wang [32-33]. Raevski et al. have explained the high dielectric constant for such a cubic system by using the Maxwell-Wagner Effect [33]. Latter, Z. Wang et al. had explained the property in terms of oxygen vacancy induced dielectric relaxation [32].

In addition to samples exhibiting promising electrical properties simultaneous presence of multiferroic properties are advantageous due to its wide scope for industrial applications. The materials exhibiting ferromagnetic ordering along with ferroelectricity are considered as multiferroic compounds [68]. The variety of complex perovskite compounds like $YMnO_3$, $YbMnO_3$, $BiFeO_3$, $BiMnO_3$, $PbFe_{0.5}Nb_{0.5}O_3$, $PbFe_{0.5}Ta_{0.5}O_3$, $BaMn_{0.5}Nb_{0.5}O_3$, $BaFe_{0.5}Nb_{0.5}O_3$, etc have shown occurrence of ferroelectricity along with magnetic ordering [38, 63, 68-80]. Among this the BFN and PFN ceramics have shown ferromagnetic behavior at low temperatures with relaxor like ferroelectric properties [38, 71, 81].

Increasing demand of miniaturization requires thin film preparation of such compounds. The Pulsed Laser Deposition (PLD) technique is one of the most promising way to prepare thin films of such complex perovskite compounds. Preparations of thin films of BFN from the application point of view have been reported [82-83]. N. Rama et.al. reported BFN thin film synthesis using PLD technique grown on $LaAlO_3$ (LAO), $NdGaO_3$ (NGO) and $SrTiO_3$ (STO) substrates. Their magnetic and transport properties were studied below room temperature region [82]. Later on, W. Zhang et.al. reported ferroelectric properties at room temperature of BFN films on $Pt/TiO_2/SiO_2/Si$ substrate prepared using PLD [83]. They also highlighted synthesis parameter dependent film properties.

References:

1. A. K. Shukla, S. Sampath and K. Vijayamohanan, Curr. Sci. **79(12),** 1656 (2000).
2. G. Yang, Z. Yue, T. Sun, J. Zhao, Z. Yang and L. Li, Appl. Phys. A. **91,** 119 (2008).
3. A. A. Bokov and Z. G. Ye, J. Mater. Sci. **41,** 31 (2006).
4. T. W. Noh, B. S. Kang, Y. W. So, B. H. Park and S. D. Bu, J. Korean Phys. Soc. **39,** S35 (2001).
5. G. H. Haertling, J. Am. Ceram. Soc. **82(4),** 797 (1999).
6. A. S. Bhalla, R. Guo, R. Roy, Mat Res Innovat. **4,** 3 (2000).
7. L. E. Cross, Ferroelectrics. **151**, 305 (1994).
8. L.E. Cross, Ferroelectrics. **76,** 241 (1987).
9. Y. X. Wang, C. L. Wang, M. L. Zhao and J. L. Zhang, Ferroelectrics. **323,** 11 (2005).
10. A. Kumar, R. S. Katiyar, C. Rinaldi, S. G. Lushnikov, and T. A. Shaplygina, App. Phys. Lett. **93,** 232902 (2008).
11. B. P. Burton, E. Cockayne, S. Tinte and U. V. Waghmare, Phys. Rev. B. **77,** 144114 (2008).
12. C. Bharti, S. N. Choudhary and T. P. Sinha, Indian J. Phys. **83**(**4**)**,** 409 (2009).
13. M. Ahart, A. Hushur, Y. Bing, Z. G. Ye, R. J. Hemley and S. Kojima, App. Phys. Lett. **94,** 142906 (2009).
14. B. Guttler, B. Mihailova, R. Stosch, U. Bismayer and M. Gospodinov, J. Molec. Struct. **661-662,** 469 (2003).
15. F. Yuan, Z. Peng and J. M. Liu, Mat. Sci. and Eng. B. **117,** 265 (2005).
16. J. Petzelt, E. Buixaderas and A. V. Pronin, Mat. Sci. and Eng. B. **55,** 86 (1998).
17. S. N. Gvasaliya, S. G. Lushnikov, I. G. Siny, I. L. Sashin, T. A. Shaplygina, R. Blinc, Physica B. **276-278,** 485 (2000).
18. S. Ke, H. Huang, H. Fan, Appl. Phys. Lett. **89,** 182904 (2006).
19. J. Liu, Chun-Gang Duan, Wei-Guo Yin, W. N. Mei, R. W. Smith and J. R. Hardy, Phys. Rev. B. **70,** 144106-1 (2004).
20. D. C. Sinclair, T. B. Adams, F. D. Morrison, and A.R. West, Appl. Phys. Lett. **80,** 2153 (2002).
21. M. C. Ferrarelli, T. B. Adams, A. Feteira, D. C. Sinclair, and A. R. West, Appl. Phys. Lett. **89,** 212904-1 (2006).
22. H. Yu, H. Liu, H. Hao, L. Guo, C. Jin, Z. Yu and M. Cao, Appl. Phys. Lett. **91,** 222911 (2007).
23. T. B. Adams, D. C. Sinclair and A. R. West, Phys. Rev. B. **73,** 094124 (2006).

24. W. Li and R. W. Schwartz, Appl. Phys. Lett. **89,** 242906 (2006).
25. S. Kwon, D. P. Cann, J. Mater. Sci. **44,** 4117 (2009).
26. M. C. Ferrarelli, D. C. Sinclair and A. R. West, Appl. Phys. Lett. **94,** 212901 (2009).
27. S. Saha and T.P. Sinha, J. Phys. Condens. Matter. **14,** 249 (2002).
28. S. Saha and T.P. Sinha. Phys. Rev. B. **65,** 134103 (2002).
29. I. P. Raevski, S. A. Kuropatkina, S. P. Kubrin, S. I. Raevskaya, V. V. Titov, D. A. Sarychev, M. A. Malitskaya, A. S. Bogatin and I. N. Zakharchenko, Ferroelectrics. **379(1),** 48 (2009).
30. S. Eitssayeam, U. Intatha, K. Pengpat, T. Tunkasiri, Science Direct. **6,** 316 (2006).
31. C. Y. Chung, Y. H. Changa, G. J. Chenb, Y. L. Chaic, Science Direct. **284,** 100 (2005).
32. Z. Wang, X. M. Chen, L. Ni, and X. Q. Liu, App. Phys. Lett. **90,** 022904 (2007).
33. I. P. Raevski, S. A. Prosandeev, A. S. Bogatin, M.A. Malitskaya, L. Jastrabik, J. Appl. Phys. **93,** 4130 (2003).
34. C. Y. Chung, Y. H. Chang, G. J. Chen and Y. L. Chai, J. Cryst. Growth. **284,** 100 (2005).
35. U. Intatha, S. Eitssayeam, J. Wang and T. Tunkasiri, Curr. Appl. Phys. **10,** 21 (2010).
36. S. Eitssayeam, U. Intatha, K. Pengpat, T. Tunkasiri, Curr. Appl. Phys. **6**, 316 (2006).
37. S. Ke, H. Fan and H. Huang, J. Electroceram. **22,** 252 (2009).
38. D. Bochenek, Z. Surowiak, J. P. Vejpravova, J. Alloys. Comp. **487,** 572 (2009).
39. S. Priya, A. Ando and Y. Sakabe, J. Appl. Phys., **94(2),** 1171 (2003).
40. C. W. A. Paschoal and E. M. Diniz, J. Phys.: Condens. Matter **21,** 075901 (2009).
41. A. Navrotsky, Chem. Mater. **10,** 2787 (1998).
42. R. C. Vickery and A. Klann, J. Chem. Phys. **27,** 1161 (1957).
43. P. K. Panda, J Mater Sci. **44,** 5049 (2009).
44. E. Cross, Nature. **432,** 24 (2004).
45. K. Uchino, Ferroelectrics. **151,** 321 (1994).
46. R. E. Schaak and T. E. Mallouk, Chem. Mater. **14,** 1455 (2002).
47. R. K. Sharma, A. Kumar, and J. M. Anthony, JOM. 53 (2001).
48. Y. Shimakawa, M. Azuma and N. Ichikawa, Materials. **153,** 4 (2011).
49. D. Serrate, J. M. De Teresa and M. R. Ibarra, J. Phys.: Condens. Matter. **19,** 023201 (2007).
50. J. V. D. Brink and D. I. Khomskii, J. Phys.: Condens. Matter. **20,** 434217 (2008).
51. M. G. Blamire, J. L. MacManus-Driscoll, N. D. Mathur, and Z. H. Barber, Adv. Mater. **21,** 3827 (2009).
52. K. Uchino, Ferroelectrics. **151,** 321 (1994).
53. J. T. Wang and C. Zhang, Ferroelectrics. **301,** 211 (2004).

54. W. Z. Zhu, A. Kholkin, P. Q. Mantas, and J. L. Baptista, J. Euro. Cera. Soc. **20,** 2029 (2000).
55. F. Yuan, Z. Peng, J.-M. Liu, Mat. Sc. and Eng. B. **117,** 265 (2005).
56. S. Eitssayeam, U. Intatha, K. Pengpat, G. Rujijanagul, K.J.D. MacKenzie and T. Tunkasiri, Current Appl. Phys. **9,** 993 (2009).
57. F. Zhao, Z. Yue, J. Pei, D. Yang, Z. Gui, and L. Li, Appl. Phys. Lett. **91,** 052903-1 (2007).
58. S. Ke, H. Huang, H. Fan, H.L.W. Chan and L.M. Zhou, Cera. Int. **34,** 1059 (2008).
59. Y. Y. Liu, X.M. Chen, X. Q. Liu, and L. Li, Appl. Phys. Lett. **90,** 192905-1 (2007).
60. Z. Abdelkafi, N. Abdelmoula, H. Khemakhem, O. Bidault and M. Maglione, J. Appl. Phys. **100,** 114111-1 (2006).
61. C. Elissalde and J. Ravez, J. Mater. Chem. **11,** 1957 (2001).
62. A. Levstik, V. Bobnar, C. Filipič, J. Holc, M. Kosec, R. Blinc, Z. Trontelj, Z. Jagličić, Appl. Phys. Lett. **91,** 012905 (2007).
63. S. Y. Cho, J. S. Kim, M. S. Jang, J Electroceram. **16,** 369 (2006).
64. W.Z. Zhu, A. Kholkin, P.Q. Mantas, J.L. Baptista, J. Euro. Cera. Soc. **20,** 2029 (2000).
65. Y. Y. Liu, X. M. Chen, X. Q. Liu, and L. Li, Appl. Phys. Lett. **90,** 192905 (2007).
66. L. Wu, X. Wang, J. H. Wang, R. Guo, A. S. Bhalla, J Mater Sci. **44,** 5420 (2009).
67. N. Rama, J. B. Philipp, M. Opel, K. Chandrasekaran, V. Sankaranarayanan, R. Gross and M. S. R. Rao, J. Appl. Phys. **95(11),** 7528 (2004).
68. K.F. Wang, J. M. Liu and Z. F. Ren, Advances in Phys. **58(4),** 321 (2009).
69. G. A. Smolenskii and V. A. Bokov, J. Appl. Phys. **35,** 915 (1964).
70. S. B. Majumder, S. Bhattacharyya, R. S. Katiyar, A. Manivannan and P. Dutta, J. Appl. Phys. **99,** 024108 (2006).
71. N. Rama, J. B. Philipp, M. Opel, K. Chandrasekaran and V. Sankaranarayanan, J. Appl. Phys. **95,** 7528 (2004).
72. N. Lampis, C. Franchini, G. Satta, A. G. Lehmann, and S. Massidda, Phys. Rev. B. **69,** 064412 (2004).
73. I. P. Raevski, S. P. Kubrin, S. I. Raevskaya, V. V. Titov, D. A. Sarychev, M. A. Malitskaya, I. N. Zakharchenko, and S. A. Prosandeev, Phys. Rev. B. **80,** 024108 (2009).
74. D. A. Sanchez, A. Kumar, N. Ortega, R. S. Katiyar and J. F. Scott, Appl. Phys. Lett. **97,** 202910 (2010).
75. H. Paik, H. Hwang, K. No, S. Kwon and D. P. Cann, Appl. Phys. Lett. **90,** 042908 (2007).

76. C. W. Nan, M. I. Bichurin, S. Dong and D. Viehland, G. Srinivasan, J. Appl. Phys. **103,** 031101 (2008).
77. X. Qi, J. Zhou, Z Yue, Z Gui, L. Li and S Buddhudu, Adv.Funct. Mater. **14(9),** 920 (2004).
78. N. Hill, J. Phys. Chem. B. **104,** 6694 (2000).
79. J. Y. Son, B. G. Kim, C. H. Kim, and J. H. Cho, Appl. Phys. Lett. **84,** 4971 (2004).
80. M. M. Kumar, A. Srinivas, and S. V. Suryanarayana, J. Appl. Phys. **87,** 855 (2000).
81. R. Blinc, P. Cevc, A. Zorko, J. Holc, M. Kosec, Z. Trontelj, J. Pirnat, N. Dalal, V. Ramachandran, and J. Krzystek, J. Appl. Phys. **101,** 033901 (2007).
82. N. Rama, J. B. Philipp, M. Opel, V. Sankaranarayanan, R. Gross and M. S. R. Rao, J. Phys. D: Appl. Phys. **40,** 1430 (2007).
83. W. Zhang, L. Li and X. M. Chena, J. Appl Phys. **106,** 104108 (2009).

CHAPTER 2

Statement of the Work and Thesis Objective

(Aim of the Present Thesis and Work Done to Achieve this Aim)

This chapter mainly focuses on the thesis objectives. The motivation for the present work and the goals decided are listed here. The short comings, contradictions and lacunae in works already done along with work needed to be done are highlighted in this chapter. Importance of present research problem indicating attempts made to understand it is explicitly explained here. To fulfill above objectives the parent compound to be investigated along with modifications or substitutions is discussed in brief. The outline of the work done along with the different sub objectives of the thesis is also presented.

2.1 Statement of the Work: (Aim of the Present Thesis):

The studies summarized in the previous chapter suggest that the large amount of work has been reported for the samples exhibiting high dielectric constant or relaxor ferroelectric behavior. Among them the double perovskite $Ba(Fe_{0.5}Nb_{0.5})O_3$ – BFN ceramic (and similar ceramic compounds) have engrossed much more attention due to its high dielectric constant in spite of having cubic crystallographic symmetry [1-10]. Simultaneously it shows relaxor like ferroelectricity and weak magnetic ordering at low temperatures [11-14]. Most of the previous studies were concentrated on either explaining such high dielectric constant values in individual systems by probing the role of only the extrinsic factors like grain and grain boundary or investigation of ferroelectricity with variation of chemical composition [1-3, 7]. Looking at the above contradicting explanations for the origin of the high dielectric constant, correlated investigations of the extrinsic contributions (microstructure properties) as well as the intrinsic contributions (chemical distortion) is crucial for a deeper understanding and optimization of the dielectric parameters.

In the present work, the origin of the high dielectric constant, in cubic $AB'B''O_3$ type perovskites is analyzed through a correlated study of the crystal structure, microstructure, optical studies, dielectric relaxation, electrical conductivity analysis and magnetic characterization.

2.2 Supplementary Thesis Objectives: (Sub Goals to Achieve Main Aim):

The main thesis objective is subdivided in the following goals.

1. The selection of the compounds: system we have selected is $Ba(Fe_{1/2}Nb_{1/2})O_3$ (BFN) compound with substitution of Co, Mn, Eu, Gd, and Y at Fe site by 50% or 100%. Selection of 3d and 4f elements are done mainly on the basis of three factors:
    a. Ionic radii balance given by tolerance factor: $t = \dfrac{(R_A + R_O)}{\sqrt{2}(R_B + R_O)}$
    b. Charge balance (3+ in present case at B'-site, with average charge at B-site is $3/2 + 5/2 = 4$).
    c. Affinity of hybridization with Oxygen 2p level of these elements.

    The selection of Co and Mn – is essentially made because Co is having one additional electron in the outermost orbital i.e., $Fe^{3+}(3d^5) \rightarrow Co^{3+}(3d^6)$; while Mn is having one electron less in the outermost orbital i.e., $Fe^{3+}(3d^5) \rightarrow Mn^{3+}(3d^4)$.

2. Fabrication of a high temperature muffle furnace for synthesis of the samples: One high temperature muffle furnace with programmable temperature control up to 16 steps (with PID controller) having upper working temperature of 1400 °C is designed to prepare the ceramic samples using solid state reaction technique.
3. Sample holder preparation for extended data collection limits: Two different dielectric sample holders (one for high temperature and another for low temperature) with perfect electromagnetic induction (EMI) shielding are prepared to collect the complex impedance data in wide frequency and temperature range (80K-800K).
4. Data modeling with different models: Attempts are made to explain the role of oxygen vacancy as well as the doping induced dielectric relaxation. The role of the conduction mechanism of charge carriers is also analyzed to explain the origin of high dielectric constant. The equivalent circuit modeling of complex impedance data, Cole-Cole model of dielectric relaxation and Jump relaxation model (JRM) are utilized for in-depth analysis.
5. Investigation of multiferroic properties of the compounds: The magnetization studies are carried out to investigate the presence of any correlation between electrical and magnetic properties of the compound.
6. Thin film preparation to probe samples suitability for industrial applications: To the best of our knowledge so far no one has studied structural and electrical properties of BFN films in the high temperature region with conducting substrate Indium Tin Oxide (ITO). The ITO coated glass substrate is found to be a suitable conducting substrate due to its wide availability, low cost, good conductivity and good lattice constant matching. Similar electrical studies are carried out on the thin films of same compositions prepared by PLD technique on ITO coated glass substrate. Studies of such films will focus on the effect of reduction in dimension on dielectric properties of compound.
7. Effects of SHI irradiation on tunability of films physical properties: The effect of Swift Heavy Ion (SHI) irradiation on samples structure and microstructure stability was also been studied. Further, the SHI irradiation effect on technologically important NTCR-PTCR transition up to high temperature region is discussed from the application point of view.

References:

1. S. Saha and T.P. Sinha, J. Phys. Condens. Matter. **14,** 249 (2002).
2. S. Saha and T.P. Sinha. Phys. Rev. B. **65,** 134103 (2002).

3. I. P. Raevski, S. A. Kuropatkina, S. P. Kubrin, S. I. Raevskaya, V. V. Titov, D. A. Sarychev, M. A. Malitskaya, A. S. Bogatin and I. N. Zakharchenko, Ferroelectrics. **379(1),** 48 (2009).
4. S. Eitssayeam, U. Intatha, K. Pengpat, T. Tunkasiri, Science Direct. **6,** 316 (2006).
5. C. Y. Chung, Y. H. Changa, G. J. Chenb, Y. L. Chaic, Science Direct. **284,** 100 (2005).
6. Z. Wang, X. M. Chen, L. Ni, and X. Q. Liu, App. Phys. Lett. **90,** 022904 (2007).
7. I. P. Raevski, S. A. Prosandeev, A. S. Bogatin, M.A. Malitskaya, L. Jastrabik, J. Appl. Phys. **93,** 4130 (2003).
8. C. Y. Chung, Y. H. Chang, G. J. Chen and Y. L. Chai, J. Cryst. Growth. **284,** 100 (2005).
9. U. Intatha, S. Eitssayeam, J. Wang and T. Tunkasiri, Curr. Appl. Phys. **10,** 21 (2010).
10. S. Eitssayeam, U. Intatha, K. Pengpat, T. Tunkasiri, Curr. Appl. Phys. **6**, 316 (2006).
11. S. Ke, H. Fan and H. Huang, J. Electroceram. **22,** 252 (2009).
12. D. Bochenek, Z. Surowiak, J. P. Vejpravova, J. Alloys. Comp. **487,** 572 (2009).
13. N. Rama, J. B. Philipp, M. Opel, K. Chandrasekaran and V. Sankaranarayanan, J. Appl. Phys. **95,** 7528 (2004).
14. R. Blinc, P. Cevc, A. Zorko, J. Holc, M. Kosec, Z. Trontelj, J. Pirnat, N. Dalal, V. Ramachandran, and J. Krzystek, J. Appl. Phys. **101,** 033901 (2007).

CHAPTER 3

Experimental Procedure

(Sample Preparation, Instrumentation and Characterization Techniques)

The sample preparation techniques for bulk and thin films are presented in the initial part. The manufacturing of high temperature muffle furnace with its safety precaution and working parameters is explained here. The detailed technique of fabrication and optimization of dielectric sample holders with built-in perfect EMI shielding for two different temperature regions (High temperature and Low temperature) are briefly mentioned in this chapter. The structural, micro structural, optical, electrical and magnetic characterization techniques along with the parameters considered for present work are mentioned here.

3.1 Sample Preparation:

To study the origin of giant dielectric constant we synthesized the complex ceramic compounds having double perovskite structure. The compounds are prepared by substitution (partially or fully) at Fe-site in $Ba(Fe_{0.5}Nb_{0.5})O_3$ (BFN). The elements used are; Co, Mn, Y, Gd, Eu, etc. The selection of these elements is done on the basis of ionic radii, tolerance factor, stability, of charged state and affinity of hybridization with oxygen 2p level. The easiest method to synthesize these compounds is solid state reaction technique generally known as ceramic synthesis route. The detail of this method is briefly discussed here. In addition the thin films of few compounds were also developed to focus the industrial applications of these compounds. The easiest, cheapest and most efficient pulsed laser deposition (PLD) technique is utilized for thin film preparation. This technique along with the film preparation parameters is discussed here. In order to investigate the swift heavy ion irradiation effects on the thin film samples, the films were irradiated with the help of particle accelerator. The swift heavy ion irradiation and preparation of irradiated samples are summarized here.

3.1.1 Solid State Reaction Technique: (Bulk Ceramic Sample Preparation):

In general the chemical composition of the material takes place in either liquid state, molten flux or gaseous state. Some times such reaction takes place in appropriate solutions. The solid-state reaction technique neither involves any molts nor uses any solvents, liquids or gases. This reaction always occurs in solid state only. The solid state reaction technique is widely used technique for production of polycrystalline ceramic compounds [1]. At room temperature usually solids do not interact with each other therefore solid state reaction requires extreme conditions like high temperature, high pressure, etc. The solid state reaction kinetics between two solids depends on the following parameters:

1. Area of contact between reacting solids: The area of contact can be maximized by reducing the particle size of initial raw powder of starting chemicals.
2. Physical diffusion of molecules: Batter diffusion of the different raw powders at the atomic level encourages the reaction between molecules.
3. Rate of nucleation: The rate of nucleation can be maximized by using reactants with crystal structures similar to that of the product.
4. Reaction temperature: The proper selection of the reaction temperature is very important to prevent the volatilization of raw chemicals and to provide enough energy to initiate the successful reaction.

5. Duration of heat treatment: The duration of heat treatment can be decided on the basis of the fact that the duration of the solid state reaction would be different for different products.

On the basis of above parameters the solid state reaction technique can be divided in to five steps:

1. Selection of appropriate starting materials: The starting raw oxides of high purity (>99.9%) are selected on the basis of their particle size and structure. The fine grained powders with similar crystal structure like final product enhances the area of contact as well as the rate of reaction.
2. Stoichiometric weighing: To minimize the chemical compositional defects the stoichiometric weighing is carried out on the basis of the formula unit, formula weight and molecular weight of raw chemicals and final compound.
3. Particle size mixing and grinding: The stoichiometric proportions of the powders are then mixed together using pestle and mortar. The homogeneous and particle size mixing is achieved by the wet mixing technique (by adding few drops of extra pure acetone). The repeated grinding is performed on such mixture to enhance the homogeneity as well as to reduce the particle size. This results in increased surface area leading to fast nucleation of final compound. Further, the increased homogeneity assures us the reduction of chemical compositional defects.
4. Pelletization: The well mixed powders are then pelletized in the form of circular disks of diameter ~13 mm at the pressure of 0.5 ton or less. Such pelletization increases the physical diffusion between molecules which encourages the reaction.
5. Heat treatment : This step is final and significant step of solid state reaction technique. The actual phase formation and final sample preparation is done in this step. The whole heat treatment process is separated in to three sub steps according to the development of final compound.
    a. Calcinations: The actual phase of the final compound is formed at this level. The homogeneously mixed and well grinded fine powders are pelletized with very low pressure at this stage. The pressure is just sufficient to increase the physical diffusion. Such pallets are fired at higher temperatures ranging from 1100 °C to 1300 °C (for details see Table 3.1) for six hours at controlled heating/cooling rate using self prepared programmable muffle furnace. The selection of appropriate temperature is done on the basis of volatilization of raw

powders and their melting points. At this stage the temperatures are below the melting/volatilization temperature.

b. Sintering: The densification of sample is done at this stage. The calcined pallets are grinded again using pestle and mortal. These powders are compacted in to circular disks again with high pressure up to 10 tons to encourage intimate contact between tiny crystallites. Such pellets are fired at temperatures ranging from 1100 °C to 1500 °C (for details see Table 3.1) for six hours which is little higher temperature than the calcination temperature and just bellow the melting point of the compound. This results in well sintered hard pellets.
c. Annealing: The sintered pellets are fired again at same temperature for 24 to 48 hours. During this process the crystallites grow larger and larger. Such larger crystallites come closer and form a well defined grain and grain boundaries in turn increase the densification of sample.

At the end of this step we get well sintered and annealed hard pallet for further characterization.

Features / benefits of solid state reaction technique :

- ✓ Usually this reaction is thermodynamically stable and ends up with inert products.
- ✓ It helps in preparing dense materials of low surface area.

Drawbacks of solid state reaction technique :

- ✗ It requires very high temperatures (1500 °C) to initiate the reaction.
- ✗ The reaction is little difficult because of slow diffusion rate of solid ions.
- ✗ The chemical compositional defects as well as macroscopic structural defects are inherent part of this technique.

On the basis of above fundamentals and facts the synthesis parameters like calcination temperature, sintering temperature and annealing temperature along with duration of heat treatment and heating / cooling rate of each sample is determined. All these parameters along with sample code and chemical formula used in the present work are presented in Table 3.1. Further, important parameters essential for the formation of the perovskite structure like tolerance factor, B site ionic radii and most stable charge state of B' site atom are also been presented in the Table 3.1.

Sr. No	Sample	Formula	Formula Weight (g/mole)	Average B' Site Radius (Å)	Over all B Site Average Radius (Å)	Tolerance Factor $t = \frac{(R_A + R_O)}{\sqrt{2}(R_B + R_O)}$	B' Site Atom	Most Stable Charge State of B' Site	Calcination Stage		Sintering Stage		*Duration of Heat Treatment Annealing
									Temperature °C	Duration of heat treatment	Temperature °C	Duration of heat treatment	
1	BFN	$Ba(Fe_{0.5}Nb_{0.5})O_3$	259.701	0.6450	0.6425	1.042	Fe	+3	1100	6h	1200	12h	24h
2	BFCN-10C	$Ba(Fe_{0.40}Co_{0.10}Nb_{0.5})O_3$	260.010	0.6380	0.6390	1.044	Fe Co	+3 +2	1100	6h	1150	12h	24h
3	BFCN	$Ba(Fe_{0.25}Co_{0.25}Nb_{0.5})O_3$	260.473	0.6275	0.6338	1.047	Fe Co	+3 +2	1100	6h	1150	12h	24h
4	BFCN-40C	$Ba(Fe_{0.10}Co_{0.40}Nb_{0.5})O_3$	260.936	0.6170	0.6285	1.049	Fe Co	+3 +2	1100	6h	1150	12h	24h
5	BCN	$Ba(Co_{0.5}Nb_{0.5})O_3$	261.245	0.6100	0.6250	1.051	Co	+2	1100	6h	1100	12h	24h
6	BMN	$Ba(Mn_{0.5}Nb_{0.5})O_3$	259.247	0.6500	0.6450	1.041	Mn	+2	1100	6h	1175	12h	24h
7	BFMN	$Ba(Fe_{0.25}Mn_{0.25}Nb_{0.5})O_3$	259.474	0.6475	0.6438	1.041	Fe Mn	+3 +2	1150	6h	1250	12h	24h
8	BGN	$Ba(Gd_{0.5}Nb_{0.5})O_3$	310.403	0.9380	0.7890	0.972	Gd	+3	1300	12h	1500	24h	48h
9	BFGN	$Ba(Fe_{0.25}Gd_{0.25}Nb_{0.5})O_3$	285.052	0.7915	0.7158	1.006	Fe Gd	+3 +3	1150	12h	1250	24h	24h
10	BEN	$Ba(Eu_{0.5}Nb_{0.5})O_3$	307.758	0.9500	0.7950	0.970	Eu	+3	1250	12h	1500	24h	48h
11	BFEN	$Ba(Fe_{0.25}Eu_{0.25}Nb_{0.5})O_3$	283.730	0.7975	0.7188	1.005	Fe Eu	+3 +3	1150	12h	1250	24h	24h
12	BYN	$Ba(Y_{0.5}Nb_{0.5})O_3$	276.231	0.9000	0.7700	0.981	Y	+3	1250	12h	1500	24h	48h
13	BGCN-10C	$Ba(Gd_{0.40}Co_{0.10}Nb_{0.5})O_3$	300.572	0.8724	0.7562	0.987	Gd Co	+3 +2	1100	12h	1200	24h	24h
14	BGCN	$Ba(Gd_{0.25}Co_{0.25}Nb_{0.5})O_3$	285.824	0.7740	0.7070	1.010	Gd Co	+3 +2	1100	12h	1200	24h	24h
15	BECN	$Ba(Eu_{0.25}Co_{0.25}Nb_{0.5})O_3$	284.502	0.7800	0.7100	1.009	Eu Co	+3 +2	1100	12h	1200	24h	24h

The rate of heating and cooling during all cycles was 120°C/h. * Annealing temperature is same as the sintering temperature only duration of heat treatment was different. The structure can be predicted using value of tolerance factor; for cubic structure $0.75<t<1.00$. All structures are predicted to be cubic.

Table 3.1: Details of prepared bulk samples, prediction of structure (using tolerance factor) and sample preparation parameters.

3.1.2 Pulsed Laser Deposition (PLD) Technique: (Thin Film Sample Preparation):

Pulsed laser deposition (PLD) technique is widely used technique [2] in the materials processing industry due to its advantageous features over other film deposition techniques. The film growth issues like stoichiometry of the film, epitaxial growth, minimization of impurities and strain free film are well resolved in PLD technique. The PLD is useful to deposit many materials that are normally difficult to deposit by other methods, e.g. multi component materials, complex oxides etc. The principle of pulsed laser deposition is a very complex physical phenomenon. It involves ablation of material in terms of plasma plume which is to be deposited on the heated substrate.

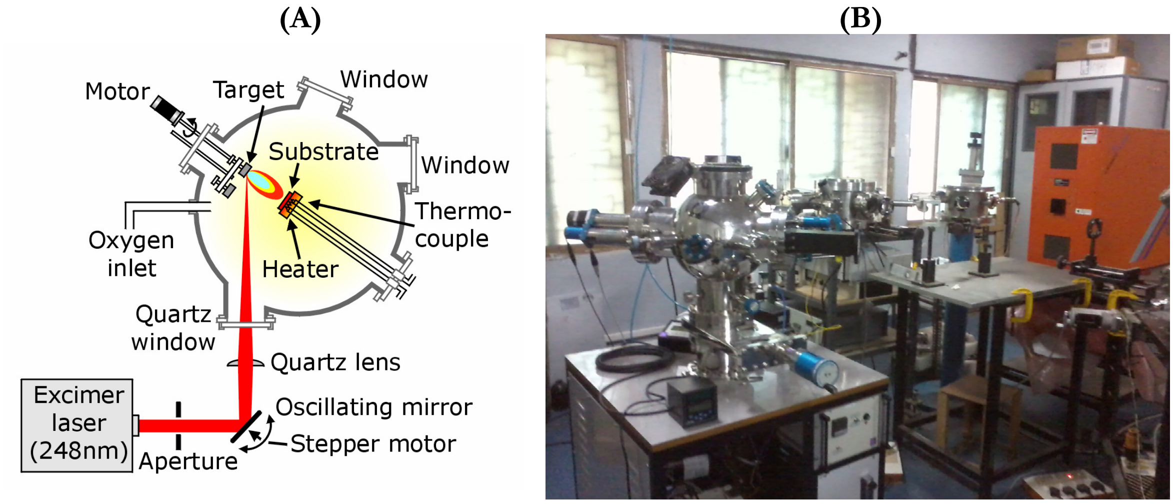

Figure 3.1: (A) Schematic diagram of Pulsed Laser Deposition technique. (B) The instrumental setup of PLD at UGC-DAE-CSR Indore centre.

The process of PLD can generally be divided into four stages:

1. Laser ablation of the target material and creation of plasma: The high-power excimer laser beam is focused on the target which is sufficient to melt and evaporate few molecules retaining its stoichiometry. This laser energy can be tuned using proper wavelength and repetition rate of the laser beam. The evaporated molecules retain the molecular structure of the target and create a plasma plume.
2. Dynamic of the plasma: Such ablated plasma plume move towards the substrate. The plasma plume will disperse inside the chamber due to presence of vacuum inside the chamber.
3. Deposition of the ablation material on the substrate: The stoichiometric plasma now reaches at the heated surface of the substrate placed a short distance from the target. The substrate heating helps in homogeneous growth of the film.

4. Nucleation and growth of the film on the substrate surface: The equilibrium between material ablation and condensation leads to the nucleation of crystallites on the surface of the substrate. Thus film grows on the surface of the substrate. The thickness of the deposited film depends on target material, energy of laser pulse, target to substrate distance and type of gas pressure in the chamber.

Each of these steps is crucial for the crystallinity, uniformity and stoichiometry of the resulting film.

The main advantages of Pulsed Laser Deposition technique over other techniques are:

- ✓ The films with similar stoichiometry as target can be prepared.
- ✓ It is very simple technique
- ✓ Majority materials like metals, metal oxides, semiconductors can be deposited in a wide variety of gaseous atmosphere.
- ✓ This technique is cost-effective for mass production of films.
- ✓ This technique is very fast compared to other techniques.

Demerits of PLD technique:

- ✗ It is difficult to grow large films.
- ✗ Proper energy selection is necessary for stoichiometry of the film.
- ✗ Plume of molecules may evaporate if proper laser energy is not supplied. This causes bad quality films
- ✗ Film composition and thickness depend on deposition conditions.
- ✗ Insulator having higher band gap can not be deposited by this technique.

In summary the PLD technique is most commonly used simplest technique to prepare films of complex compounds at large scale.

Thin films of few selected complex ceramic compounds (see Table 3.2) were deposited by PLD technique. Indium tin oxide (ITO) coated glass was utilized as conducting substrate. The bulk targets of ceramic compounds were synthesized in pure single phase by conventional solid state reaction technique. The well sintered disks of 25 mm diameter and 4 - 6 mm thickness were utilized as PLD target. The substrate was mounted at 3.5 - 4 cm from the target after ultrasonic cleaning for 10 min with acetone and then methanol. The laser source of 248 nm wavelength and 220 mJ energy with repetition rate of 10 Hz was utilized for deposition. The deposition chamber was evacuated down to a base pressure of 1×10^{-5} torr before deposition. The deposition was carried out at 300 °C - 400 °C with oxygen partial pressure of 250 m torr for 30 - 40 minutes. After deposition the chamber was completely filled with the oxygen and then cooled down to room temperature. The as deposited films were annealed in air atmosphere at 600 °C up to 1 hour for batter crystallinity [3]. The detailed deposition conditions for each film with sample code are listed in Table 3.2.

Sr. No.		1	2	3	4	5	6	7	8
Prepared Film Sample		BFN-1	BFN-2	BFCN	BCN	BMN-1	BMN-3	BGCN-1	BGCN-2
Film Deposition Parameters	Target Substrate Distance	4 cm	3.5 cm	3.5 cm	3.5 cm	3.5 cm	3.5 cm	3.5 cm	3.5 cm
	Substrate Temperature	300 °C	400 °C	400 °C	400 °C	300 °C	400 °C	400 °C	400 °C
	Deposition Time	40 m	40 m	40 m	40 m	60 m	40 m	40 m	40 m

Some Common Film Deposition Parameters:

Laser Energy : 220 mJ
Energy Density : 9.5 J/cm^2
Laser Wavelength : 248 nm
Repetition Rate : 10 Hz
Substrate : ITO/Glass
Initial Vacuum : 1×10^{-5} Torr
Oxygen Partial Pressure : 250 mTorr
Substrate Cooling Environment : Oxygen filled up to 1 atm.

Post Heat Treatment : Annealing at 600 °C for 1 h.

Table 3.2: The details of thin film samples prepared using PLD along with film deposition parameters.

3.1.3 Swift Heavy Ion (SHI) Irradiation:

Swift heavy ion irradiation is one type of particle radiation treatment through which physical properties of the materials can be modified. The proper selection of projectile particles, particle fluence and energy of the particle beam enable us to tune the desirable properties of the material. The Swift Heavy Ions are accelerated using the particle accelerators. Such accelerated high energy ions penetrate the solids and loose their energy mainly by electronic stopping over nuclear stopping. The energy loss by electronic stopping releases heat and creates straight line track containing amorphous material of few nanometer diameter. The energy transfer between the heavy projectile ion and the target are described using two different models.

1. **Thermal Spike Model:** According to this model the accelerated particles interact with the target and loose their energy according to the radiation sensitivity of the target. The radiation sensitivity of different materials depends on their thermal conductivity and their melting temperature. If the temperature produced by irradiation exceeds the melting temperature a liquid is formed. This heat is rapidly absorbed by the surrounding results in quenching of the local area. This creates cylinder of disordered material along the path of the projectile [4-5].

2. **Coulomb Explosion Model:** According to this model when charged projectile enters the surface of target it experience strong electromagnetic field into the atomic motion. Here the repulsion between the like charges can break the bonds of target. This results in local explosion of solid in terms of plasma creation. This results in local defects along the ion track [5].

Ultimately through either heating mechanism the swift heavy ions generates cylindrical track of amorphous material.

In the present work SHI irradiation study was performed using pelletron accelerator at IUAC, New Delhi. For irradiation, the films were mounted on a copper target ladder using silver paste inside a vacuum of 1×10^{-6} torr. Films were irradiated at room temperature using O^{7+} / Ag^{15+} ions having energy of 98 MeV / 200 MeV for different fluences viz. 5×10^{11}, 1×10^{12}, 5×10^{12} and 1×10^{13} ions per cm^2. The details of the irradiation for pristine films having suffix P (without irradiation) along with irradiated films having suffix A, B, C and D (respectively for fluence 1×10^{12} ions per cm^2, 5×10^{12} ions per cm^2, 1×10^{13} ions per cm^2 and 5×10^{11} ions per cm^2) are presented in the Table 3.3.

Sr. No.	Sample	Sample Details	Irradiation beam type	Irradiation Beam Energy	Irradiation Fluence (ions per cm^2)
1	BFN-1	As Prepared	-	-	-
2	BFN-1-An-P	Annealed	-	-	-
3	BFN-1-An-A	Annealed and Irradiated	O^{7+}	98 MeV	1×10^{12}
4	BFN-1-An-B	Annealed and Irradiated	O^{7+}	98 MeV	5×10^{12}
5	BFN-1-An-C	Annealed and Irradiated	O^{7+}	98 MeV	1×10^{13}
6	BFN-2	As Prepared	-	-	-
7	BFN-2-An-P	Annealed	-	-	-
8	BFN-2-An-A	Annealed and Irradiated	O^{7+}	98 MeV	1×10^{12}
9	BFN-2-An-B	Annealed and Irradiated	O^{7+}	98 MeV	5×10^{12}
10	BFN-2-An-C	Annealed and Irradiated	O^{7+}	98 MeV	1×10^{13}
11	BFCN	As Prepared	-	-	-
12	BFCN-An-P	Annealed	-	-	-
13	BFCN-An-A	Annealed and Irradiated	O^{7+}	98 MeV	1×10^{12}
14	BFCN-An-B	Annealed and Irradiated	O^{7+}	98 MeV	5×10^{12}
15	BFCN-An-C	Annealed and Irradiated	O^{7+}	98 MeV	1×10^{13}
16	BCN	As Prepared	-	-	-
17	BCN-An-P	Annealed	-	-	-
18	BCN-An-A	Annealed and Irradiated	O^{7+}	98 MeV	1×10^{12}
19	BCN-An-B	Annealed and Irradiated	O^{7+}	98 MeV	5×10^{12}
20	BCN-An-C	Annealed and Irradiated	O^{7+}	98 MeV	1×10^{13}
21	BMN-1	As Prepared	-	-	-
22	BMN-1-An-P	Annealed	-	-	-
23	BMN-1-An-A	Annealed and Irradiated	O^{7+}	98 MeV	1×10^{12}

Sr. No.	Sample	Sample Details	Irradiation beam type	Irradiation Beam Energy	Irradiation Fluence (ions per cm^2)
24	BMN-1-An-B	Annealed and Irradiated	O^{7+}	98 MeV	5×10^{12}
25	BMN-1-An-C	Annealed and Irradiated	O^{7+}	98 MeV	1×10^{13}
26	BMN-3	As Prepared	-	-	-
27	BMN-3-An-P	Annealed	-	-	-
28	BMN-3-An-A	Annealed and Irradiated	O^{7+}	98 MeV	1×10^{12}
29	BMN-3-An-B	Annealed and Irradiated	O^{7+}	98 MeV	5×10^{12}
30	BMN-3-An-C	Annealed and Irradiated	O^{7+}	98 MeV	1×10^{13}
31	BGCN-1	As Prepared	-	-	-
32	BGCN-1-An-P	Annealed	-	-	-
33	BGCN-1-An-D	Annealed and Irradiated	Ag^{15+}	200 MeV	5×10^{11}
34	BGCN-1-An-A	Annealed and Irradiated	Ag^{15+}	200 MeV	1×10^{12}
35	BGCN-1-An-B	Annealed and Irradiated	Ag^{15+}	200 MeV	5×10^{12}
36	BGCN-2	As Prepared	-	-	-
37	BGCN-2-An-P	Annealed	-	-	-
38	BGCN-2-An-A	Annealed and Irradiated	O^{7+}	98 MeV	1×10^{12}
39	BGCN-2-An-B	Annealed and Irradiated	O^{7+}	98 MeV	5×10^{12}
40	BGCN-2-An-C	Annealed and Irradiated	O^{7+}	98 MeV	1×10^{13}

Table 3.3: The details of thin film samples with their irradiation conditions.

3.1.4 Summary of Prepared Samples: (Bulk and Thin Film Samples):

The samples to be investigated are classified in two different categories; Bulk ceramic samples and thin film samples. These samples are sub classified in several groups for the ease of comparative and comprehensive analysis.

Bulk samples (Classified in the group of seven different series)

1. 100% series - [$Ba(X_{0.5}Nb_{0.5})O_3$] where X=Fe, Co, Mn, Gd, Eu, Y.
    a. BFN - $Ba(Fe_{0.5}Nb_{0.5})O_3$
    b. BCN - $Ba(Co_{0.5}Nb_{0.5})O_3$
    c. BMN - $Ba(Mn_{0.5}Nb_{0.5})O_3$
    d. BGN - $Ba(Gd_{0.5}Nb_{0.5})O_3$
    e. BEN - $Ba(Eu_{0.5}Nb_{0.5})O_3$
    f. BYN - $Ba(Y_{0.5}Nb_{0.5})O_3$
2. BFCN series - [$Ba(Fe_{0.5-X}Co_XNb_{0.5})O_3$] where X=0, 0.10, 0.25, 0.40, 0.50
    a. BFN - $Ba(Fe_{0.5}Nb_{0.5})O_3$
    b. BFCN-10C - $Ba(Fe_{0.40}Co_{0.10}Nb_{0.5})O_3$
    c. BFCN - $Ba(Fe_{0.25}Co_{0.25}Nb_{0.5})O_3$
    d. BFCN-40C - $Ba(Fe_{0.10}Co_{0.40}Nb_{0.5})O_3$
    e. BCN - $Ba(Co_{0.5}Nb_{0.5})O_3$
3. BFMN series - [$Ba(Fe_{0.5-X}Mn_XNb_{0.5})O_3$] where X=0, 0.25, 0.50

   a. BFN - $Ba(Fe_{0.5}Nb_{0.5})O_3$
   b. BFMN - $Ba(Fe_{0.25}Mn_{0.25}Nb_{0.5})O_3$
   c. BMN - $Ba(Mn_{0.5}Nb_{0.5})O_3$

4. BFGN series - $[Ba(Fe_{0.5-X}Gd_XNb_{0.5})O_3]$ where X=0, 0.25, 0.50
   a. BFN - $Ba(Fe_{0.5}Nb_{0.5})O_3$
   b. BFGN - $Ba(Fe_{0.25}Gd_{0.25}Nb_{0.5})O_3$
   c. BGN - $Ba(Gd_{0.5}Nb_{0.5})O_3$

5. BFEN series - $[Ba(Fe_{0.5-X}Eu_XNb_{0.5})O_3]$ where X=0, 0.25, 0.50
   a. BFN - $Ba(Fe_{0.5}Nb_{0.5})O_3$
   b. BFEN - $Ba(Fe_{0.25}Eu_{0.25}Nb_{0.5})O_3$
   c. BEN - $Ba(Eu_{0.5}Nb_{0.5})O_3$

6. BGCN series - $[Ba(Gd_{0.5-X}Co_XNb_{0.5})O_3]$ where X=0, 0.10, 0.25, 0.50
   a. BGN - $Ba(Gd_{0.5}Nb_{0.5})O_3$
   b. BGCN-10C - $Ba(Gd_{0.40}Co_{0.10}Nb_{0.5})O_3$
   c. BGCN - $Ba(Gd_{0.25}Co_{0.25}Nb_{0.5})O_3$
   d. BCN - $Ba(Co_{0.5}Nb_{0.5})O_3$

7. BECN series - $[Ba(Eu_{0.5-X}Co_XNb_{0.5})O_3]$ where X=0, 0.25, 0.50
   a. BEN - $Ba(Fe_{0.5}Nb_{0.5})O_3$
   b. BECN - $Ba(Eu_{0.25}Co_{0.25}Nb_{0.5})O_3$
   c. BCN - $Ba(Co_{0.5}Nb_{0.5})O_3$

Thin film samples (Classified in the five different groups)

1. BFN-1 films (substrate temperature 300 °C.)
   a. BFN-1 - As prepared
   b. BFN-1-An-P - Annealed
   c. BFN-1-An-A - Annealed and irradiated with O^{7+} fluence 1×10^{12}
   d. BFN-1-An-B - Annealed and irradiated with O^{7+} fluence 5×10^{12}
   e. BFN-1-An-C - Annealed and irradiated with O^{7+} fluence 1×10^{13}

2. BFN-2 films (substrate temperature 400 °C.)
   a. BFN-2 - As prepared
   b. BFN-2-An-P - Annealed
   c. BFN-2-An-A - Annealed and irradiated with O^{7+} fluence 1×10^{12}
   d. BFN-2-An-B - Annealed and irradiated with O^{7+} fluence 5×10^{12}
   e. BFN-2-An-C - Annealed and irradiated with O^{7+} fluence 1×10^{13}

3. BFCN films (substrate temperature 400 °C.)
   a. BFCN - As prepared
   b. BFCN-An-P - Annealed
   c. BFCN-An-A - Annealed and irradiated with O^{7+} fluence 1×10^{12}
   d. BFCN-An-B - Annealed and irradiated with O^{7+} fluence 5×10^{12}
   e. BFCN-An-C - Annealed and irradiated with O^{7+} fluence 1×10^{13}

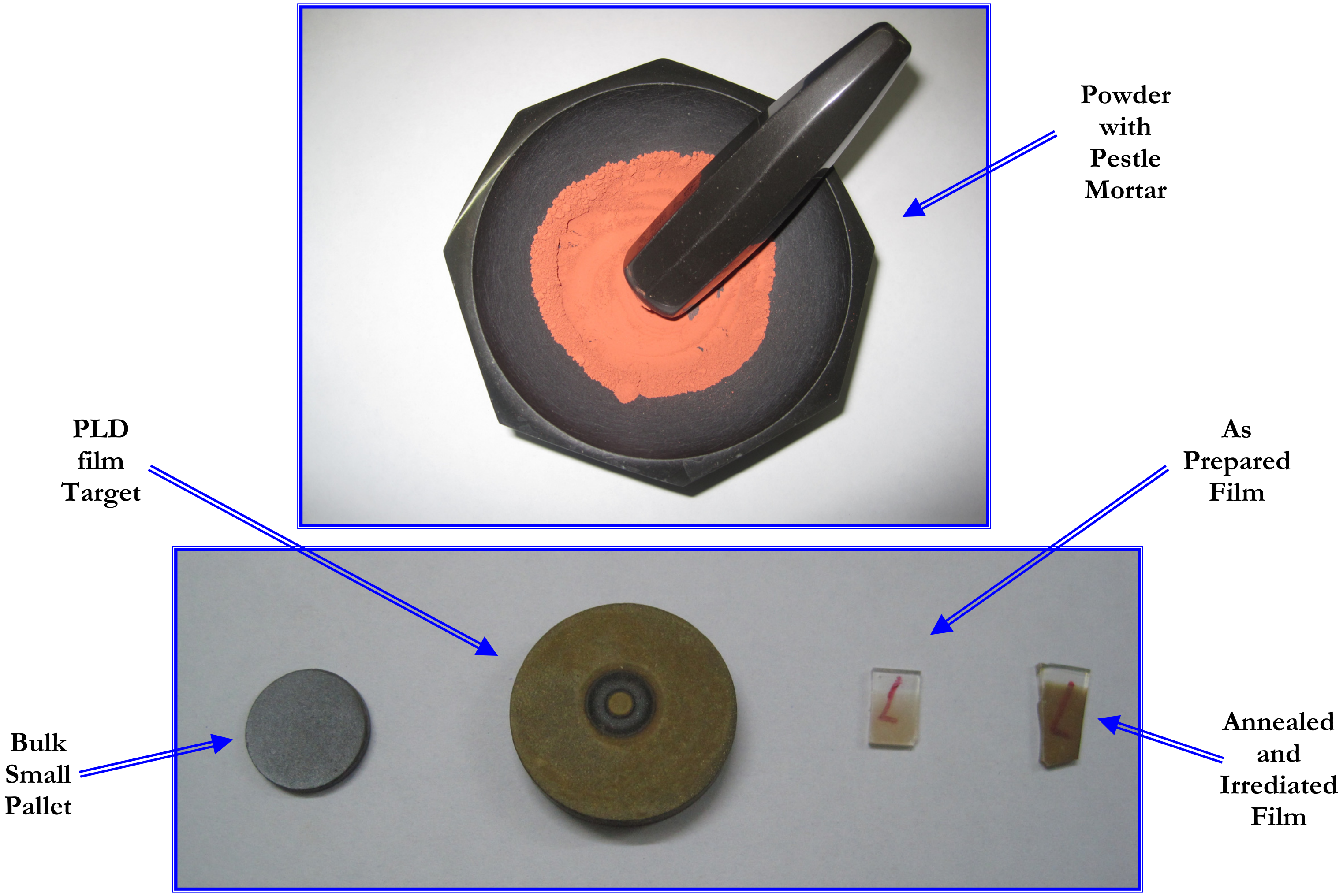

Figure 3.2: The images of prepared samples: pestle-mortar powder, bulk small pallet, PLD target, as prepared film and irradiated film.

4. BCN films (substrate temperature 400 °C.)
    a. BCN - As prepared
    b. BCN-An-P - Annealed
    c. BCN-An-A - Annealed and irradiated with O^{7+} fluence 1×10^{12}
    d. BCN-An-B - Annealed and irradiated with O^{7+} fluence 5×10^{12}
    e. BCN-An-C - Annealed and irradiated with O^{7+} fluence 1×10^{13}
5. BMN-1 films (substrate temperature 300 °C.)
    a. BMN-1 - As prepared
    b. BMN-1-An-P - Annealed
    c. BMN-1-An-A - Annealed and irradiated with O^{7+} fluence 1×10^{12}
    d. BMN-1-An-B - Annealed and irradiated with O^{7+} fluence 5×10^{12}
    e. BMN-1-An-C - Annealed and irradiated with O^{7+} fluence 1×10^{13}
6. BMN-3 films (substrate temperature 400 °C.)
    a. BMN-3 - As prepared
    b. BMN-3-An-P - Annealed
    c. BMN-3-An-A - Annealed and irradiated with O^{7+} fluence 1×10^{12}
    d. BMN-3-An-B - Annealed and irradiated with O^{7+} fluence 5×10^{12}
    e. BMN-3-An-C - Annealed and irradiated with O^{7+} fluence 1×10^{13}
7. BGCN-1 films (substrate temperature 400 °C.)
    a. BGCN-1 - As prepared
    b. BGCN-1-An-P - Annealed
    c. BGCN-1-An-A - Annealed and irradiated with O^{7+} fluence 1×10^{12}
    d. BGCN-1-An-B - Annealed and irradiated with O^{7+} fluence 5×10^{12}
    e. BGCN-1-An-C - Annealed and irradiated with O^{7+} fluence 1×10^{13}
8. BGCN-2 films (substrate temperature 400 °C.)
    a. BGCN-2 - As prepared
    b. BGCN-2-An-P - Annealed
    c. BGCN-2-An-A - Annealed and irradiated with O^{7+} fluence 1×10^{12}
    d. BGCN-2-An-B - Annealed and irradiated with O^{7+} fluence 5×10^{12}
    e. BGCN-2-An-D - Annealed and irradiated with O^{7+} fluence 5×10^{11}

3.2 Instrumentation:

The designing and fabrication of;

1. Programmable high temperature muffle furnace
2. Sample holders for electrical characterization
    a. Programmable high temperature sample holder
    b. Programmable low temperature sample holder

are briefly summarized in this section.

3. 2.1 Designing and Fabrication of Programmable High Temperature Muffle Furnace: (Working Temperature Up to 1500 °C.)

Motivation:

The solid state reaction technique of sample preparation requires high temperature muffle furnace. The conventional available box furnaces are having kanthal or super kanthal alloy wires as heating elements. The limitation of such heating element is they can not produce temperatures more than 1200 °C, as their melting point is near around 1300 °C. Such conventional box furnaces are unable to serve the purpose of providing heat treatment at elevated temperatures. Therefore to fulfill the requirement of one high temperature muffle furnace up to 1500 °C is designed.

Designing and Fabrication with Calculation:

The heating elements of silicon carbide (SIC) are utilized to handle such high temperatures. The dumbbell shape SIC rods with total length of 600 mm having average resistance of 3.5 Ω are mounted in series of six elements. Hence the total resistance of the furnace becomes 21 Ω through which maximum current of 11 A can flow when the furnace is connected with regular single phase AC source of 230V. This current is far below the maximum safe current limit of domestic house hold power source and accessories. The hot-zone length of the rod is 150 mm, hot-zone diameter is 8 mm and cold-zone diameter is 14 mm. The main inner core of the furnace is designed from the rectangular alumina box of 6”×6”×12” along with strips of moonlight stone (can sustain temperature up to 1800 °C). The high temperature and high density ceramic wool is wrapped around the core for batter insulation. The main frame of the furnace is prepared by welding the steel angles. The outer steel framework is then covered with asbestos sheets. The connection of rod with each other is main difficult task, as during continuous use the contacts handle very high temperatures with very high currents. At such extreme conditions the local sparking may melt the clips, connecting strips and wires. To eliminate any possibilities of such sparking, aluminum braid is used as buffer layer between the silvered end of rod and connecting strips. The connecting wires between two rods are also replaced by aluminum braid. Further to keep the connecting ends of the rod at much reduced temperature the all connections are kept in the air outside the insulation. The B-type thermocouple (Pt – Pt-Rh) is used to measure such high temperatures as it ensures more accuracy and reliability than other thermocouples.

Figure 3.3: The high temperature muffle furnace with the few memorable moments of fabrication.

Programming and Tuning:

The Selec-India make PID profile temperature controller, PR-502 is used to program and regulate the function of this furnace. The regulation of heating cooling rate, programmed ramping and soak-timings with 10 profile program each having 16 steps is possible using this controller. The PR-502 profile controller is available in two different control actions for linear DC output; 0-10V DC output and 4-20 mA DC output. This output of the controller regulates the high power of the furnace through relay. Here for batter power regulation 4-20 mA current output mode is selected with local available solid state relay. The whole assembly with proper connections is mounted in a control box at top of the furnace. The furnace is then tuned for the PID action.

3.2.2 Sample Holders for Electrical Characterization: (Having Perfect EMI Shielding with Temperature Range 80 K to 800 K):

Motivation:

In depth analysis of dielectric relaxation and electrical conduction, as a function of wide frequency and temperature range, is essential to understand the mechanism of relaxation/conduction. The available old sample holder for electrical measurement is unable to sustain high temperatures because of Teflon rod as its part. The softening temperature of typical Teflon rod is 500 K only, which limits the user to use this sample holder in the temperature range of 300 K – 500 K only. The electrodes of that old sample holder were prepared using spring loaded rods with pellet shaped electrodes. Electrode with such an assembly limits the size and shape of the sample to be measured. In addition whole assembly of sample holder is kept inside a furnace to increase its temperature. The furnace is made up from conventional accessory and is not having EMI shielding. Furnace of this kind can introduce large noises in the measured data at low frequency region, below 100 Hz. This further limits the user to collect data between 100 Hz – 1MHz only. Apart from this the whole system does not have any programmable controls. The temperature of the furnace is controlled manually using mechanical contact thermometer without any heating/cooling rate. Thus the available old sample holder is having limitations of temperature range, frequency range, sample shape and sample size along with very poor precision and accuracy in regulating the temperatures.

These essential requirements motivated myself to prepare sample holders which can be useful for very low frequency measurements (i.e. should have perfect EMI shielding) along with elevated temperature range of 80 K – 800 K. I prepared two different sample holders with perfect EMI shielding to overcome the limitations of the conventional sample holder: (1) High temperature sample holder – without vacuum (temperature range 300 K – 800 K) and (2) Low temperature sample holder – with vacuum (temperature range ~ 80 K – 350 K). The detailed technique of preparation and optimization of the sample-holder with perfect EMI shielding is explained here.

3.2.2.1 Programmable High Temperature Sample Holder: (Having Temperature Range 300 K to 800 K):

Designing and fabrication:

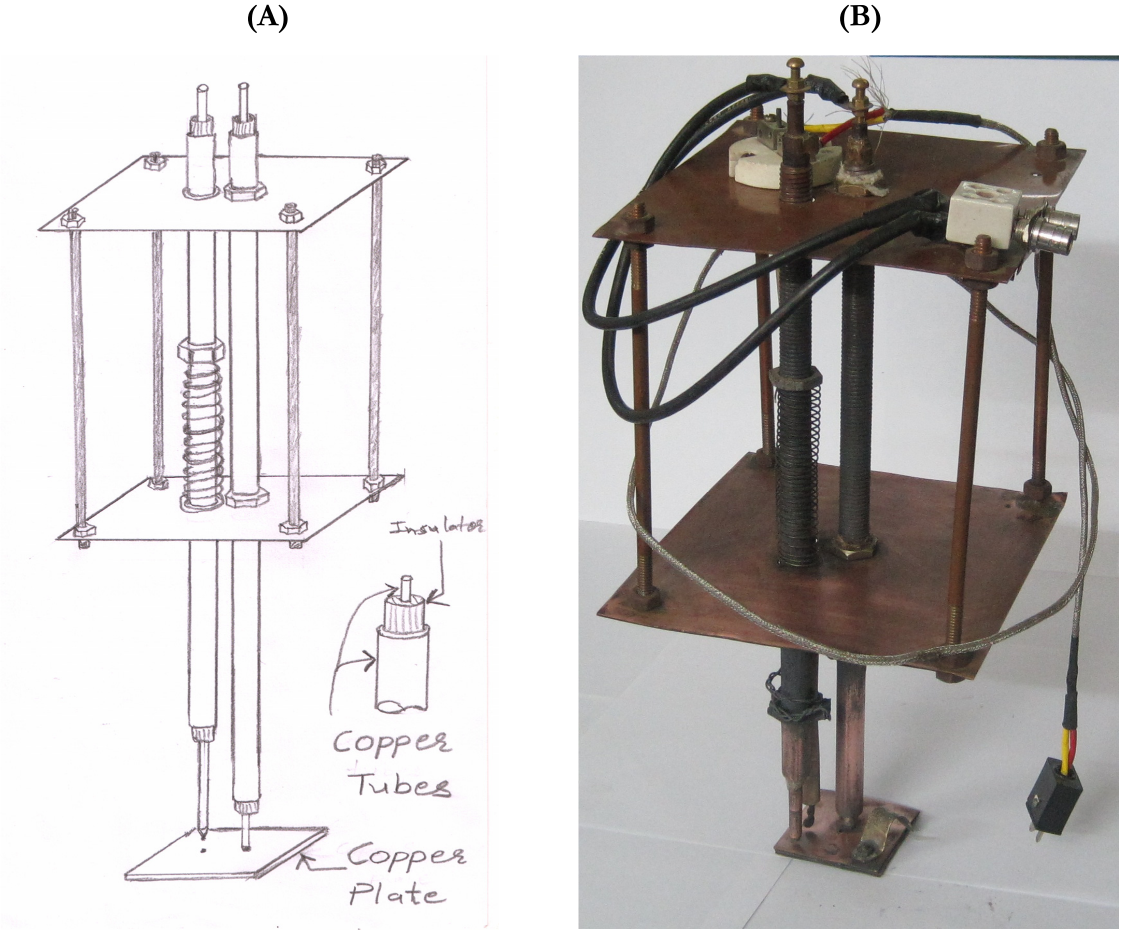

Figure 3.4: (A) A sketch of High Temperature sample holder. (B) Image of Prepared High temperature sample holder.

The perfect EMI shielding is essential requirement for low frequency measurements. To achieve this property I redesigned the furnace by selecting cylindrical metallic (stainless steel) core with metallic bottom base. The electrical winding of heating coil is separated from the metallic core using thin sheets of mica. The electrodes of the sample holder are designed in such a way that it remains co-axial up to the sample surface instead of a simple metallic rod. The co-axial electrodes are prepared using two hollow pipes of copper. The inner pipe and outer pipe are separated using glass-mica-glass sheets. Thus EMI shielding is achieved from the instrument leads to the sample surface through shielded connections of BNC cable with co-axial electrodes. To provide shielding at the sample mounting area, long vertical electrodes are designed with two horizontal metallic plates of copper as shown in the Figure 3.4. Such sample holder is then inserted inside the furnace having EMI shielding with metallic top lid. Thus the perfect EMI shielding is achieved to measure electrical data at low frequency region. Further the use of material like mica and metal enables us to use sample holder at higher temperatures up to 800 K. To make the sample mounting area compatible with any shape and size of sample the top electrode is made aero head with electrode diameter of just 1.5 mm^2. This modification made the sample holder more useful for variety of samples.

Programming, calibration and optimization:

To promise the precession and accuracy of temperature measurement the furnace functions are programmed with the help of PID temperature controller (PID-500, Selec India make) and solid state relay. The computerization of the setup is done with indirect arrangement. The batch measurement program of the instrument can measure multiple data with respect to time. The temperature can also be programmed to increase with time using ramp rate. Thus by combining these two different time dependent process we can collect data automatically at different temperatures in increasing order.

Further, in order to ensure the precision and consistency of the data the sample holder was calibrated by collecting data of a standard sample ($BaFe_{0.5}Nb_{0.5}O_3$) at three different instruments. The data were collected at IUAC New Delhi (Agilent 4284-A precision LCR meter), UGC-DAE-CSR, Indore (Novocontrol Alpha A high performance frequency analyzer) and at our department on self prepared sample holder (using Solartron 1260 Impedance Analyzer). We found significant deviation in the data collected using newly prepared sample holder. The sample holder as well as the data collection software is then optimized by inserting short circuit and open circuit nulling files. After completing this calibration we again collected the data using modified data collection software. The collected data for calibration were found in accordance with the data collected on other instrument.

3.2.2.2 Programmable Low Temperature Sample Holder: (Having Temperature Range 80 K (LN_2) to 350 K):

Designing and Fabrication:

In order to facilitate the complete understanding of the electrical processes in these compounds, low temperature measurements were required. The vacuum is an essential requirement of low temperature sample holder because the surrounding air and moisture can easily condense on the surface of the sample at Liquid nitrogen (LN_2) temperature. In low temperature sample holder the stainless steel pipes and cup are welded as shown in the Figure 3.5 to prepare the base structure of sample holder. All the joints are connected with vacuum connectors. The perfect EMI shielding at low temperatures inside the pipe is achieved by preparing coaxial metallic tubes. Such co-axial tubes are prepared using thin stainless steel tubes and stainless steel wire (of 1mm diameter) at its axis separated by alumina bids.

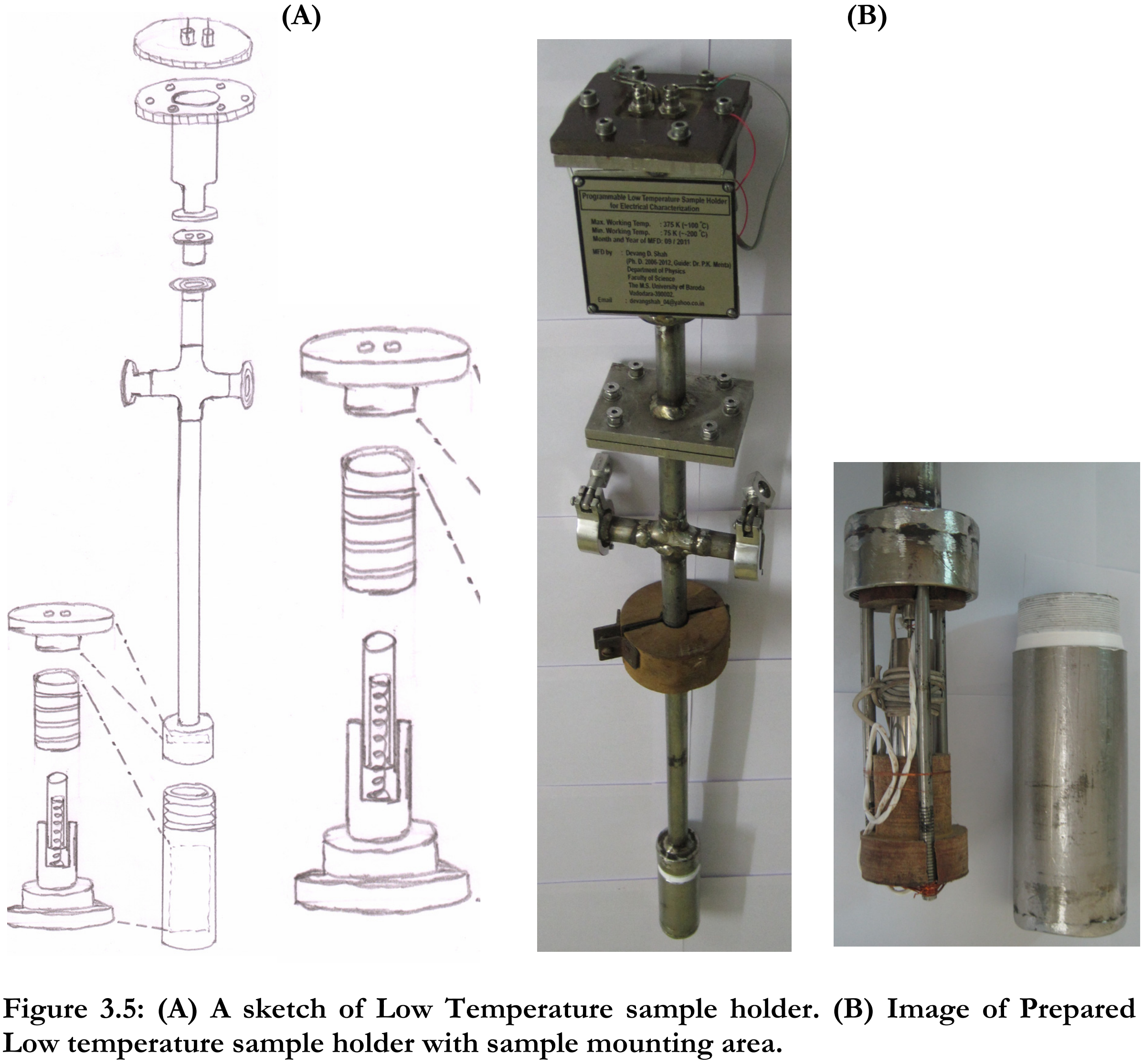

Figure 3.5: (A) A sketch of Low Temperature sample holder. (B) Image of Prepared Low temperature sample holder with sample mounting area.

Figure 3.6: The EMI shielding at the junction of cable and electrode wire along with connector.

The main sample mounting area is designed inside the bottom cup. A spring loaded bottom electrode is mounted inside the insulator cavity (Fabric rod – hylum). This insulator cavity is then attached with the lid of the bottom cup. The bottom electrode is surrounded with the heater with non inductive winding. The co-axial tube with 1mm thick central wire acts as top electrode. The platinum resistance PT-100 was mounted as sensor to measure such low temperatures. The sensor and the top electrode are mounted in the lid of the bottom cup. This design is shown in the Figure 3.5 (A). All joints and connections of co-axial wires are shielded properly with aluminum foil. Thus perfect EMI shielding is achieved through series connection of co-axial wires with the co-axial tubes using BNC vacuum connectors. The low temperatures can be achieved by dipping the sample holder inside the liquid nitrogen container after evacuating it.

Programming, calibration and optimization:

To measure the data with programmed temperatures the Lake Shore 331 temperature controller was connected with the instrument. The tuning of the heater and calibration of the sample holder is done as per the method mentioned in above section 3.2.2.1. The optimized condition is then used to collect the data.

3.3 Characterization Techniques:

The prepared samples were characterized under three different categories:

1. Structural characterization (crystal structure and microstructure studies)
2. Optical and electrical studies (optical spectroscopy with electrical transport)
3. Magnetic characterization (magnetization and hysteresis)

The different characterization techniques along with its necessity and applications are presented in this section. Further, the methods of actual data collection, instrumental parameters, pre treatment applied to the sample along with the details of utilized instrument are briefly summarized here.

3.3.1 Structural Characterization: (Crystal Structure and Microstructure Studies):

The purity and structural perfections of prepared sample are very important features of any material. The major properties of the material like; optical property, electrical property, magnetic property, thermal property, etc. are largely depends on the structural imperfections and chemical impurity of the material. The compositional purity and structural perfections can be quantitatively analyzed using structural characterization techniques. Further, the macroscopic structural aspects like grain growth features affect largely the overall property of material. The Structural characterization is carried out using different techniques:

1. X-ray diffraction (XRD) (Crystal structure analysis)
2. Scanning electron microscopy (SEM) (Microstructure Analysis)
3. Atomic force microscopy (AFM) (Microstructure Analysis)
4. Differential scanning calorimetry (DSC) (Thermal analysis of structural transition)
5. Thermal Gravimetric Analysis (TGA) (thermal analysis of structural stability)

3.3.1.1 X-Ray Diffraction (XRD): (Crystal Structure Analysis):

Necessity of this technique:

To understand and tune the properties of any material we need to standardize the material first. It is only possible when we prepare such material in pure phase. The absence of any impurity (liquid) phase in the prepared compound provides guarantee to use it in the industrial applications. The XRD can provide information about crystal structure, unit-cell dimensions, Wyckoff positions of atoms and crystal symmetry. All these information can be used to simulate each and every property of materials. Further, the quantification of the pure and impure phase (or two different pure phases) can be easily done by analyzing the XRD pattern.

Working Principle:

The X-rays are very important tool to investigate the crystal structure of any material, as their wavelength is quite comparable with the unit-cell dimensions of general crystalline material. The beam of monochromatic x-rays, when applied to any crystalline material, interact with the structural planes of the lattice and produces diffraction. The each lattice point of the plane acts as a slit. This phenomenon is well explained by W. L. Bragg in the form of Bragg's condition or Bragg's law [6];

$$2d \sin\theta = n\lambda\ , \qquad \text{……} \ (3.1)$$

Here, d is inter planer spacing depends on the material to be investigated, θ is angle between incident beam and the set of lattice planes, n is any integer (1,2,3,…) and λ is wavelength of incident monochromatic beam of x-rays. According to this law for a given set of parallel planes the diffraction will give maxima only in that direction for which the angle will satisfy the Bragg's law (see Figure 3.7). Thus the different possible sets of plane available in the compound constitute different diffraction peaks at different angles for which the Bragg's condition is satisfied. The scattering of x-rays from any set of plane depends on the type of atoms (or molecules), number of atoms and their Wyckoff positions.

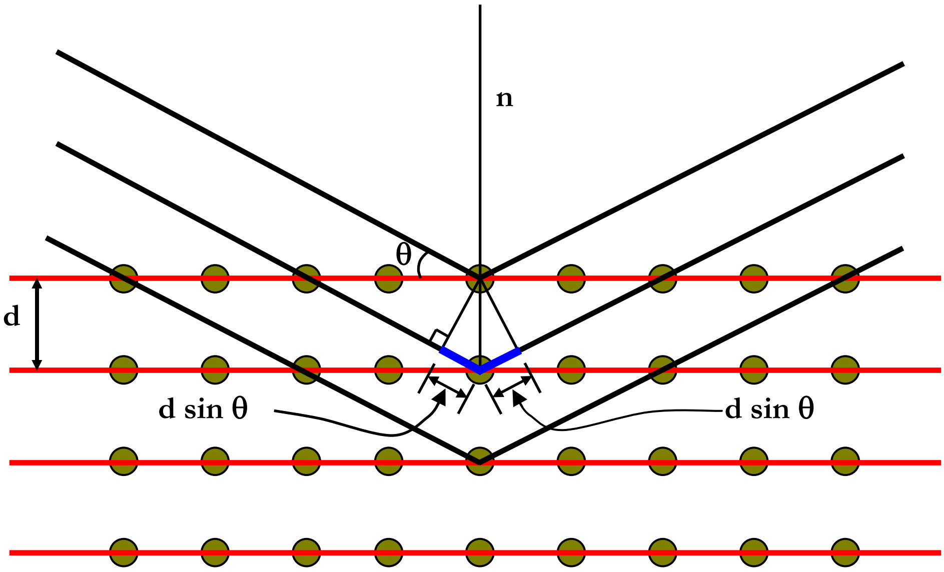

Figure 3.7: The ray diagram of Bragg's Law depicting diffraction of X-rays by sets of atomic planes parallel to each other.

Applications:

Using the peak positions of XRD pattern we can find,

- The d values and hkl values associated with each set of parallel planes.
- The symmetry of unit cell as it is related with the number of peaks available.
- The crystal system and space group from the systematic absence or presence of peak and peak splitting.
- The lattice parameters of the system.
- Percentage densification of the samples

The peak intensity is directly related to the density of atoms/molecules in particular set of parallel planes, so it will help in determination of,

- Wyckoff position of each atom.
- Occupancy of atoms
- Thermal vibration of atoms.

The peak broadening is related with the thermal vibration, Instrumental divergence and order of crystalline nature (long range/short range order). It helps in determination of,

- Thermal vibration parameters

- Crystallite size through Debye scherrer formula [6]
- Crystallite size and induced strain using Williamson-Hall plot [6]

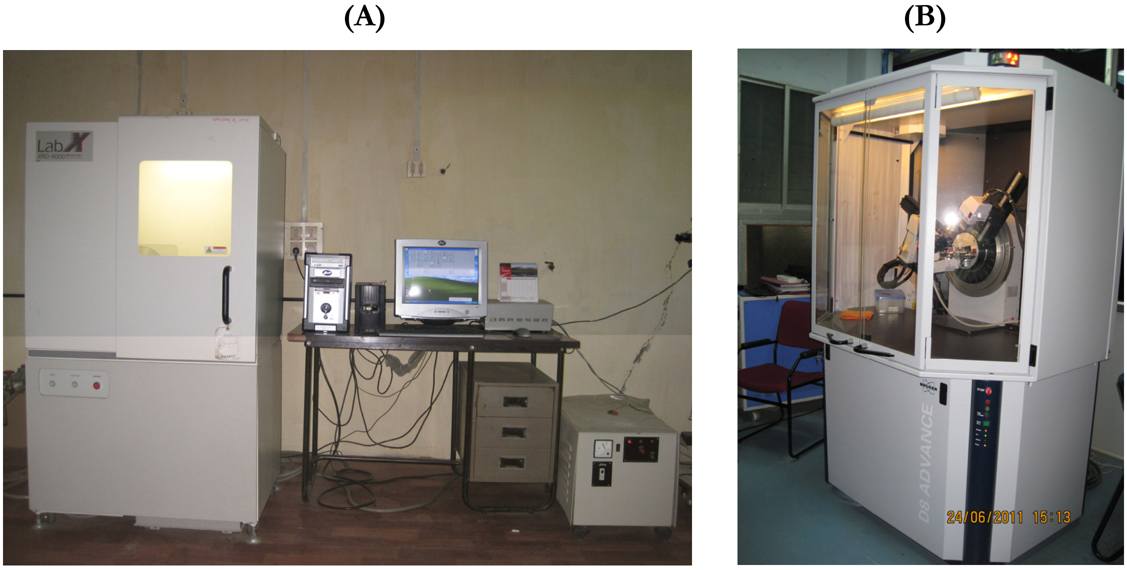

Figure 3.8: (A) The XRD setup at our department, SHIMADZU XRD 6000. (B) The XRD setup at UGC-DAE-CSR Indore centre, Bruker D8 Advanced.

Actual data collection and sample requirement:

The powders of annealed pallets were used to collect the x-ray diffraction data. The measurements of Bulk samples were performed using SHIMADZU-XRD-6000. The Cu-K_α radiation (wavelength 1.54 Å) with θ-2θ geometry was used to collect the XRD data. The scanning was performed from 2θ=10°-110° with a step of 0.02° and a scanning rate of 1.0° per minute. The data collection was done using conventional solid state detector.

The x-ray diffraction measurements for film samples were carried out at UGC-DAE-CSR, Indore, using Bruker D8 advance X-ray diffractometer. The x-rays were produced using a sealed X-ray tube giving monochromatic wavelength of 1.54 Å (Cu-K_α). The x-rays were detected using a fast counting detector based on Silicon strip technology (Bruker LynxEye dtector).

3.3.1.2 Scanning Electron Microscopy (SEM):

Necessity of this technique:

The Scanning Electron Microscopy (SEM) is a very useful technique to collect information about the topography (surface features of an object), morphology (shape and size of the particles making up the object) and composition (the elements and compounds of the object with their relative amount). The magnification of typical optical microscope is up to ~500× while the SEM can magnify any object up to ~300000×, along with resolution of few nanometers.

Working Principle:

Electron Microscopes use a beam of highly energetic electrons to examine objects at very small size. A stream of such high energy electrons is accelerated towards the specimen under high vacuum. This stream is confined and focused using metal apertures and magnetic lenses into a thin, focused, monochromatic beam as shown in the Figure 3.9(A).

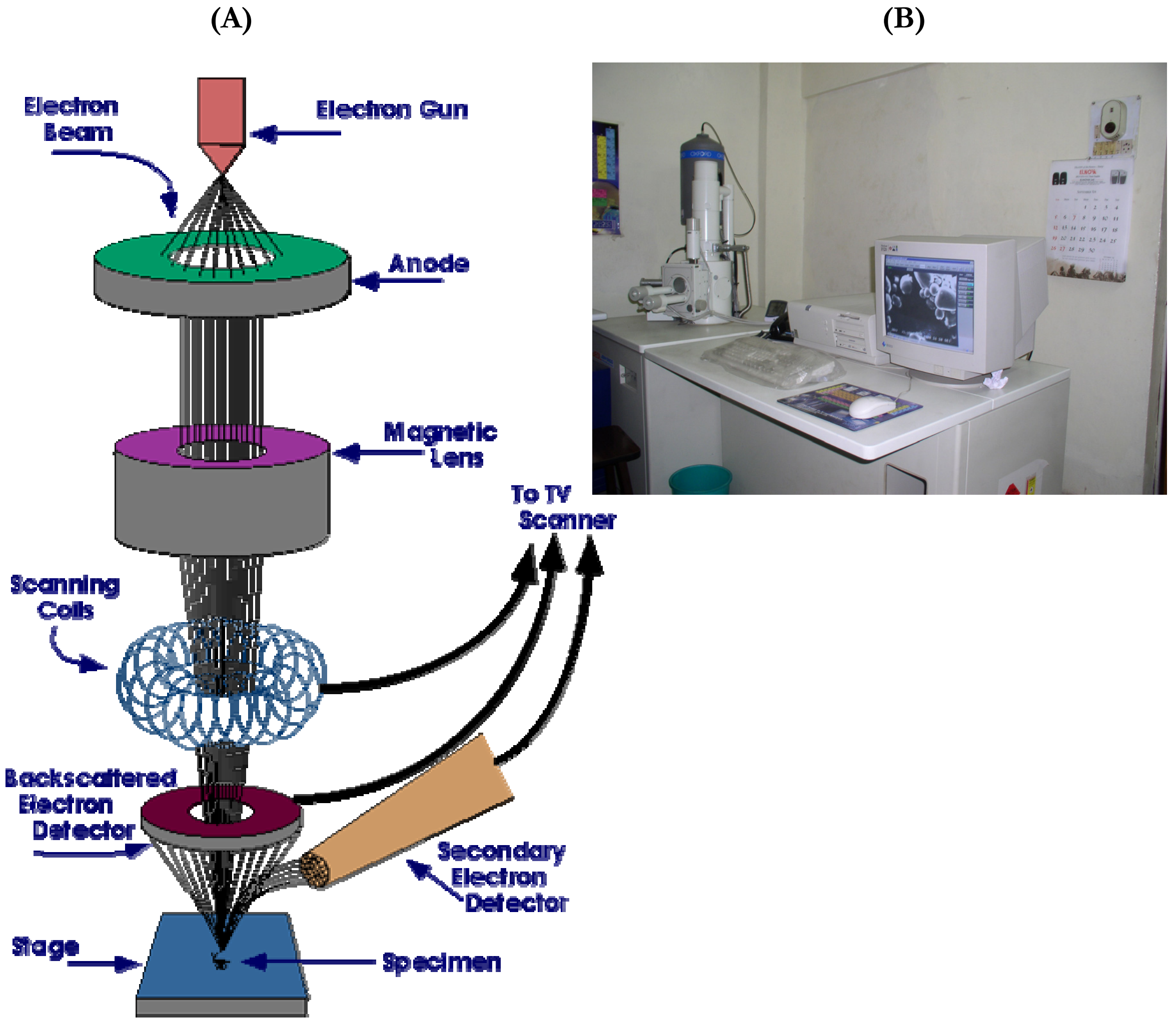

Figure 3.9: (A) A schematic diagram of scanning electron microscopy taken from: Purdue university website, http://www.purdue.edu/rem/rs/sem.htm#1, Original from Iowa State University SEM Home page. (B) The SEM setup at UGC-DAE-CSR Indore centre.

When a sample is bombarded with electrons, secondary electrons from the sample are produced through inelastic scattering. These secondary electrons are having very low energies.

Therefore only few secondary electrons which are near to the surface can escape the sample surface and contribute to form surface topography. In addition several incident electrons are backscattered from the specimen surface through elastic scattering. The images formed by such back scattered electrons can also provide information about the distribution of different elements in the sample. Further, the ejected secondary electron from the sample surface leaves electron vacancy. Such vacancy is filled by an electron from a higher shell, resulting in emission of X-ray. The number of emitted X-rays along with their energy gives information about the element. This technique is known as Energy Dispersive X-ray spectrometry (EDS or EDX). In practice, EDS is most often used for qualitative elemental analysis.

Applications:

Surface topography for every kind of samples like; metals, ceramics, glass, dust, hair, teeth, bones, minerals, wood, paper, plastics, polymers, etc. can be done using SEM. It can also be used for qualitative and quantitative chemical composition analysis of the sample surface using EDS. Backscattered are used to form diffraction images.

Actual data collection and sample requirement:

The microstructure photographs of the annealed bulk samples were collected using a scanning electron microscope SEM JEOL JSM 5600: F-Model at UGC-DAE-CSR, Indore centre. Few photographs were collected using SEM JEOL JSM 5610 at Department of Metallurgical and Materials Engineering, Faculty of Technology, The M. S. University of Baroda, Vadodara. The SEM photographs were collected for three different regions of each sample to ensure the correctness of the results. Further the data were collected at different magnification to study its growth features. To eliminate any electron charging effect on the sample-surface all the samples were coated with transparent silver/aluminum coating of ~50 Å. Such top conducting surfaces are then grounded with the instrument using conducting silver paint.

3.3.1.3 Atomic Force Microscopy (AFM):

Necessity of this technique:

Atomic Force Microscopy (AFM) is an advanced technique to scan the material surface with enhanced resolution up to fractions of nanometer (~2 Å) with much higher magnification (~$\times 10^7$). It can scan extremely small surface features up to a single atomic scale. This method does not require vacuum. This makes it possible to study biological macromolecules and even living organisms using AFM. The insulating samples can be scanned easily using AFM without any surface coating. The different type of samples like; polymers, ceramics, composites, glass, and biological samples also can be scanned using AFM. Apart from surface imaging it can measure magnetic and electrical signals of the surface atoms.

Working Principle:

The scanning of sample surface is done using a tiny cantilever in AFM. The tip of such cantilever is of the order of few nanometers. The cantilever experiences attractive and repulsive forces by the surface atoms when it approaches the sample surface. Therefore the tip moves up and down according to such surface forces, which are measured using a laser beam reflected from the top surface of the cantilever (see Figure 3.10 and sketch). This motion of the cantilever is then converted into surface image using electronic circuits. Several special tips used in AFM can measure different type of forces like; mechanical contact force, van-der Waals force, chemical bonding, electrostatic forces, magnetic forces etc.

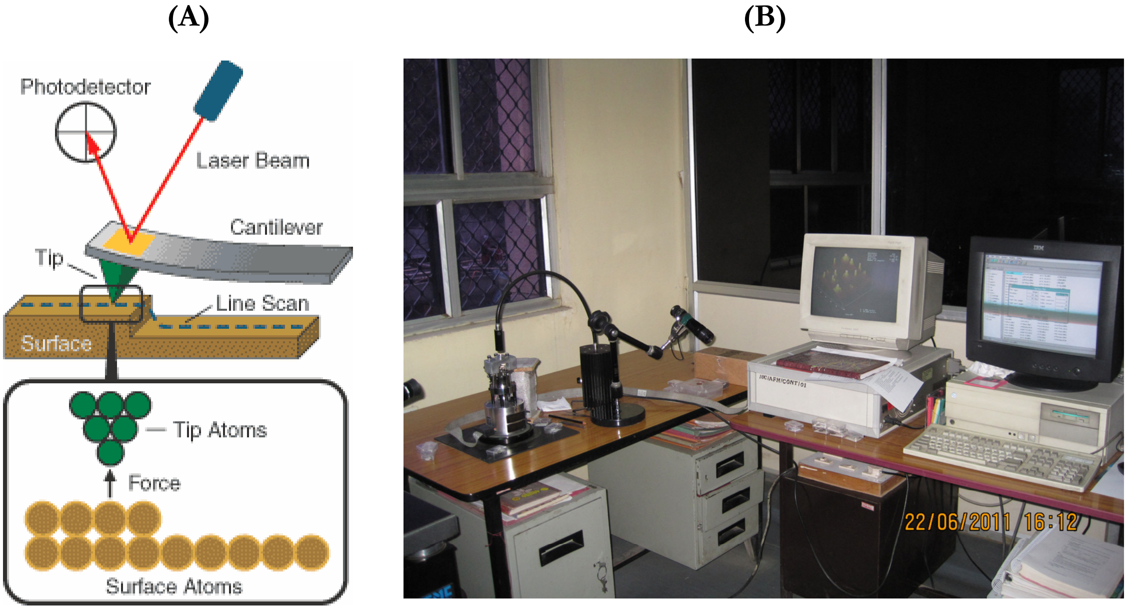

Figure 3.10: (A) A schematic diagram of Atomic force microscopy; Ref: web site of agilent technologies. (B) The SEM setup at UGC-DAE-CSR Indore centre.

AFM is classified under three different modes according to the scanning methodology:

1. **Contact Mode**: The tip is in contact with the sample surface and scans the surface by balancing the forces between tip and the surface atoms. The force is made constant using feedback loop in this method. Typically rigid samples can be scanned using this mode.
2. **Non Contact Mode**: Here the tip is few nanometer above the surface of the material vibrating with frequency little higher than the resonant frequency of tip. The amplitude of such vibrations are generally very small (<10 nm). It scans the sample by measuring

the interaction of long range forces with the cantilever tip. It can easily scan liquid layers on the solid surfaces or soft materials without damaging the sample surface.

3. **Tapping mode**: This mode is similar to non contact mode with amplitudes large up to 100-200 nm. Therefore when tip comes closer to the surface the interaction forces act on the tip and reduces the amplitude of the tip. This method can measure short range forces also along with long range forces without damaging sample surface or the tip.

Applications:

The AFM can provide 3D surface topography. It can give atomic resolution with ultra-high vacuum (UHV). The different type of tips can be used to measure magnetic, electrical, thermal, mechanical and optical properties of the material at atomic scale. AFM can be combined with other optical microscopy techniques, enable it to perform photovoltaic measurements.

Actual data collection and sample requirement:

The surface images of our all the films were collected using atomic force microscope AFM Nanoscope III at UGC-DAE-CSR, Indore centre. The tapping mode of the data collection technique is utilized for batter imaging. The AFM images were collected for two different regions with four different scan sizes to ensure the homogeneity of samples.

3.3.1.4 Differential Scanning Calorimetry (DSC):

Necessity of this technique:

The properties of any material like; electrical, mechanical, magnetic, optical, thermal etc. are extensively dependent on the temperature dependent physical or chemical changes. The comprehensive analyses of such thermal changes enable us to predict significant transitions in the material properties. The quantitative as well as qualitative analyses of such changes involve study of endothermic-exothermic processes along with changes in heat capacity. The Differential Scanning Calorimetry (DSC) measures such changes through the temperatures and heat flows associated with transitions in materials. The measurements through DSC are under controlled atmosphere as a function of time and temperature.

Working Principle:

When the sample undergoes a physical transformation such as phase transitions, the heat flow will increase or decrease in order to maintain the temperature of the sample equal to the reference. The amount of heat flowing into the sample depends on the type of transformation (i.e. exothermic or endothermic). The difference in heat flow between the sample and reference enables DSC to measure the amount of heat absorbed or released during such transitions.

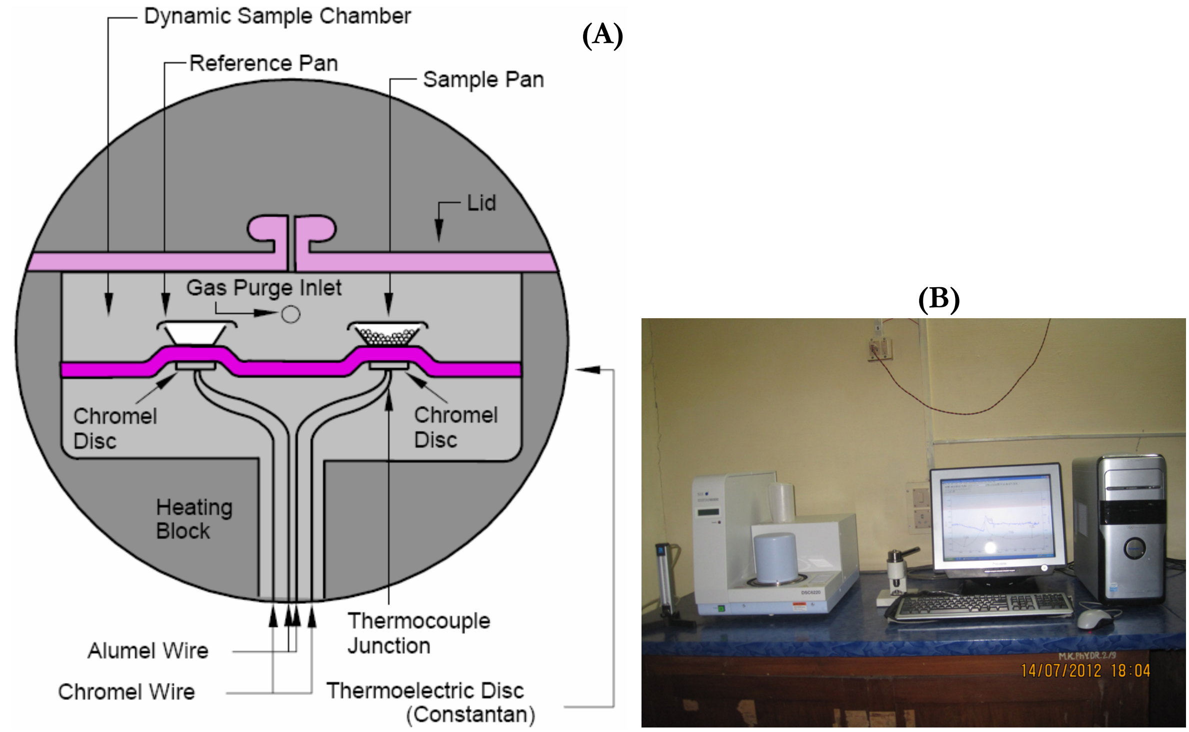

Figure 3.11: (A) A schematic diagram of DSC, Ref: (B) The DSC setup at our department.

Applications:

Differential Scanning Calorimetry is a valuable tool to characterize the temperature dependent properties of materials. The properties like; phase change, glass transition temperature (Tg), crystallization temperature (Tc), melting and boiling points, etc. can be directly observed from DSC curves. In addition, detailed analysis using DSC can be useful to study specific heat, sample purity, enthalpy of transitions, heats of fusion, etc.

Actual data collection and sample conditions:

The possibilities of thermal transitions and structural changes are studied using DSC 2910 (TA Instruments Inc., USA) system at UGC-DAE-CSR, Indore centre, as well as using EXSTAR 6000 DSC 6220, SII Nanotechnologies inc., at our department. The measurements were performed between RT (300 K) to 825 K at the rate of 10 K/min. Small peaces of sample were used instead of powder sample to ensure better results.

3.3.1.5 Thermal Gravimetric Analysis (TGA):

Necessity of this technique:

Thermal (or Thermo) gravimetric analysis (TGA) is one of the members of the thermal analysis techniques used to characterize a wide variety of materials. It is complimentary and supplementary characterization to the most commonly used thermal analysis technique, DSC. This technique is useful to analyze those materials which exhibit either mass loss or mass gain due to decomposition, oxidation or loss of volatile particles.

Working Principle:

Thermal gravimetric analysis measures the change in the mass of a sample as a function of temperature or as a function of time in a controlled atmosphere. The observed mass difference can be co-related with temperature induced phenomena like; absorption/adsorption of gases, drying, dehydration, sublimation, vaporization, decomposition, solid-solid reactions, magnetic transitions, etc.

Applications:

This technique can provide information about the stability of the material over a measured temperature range. It helps in determining composition of the mixture, corrosion of metals, calcinations of minerals, reaction kinetic studies. This technique also determines available volatile content and moisture trapped in the sample.

Actual data collection and sample conditions:

The thermo gravimetric analysis data of powder samples were collected under nitrogen atmosphere using a EXSTAR 6000 TG/DTA 6300 instrument, SII nanotechnologies inc. at Department of Geology, Faculty of Science, The M. S. University of Baroda, Vadodara.

3. 3. 2 Optical and Electrical Studies: (Optical Spectroscopy with Electrical Transport):

The electrical properties of the sample depend on intrinsic as well as extrinsic parameters. The intrinsic parameters like; atomic position, symmetry of charge centers, charged states of the constituent ions, electro negativity of the ions, stability of charged states etc., significantly affect the electrical as well as optical properties of the materials. The direct influence of these parameters is explained in terms of polarization, tilting of oxygen octahedron, structural distortions and frequency/temperature relaxations of dipoles by many research groups [7-12]. Very few research groups have identified effect of extrinsic parameters in terms of oxygen vacancies, grain features and defects [13-17]. This controversial issue of intrinsic/extrinsic parameters to explain electrical properties of materials require in depth analysis of all these parameters. The optical spectroscopy along with electrical studies provides fruitful and complimentary information regarding the contributing factors. The optical and electrical studies can be carried out using the following methods:

1. Ultra violet - visible (UV-Vis.) spectroscopy
2. Complex impedance spectroscopy
3. Polarization vs. electrical field (P-E) (Electrical hysteresis curve)

3.3.2.1 Ultra Violet - Visible (UV-Vis.) Spectroscopy:

Necessity of this technique:

The Ultra Violet - Visible (UV-Vis.) spectroscopy is a very useful tool for the investigation of electronic transitions and the energy band gap of any material. The shape and edge position of the optical absorption spectra determines type of crystallinity and energy band gap of the compound. In general broad edge represents glassy state of material. The broad edge may also represent presence of more than one band edges in the compound as well as gives insight of possible imperfections.

Working Principle:

When UV-visible radiation interacts with matter, it gets absorbed by the molecules, resulting in increased energy of the molecules. The wavelength of the absorbed light is always equivalent to the energy required to move an electron from a lower energy level to a higher energy level. This results in a sharp absorbance edge in the absorption spectra of the material. The energy associated with this edge gives energy band gap of the compound. In practice the band structure of materials not possessing sharp band gap results in broadening of the edge in the absorption spectra of material.

Applications:

The UV-Vis. spectroscopy is primarily useful to determine the energy band gap of semi-conducting materials. The broadening of band edge helps in prediction of possible splitting of bands.

Actual data collection and sample requirement:

The UV-Vis spectroscopic measurements of the bulk samples were collected at room temperature in the range of 300 nm to 850 nm. The data were collected in the universal reflectance mode using Perkin Elmer Lambda 950 at UGC-DAE-CSR, Indore centre. The data of film samples were collected in the transmittance mode with ITO/glass substrate on the reference side.

3.3.2.2 Complex Impedance Spectroscopy:

Necessity of this technique:

The complex impedance spectroscopy is a versatile tool to investigate the electrical properties of the material. It can significantly separate out the contribution of intrinsic and extrinsic factors. The qualitative as well as quantitative analysis in terms of relaxation parameters along with activation energy empowers this technique to focus on the mechanisms of electrical conduction.

Working Principle:

When an external alternating voltage signal is applied to any material its molecules try to obey the external signal in order to eliminate its effect. The molecule or dipoles formed in the material try to orient with the frequency of external field up to natural frequency of the dipole. If frequency of external signal exceeds the natural frequency of dipole, the dipole starts lagging behind the signal. This process is known as relaxation and is well explained by Debye [18]. There after for real materials K. S. Cole and R. H. Cole made significant corrections to this theory [18-20]. The complex impedance spectroscopy data can be analyzed under four different representations. These each representation has its own unique advantage and abilities.

1. **Impedance representation**: This representation can separate the contribution of extrinsic factors like grain, grain boundary and space charge contribution
2. **Permittivity representation**: Here the contribution from permanent dipole, induced dipole and free charge carries can be separated.
3. **Electric modulus representation**: The space charge–dipole interaction can be probed effectively through the electrical modulus representation.
4. **Conductivity representation**:The investigation of conductivity carriers along with charge induced relaxation can be effectively and quantitatively studied using this representation.

Applications:

This technique is useful in separating out the contributions of extrinsic and intrinsic factors. It helps in prediction of type of conduction carriers and type of relaxing elements. It can find out permanent static polarization, contribution of conductivity, relaxation parameters, etc. These all information collectively helps to understand the electrical property of material.

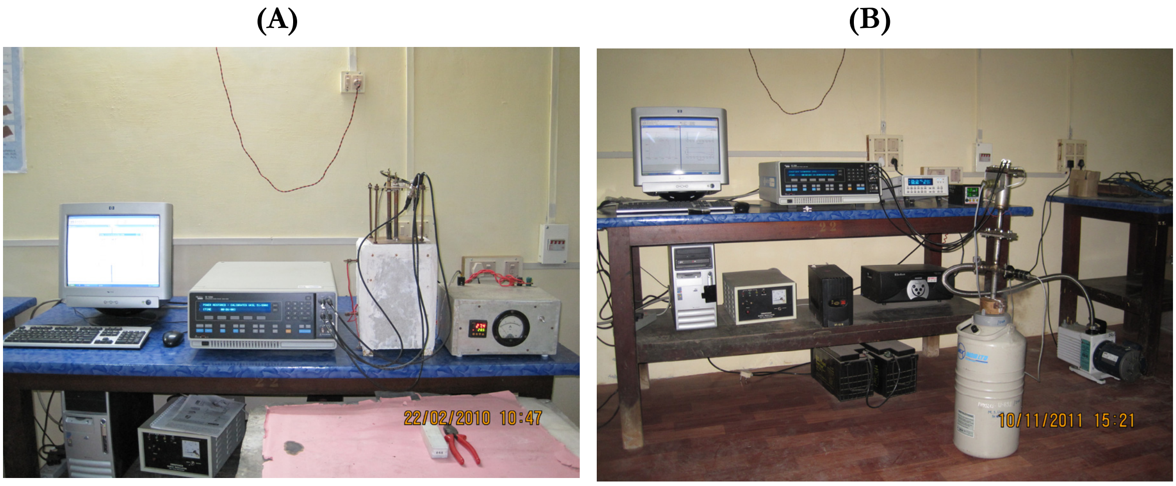

Figure 3.12: (A) The impedance spectroscopy setup for high temperature measurement. (B) The impedance spectroscopy setup for low temperature measurement.

Actual data collection and sample requirement:

The electrical characterization requires conducting electrodes on the sample surface. Therefore, the pellets of bulk samples were first polished and then electrodes were made using silver paste. The complex impedance data were collected at different temperatures, with an interval of 5K, using a Solatron-1260 Impedance Analyzer in the frequency range of 1 Hz to 1×10^7 Hz. The temperature was increased from 80 K to 350 K and 350 K to 750 K, at a constant heating rate of 0.5 K/min. The complex impedance data of the samples having high impedance values ($>10^9$ Ω) were collected using Alpha-A high performance frequency analyzer, Novocontrol technologies, Germany, at UGC-DAE-CSR, Indore centre. The data of film samples were collected from 300 K to 750 K. The step made during film preparation on ITO substrate through masking method was used as bottom electrode. The top electrode is prepared by making a small circular spot on the top surface of film.

The collected impedance data were converted into permittivity, electric modulus and conductivity data using appropriate sample dimensions.

3.3.2.3 Polarization vs. Electrical field (P-E): (Electrical Hysteresis Curve)

Necessity of this technique:

The ferroelectricity is very significant property of some special materials which empower these materials to be used in the industries like; communication technology, high energy storage devices, electronic industries, etc. The well defined polarization vs. electrical field loop (P-E loop) is a unique and essential characteristic of ferroelectric materials. Further, much important information like; type of the material (ferroelectric, paraelectric or simple dielectric), maximum polarization, dielectric strength of material, etc can be inferred from the shape and size of the P-E loop.

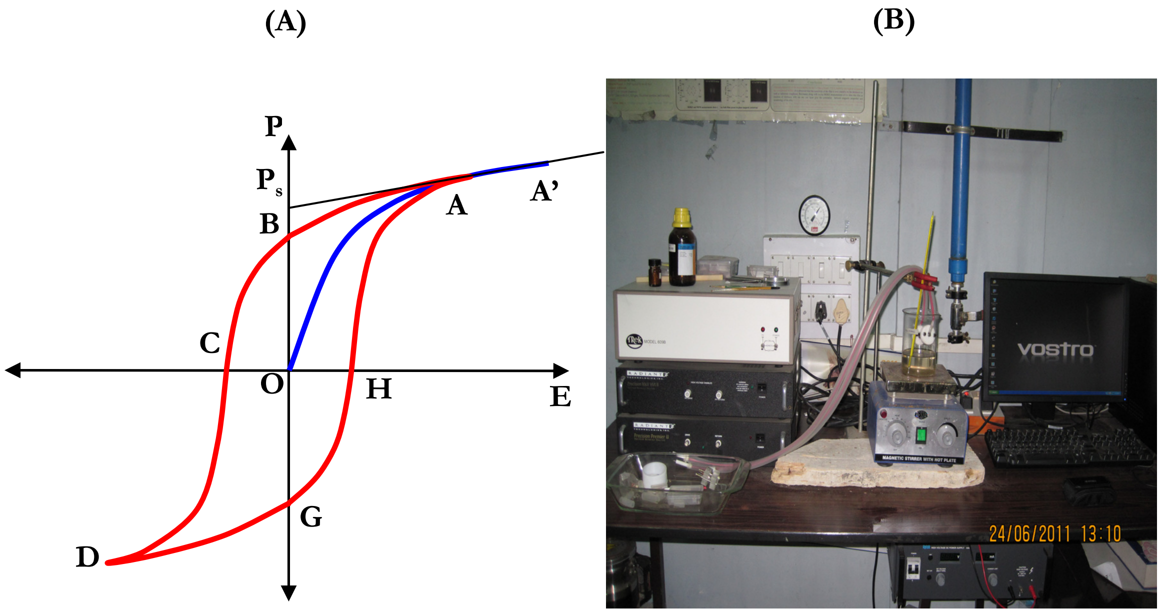

Figure 3.13: (A) A diagram showing P-E hysteresis loop for ferroelectric materials. (B) The PE setup at UGC-DAE-CSR Indore, centre.

Working Principle:

The randomly oriented dipoles of the ferroelectric material get aligned with the external electric field. This alignment of dipoles contributes to the net total polarization of the material. The net polarization of the material increases with increase in external electric field and becomes nearly constant at particular value of polarization. This value of polarization is known as saturation polarization (P_S) and it remains nearly constant with further increment in the external electric field (see Figure 3.13).

The polarization does not follow the same path on reversal of external electrical filed (AB path in the Figure 3.13). When the external electrical field is reduced to zero the net polarization does not returned back to zero but it retains some polarization known as remanent polarization (P_R) or spontaneous polarization. The spontaneous polarization can be reduced to zero by applying reverse electric field known as coercive field (OC in the Figure 3.13). The identical saturation polarization in reverse direction can be achieved by applying reverse electric field of equal amount. This saturation polarization is known as reverse saturation polarization. This polarization reduces to the reverse remanent polarization on switching of the external electrical field gradually. The reverse coercive field (OH in the Figure 3.13, applied in the forward direction) is required to bring material back at zero polarization. Further increase in external electric field leads to saturation polarization as shown in the figure by HA curve. Thus the whole polarization vs. electrical field curve follows a closed cycle ABCDGHA. This loop is known as electrical hysteresis loop.

Applications:

The P-E loop measurement is one of the necessary characterizations to ensure the ferroelectric nature of the material. It distinguishes the materials in terms of dielectric insulators, ferroelectrics, and relaxor ferroelectrics. The measurement of remanent polarization can be utilized to design capacitor in the industries. The dielectric strength of the material can be determined using this measurement. The shape of the loop helps in identification of leaky nature of the material.

Actual data collection and sample requirement:

The polarizations vs. electrical field data of the samples were collected using Hysteresis Version: 4.4.0 - Radiant Technologies, Inc., at UGC-DAE-CSR, Indore centre. The samples were polished and electrodes were developed by conducting silver paint on both the flat surfaces of the pallet. The data were collected at room temperature using spring loaded sample holder. The P-E loops were generated with different amplitude and frequency values of applied electric field.

3.3.3 Magnetic Characterization: (Magnetization and Hysteresis):

The magnetic transport properties of the material or molecule depend on the number of available free electrons in the constituent atoms. It also depends on the magnetic interaction between two neighboring magnetic atoms, generally known as exchange interaction. The magnetic properties of the material combined with the electrical properties like ferroelectricity results in multiferroic nature of the material. The magnetic measurements deal with the measurement of magnetization and magnetic moment as a function of applied magnetic field and temperature. Thus the magnetic characterization includes:

1. Magnetization vs. H-field (M-H) curve: (magnetic hysteresis curve)
2. Temperature and field dependent magnetization: (M-T curve)

The detailed analysis of magnetic interactions using above both magnetic characterizations requires magnetic measurement at low temperatures and high magnetic fields. The vibrating sample magnetometer (VSM) technique is the most efficient technique for low temperature and high magnetic field studies.

Vibrating Sample Magnetometer (VSM): a Technique for Magnetic Characterization:

VSM is widely used technique for characterization of magnetic materials. It measures hysteresis curve and magnetic moments at variable temperature and field to characterize ferromagnetic as well as paramagnetic materials.

The VSM works on very basic principle of Faraday's law. The magnetic field can be induced by vibrating a magnetic sample inside a dc applied magnetic field. The induced magnetic field is correlated with the magnetic moment of the sample. The apparatus of VSM consist of a rod attached with a vibrator, which vibrates the rod at a particular frequency (see Figure 3.14(A)). The sample is mounted at the end of this rod and placed between a set of peak up coils. The magnetic material gets magnetized when external magnetic field is applied on it. The magnetized sample vibrates between the peak-up coils and induces ac voltage in the circuit containing peak up coils. This voltage signal is then converted in to the magnetic moment (M) of the sample. Thus by changing the external magnetizing field and by measuring corresponding magnetic moment one can obtain M-H hysteresis loop. Similarly, the magnetic moment at different temperatures, i.e. M-T curve can also be measured using VSM.

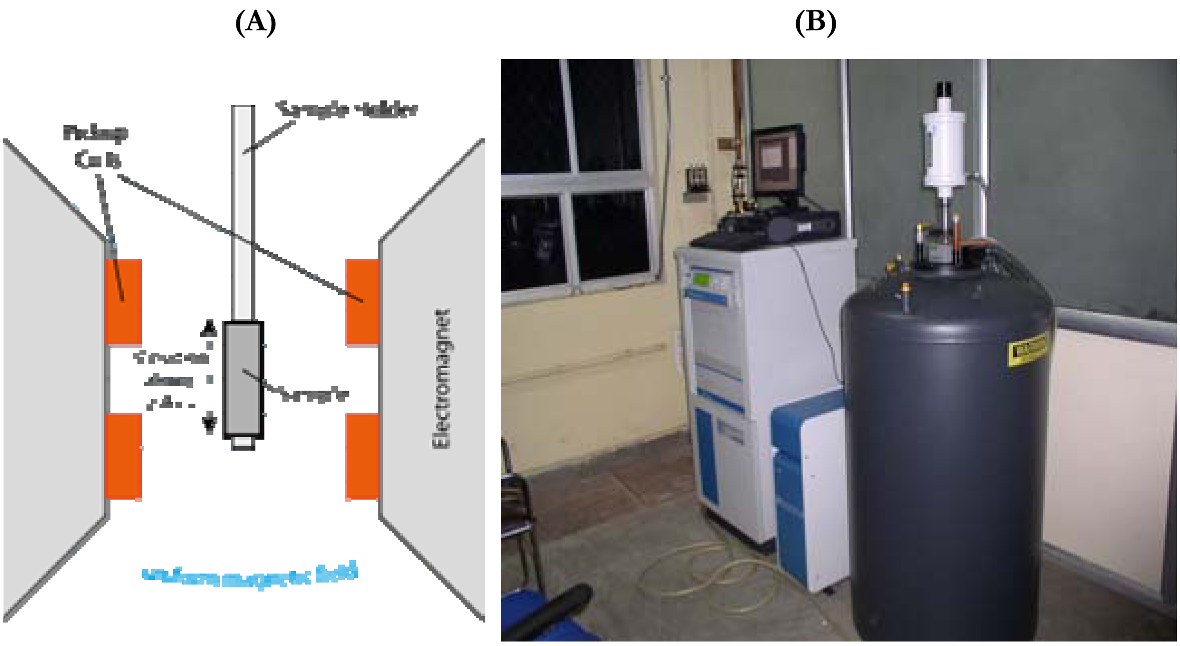

Figure 3.14: (A) A diagram showing working principle of VSM. (B) The PPMS-VSM setup at UGC-DAE-CSR Indore centre.

3.3.3.1 Magnetization vs. H-field (M-H) Curve: (Magnetic Hysteresis Curve):

Necessity of this technique:

The magnetic hysteresis curve is useful to classify the magnetic materials in two major categories: hard magnetic materials and soft magnetic materials. The hard magnetic materials require high magnetic field to magnetize or demagnetize. The energy loss is also very high for such materials. They can be used as permanent magnets and magnetic recording media like; magnetic tapes, hard disks, and credit cards. The soft magnetic materials can easily be magnetized or demagnetized with comparatively low magnetic field. These properties promise to use such materials for magnetic cores or recording heads.

The shape and size of magnetic hysteresis curve facilitates to determine the material specific parameters like; saturation magnetization, remnant magnetization, coercive field, type of material (ferromagnetic, paramagnetic, diamagnetic, etc.) and energy loss by the material.

Working Principle:

The all magnetic materials are made up of randomly oriented magnetic domains in demagnetized condition. The net magnetic moment of the material is zero in this condition. The external magnetizing field, when applied to the sample, orients the domains in the direction of field results in net non-zero magnetic moment of the material in the direction of the field. The nature of magnetic field dependent magnetization is different for various types of magnetic materials. The relation between magnetizing field and magnetic moment for different types of materials are shown in the Figure 3.15 (A).

Diamagnetic materials: The diamagnetic materials show very small and negative magnetization as shown in the Figure 3.15(A). The magnetization is proportional to the field and becomes zero in the absence of the field. This is a common characteristic of all the materials. The materials with no net magnetic moments (i.e. no unpaired electrons) show diamagnetism.

Paramagnetic materials: The paramagnetic materials show positive magnetic moment. The net magnetic moment is proportional to the applied magnetic field. The magnetic moment in these materials is due to presence of un-paired electron. It becomes zero similar to the diamagnetic materials when field is reversed back to zero, because of the absence of the magnetic interactions between un-paired electrons.

Ferromagnetic materials: The magnetization for these materials is very high due to exchange interactions between the un-paired electrons. The magnetization is not reversible and material sustains net magnetic moment after removal of the external magnetizing field. These materials show a well defined M-H hysteresis loop.

Ferrimagnetic materials: The magnetic moment is due to two different lattices. The net magnetic moment is thus due to anti-parallel alignment of these constituent moments. These interactions between two different magnetic moments are known as super-exchange interactions. Thus the net magnetic moment is less then the ferromagnetic materials.

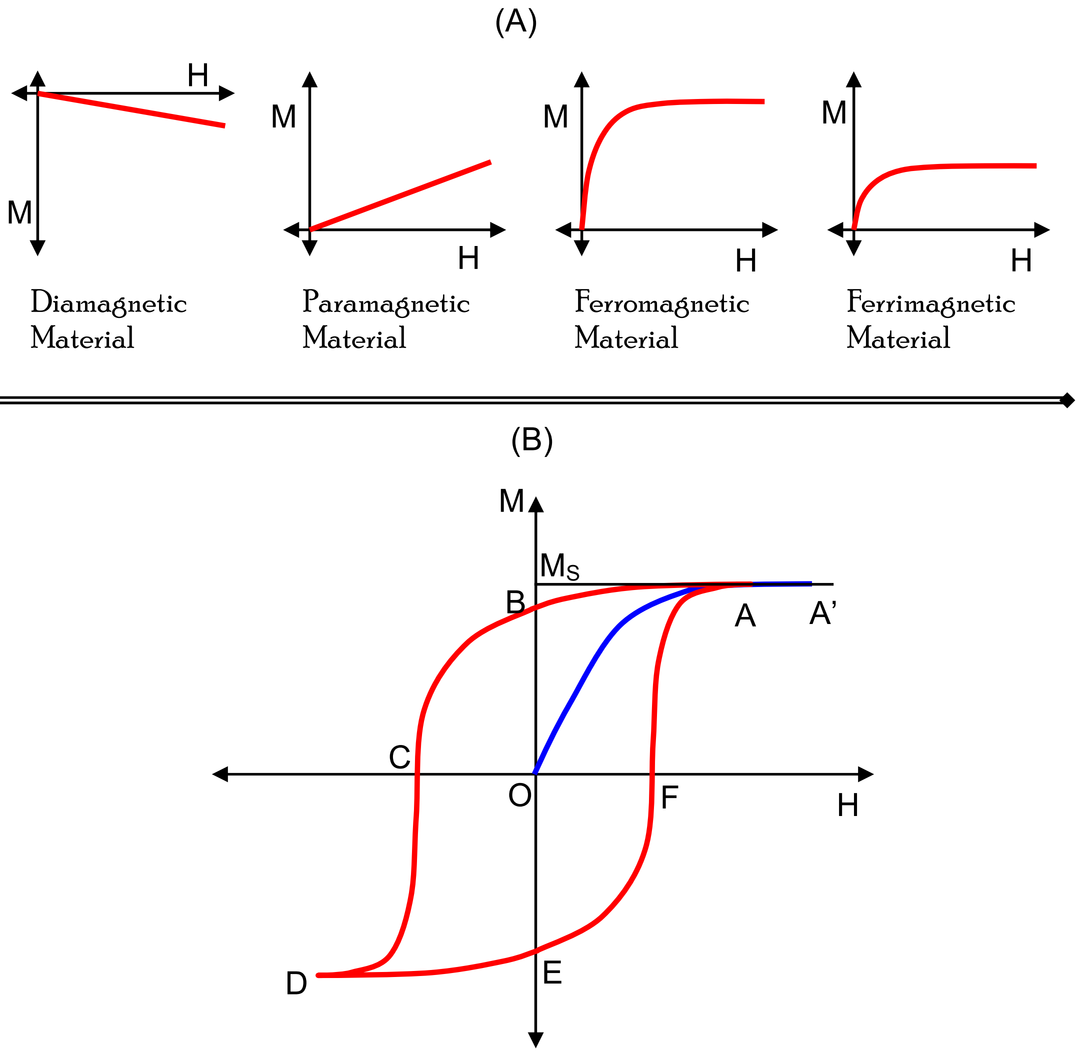

Figure 3.15: (A) The diagrams of magnetizing field (H) dependent magnetic moment for different type of magnetic materials. (B) The M-H hysteresis loop for Ferromagnetic materials.

M-H hysteresis loop for ferromagnetic materials: The net magnetization of ferromagnetic material is very high due to exchange interaction. The magnetization increases with external magnetizing field and gets saturated at very high fields as shown in the Figure 3.15(B) (AA' curve). This nearly constant value of magnetization is known as saturation magnetization (M_S).

The magnetization curve for ferromagnetic materials can not be reversed and net non zero magnetization sustains after removal of the applied magnetic field (AB curve). This non-zero magnetization is known as remanent magnetization (M_R). The reversed magnetizing field is required to eliminate this remanent polarization. This reversed field is known as coercive field (OC). The further increase in reverse magnetizing field reverses the magnetization of the sample and saturates it at high enough field. The reverse saturation magnetization (CD curve), reverse remanent magnetization (OE) and reverse coercive field (OF acting in the forward direction) can be obtained similar to the forward parameters. Further, the curve meets again the saturation on increasing the forward magnetizing field as shown by the FA curve. Collectively the whole curve ABCDEFA is known as ferromagnetic hysteresis loop.

Applications:

The M-H hysteresis curve can be used to distinguish the type of magnetism present in the material. The value of remanent polarization obtained from the M-H curve can be utilized in designing suitable applications like; sensor, permanent magnet, recording media, etc. The area of under the curve represents energy loss by the sample. The curves collected at different temperatures enable us to determine the magnetic phase transition if any.

Actual data collection and sample requirement:

The M–H curve measurements of the samples were carried out using a Quantum Design 14 Tesla physical properties measurement system-vibrating sample magnetometer (PPMS-VSM) at UGC-DAE-CSR Indore centre. The hysteresis curves were developed at two different temperatures; room temperature (300 K) and low temperature (5 K). The solid rectangle shaped samples were sliced from the annealed circular pallets to collect the data.

3.3.3.2 Temperature and field dependent Magnetization: (M-T Curve):

Necessity of this technique:

The temperature dependent magnetization curves are useful to identify the possible magnetic phase transition. The ferromagnetic to anti-ferromagnetic (FM-AFM) and ferromagnetic to paramagnetic (FM-PM) phase transition temperatures can be obtained using this technique.

Working Principle:

The measured magnetic moment (M) of the sample can be collected at different temperatures by using the cryogenic system. The curie law explains the relation between susceptibility (χ) and temperature for paramagnetic salts. The magnetic phase transition temperatures can not be altered with the applications of the magnetizing field H will not alter the genuine transition temperature. However the amount of magnetization changes with the field and history of the sample. This fact helps in identification of ferromagnetic and paramagnetic materials. This require the experiment to be performed under zero field cooled (ZFC) and field cooled (FC) condition.

Applications:

This measurement helps in identification of magnetic phase transition temperatures of the samples. The experiment performed under ZFC-FC condition helps in identification of genuine transitions.

Actual data collection and sample requirement:

The M–T measurements were carried out using a Quantum Design 14 Tesla physical properties measurement system-vibrating sample magnetometer (PPMS-VSM) at UGC-DAE-CSR Indore centre between temperatures 5 K to 300 K.

References:

1. A. R. West, Solid State Chemistry and its Applications, John Wiley and Sons, Singapore (2003).
2. Hand Book of Thin Film Materials Vol. 1 (Deposition and processing of Thin Films) edited by Hari singh Nalwa Academic Press, USA, (2002).
3. S. T. Tan, B. J. Chen, X. W. Sun, W. J. Fan, H. S. Kwok, X. H. Zhang and S. J. Chua, J. Appl Phys. **98,** 013505 (2005).
4. S. Chandramohan, R. Sathyamoorthy, P. Sudhagar, D. Kanjilal, D. Kabiraj, K. Asokan, V. Ganesan, T. Shripathi, U.P. Deshpande, Appl Phys A. **94,** 703 (2009).
5. R. Kumar, R. J. Choudhary and S. I. Patil, Solid State Commun. **106,** 805 (1998).
6. B. D. Cullity, "The Structure of Polycrystalline Aggregates," in Elements of X-ray diffraction, Massachusetts, U.S.A.: Addison-Wesley Publishing Company, Inc., pp. 259-296 (1956).
7. G. H. Haertling, J. Am. Ceram. Soc. **82(4),** 797 (1999).
8. L.E. Cross, Ferroelectrics. **76,** 241 (1987).
9. S. Ke, H. Huang, H. Fan, Appl. Phys. Lett. **89,** 182904 (2006).
10. J. Liu, Chun-Gang Duan, Wei-Guo Yin, W. N. Mei, R. W. Smith and J. R. Hardy, Phys. Rev. B. **70,** 144106-1 (2004).
11. S. Saha and T.P. Sinha, J. Phys. Condens. Matter. **14,** 249 (2002).
12. S. Saha and T.P. Sinha. Phys. Rev. B. **65,** 134103 (2002).

13. D. C. Sinclair, T. B. Adams, F. D. Morrison, and A.R. West, Appl. Phys. Lett. **80,** 2153 (2002).
14. M. C. Ferrarelli, T. B. Adams, A. Feteira, D. C. Sinclair, and A. R. West, Appl. Phys. Lett. **89,** 212904-1 (2006).
15. Z. Wang, X. M. Chen, L. Ni, and X. Q. Liu, App. Phys. Lett. **90,** 022904 (2007).
16. I. P. Raevski, S. A. Prosandeev, A. S. Bogatin, M.A. Malitskaya, L. Jastrabik, J. Appl. Phys. **93,** 4130 (2003).
17. F. Zhao, Z. Yue, J. Pei, D. Yang, Z. Gui, and L. Li, Appl. Phys. Lett. **91,** 052903-1 (2007).
18. K.C. Kao, Dielectric phenomena in solids, Elsevier Academic Press, USA, (2004).
19. R.H. Cole, the J. Chem. Phys. **23,** 493 (1955).
20. K.S. Cole and R.H. Cole, J. Chem. Phys. **9,** 341 (1941).

CHAPTER 4

Results and Discussion (Bulk)

(Structural, Electrical, Optical and Magnetic Characterization of Bulk Samples)

The main analysis work of the thesis is presented in this chapter. The collected data were analyzed comprehensively and represented for the purpose of comparative study. The relative studies of all compounds were done using different characterization techniques. This chapter is bifurcated in to three sub chapters on the basis of the different studies:

Chapter 4A-Structural Characterization
Chapter 4B-Optical and Electrical Characterization
Chapter 4C-Magnetic Characterization

CHAPTER 4A

Results and Discussion (Bulk): Structural Characterization

(Structural, Micro structural and Thermal Characterization of Bulk Samples)

The crystal structure and other crystallographic data of all the samples are identified in detail. The rietveld refinement technique is used for crystallographic studies. Crystallographic parameters like, lattice parameter, space group, thermal parameters, Wyckoff positions of each element are determined using refined data. The microstructure studies using SEM and AFM were carried out to correlate the macroscopic factors with the observed giant dielectric parameters.

4.A.1 Crystallographic Structural Studies: (X-Ray Diffraction - XRD):

In order to standardize quality of the prepared samples we under took the crystallographic structural studies through diffraction pattern using monochromatic X-rays. The preliminary analyses of the collected data were done using 'PowderX' software. The basic crystal structure and unit cell parameters were determined through fitting the observed patterns. The quantitative analysis like crystallite size determination and strain measurement were done for all the samples. The Debye scherrer method (Equation 4.A.1) as well as Williamson – Hall equation (Equation 4.A.2) was utilized to measure the crystallite size of the prepared samples [1].

$$\beta = \frac{0.9\lambda}{L\cos\theta}, \qquad \text{…… (4.A.1)}$$

$$\beta\cos\theta = \frac{0.9\lambda}{L} + 4\varepsilon\sin\theta, \qquad \text{…… (4.A.2)}$$

Here β is FWHM determined from the XRD pattern, θ is Bragg angle, λ is wave length of X-rays used, L is crystallite size and ε is strain. The plot between $\beta\cos\theta$ and $\sin\theta$ is known as Williamson – Hall plot. It gives a straight line having intercept $0.9\lambda/L$ and slope 4ε. The values of crystallite size L and strain ε can be determined accurately using intercept and slope of the Williamson – Hall plot as it distinguishes the strain broadening and broadening due to crystallite size [2].

The in-depth analysis of XRD data using Rietveld refinement is likely to provide us information on Wyckoff position of the elements, thermal vibrations, space group, etc. These data are very useful to simulate transport properties of any material. The XRD patterns for three samples were refined using Rietveld refinement technique.

The results are presented and discussed in group of seven different series. The bellow sections explain systematic change due to doping or substitution of different elements in BFN.

4.A.1.1 X-Ray Diffraction Analysis of 100% Series: [$Ba(X_{0.5}Nb_{0.5})O_3$] (where X=Fe, Co, Mn, Gd, Eu, Y):

The samples of this series are prepared to study effect of complete replacement of Fe by transition elements (Co and Mn) and rare earth elements (Gd, Eu and Y) in BFN ceramic. The collected XRD patterns of BFN, BCN, BMN, BGN, BEN and BYN compounds are shown in the Figure 4.A.1.

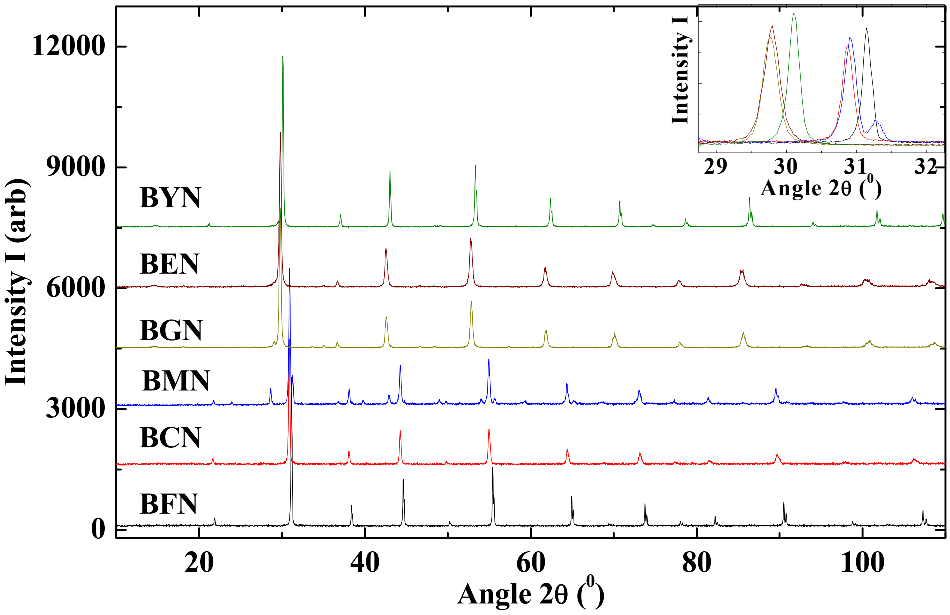

Figure 4.A.1: XRD patterns of BFN, BCN, BMN, BGN, BEN and BYN ceramics. (All patterns are uplifted by 1500 cps from the bellow pattern except BFN.) Inset shows gradual shifting of main intense peak for each of the compounds.

The absence of any impurity peak justifies single phase formation for all the samples. The peaks of all XRD patterns are indexed with the cubic symmetry. The observed cubic symmetry for all these samples are in accordance with the predicted cubic symmetry through tolerance factor value (~1) presented in Table 3.1. The cubic symmetry for all these samples confirms none existence of any significant tilting of the oxygen octahedron in the present systems. The best fitted unit cell parameters for BFN, BCN, BMN, BGN, BEN and BYN are $a = 4.0529\,\overset{o}{\mathrm{A}}$, $a = 4.0886\,\overset{o}{\mathrm{A}}$, $a = 4.0909\,\overset{o}{\mathrm{A}}$, $a = 4.2401\,\overset{o}{\mathrm{A}}$, $a = 4.2539\,\overset{o}{\mathrm{A}}$ and $a = 4.2086\,\overset{o}{\mathrm{A}}$ respectively. The increment in lattice parameter on replacement of Fe by different elements clearly suggests incorporation of these elements in the unit cell as well as resultant expansion in the unit cell. The observed systematic expansion in the unit cell for the samples BYN, BGN and BEN is due to replacement of larger B-site ions; Y^{3+}, Gd^{3+} and Eu^{3+} in place of Fe^{3+} (see Table 3.1 for respective ionic radii). The expansion in unit cell of BCN and BMN is in contradiction with the smaller ionic radii of Co^{3+} and nearly comparable ionic radii of Mn^{3+} with Fe^{3+} (see Table3.1). The likely reason for such an observed expansion for BCN and BMN is due to the removal of degeneracy in unevenly filled t_{2g} levels of O2p-Co3d^6/O2p-Mn3d^4 in comparison with the degenerate O2p-Fe3d^5 levels leading to a weak John-Teller Effect [3-4]. The delocalization of the orbital leads to a softening of the overlap, which in turn leads to the expansion of the unit cell. Further, we calculated the percentage densification using the unit cell parameters. The percentage densification (more than 75%), indicate that the samples are of good quality (see Table 4.A.1).

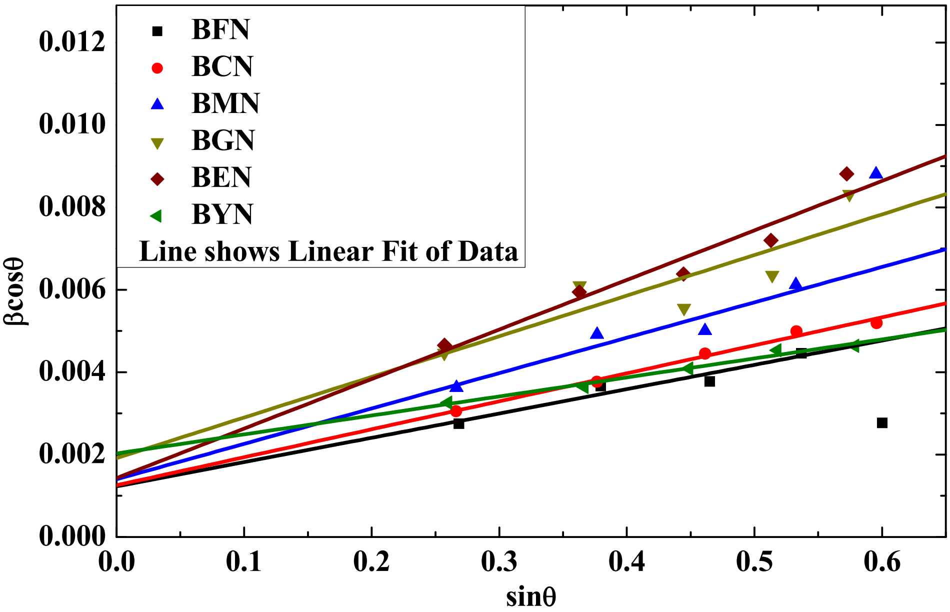

Figure 4.A.2: Williamson – Hall plot for BFN, BCN, BMN, BGN, BEN and BYN.

The Figure 4.A.2 shows Williamson – Hall plot for above six samples. The crystallite size and induced strain are calculated from the fitting parameters. The obtained crystallite size and strain values are tabulated in Table 4.A.1. The other crystallographic parameters along with formula unit and formula weight are also presented in Table 4.A.1.

4.A.1.2 X-Ray Diffraction Analysis of BFCN Series: [$Ba(Fe_{0.5-X}Co_XNb_{0.5})O_3$] (where X=0, 0.10, 0.25, 0.40, 0.50):

The structural changes induced by gradual substitution of Fe by Co are studied in this section. The XRD patterns of all samples are presented in Figure 4.A.3. The XRD patterns clearly suggest pure single phase formation for these compounds. The inset of figure shows that the peaks are gradually shifting towards lower 2θ values with increment in Co concentration. This clearly suggests expansion of unit cell on gradual replacement of Fe^{3+} by Co^{3+}. The fitting of all XRD patterns are resulted in to cubic symmetry of the samples. It is in agreement with results predicted through tolerance factor calculated in Table 3.1. The obtained unit cell parameters for BFN, BFCN-10C, BFCN, BFCN-40C and BCN are $a = 4.0529\,\overset{o}{A}$, $a = 4.0569\,\overset{o}{A}$, $a = 4.0692\,\overset{o}{A}$, $a = 4.0727\,\overset{o}{A}$ and $a = 4.0886\,\overset{o}{A}$ respectively. The values of unit cell parameters

Sr. No	Sample	Formula	Formula Weight (g/mole)		Crystal System	Lattice Parameter a (Å)	Unit cell Volume ($Å^3$)	Density Calculated ρ_c (g/cm^3)	Density Measured ρ_m (g/cm^3)	Percentage Densification $\left(\frac{\rho_m}{\rho_c}\times 100\right)$	Crystallite size (nm)		Percentage Strain
											Debye Scherrer	Williamson-Hall	
1	BFN	$Ba(Fe_{0.5}Nb_{0.5})O_3$	259.701		Cubic	4.0529	66.5729	6.4778	5.4218	83.7	41	113	0.0017
2	BFCN-10C	$Ba(Fe_{0.40}Co_{0.10}Nb_{0.5})O_3$	260.010		Cubic	4.0569	66.7702	6.4663	5.9676	92.3	38	117	0.0021
3	BFCN	$Ba(Fe_{0.25}Co_{0.25}Nb_{0.5})O_3$	260.473		Cubic	4.0692	67.3794	6.4193	5.8319	90.8	33	290	0.0026
4	BFCN-40C	$Ba(Fe_{0.10}Co_{0.40}Nb_{0.5})O_3$	260.936		Cubic	4.0727	67.5534	6.4141	5.7048	88.9	34	105	0.0025
5	BCN	$Ba(Co_{0.5}Nb_{0.5})O_3$	261.245		Cubic	4.0886	68.3477	6.3471	5.4368	85.7	34	110	0.0033
6	BMN	$Ba(Mn_{0.5}Nb_{0.5})O_3$	259.247		Cubic	4.0909	68.4631	6.2879	5.3165	84.6	27	99	0.004
7	BFMN	$Ba(Fe_{0.25}Mn_{0.25}Nb_{0.5})O_3$	259.474		Cubic	4.0677	67.3049	6.4017	3.3453	52.3	31	722	0.003
8	BGN	$Ba(Gd_{0.5}Nb_{0.5})O_3$	310.403		Cubic	4.2401	76.2304	6.7616	5.0374	74.5	23	72	0.0041
9	BFGN	$Ba(Fe_{0.25}Gd_{0.25}Nb_{0.5})O_3$	285.052	BFGN-BFN	Cubic	4.0922	68.5284	6.5886	4.5881	69.6	23	224	0.0026
				BFGN-BGN	Cubic	4.2201	75.1568				17	93	0.0012
10	BEN	$Ba(Eu_{0.5}Nb_{0.5})O_3$	307.758		Cubic	4.2539	76.9772	6.6389	6.0585	91.3	22	97	0.0025
11	BFEN	$Ba(Fe_{0.25}Eu_{0.25}Nb_{0.5})O_3$	283.730	BFEN-BFN	Cubic	4.0674	67.29	6.5749	3.8101	57.9	22	473	0.0024
				BFEN-BEN	Cubic	4.2363	76.0256				24	78	0.0039
12	BYN	$Ba(Y_{0.5}Nb_{0.5})O_3$	276.231		Cubic	4.2086	74.544	6.1533	4.9341	80.2	35	68	0.0018
13	BGCN-10C	$Ba(Gd_{0.40}Co_{0.10}Nb_{0.5})O_3$	300.572		Cubic	4.2211	75.2102	6.6362	4.1969	63.2	28	175	0.0037
14	BGCN	$Ba(Gd_{0.25}Co_{0.25}Nb_{0.5})O_3$	285.824	BGCN-BCN	Cubic	4.0865	68.2424	6.6507	5.0024	75.2	22	66	0.0017
				BGCN-BGN	Cubic	4.2075	74.4856				18	123	0.0021
15	BECN	$Ba(Eu_{0.25}Co_{0.25}Nb_{0.5})O_3$	284.502	BECN-BCN	Cubic	4.0869	68.2625	6.5819	5.1909	78.9	22	49	0.0026
				BECN-BEN	Cubic	4.2226	75.2904				22	409	0.0025

Table 4.A.1: The crystallographic parameters along with percentage densification, crystallite size and induced lattice strain.

confirm observed systematic expansion in the unit cell. The likely reason for such expansion is a weak John-Teller Effect as discussed earlier.

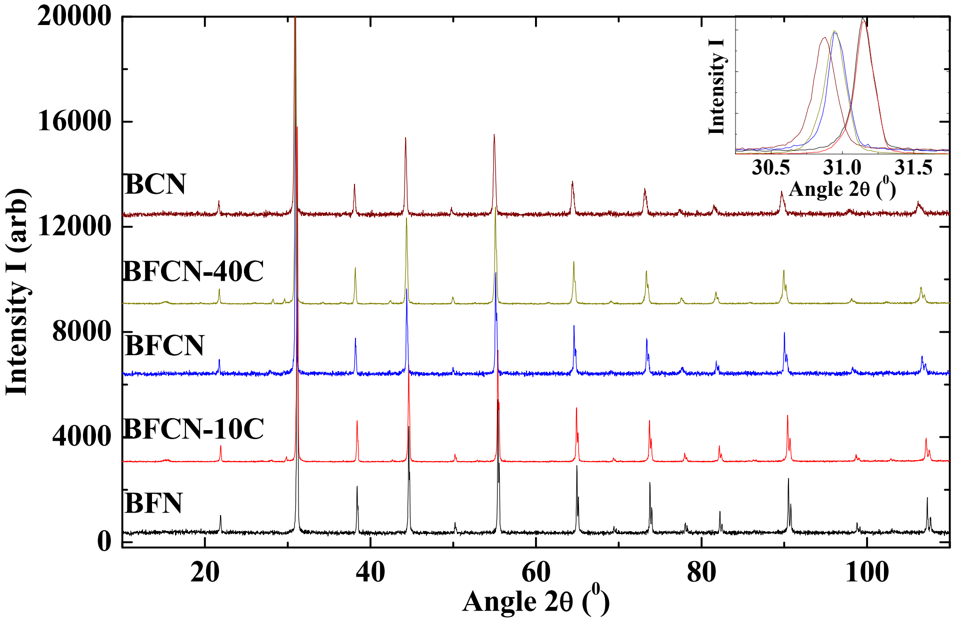

Figure 4.A.3: XRD patterns of BFN, BFCN-10C, BFCN, BFCN-40C and BCN ceramics. (All patterns are uplifted by 1500 cps from the bellow pattern except BFN.) Inset shows gradual shifting of main intense peak for each of the compounds.

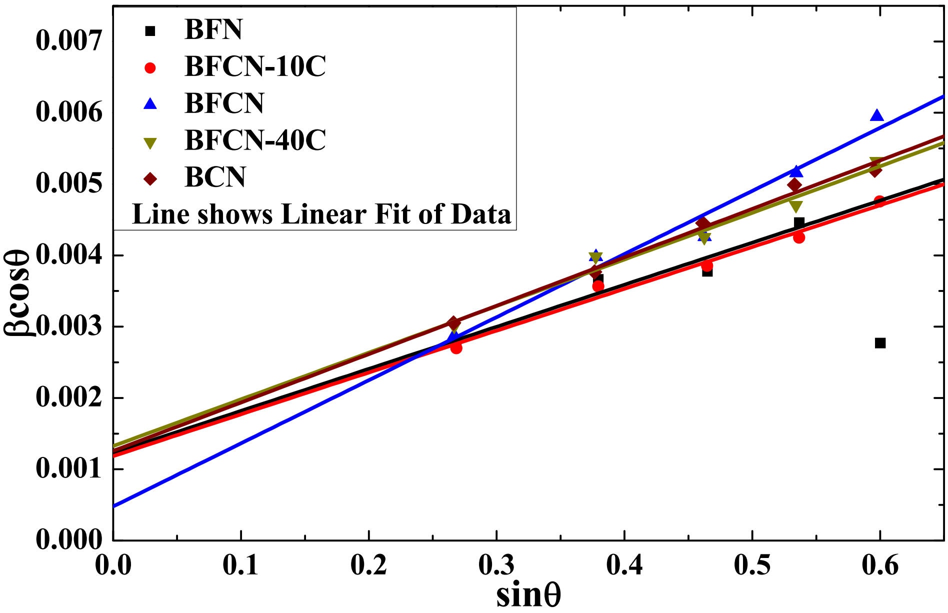

Figure 4.A.4: Williamson – Hall plot for BFN, BFCN-10C, BFCN, BFCN-40C and BCN.

Further, the obtained single phase for the intermediate samples BFCN-10C, BFCN and BFCN-40C clearly suggests that the crystallites of BFN and BCN are perfectly merged in to each other and developed an another crystallite. This new merged crystallite is likely having the new chain of –Fe–Nb–Co–Nb–Fe – instead of separate chains of –Fe–Nb–Fe– and –Co–Nb–Co– inside a grain. The crystallite size and lattice strain determination is done using Williamson – Hall equation.

The Figure 4.A.4 shows Williamson – Hall plot for these samples. The crystallite size and induced strain are calculated from the slope and intercept of the straight line fitting. The values are tabulated in Table 4.A.1. The other crystallographic parameters along with formula unit and formula weight are also presented in Table 4.A.1.

The in-depth analysis of the crystal structure using Rietveld refinement is done for three samples of this series. The Figure 4.A.5 shows refined XRD patterns for BFN, BFCN and BCN samples [4]. The Wyckoff positions, thermal parameters, refined and more precise unit cell parameters, etc were determined through Rietveld refinement. The details of refined parameters are presented in Table 4.A.2. The goodness parameter of Rietveld refinement (S~1.26) along with the percentage densification confirms the good quality of the samples.

Sample	BFN	BFCN	BCN
Empirical formula	$BaFe_{1/2}Nb_{1/2}O_3$	$BaFe_{1/4}Co_{1/4}Nb_{1/2}O_3$	$BaCo_{1/2}Nb_{1/2}O_3$
Formula weight	259.701 g/mole	260.473 g/mole	261.245 g/mole
Structure	Cubic	Cubic	Cubic
Space Group	P_m3_m	P_m3_m	P_m3_m
a = b = c	4.0583 Å	4.0681 Å	4.0914 Å
Volume	66.8394 Å^3	67.3248 Å^3	68.4882 Å^3
Density calculated	6.4519 g/cm^3	6.4245 g/cm^3	6.3340 g/cm^3
Density measured	5.4218 g/cm^3	5.8319 g/cm^3	5.4368 g/cm^3
Percentage densification	84.0342 %	90.7759 %	85.8341 %
$\alpha = \beta = \gamma$	90	90	90
R_P	8.92	7.93	7.45
R_{WP}	11.59	10.17	9.71
R_{exp}	8.99	8.56	7.99
S	1.29	1.19	1.21

Table 4.A.2: The crystallographic structural parameters obtained through rietveld refinement of BFN, BFCN and BCN ceramics.

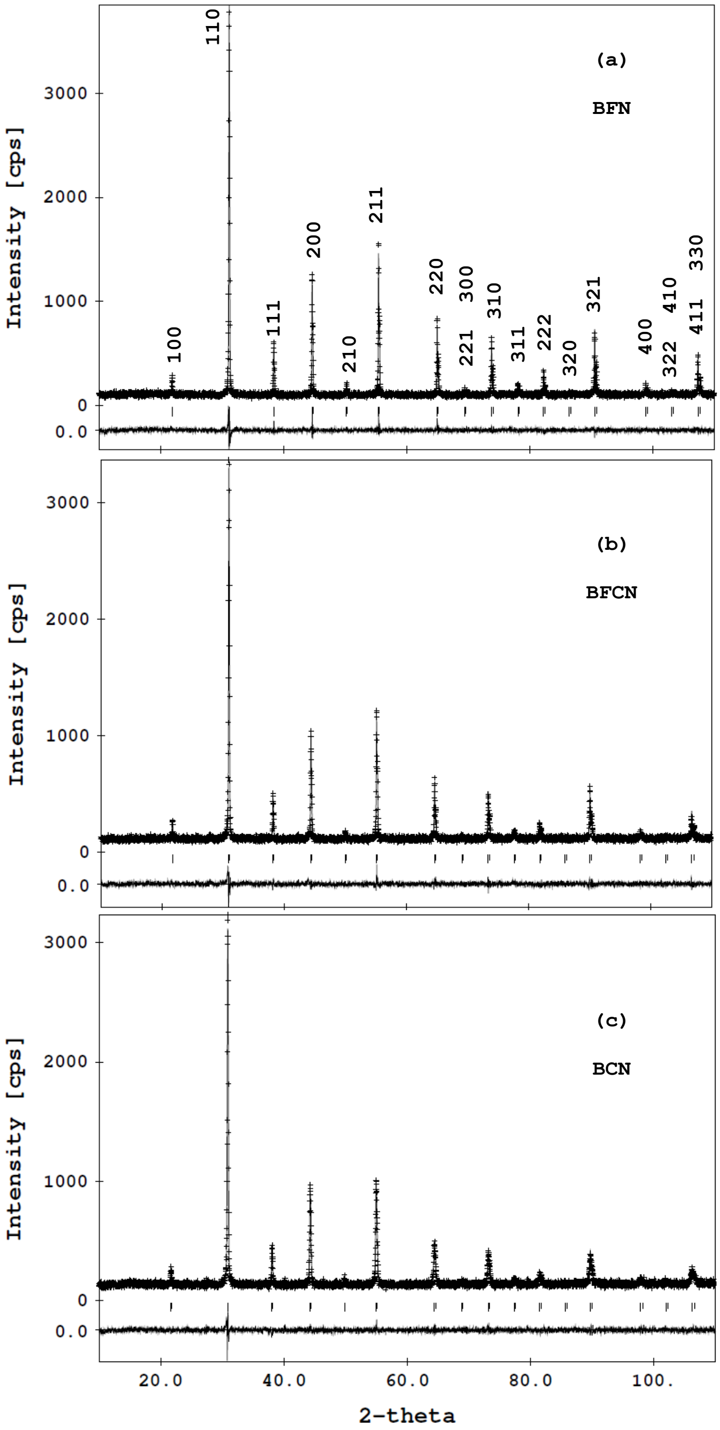

Figure 4.A.5: The observed (+sign), calculated (continuous line), and difference (bottom line) profiles obtained after the Rietveld refinement of (a)BFN, (b)BFCN, (c)BCN. The vertical bars denote position of the Bragg reflection. The corresponding sets of (hkl) planes are shown in the brackets [4].

4.A.1.3 X-Ray Diffraction Analysis of BFMN Series: [$Ba(Fe_{0.5-X}Mn_XNb_{0.5})O_3$] (where X=0, 0.25, 0.50):

The effect of Mn doping on structural modifications are studied here through XRD analysis. The collected XRD patterns of BFN, BFMN and BMN are presented in Figure 4.A.6. The inset figure shows gradual shifting of XRD peaks towards lower angles with increase in Mn concentration. It clearly suggests expansion in unit cell volume as Mn concentration increases.

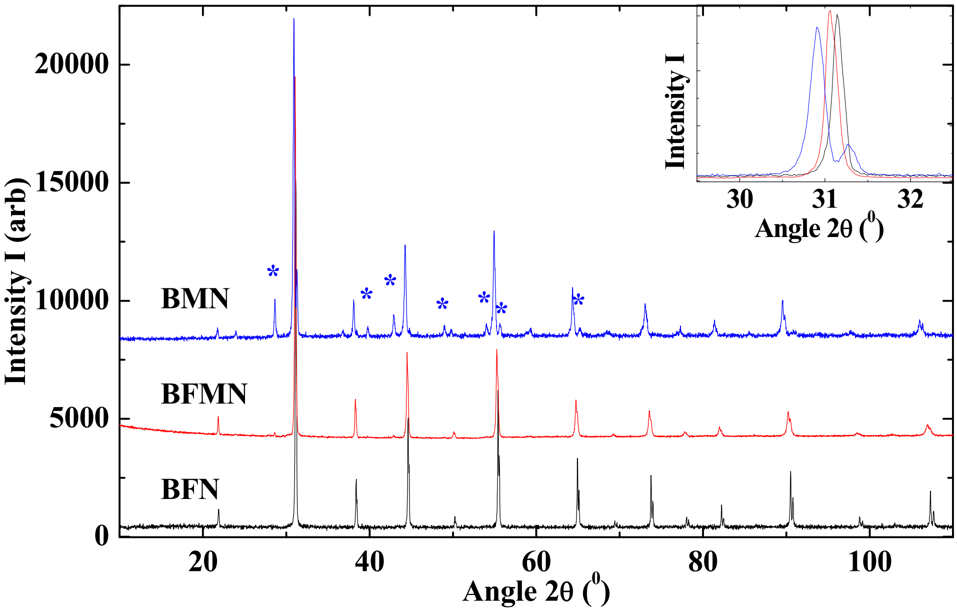

Figure 4.A.6: XRD patterns of BFN, BFMN and BMN ceramics. (All patterns are uplifted by 4000 cps from the bellow pattern except BFN.) The peaks for BMN indicated with * belongs to impurity phase. Inset shows gradual shifting of main intense peak for each of the compounds.

The XRD patterns of BFN and BFMN are found in single cubic phase while few impurity peaks (indicated as *) were detected for the BMN sample. Though the amount of impurity phase is very less (~7%) and the majority structure reflects cubic symmetry similar to the BFN and BFMN ceramic. The observed single phase for the BFMN ceramic violates existence of distinct BFN and BMN phase in the intermediate ceramic BFMN. The new BFMN phase consists of a new chain –Fe–Nb–Mn–Nb–Fe – instead of separate chains of –Fe–Nb–Fe– and –Mn–Nb–Mn– corresponding to BFN and BMN ceramics.

The unit cell parameters were determined for these samples by fitting the observed patterns using PowderX software. The obtained unit cell parameters for BFN, BFMN and BMN ceramic are $a = 4.0529\,\overset{o}{A}$, $a = 4.0677\,\overset{o}{A}$ and $a = 4.0909\,\overset{o}{A}$ respectively. This clearly confirms expansion of unit cell on gradual replacement of Fe^{3+} by Mn^{3+}. The possible reason for such expansion is weak John-Teller Effect induced by delocalization of orbital as discussed earlier.

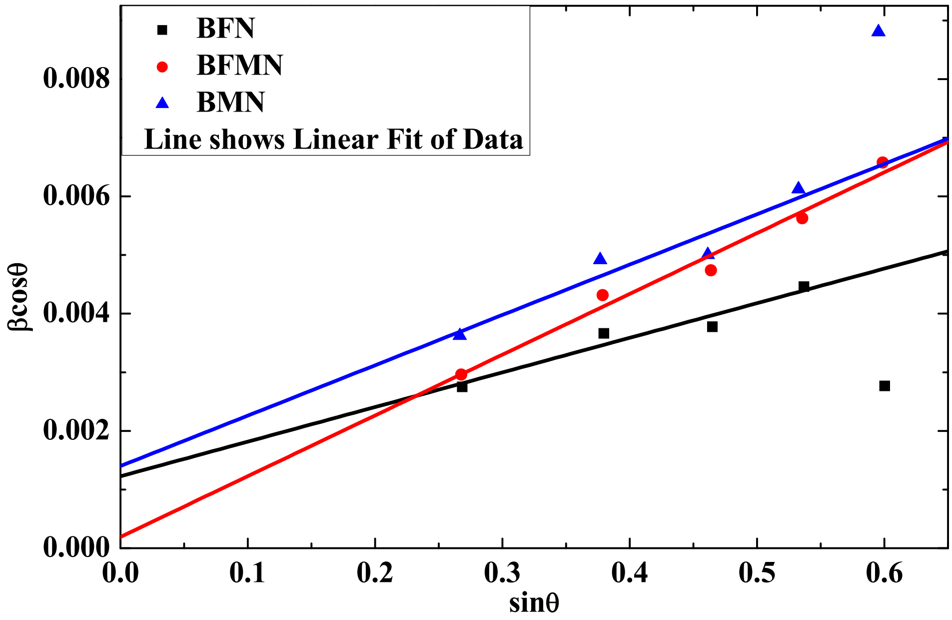

Figure 4.A.7: Williamson – Hall plot for BFN, BFMN and BMN.

The crystallite size and lattice strain are determined for these samples using Williamson – Hall plot shown in the Figure 4.A.7. The values of crystal structure parameters along with crystallite size and lattice strain are presented in Table 4.A.1.

4.A.1.4 X-Ray Diffraction Analysis of BFGN Series: $[Ba(Fe_{0.5-X}Gd_XNb_{0.5})O_3]$ (where X=0, 0.25, 0.50):

The structural changes induced by substitution of Fe by Gd are analyzed in this section. The room temperature XRD patterns of BFN, BFGN and BGN ceramics are shown in the Figure 4.A.8. The absence of any extra peak related with impurity phase confirms pure phase formation in our samples. The XRD pattern for BFGN ceramic clearly shows two distinct pure phases co-existing in the compound. The comparison of the XRD pattern of BFGN with the XRD patterns of parent BFN and BGN compounds confirms that the observed both phases are related with the BGN and BFN phase. The co-existence of separate crystallites related to BFN and BGN is likely to produce distinct chains of –Fe–Nb–Fe– and –Gd–Nb–Gd– inside a grain. Although, the coordination number and valence states of Fe and Gd is the same but larger ionic size of Gd^{3+} in comparison to Fe^{3+} leads to the presence of identifiable separate phases of BFN and BGN [5]. The fitting of XRD patterns revealed that the one phase of BFGN nearly matches with the BGN having similar cubic symmetry and lattice parameter

$a = 4.2201\ \overset{o}{A}$ while the second phase with identical matrix is related to cubic BFN compound but its lattice parameter is stretched out from $a = 4.0529\ \overset{o}{A}$ to $a = 4.0922\ \overset{o}{A}$. The observed expansion in BFN unit cell is likely due to the influence of larger BGN unit cells.

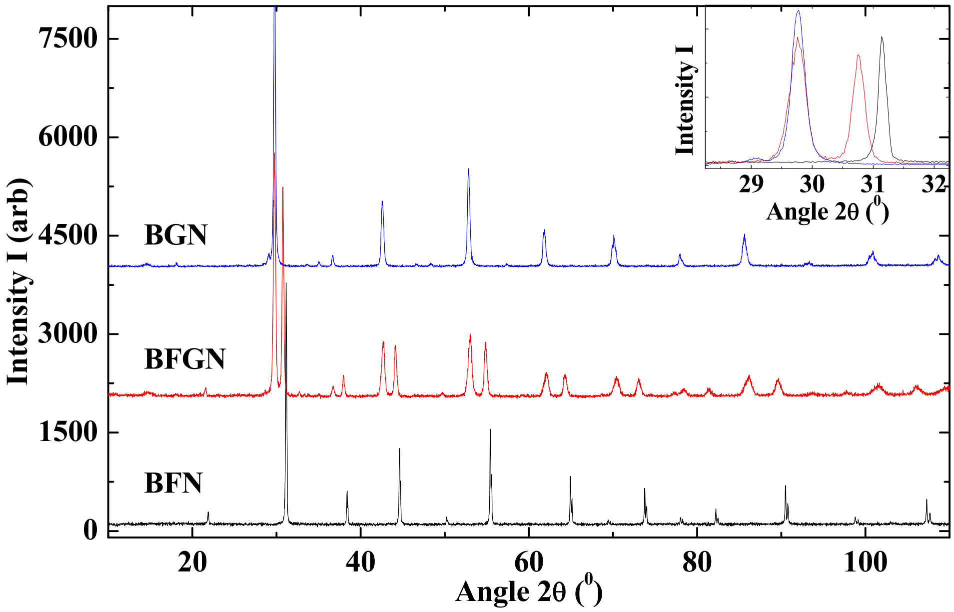

Figure 4.A.8: XRD patterns of BFN, BFGN and BGN ceramics. (All patterns are uplifted by 2000 cps from the bellow pattern except BFN.) Inset shows stretching in the developed BFN phase of BFGN compound.

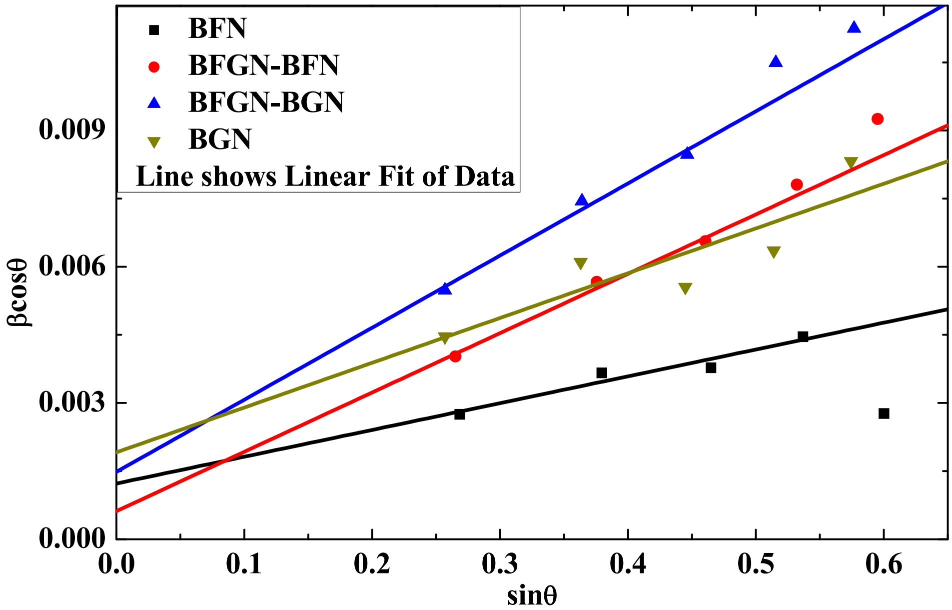

Figure 4.A.9: Williamson – Hall plot for BFN, BFGN (BFN phase), BFGN (BGN phase) and BGN.

The crystallite size and the lattice strain are calculated for each phase of the compounds. The data are obtained by fitting the Williamson – Hall plot as shown in the Figure 4.A.9. The crystallographic parameters along with strain, crystallite size and percentage densification are presented in the Table 4.A.1.

4.A.1.5 X-Ray Diffraction Analysis of BFEN Series: [$Ba(Fe_{0.5-X}Eu_XNb_{0.5})O_3$] (where X=0, 0.25, 0.50):

The effect of Eu doping on the structural properties of BFN ceramic are investigated here. The XRD patterns of BFN, BFEN and BEN are shown in the Figure 4.A.10. The XRD patterns do not have any impurity peaks suggests pure phase formation for the compounds. The inset of Figure 4.A.10 shows that the observed pure double phases for the intermediate BFEN compound are related with the BFN and BEN compounds.

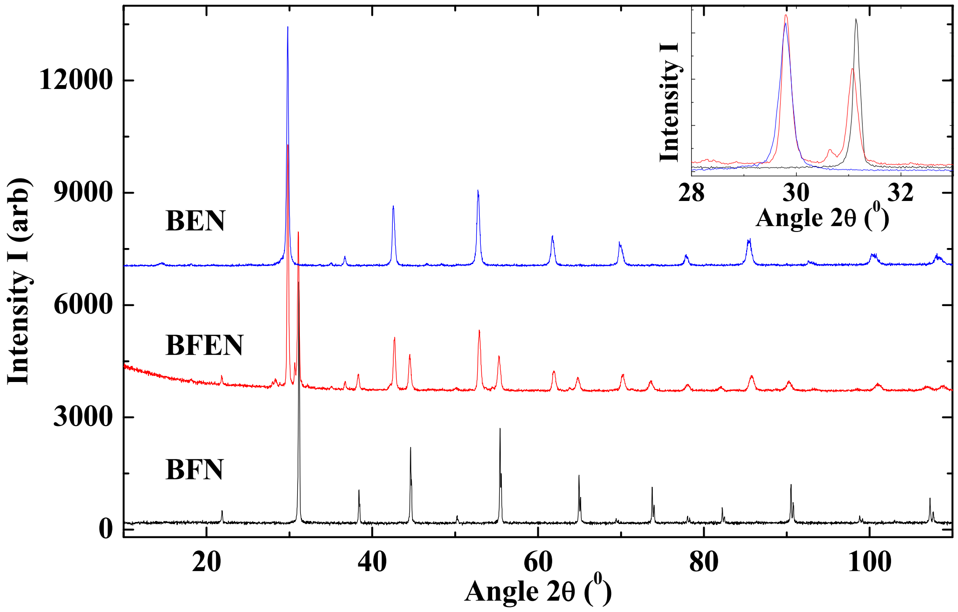

Figure 4.A.10: XRD patterns of BFN, BFEN and BEN ceramics. (All patterns are uplifted by 3500 cps from the bellow pattern except BFN.) Inset shows stretching in the developed BFN and BEN phase of BFEN compound.

The quantitative analysis of the data is done by fitting the patterns with XRD analysis software. The both phases of BFEN compound are analyzed separately. The obtained unit cell parameters for BFEN compounds are $a = 4.0674\ \overset{o}{A}$ and $a = 4.2363\ \overset{o}{A}$ respectively for BFN and BEN phase. The observed expansion and contraction in lattice parameter of BFN and BEN is not so significant in comparison to the BFGN ceramic. This results points towards the weak mutual interaction between the chains of chains of –Fe–Nb–Fe– and –Eu–Nb–Eu– in comparison to the interaction between chains –Fe–Nb–Fe– and –Gd–Nb–Gd– of BFGN ceramic. The presence of identifiable separate phases of BFN and BEN in BFEN ceramic could be due to large difference in the ionic radii of Eu^{3+} in comparison to Fe^{3+}.

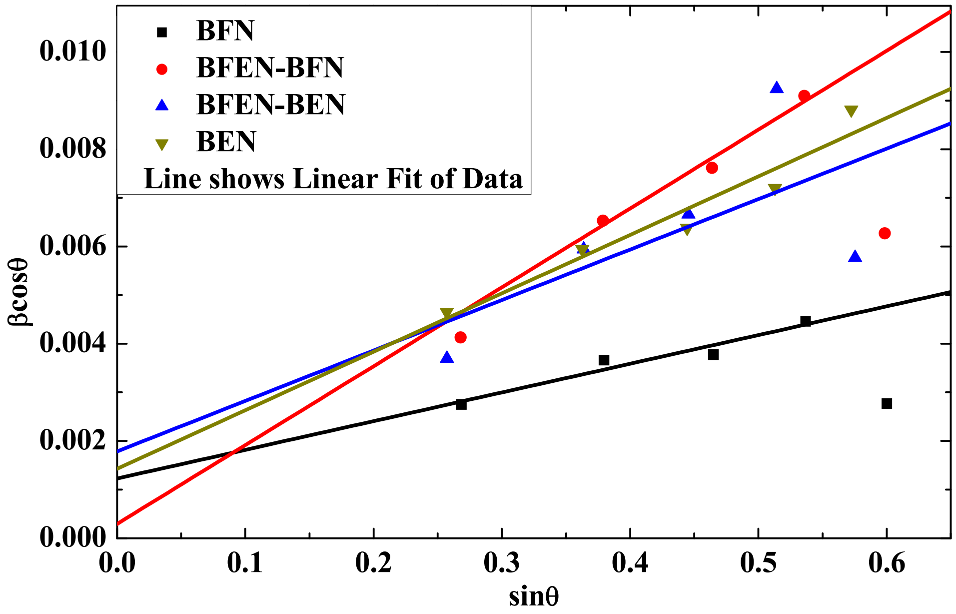

Figure 4.A.11: Williamson – Hall plot for BFN, BFEN (BFN phase), BFEN (BEN phase) and BEN.

The crystallite size and lattice strain measurement of the sample is done by fitting the XRD data using Williamson – Hall equation. The typical Williamson – Hall plots for BFN, BFEN and BEN compounds are shown in the Figure 4.A.11. The observed both phases are analyzed separately for the BFEN compound. The results obtained are presented in Table 4.A.1.

4.A.1.6 X-Ray Diffraction Analysis of BGCN Series: [$Ba(Gd_{0.5-X}Co_XNb_{0.5})O_3$] (where X=0, 0.10, 0.25, 0.50):

The effect of gradual substitution of Gd by transition element Co is analyzed for the structural modifications in BGN ceramic. The XRD patterns for BGN, BGCN-10C, BGCN and BCN are presented in the Figure 4.A.12. The absence of impurity peaks in the XRD patterns of all compounds clearly reflects pure phase formation. The XRD pattern for the BGCN-10C shows single phase formation while for the BGCN compound it shows double phase formation related with BGN and BCN. The inset of Figure 4.A.12 clearly separates these two phases. The different nature of the XRD patterns for both intermediate compounds reflects that the interaction between –Gd–Nb–Gd– and –Co–Nb–Co– chains are quite different for both the compounds. These chains merge into each and results in a new chain –Gd–Nb–Co–Nb–Gd– for the BGCN-10C compound while it remains separate for BGCN compound. The higher concentration of BGN unit cells can easily modify the unit cell dimension of BCN and merges them in to a single chain in BGCN-10C compound. The presence of identifiable separate phases of BGN and BCN in BGCN ceramic could be due to nearly equal amount of available crystallites related to BGN and BCN. They are not been able to merge themselves in to each other due to larger difference in the ionic radii of Gd^{3+} in comparison to Co^{3+}. This interaction not only depends on the difference between ionic radii but also on the relative concentration of Co.

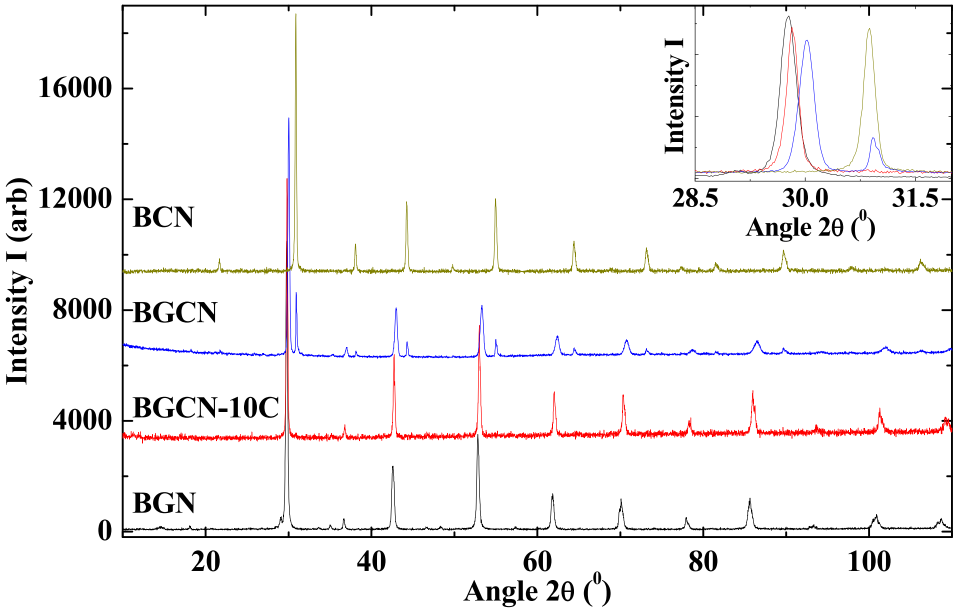

Figure 4.A.12: XRD patterns of BGN, BGCN-10C, BGCN and BCN ceramics. (All patterns are uplifted by 3500 cps from the bellow pattern except BGN.) Inset shows gradual shifting of main peak as well as stretching in the developed BGN and BCN phase of BGCN compound.

The fitting of the XRD patterns is done for each observed phases. The unit cell parameter obtained by fitting for BGCN-10C is $a = 4.2211\ \overset{o}{A}$ while for BGCN it is stretched out to $a = 4.2075\ \overset{o}{A}$ and $a = 4.0865\ \overset{o}{A}$ respectively corresponding to BGN and BCN phase. The observed stretching confirms the possible interaction between the chains of –Gd–Nb–Gd– and –Co–Nb–Co–.

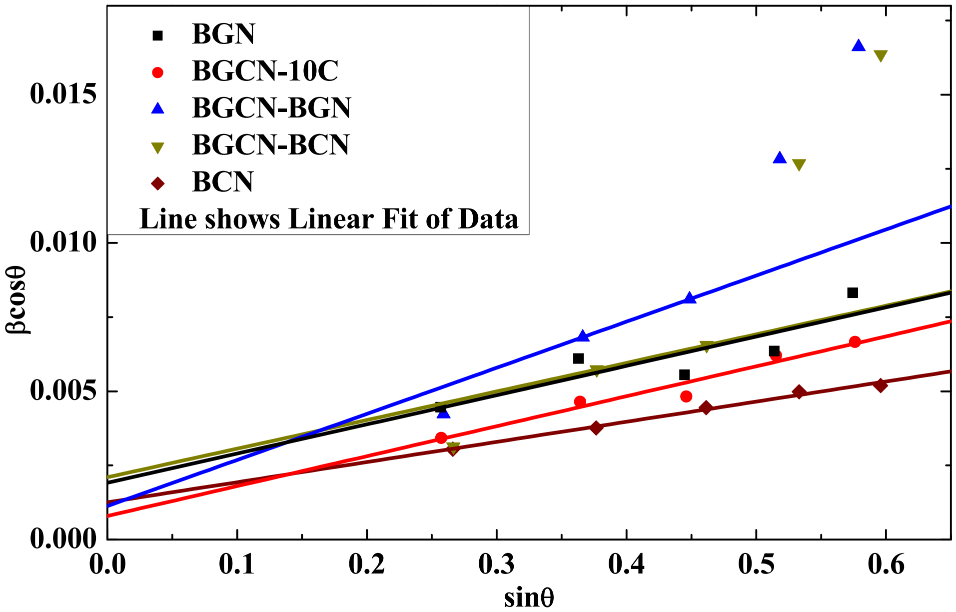

Figure 4.A.13: Williamson – Hall plot for BGN, BGCN-10C, BGCN (BGN phase), BGCN (BCN phase) and BCN.

The crystallite size and lattice strain measurement of each observed phase is done using Williamson – Hall plot. The typical Williamson – Hall plots for BGN, BGCN-10C, BGCN and BCN compounds are shown in the Figure 4.A.13. The results obtained are presented in Table 4.A.1.

4.A.1.7 X-Ray Diffraction Analysis of BECN Series: [$Ba(Eu_{0.5-X}Co_XNb_{0.5})O_3$] (where X=0, 0.25, 0.50):

The structural modifications in BEN ceramic carried out by substitution of Eu by Co are analyzed in this section. The XRD patterns of BEN, BECN and BCN are presented in the Figure 4.A.14. There is no any peak detected related to the impurity phase confirms the pure phase formation for all compounds. The intermediate compound BECN shows double phase formation. It is clear from the inset of Figure 4.A.14 that these both phases are related to the BEN and BCN compounds. The quantitative analysis of the data is done by fitting the patterns using XRD analysis software. The both phases of BECN compound are analyzed separately.

The obtained unit cell parameters for BECN compounds are $a = 4.2226\ \overset{o}{A}$ and $a = 4.0869\ \overset{o}{A}$ respectively for BEN and BCN phase. Similar to the BFEN compound, no significant contraction or Expansion is observed, in the lattice parameter of BEN and BCN phase of BECN ceramic. It clearly reflects very weak mutual interaction between the chains of –Eu–Nb–Eu– and –Co–Nb–Co– in BECN ceramic. The presence of identifiable separate phases of

BEN and BCN in BECN ceramic could be due to large difference in the ionic radii of Eu^{3+} in comparison to Co^{3+}.

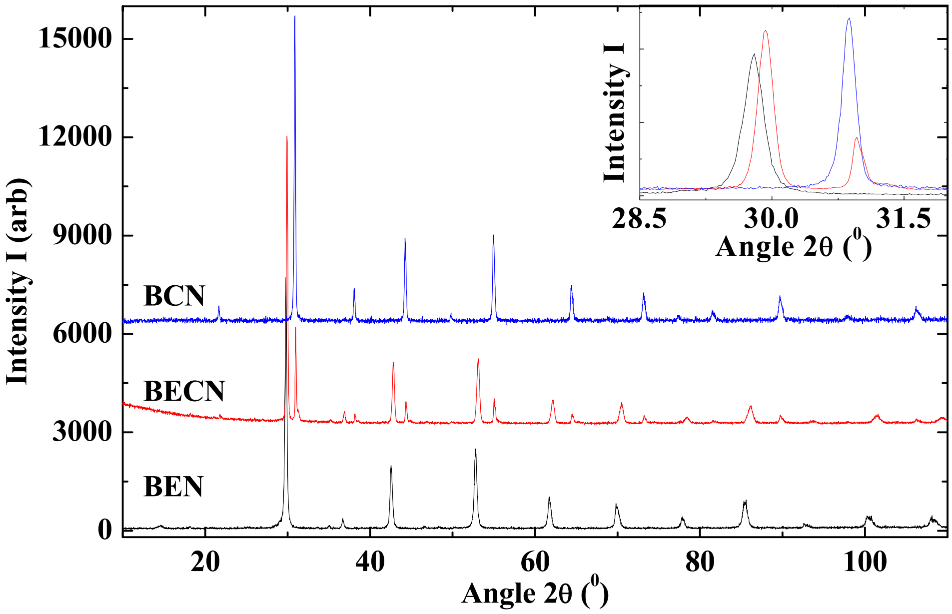

Figure 4.A.14: XRD patterns of BEN, BECN and BCN ceramics. (All patterns are uplifted by 3500 cps from the bellow pattern except BEN.) Inset shows stretching in the developed BEN and BCN phase of BECN compound.

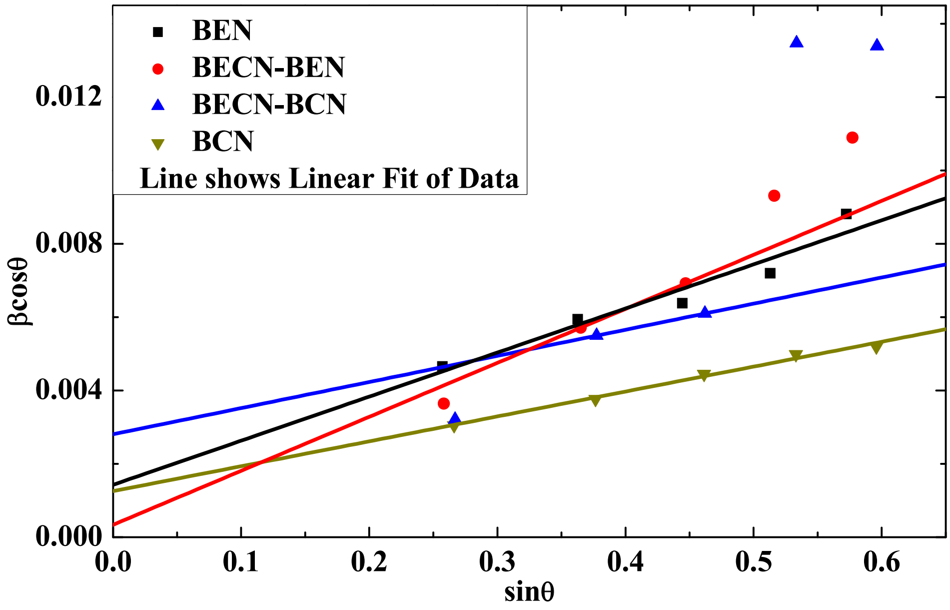

Figure 4.A.15: Williamson – Hall plot for BEN, BECN (BEN phase), BECN (BCN phase) and BCN.

The crystallite size and lattice strain measurement of each identified phase is done separately using Williamson – Hall plot. The typical Williamson – Hall plots for BEN, BECN and BCN compounds are shown in the Figure 4.A.15. The results obtained are presented in Table 4.A.1.

4.A.1.8 Summary of Crystallographic Structural Studies:

The XRD patterns of the prepared samples confirm the pure phase formation of the compounds. The refinement of the XRD patterns reveals that the lattice of the compounds expands as we substitute the Fe by other elements like Co, Mn, Gd, Eu and Y. The observed systematic expansion in the unit cell of BYN, BGN and BEN is due to gradual replacement of larger B-site ions; Y^{3+}, Gd^{3+} and Eu^{3+} in comparison to small Fe^{3+}. On the other hand the expansion in unit cell of BCN and BMN is due to the removal of degeneracy in unevenly filled t_{2g} levels of O2p-Co3d^6/O2p-Mn3d^4 in comparison with the degenerate O2p-Fe3d^5 levels. The delocalization of the orbital leads to a softening of the overlap, which in turn leads to the expansion of the unit cell. Further for the intermediate samples like BFCN and BFMN we obtained merged crystallite of BFN and BCN/BMN. On the other hand for the compounds like, BFGN, BFEN, BGCN and BECN we identified co-existence of two separate crystallites. The ionic radii of the Fe site element along with the concentration of the substituted element play a crucial role to generate chains of separate or merged crystallites.

4.A.2 Micro Structural Characterization: (Scanning Electron Microscopy – SEM):

The quality and density of the well sintered sample is determined using Scanning Electron Microscopy. The SEM micrographs of the sintered and annealed samples are collected at room temperature. The grain growth, grain boundary features, liquid phase formation, porosity and density of the material are observed through SEM measurements. The SEM micrographs were collected with three different magnifications at three different regions of the sample to ensure the correctness of the results. The collected micrographs are presented in groups of seven different series as shown in the Figure 4.A.16 and Figure 4.A.17.

The biggest grains of around 10 μm are observed for the parent compound BFN among all ceramic compounds. The compound BCN, in which Fe is completely substituted by Co, exhibited smallest grains of nearly 1 μm. The grains of around 2 μm are found in the micrographs of BMN, BGN and BYN compounds. The Eu rich BEN compound has shown grains of around 8-10 μm.

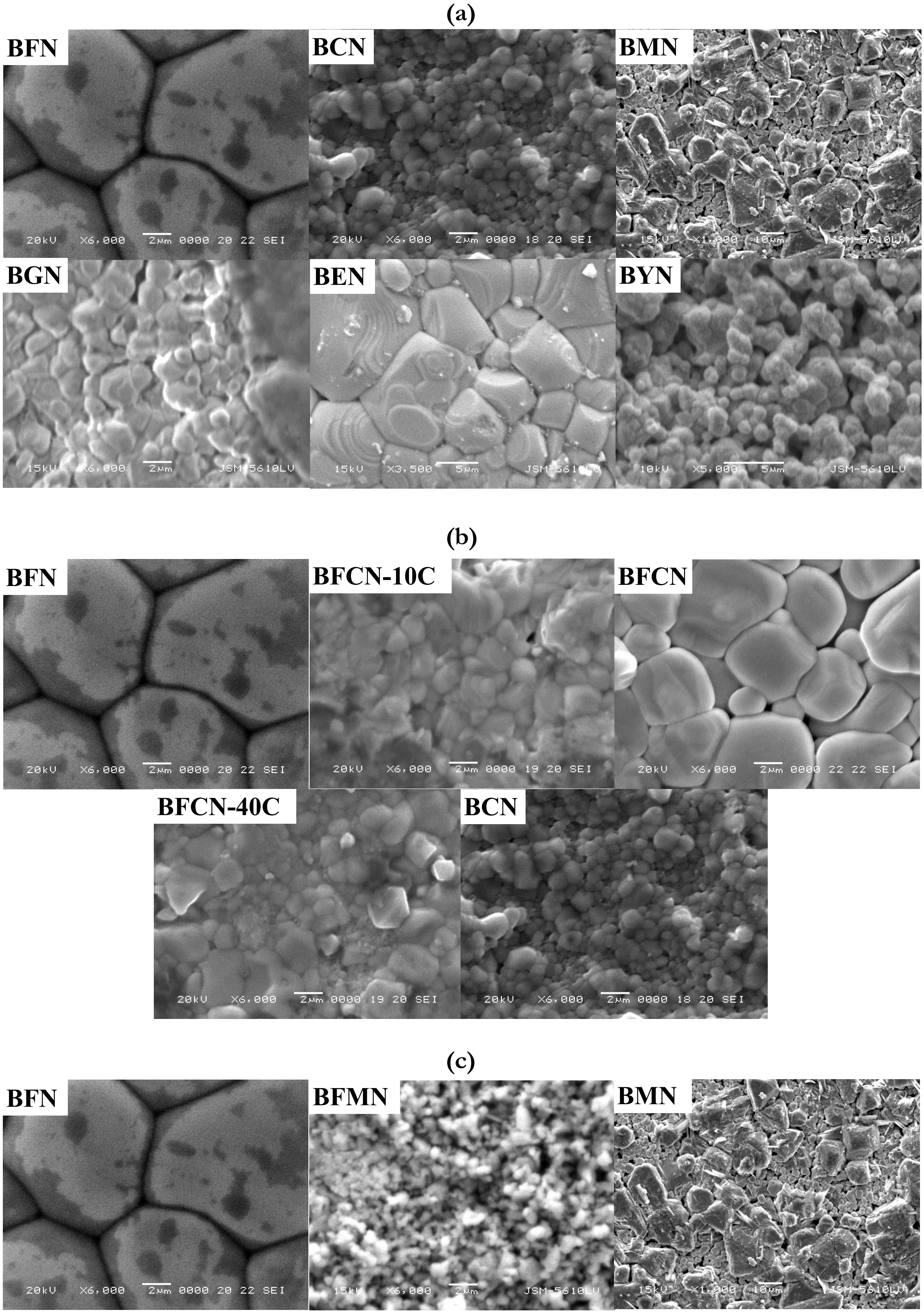

Figure 4.A.16: SEM micrographs of (a) 100% series, (b) BFCN series and (c) BFMN series.

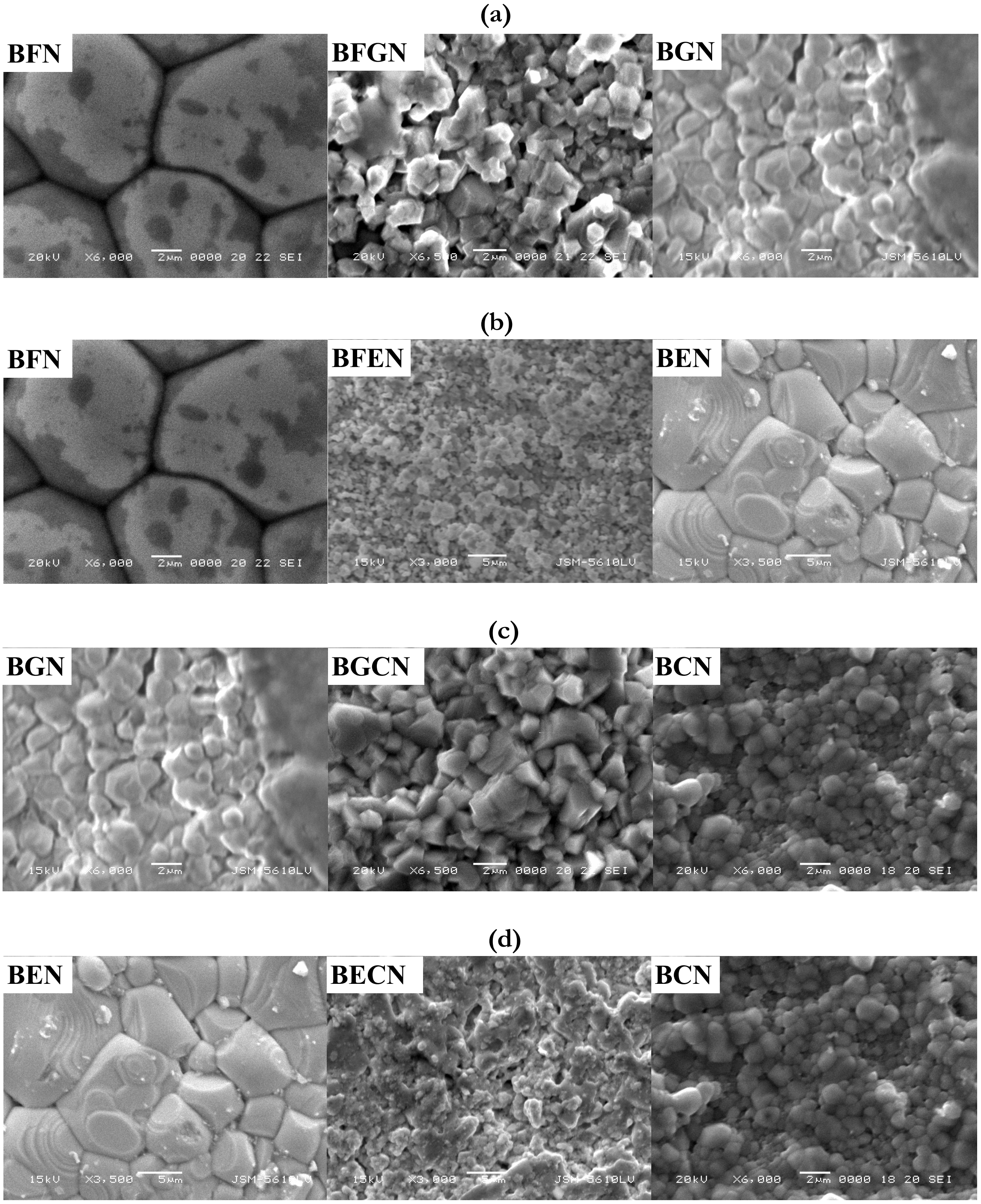

Figure 4.A.17: SEM micrographs of (a) BFGN series, (b) BFEN series, (c) BGCN series and (d) BECN series.

The intermediate compound BFCN is also having larger grains of around 5-10 μm. The other intermediate compounds like, BFCN-10C, BFCN-40C, BFGN, BGCN and BECN have developed grains of around 2-3 μm. The rest intermediate compounds, BFMN and BFEN, have shown smaller grains of around 1 μm. Thus no any systematic change in the grain growth is observed with the Fe substitution. Further all the images show dense growth of the grains confirming good quality of the samples.

4.A. 2.1 Summary of Micro Structural Characterization:

The well defined grains are observed for all samples in the collected micrographs. The biggest grains of 10 μm are obtained for parent compound BFN. The smallest grains (~1 μm) are obtained for BCN compound. The Eu rich compound BEN and intermediate compound BFCN have also shown larger grain of 8-10 μm. There is no systematic relation between grain growth parameters and composition of the compounds. The majority of intermediate samples have shown grain size of around 2 μm.

4.A. 3 Thermal Analysis: (Differential Scanning Calorimetry – DSC and Thermal Gravimetric Analysis – TGA):

The electric as well as magnetic transport properties of the compounds strongly depend on the structural transformations of the compounds. The structural transformations along with phase transitions and deformations can be easily identified using thermal analysis techniques. The impurities available in the compound also affect such thermal transitions. In the present study the possibilities of such thermal transitions are studied using two different methods, DSC and TGA. Only few selected samples are studied to judge possibilities of structural phase transitions.

4.A. 3.1 Differential Scanning Calorimetry – DSC:

The DSC method involves study of heat flow with the change in time and temperature. The Figure 4.A.18 shows temperature dependent heat flow measurement for BFN and BCN ceramics. The heat flow generates a broad peak followed by a sub peak as shown in the figure. The observed transitions are very weak as the height of peak is considerably small in comparison to the absolute heat flow values. The transition temperature for BFN is around 550 K which shifts towards lower temperatures for the Co rich sample BCN (around 505 K). The first transition can be clearly identified using differential curves of collected data. The second transition is very weak and could not be identified using differential curve. The DSC curves for BGN and BEN are presented in Figure 4.A.19. There is absence of any observable transition which can be noticed from the temperature dependent heat flow measurement. The BGN compound has shown a sharp but very weak step in the temperature dependent heat flow measurement at near around 650 K. This sharp transition is clearly observed in the differential DSC curve. The observed sharp transition suggests possibilities of possible phase transition at this temperature. The BEN compound has not shown any clear transition in the measured temperature range.

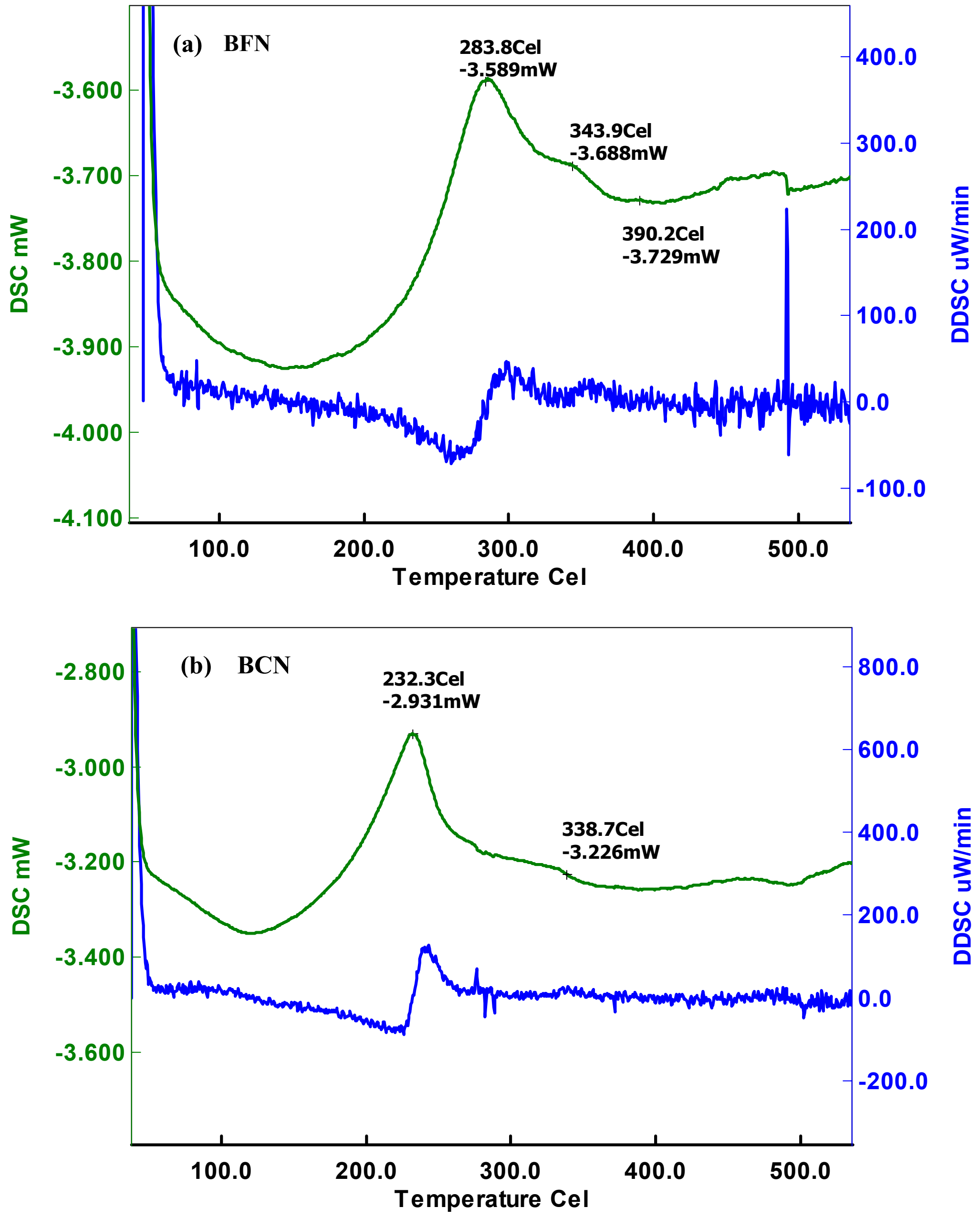

Figure 4.A.18: Temperature dependent heat flow and differential DSC curves for (a) BFN and (b) BCN.

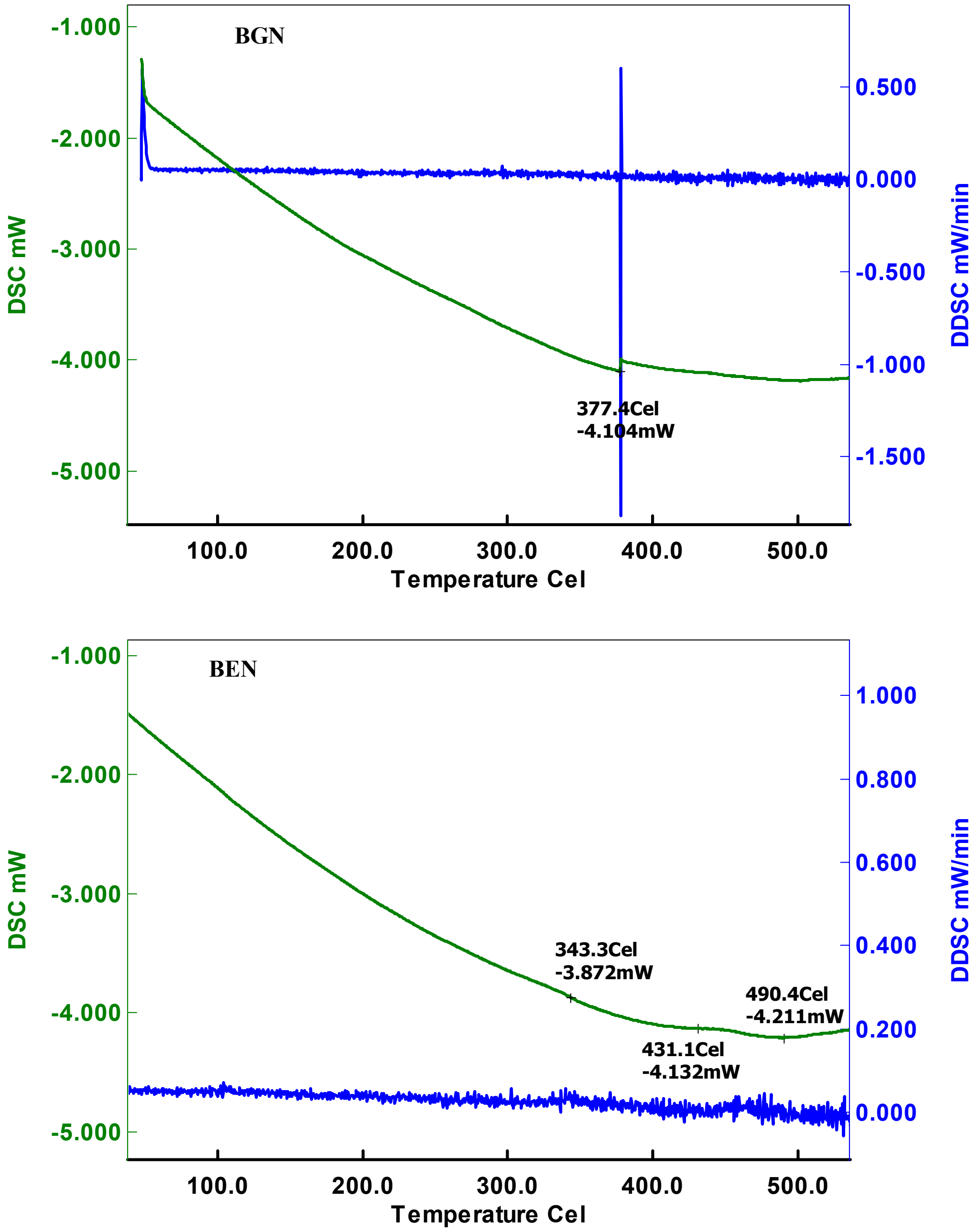

Figure 4.A.19: Temperature dependent heat flow and differential DSC curves for (a) BGN and (b) BEN.

4.A.3.2 Thermal Gravimetric Analysis – TGA:

The thermal transformations in which mass loss or mass gain is involved can be studied using TGA technique. The Figure 4.A.20 shows TGA curve for three samples BFN, BFCN and BCN. The figure shows percentage change in mass of the sample with increase in its temperature.

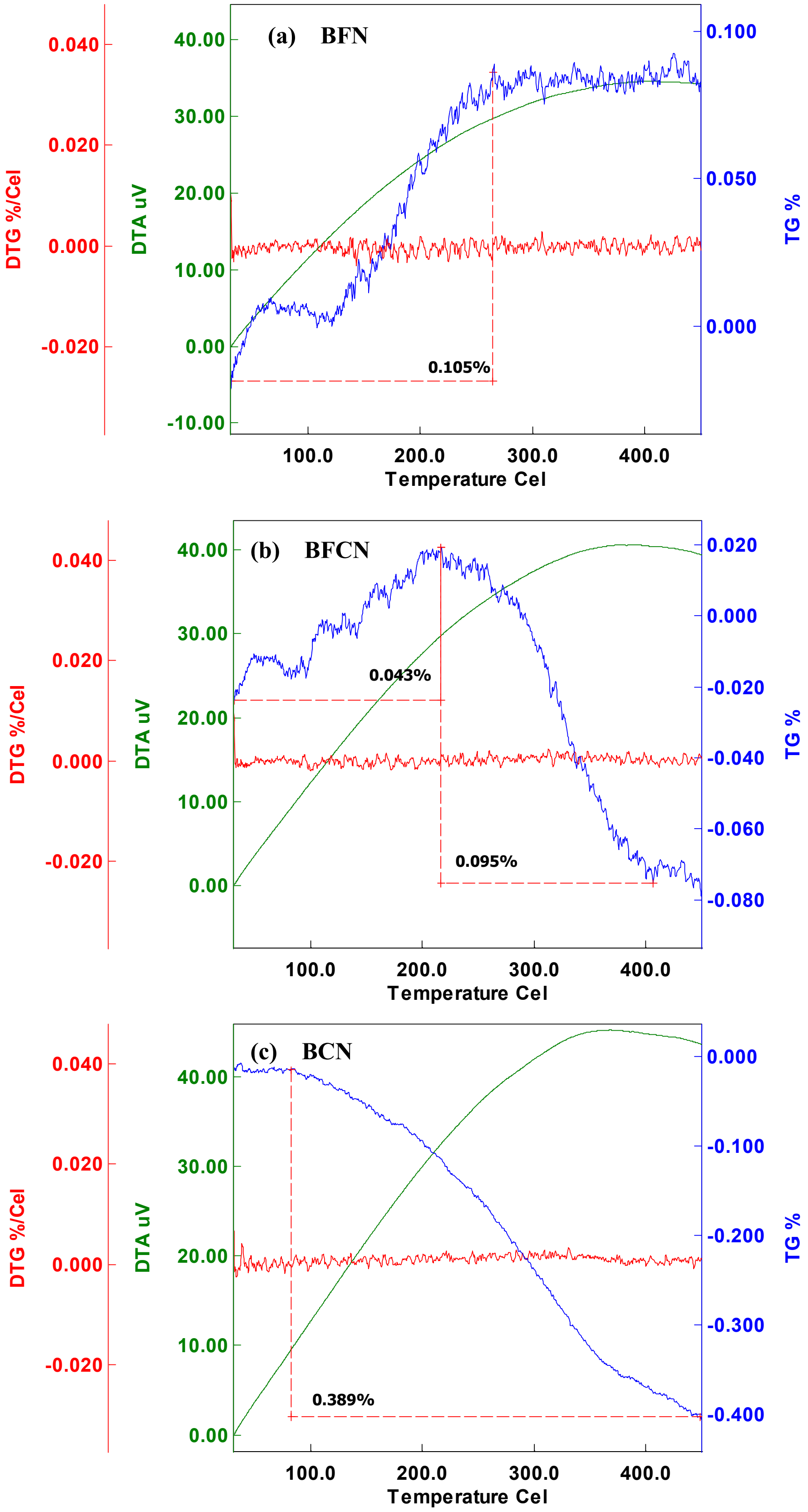

Figure 4.A.20: The figure shows temperature dependent percentage mass change and differential TG curves for (a) BFN (b) BFCN and (c) BCN.

The calculation of percentage weight change is presented in the figure. The BFN sample has shown mass gain of 0.1% in the TGA curve from 375 K to 550 K. On the other hand BCN compound has exhibited mass loss of 0.4% in the temperature range 375 K to 725 K. The intermediate compound BFCN has only shown initial mass gain of 0.05% up to 500 K, which is followed by mass loss of 0.1% after 500 K. The observed very less values of mass gain or mass loss suggest that it is only linked with the oxygen vacancies available at grain or grain boundaries rather than bulk exchanges of oxygen from compound. The development of oxygen vacancies in the grain and grain boundaries are unavoidable part of ceramic synthesis method [6-7]. The mass gain observed in BFN ceramic suggests that the compound reacts with the oxygen available in the air leading to saturation of oxygen vacancies. The mass loss observed for BCN compound suggests that the compound generates more oxygen vacancies and liberates oxygen in the air. The observed mass gain for the intermediate compound BFCN up to 500 K suggest dominating nature of BFN crystallites in this temperature range, on the other hand beyond 500 K the BCN crystallites dominates and compound shows overall mass loss. Further, above analysis suggest the absence of any crystallographic structural transitions in these compounds, except in BGN, between room temperature and 700K.

4.A.3.3 Summary of Thermal Analysis:

The DSC curves of BFN and BCN ceramic have shown weak and broad thermal transition over a wider temperature span. The observed transition is very weak and is followed by subsequent weaker transitions. The TGA curve has shown mass gain for BFN and mass loss for BCN compound. The observed very less amount of change in percentage mass is related with the oxygen vacancies at grain and grain boundaries. The intermediate compound BFCN has shown mixed nature confirming possibilities of oxygen vacancies. The DSC curves for BGN and BEN ceramic have not shown any broad thermal transitions in the temperature dependent heat flow curve. A very weak signal for BEN ceramic is observed in the differential DSC curve. The BGN ceramic have shown a small but very sharp transition at 650 K is likely due to any possible phase transition.

4.A.4 Summary of Structural Characterization (Bulk):

The complex ceramic compounds are synthesized in pure phase by partial or full substitution of Fe by Co, Mn, Gd, Eu and Y elements. The compounds BFN, BCN, BMN, BGN, BEN, BYN, BFCN-10C, BFCN, BFCN-40C, BFMN and BGCN-10C have exhibited single phase formation while the compounds BFGN, BFEN, BGCN and BECN have shown double phase formation. The micrographs of the sample have confirmed batter grain formation and less porosity of the samples. The percentage densification calculated using XRD parameters exhibits good quality of the annealed compounds. The crystallite size as well as lattice strain is also determined for the prepared compounds. The thermal analysis of the compounds suggests very broad transition induced by oxygen vacancies for BFN, BFCN and BCN compounds. The BEN compound has shown a weak sharp transition at higher temperature could be possible phase transition.

References:

1. B. D. Cullity, The Structure of Polycrystalline Aggregates, in Elements of X-ray diffraction, Massachusetts, U.S.A.: Addison-Wesley Publishing Company, Inc., pp. 259-296 (1956).
2. G. K. Williamson and W. H. Hall, Acta Metall. **1**, 22 (1953).
3. J.D. Lee, Concise Inorganic Chemistry, Fifth edition, second Indian reprint, Blackwell Science Asia Pty Ltd, Victoria 3053, Australia, (2006).
4. D. D. Shah, P.K. Mehta, M. S. Desai, C. J. Panchal, J. of Alloys and Comp. **509,** 1800 (2011).
5. D. D. Shah and P. K. Mehta, AIP Conf. Proc. **1447,** 1017 (2012).
6. C. Ang, Z. Yu and L.E. Cross., Phys. Rev. B. **62,** 228 (2000).
7. S. Bu, E. Shin and G. Park, Appl. Phys. Lett. **73,** 1442 (1998).

CHAPTER 4B

Results and Discussion (Bulk): Optical and Electrical Characterization

(Optical Spectroscopy, Dielectric Spectroscopy and Electrical Polarization Studies of Bulk Samples)

The results obtained through dielectric spectroscopy and optical studies are combined with the structural results to probe contribution of grain boundary (i.e. extrinsic factor). Extended studies are carried out by doping of different elements to probe the chemical substitution effect (i.e. intrinsic factor). To understand the conduction mechanism and to identify the reason for giant dielectric constant with significant loss the studies are extended to the ac conductivity analysis. Conclusions were drawn using different model fitting of such conductivity data as well as the optical spectroscopy data. The detailed analysis is systematically explained in this chapter.

4.B.1 Optical Spectroscopy: Ultra Violet - Visible (UV-Vis.) Spectroscopic Analysis:

The UV-Vis. spectroscopy is primarily useful to determine the energy band gap of semi-conducting materials. The optical characterization of the prepared samples was performed by UV–vis reflectance measurements. The data were collected in the universal reflectance mode. The inset figures shown in the graphs of Figure 4.B.1 shows such collected reflectance data plotted against the energy of incident photons for three samples.

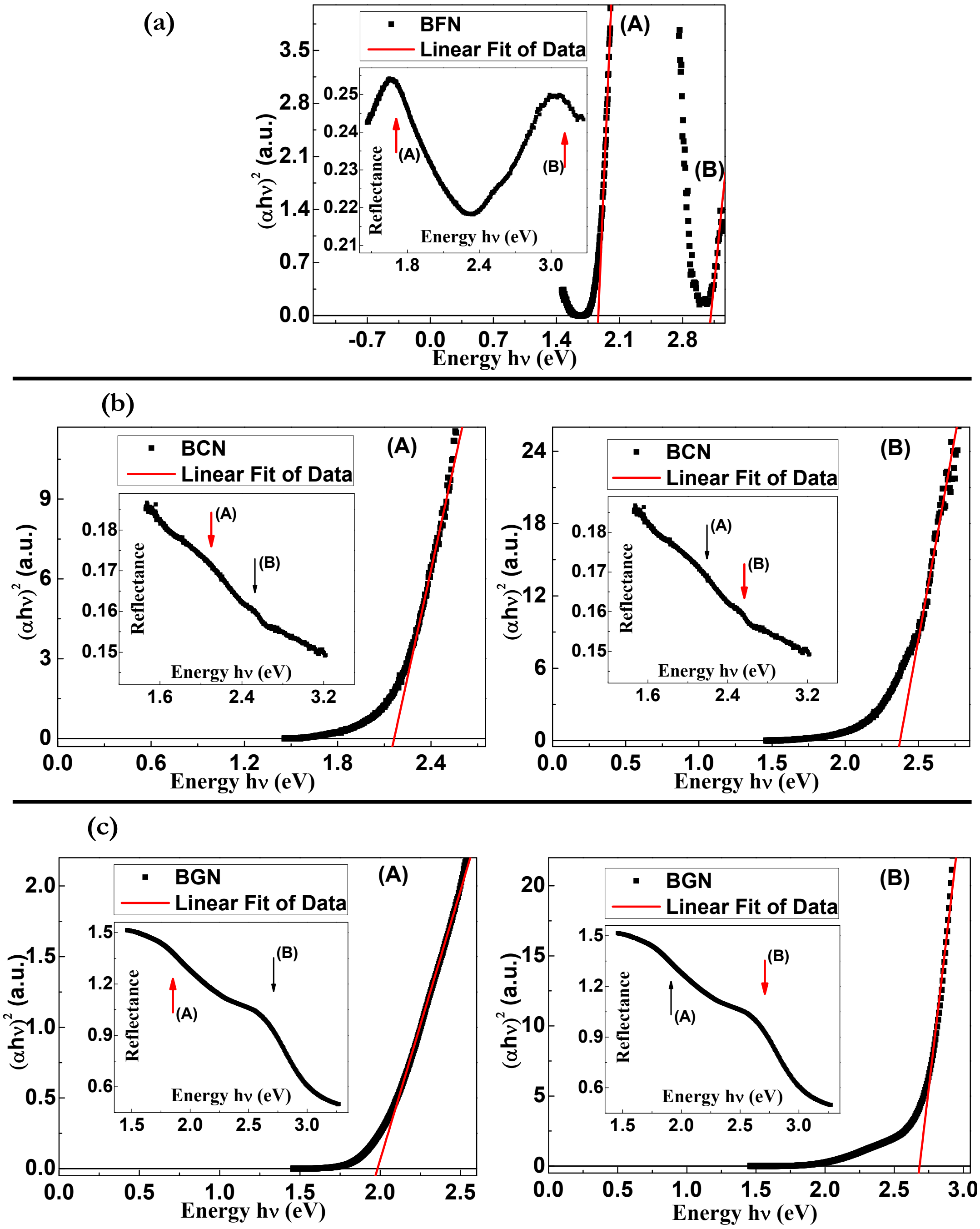

Figure 4.B.1: The Tauc's plot for (a) BFN (b) BCN and (c) BGN obtained from the UV-VIS reflectance data. Inset shows corresponding reflectance data.

The optical absorption coefficient, α; can be calculated from the reflectance data using the formula [1]:

$$\alpha = C\left[\ln\left(\frac{R_{\max} - R_{\min}}{R - R_{\min}}\right)\right] \qquad \text{...... (4.B.1)}$$

where, R is the collected reflectance data, $R_{\max}$ and $R_{\min}$ are maximum and minimum values of observed reflectance data respectively and C is a constant. The relation between incident photon energy $h\nu$ and absorption co-efficient α can be given by well-known Davis and Mott equation [2]:

$$\alpha h\nu = \left[D\left(h\nu - E_g\right)\right]^{\gamma} \qquad \text{...... (4.B.2)}$$

where, constant D is the edge width parameter and E_g represents energy band gap. The parameter γ depends on the type of transition occurs in the material. In the present case we considered $\gamma = 1/2$ corresponding to the direct allowed transition. The plot between $(\alpha h\nu)^2$ and $h\nu$, generally known as Tauc's plot [3-4], is developed for all the samples to calculate activation energy values. The direct band gap energy E_g can be obtained by extrapolating the linear part of the Tauc's plot.

Sr. No	**Sample**	**Formula**	**Optical Band Gap Energies Eg (eV)**		
			Using 1st Edge	**Using 2nd Edge**	**Using 3rd Edge**
1	BFN	$Ba(Fe_{0.5}Nb_{0.5})O_3$	1.86	3.11	-
2	BFCN	$Ba(Fe_{0.25}Co_{0.25}Nb_{0.5})O_3$	2.85	-	-
3	BCN	$Ba(Co_{0.5}Nb_{0.5})O_3$	2.16	2.37	-
4	BGN	$Ba(Gd_{0.5}Nb_{0.5})O_3$	1.98	2.68	-
5	BFGN	$Ba(Fe_{0.25}Gd_{0.25}Nb_{0.5})O_3$	2.21	-	-
6	BEN	$Ba(Eu_{0.5}Nb_{0.5})O_3$	1.94	2.22	2.58
7	BYN	$Ba(Y_{0.5}Nb_{0.5})O_3$	1.81	2.82	-

Table 4.B.1: The optical band gap values obtained from Tauc's plot.

The Figure 4.B.1 shows representative Tauc plots for three different samples viz. BFN, BCN and BGN. It is revealed from the figure that the samples show two distinct energy band edges. The analyses of both the edges (edge A and edge B) have been carried out to calculate the band gap energy values. The obtained values of energy band gap E_g for different composition are presented in the Table 4.B.1. The obtained values of energy band gap E_g (in the range of 1.8 eV to 3.2 eV) suggest that our samples belong to a category of wide band gap semiconductors.

4.B. 2 Complex Impedance Spectroscopy: Dielectric Spectroscopy:

The electrical transport properties of the samples were studied with the variation of frequency as well as temperature. The complex impedance data were collected in the frequency range of 10^0 Hz to 10^7 Hz at different temperatures. The temperature was increased at a constant heating rate of 0.5 K/min from 80 K to 750 K at an interval of 5 K. The collected impedance data were converted in to complex permittivity data using the sample dimensions and standard equations given bellow.

$$\varepsilon^* = \varepsilon' + i\varepsilon'' \qquad \text{…… (4.B.3)}$$

$$\varepsilon' = \frac{-d}{\omega\varepsilon_0 A}\frac{Z''}{\left(Z'^2 + Z''^2\right)} \qquad \text{…… (4.B.4)}$$

$$\varepsilon'' = \frac{-d}{\omega\varepsilon_0 A}\frac{Z'}{\left(Z'^2 + Z''^2\right)} \qquad \text{…… (4.B.5)}$$

Here, d is thickness of the pallet, A is area of the electrode prepared on the sample surface and ε_0 is permittivity of vacuum. The frequency response of real impedance data $Z'(f)$, imaginary impedance data $Z''(f)$, real permittivity data $\varepsilon'(f)$, and imaginary permittivity data $\varepsilon''(f)$, are presented in the Figure 4.B.2, Figure 4.B.3, Figure 4.B.4 and Figure 4.B.5 respectively for BFCN series. The observed values of real impedance data (Figure 4.B.2) show that the samples belong to semi-conducting region. The over all values of impedance decreases with increase in temperature justify NTCR nature of their resistance.

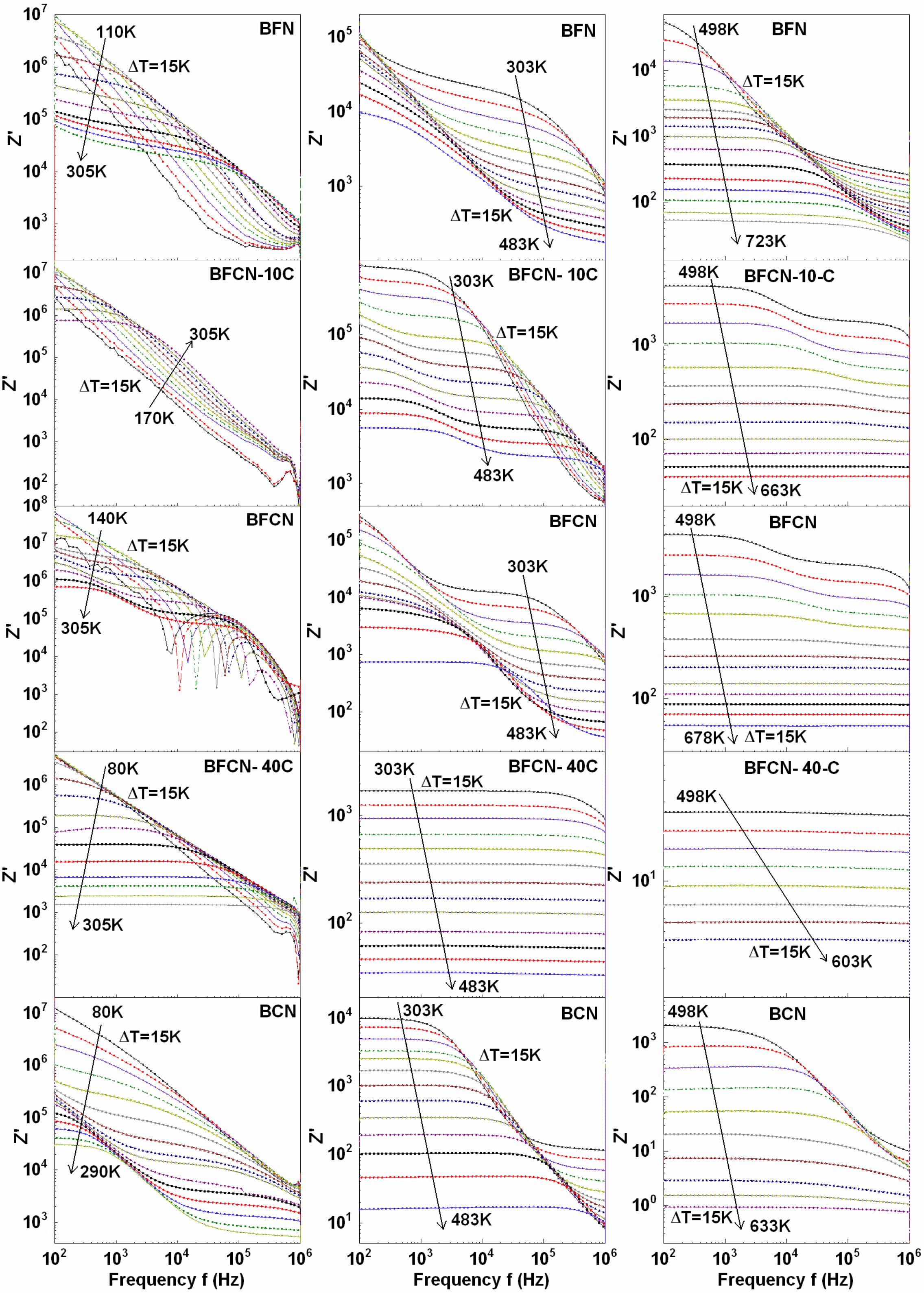

Figure 4.B.2: Real part of complex impedance data for samples of BFCN series in low temperature, mid temperature and high temperature regions.

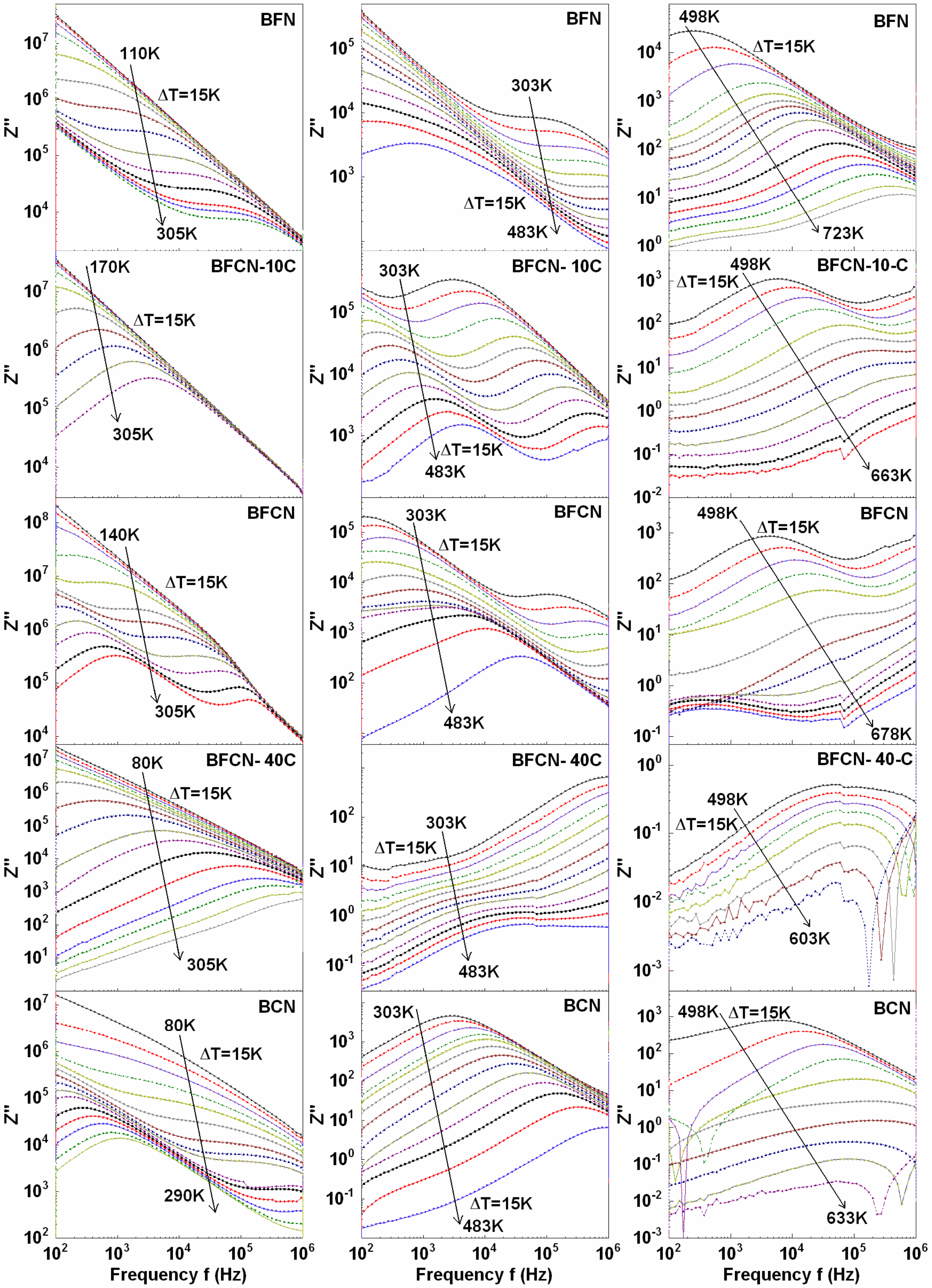

Figure 4.B.3: Imaginary part of complex impedance data for samples of BFCN series in low temperature, mid temperature and high temperature regions.

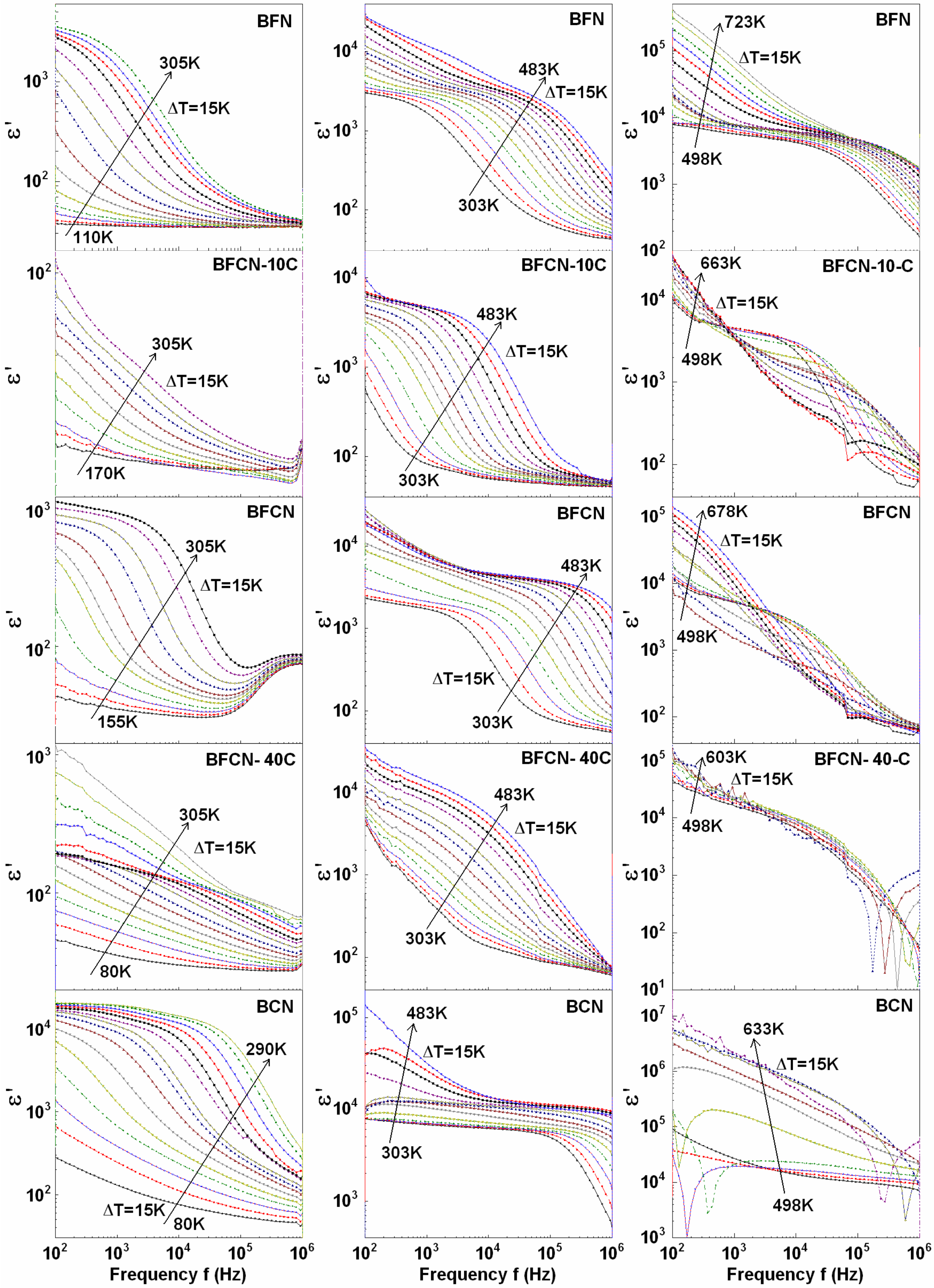

Figure 4.B.4: Real part of complex permittivity data for samples of BFCN series in low temperature, mid temperature and high temperature regions.

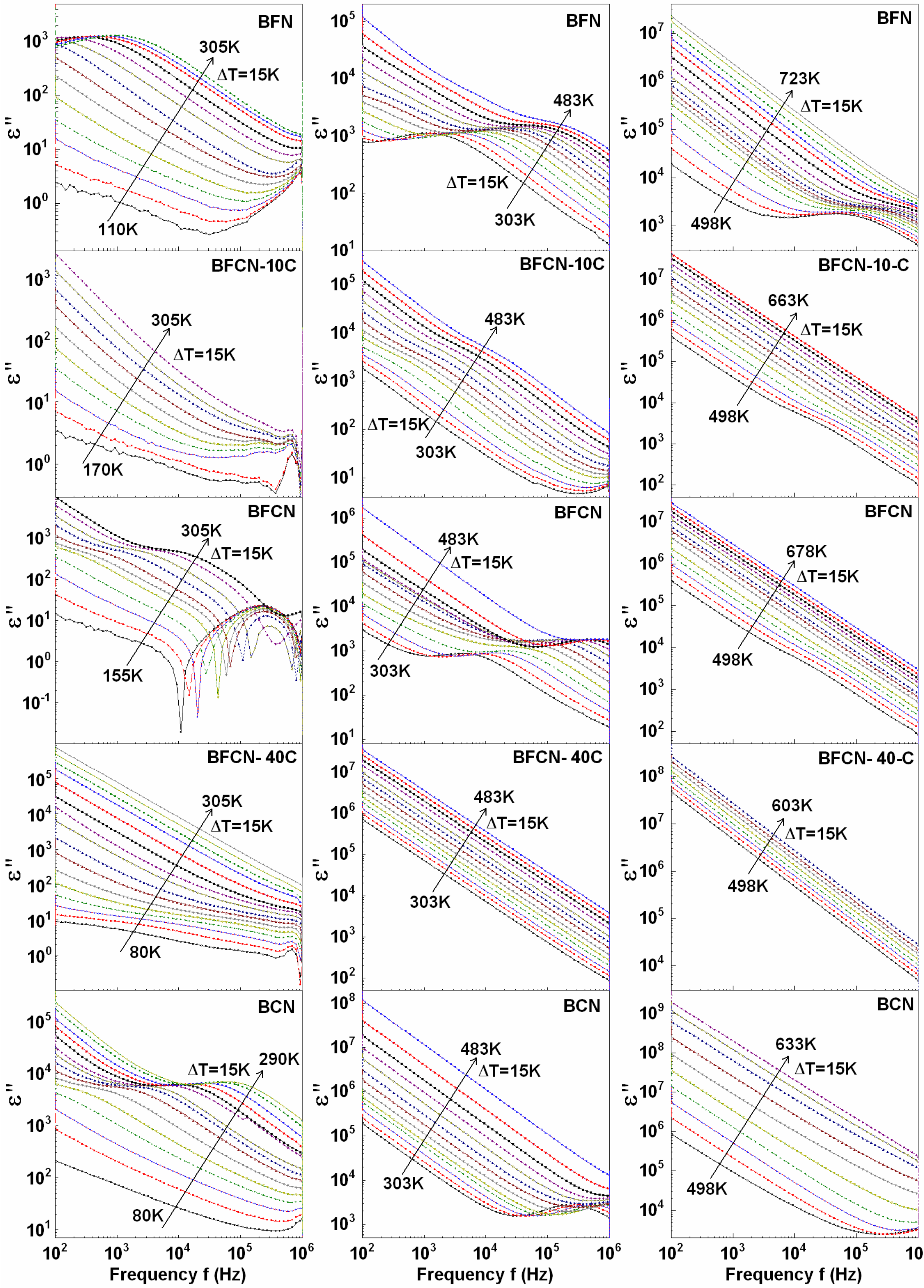

Figure 4.B.5: Imaginary part of complex permittivity data for samples of BFCN series in low temperature, mid temperature and high temperature regions.

The clear dispersion and broad relaxation peak is observed in the real as well as imaginary part of the impedance data. The similar frequency dispersion is observed for the other prepared samples also. The frequency response of the real permittivity data (dielectric constant), $\varepsilon'(f)$, are shown in the Figure 4.B.4 for the samples of BFCN series. The wide dispersion of data is observed for these samples in the entire temperature range. The similar frequency dispersion is observed for majority of samples in the measured temperature interval. Among them the Co rich sample, BCN has shown unique frequency independent nature in the temperature range of 250 K to 450 K with relatively high values of dielectric constant. This linear property of the BCN sample empowers it to be utilized for stable-value capacitors and sensors in a wide frequency and temperature range. The values of the real permittivity are very high (~10^4) for each sample of BFCN series. This is in contradiction to the general observation that the dielectric constants for cubic structures must be very small. This observed contradicting results clearly suggests that the high values of dielectric constants are not originated from the intrinsic factors responsible for the cubic symmetry. Under this condition, the observed high dielectric constant points to a significant contribution of the extrinsic factors only. The role of the extrinsic factors like, grain and grain boundaries is well explained by the Maxwell-Wagner theory of extrinsic factors [5-13]. The Maxwell-Wagner model infers that the dielectric constant is directly proportional to the grain size of the samples. In contrast to the above theory we observed that the BCN sample having the smallest grain size, (Figure 4.A.15 (a)) shows highest dielectric constant (~10000 at 300 K, 1 kHz). On the other hand, BFN having the largest grain size (Figure 4.A.15 (a)), shows lowest dielectric constant (~2000 at 300 K, 1 kHz) among this series. In addition, the dielectric constant values for BEN sample which exhibited 2nd largest grain size(~8 μm) show very low dielectric constant (~40 at 300 K, 1 kHz) (Figure 4.B.6) among all the prepared samples. A comparison of the real permittivity data in the prepared samples (Figure 4.B.6) shows that the overall dielectric constant values increases when Fe is substituted by 3d elements Co and Mn. On the other hand it decreases for the samples in which Fe is substituted by 4f elements Gd, Eu and Y. It should be noted here that the crystal structure remains cubic in each of these cases. The reason for the high dielectric constant therefore is not just the grain-boundary and the grain-size dependent extrinsic factors, but a significant contribution of the intrinsic factors related to chemical substitution induced localized electronic structure modifications also play a crucial role [14].

The imaginary permittivity data for each of the prepared sample show monotonic variation with frequency. The samples have not shown any clear Debye type relaxation peak. The observed nature of the relaxation peak indicates that in the low frequency region ($<10^4$ Hz), dipolar relaxation is masked by free charge relaxation [14-15]. The free surface charges responsible for low frequency relaxation are generated by the oxygen vacancies available at grain and grain boundaries. The development of oxygen vacancies is an unavoidable product of the high temperature ceramic synthesis technique [16-17]. Further, the absolute values of imaginary permittivity (Figure 4.B.5) are very high for the Co and Mn rich samples. This observed high values of imaginary permittivity points towards relatively more conducting nature of these samples [18]. The excess conductivity in Co and Mn rich samples could be due to doping of additional electron/ hole at the local level on replacement of Fe^{3+} ($3d^5$) by Co^{3+} ($3d^6$) or Mn^{3+} ($3d^4$). Such an additional charge carriers may also affect the low frequency dielectric relaxation.

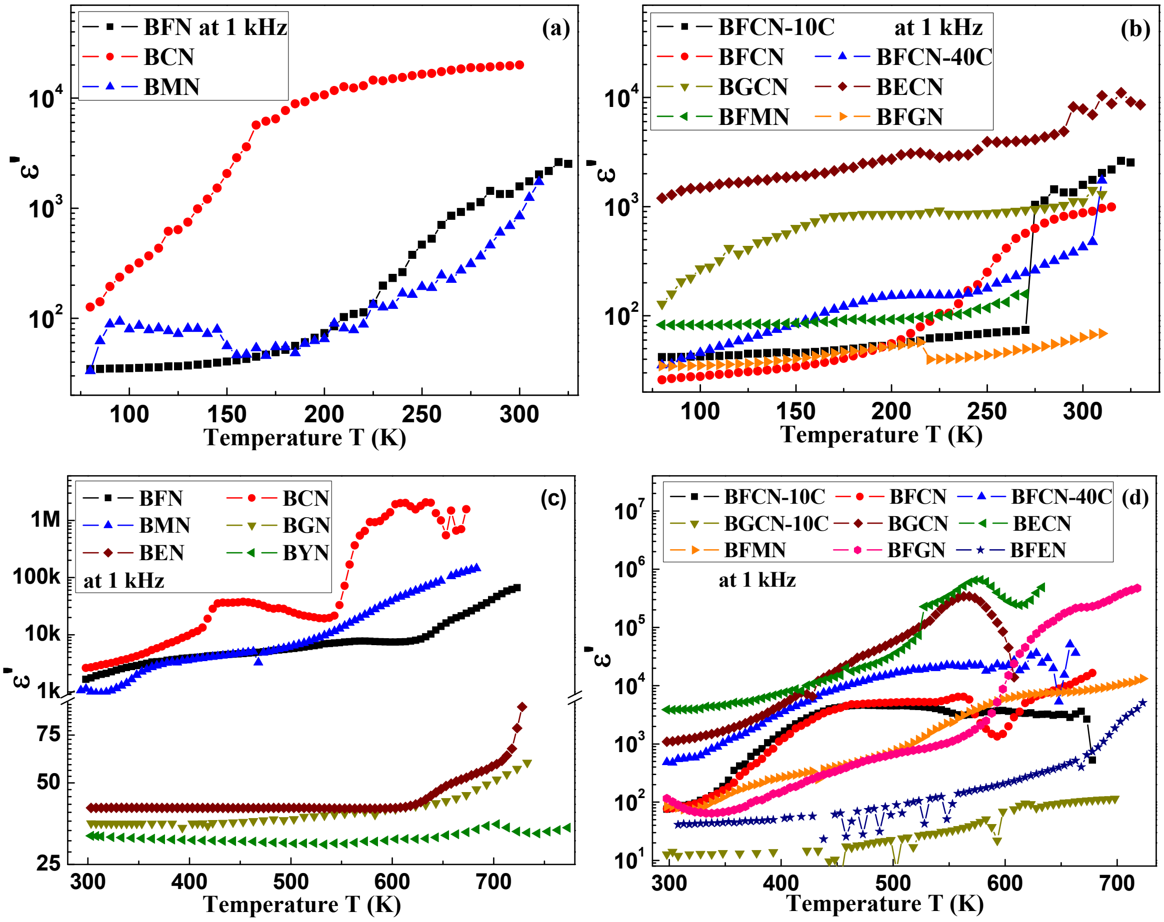

Figure 4.B.6: The temperature dependent real permittivity data obtained at 1 KHz frequency for (a) 100% samples and (b) intermediate samples for below room temperature region, (c) 100% samples and (d) intermediate samples for above room temperature region.

The temperature dependent dielectric constant values of all the samples, collected at 1 kHz, are presented in the Figure 4.B.6. The samples prepared with 3d transition elements (BFN, BCN and BMN) have shown relatively higher values of dielectric constant than the samples prepared with rare earth elements (BGN, BEN and BYN). Instead of a sharp ferroelectric transition the samples like BFN, BCN, BGCN and BECN have shown very broad relaxor like transition over a wide temperature interval. Surprisingly the intermediate compounds like BECN, BGCN and BFGN have shown giant values of dielectric constant ($\sim 5\times10^5$) suggesting that the observed two distinct chains of crystallites (related to observed two different phases in this compounds) mutually interacts with each other to give such giant values. It should be noted further that the giant values are dominantly exhibited by Co substituted samples.

By and large the giant dielectric constant values, which are neither caused by the intrinsic polarization induced ferroelectricity nor generated from the grain and grain boundary related Maxwell Wagner effect, need further investigation in the light of observed free charge conduction induced dielectric relaxation. In this regard the role of intrinsic and/or extrinsic factors for the observed high dielectric constant is investigated by the in-depth quantitative analysis of the collected data. The impedance representation, permittivity representation, electric modulus representation and conductivity representation are applied as a tool for such an investigation [14-15]. The contribution of different factors (intrinsic and/or extrinsic) can easily be separated out in each frequency and temperature region using these four representations. In the following four sections we have briefly explained the analysis techniques adopted for the above mentioned different representations.

A. Impedance Representation: Complex Impedance Analysis: This representation can separate the contribution of extrinsic factors like grain, grain boundary and space charge contribution. According to the Maxwell Wagner theory, the complex impedance plot (Z'' vs. Z') exhibits different semicircular arcs related to grain, grain boundaries and space charges. Such an arc observed in the complex impedance plot is equivalent to a parallel combination of capacitor and resistor. Therefore equivalent circuit modeling for the observed complex impedance data is likely to provide us paired values of capacitance and resistance for each arc relating it to Grain, grain boundary or space charges. Further, the grain and grain boundary relaxation frequencies also can be determined from the complex curve fitting. The complex impedance spectra of BFCN, collected at three different temperatures are shown in the Figure 4.B.7. The semi circular arc related with grain and grain boundaries are clearly visible in the figure. The overall resistance of sample decreases with increase in temperature. The similar behavior of complex impedance data is recorded for rest of the samples. The equivalent circuit modeling of semicircular arcs related to grain or grain boundary provides us information about the capacitance, resistance and relaxation frequencies responsible for that arc.

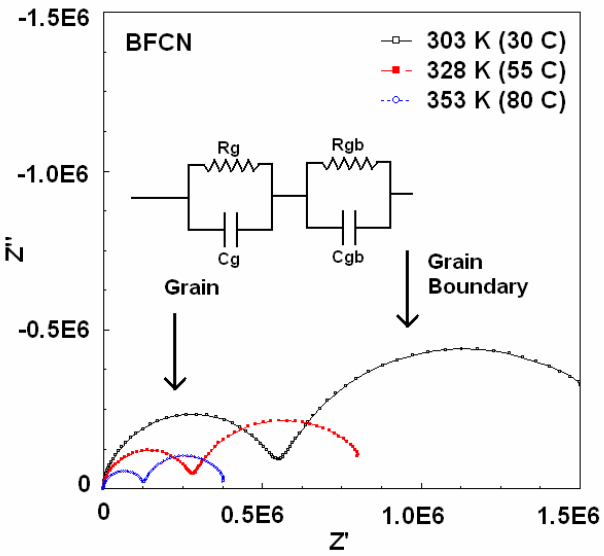

Figure 4.B.7: Impedance Cole-Cole plots for BFCN at three different temperatures.

For qualitative analysis, the similar circuit modeling of complex impedance data is carried out for each of the samples in the entire temperature range. This analysis has resulted in to a set of temperature dependent values of grain resistance (R_g), grain capacitance (C_g), grain relaxation time (τ_g), grain boundary resistance (R_{gb}), grain boundary capacitance (C_{gb}) and grain boundary relaxation time (τ_{gb}) for each of our samples. The temperature dependent analysis of these parameters is likely to provide us information regarding the activation energies of the spices responsible for the observed response. Such a temperature dependent analysis of R_g, τ_g, R_{gb} and τ_{gb} can be done using Arrhenius law for resistance and relaxation time given by Equation 4.B.6 and Equation 4.B.7, respectively.

$$R = R_0 \exp\left(\frac{E_a}{k_B T}\right), \text{ Arrhenius law for resistance} \qquad \ldots\ldots \text{(4.B.6)}$$

$$\tau = \tau_0 \exp\left(\frac{E_a}{k_B T}\right), \text{ Arrhenius law for relaxation time} \qquad \ldots\ldots \text{(4.B.7)}$$

The above equations suggest that a plot between inverse temperature and logarithmic values of resistance (or relaxation time) gives a straight line. The activation energy values can be determined using the slope of such a straight line known as Arrhenius plot. The activation energy values, obtained using the Arrhenius plot of R_g, τ_g, R_{gb} and τ_{gb} in different temperature regions, focus on the mechanism of conduction and relaxation process. Further, the temperature dependent nature of grain capacitance C_g and grain boundary capacitance C_{gb} focus on the role of oxygen vacancies.

B. Permittivity Representation: Complex Permittivity Analysis: The contribution from permanent dipole, induced dipole and free charge carries can be separated using this representation. Similar to the complex impedance plot, complex permittivity plot (generally known as Argand diagram) also shows a single semicircular arc. The semicircular arc observed in the Argand diagram (ε'' vs. ε' plots) can be explained using Debye theory of dielectric relaxation.

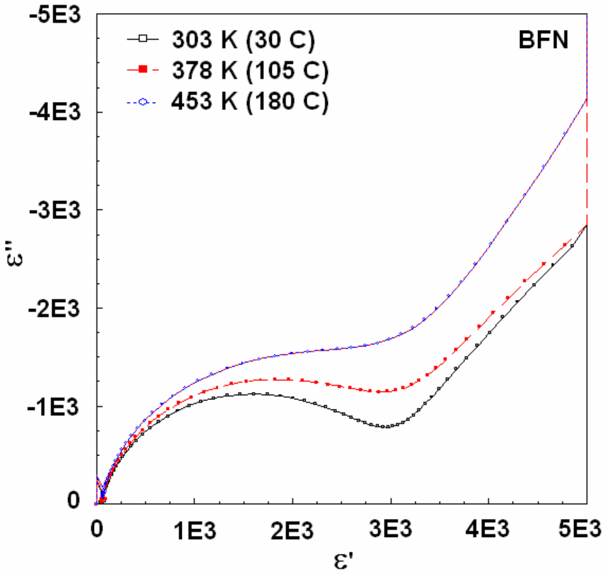

Figure 4.B.8: The permittivity Cole-Cole plots for BFN at three different temperatures.

According to this theory a material having an ideal dipolar relaxation shows a semicircular arc which intersects the ε' axis at high frequency as well as at low frequency end. In contrast to the Debye theory the complex permittivity plots observed for our samples show a rapid increase in the ε'' values instead of an intersect at ε' axis at low frequencies. Such deviations observed for BFN sample at three different temperatures are shown in the Figure 4.B.8. Therefore it is revealed that the observed complex permittivity data of our samples obey the Cole-Cole equation; a modified version of Debye theory.

The Equation 4.B.8 represents such a Cole-Cole equation of dielectric relaxation [14,19].

$$\varepsilon^* = \varepsilon' + i\varepsilon'' = \varepsilon_\infty + \frac{\Delta\varepsilon}{1+\left(i\omega\tau\right)^{1-\alpha}} - i\frac{\sigma_{dc}}{\varepsilon_0\omega} \qquad \ldots\ldots \text{(4.B.8)}$$

Here, τ is the mean relaxation time instead of the single relaxation time of pure Debye process while the Cole-Cole parameter α indicates the width of the relaxation time distribution and provides a measure of the poly-dispersive nature. The last term at the right-hand-side is due to the high conducting behavior contributing only to the imaginary part [19], which is due to the displacement of charge carriers, rather than the effect of the polarization mechanism. The fitting of the Cole-Cole equation was performed for each sample in the entire temperature range to focus on the dispersive and the conducting nature of our samples. The poly dispersive nature of sample and distribution of relaxation time can be understood through the temperature dependent values of Cole-Cole parameter α. Here the values of α close to zero suggest mono dispersive Debye type relaxation, while the values deviating from zero suggest poly dispersive non Debye type relaxation. The more deviation of Cole-Cole parameter α from zero suggests more deviation from Debye type relaxation and increased poly dispersive nature of the samples. The temperature-dependent analysis of the relaxation time, τ, is a very useful tool to study nature of the dipoles and their interaction with the conducting free charges. Since the product $\omega\tau$ becomes unity at $\varepsilon''_{\max}$ the value of relaxation time, τ, can be calculated using ω at $\varepsilon''_{\max}$. It is difficult to determine $\varepsilon''_{\max}$ using $\varepsilon' = \frac{\varepsilon_S + \varepsilon_\infty}{2}$ for the samples obey Cole-Cole equation. The alternate and more accurate way to determine $\varepsilon''_{\max}$ value is to consider the relation [20]:

$$\varepsilon''_{\max} = \frac{(\varepsilon_S - \varepsilon_\infty)}{2} \tan\left(\frac{(1-\alpha)\pi}{4}\right) \qquad \text{...... (4.B.9)}$$

Using this relation, we have determined the mean relaxation time τ. The temperature dependent analysis of the relaxation time helps to understand the relaxation process in detail. The Arrhenius equation (Equation 4.B.7) is a useful tool to analysis such temperature dependent response of relaxation time τ. The activation energy values obtained from such Arrhenius plot helps in identification of the type of dipoles involved in the relaxation process.

C. **Electric Modulus Representation: Complex Electric Modulus Analysis:** The space charge–dipole interaction can be probed effectively through the electrical modulus representation. The observed contribution of high electrical conductivity in the low frequency dielectric relaxation (see Figure 4.B.5) can be suppressed effectively in the electric modulus representation [20, 24, 27]. The complex electric modulus $M^*(\omega)$ is defined as the inverse of the complex permittivity $\varepsilon^*(\omega)$:

$$M^* = \frac{1}{\varepsilon^*} = M' + iM'' \qquad \text{...... (4.B.10)}$$

Where, $M' = \dfrac{\varepsilon'}{\varepsilon'^2 + \varepsilon''^2}$, real part of electric modulus ...... (4.B.11)

and $M'' = \dfrac{-\varepsilon''}{\varepsilon'^2 + \varepsilon''^2}$, imaginary part of electric modulus ...... (4.B.12)

The complex permittivity data is converted in to complex modulus data using above two equations; Equation 4.B.11 and Equation 4.B.12, for all the samples. The frequency response of real and imaginary parts of electric modulus data, for the samples of BFCN series, are presented in the Figure 4.B.9 and Figure 4.B.10 respectively. The data are presented in the group of three different temperature regions. It is observed from the Figure 4.B.10 that, the measured low frequency relaxation peak in the $\varepsilon''(f)$ curve is now clearly resolved for each of the samples.

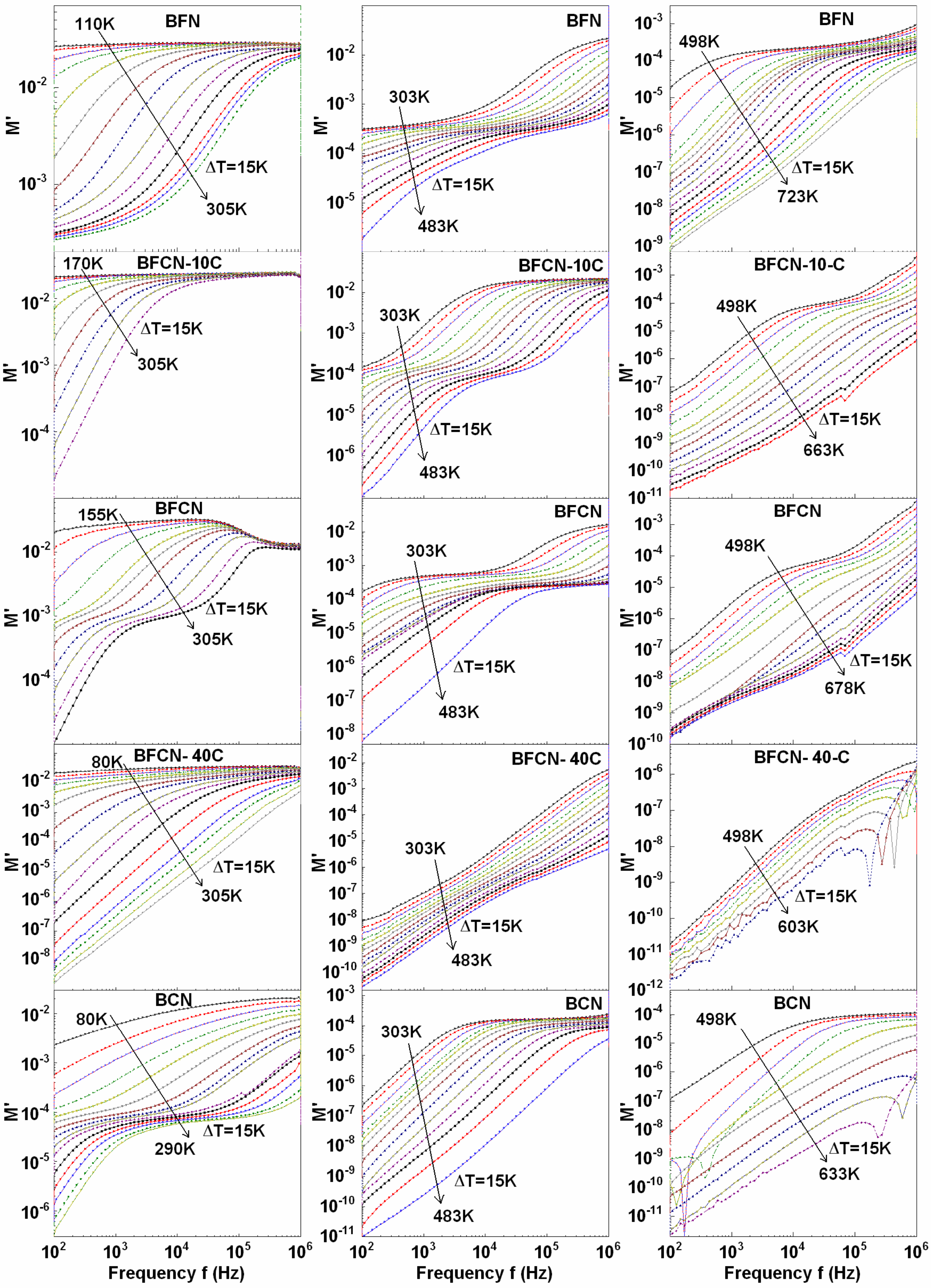

Figure 4.B.9: Real part of complex modulus data for samples of BFCN series in low temperature, mid temperature and high temperature regions.

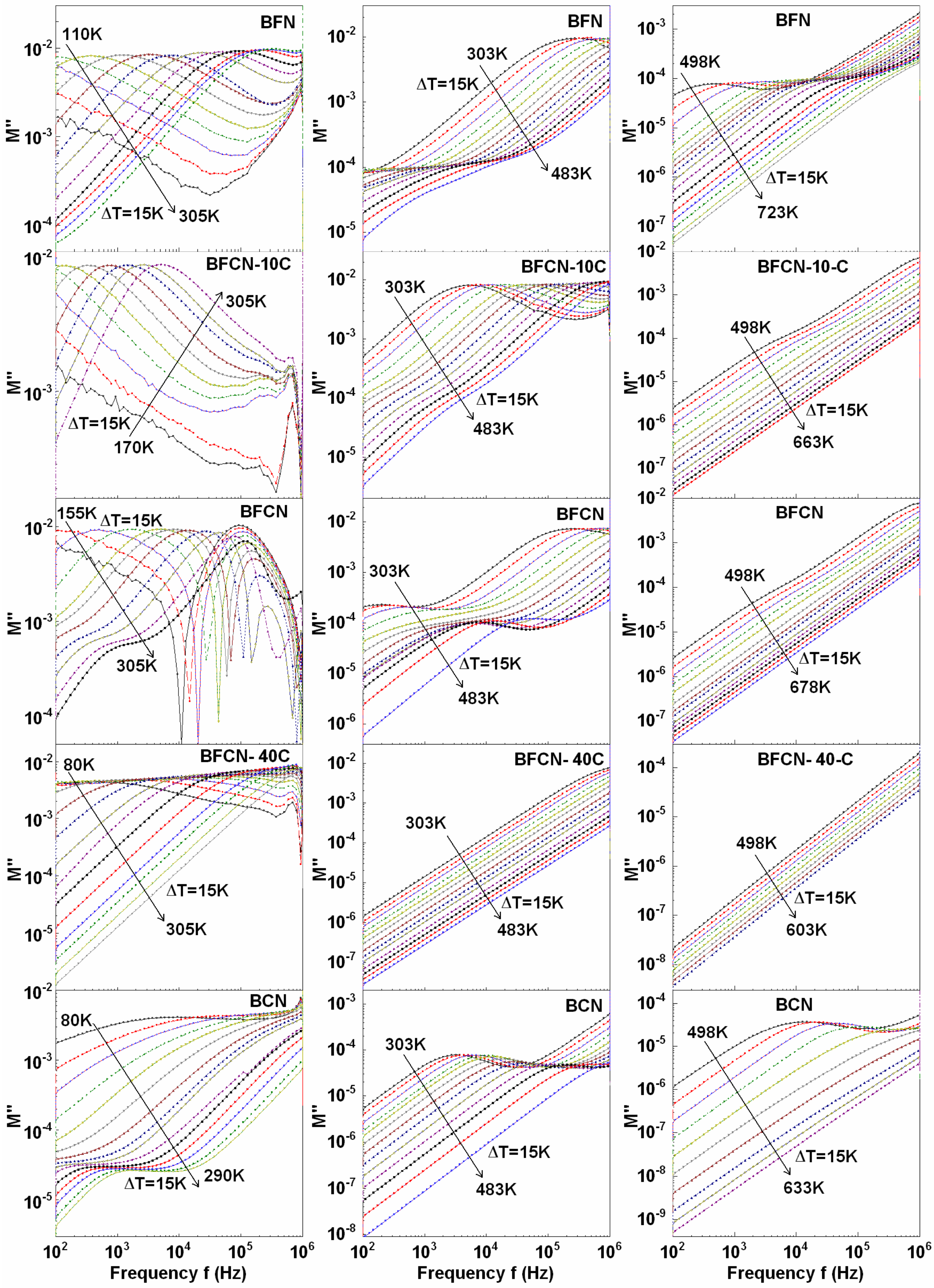

Figure 4.B.10: Imaginary part of complex modulus data for samples of BFCN series in low temperature, mid temperature and high temperature regions.

The non Debye type nature of the peak suggests significant contribution from free charge carriers. The in-depth analysis of electric modulus data are carried out using values of relaxation time τ for entire temperature range. The mean relaxation time τ is calculated by equating $\omega\tau$ to unity at the peak value of $M''(f)$. The Arrhenius equation (Equation 4.B.7) is utilized to analyze the temperature dependent response of relaxation time τ. The activation energy values obtained from such Arrhenius plot helps in identification of the interaction between space charge and dipoles involved in the relaxation process.

D. Conductivity Representation: Ac Conductivity Analysis: The observed free charge induced dielectric relaxation at low frequencies (Figure 4.B.5) requires a detailed investigation of the conduction mechanism. The investigation of the carriers responsible for conductivity along with charge induced relaxation can be studied effectively and quantitatively using conductivity representation. The ac conductivity values can be obtained using the imaginary part of permittivity using the relation;

$$\sigma' = -\omega\varepsilon_0\varepsilon'' \qquad \text{...... (4.B.13)}$$

The ac conductivity values for all the samples in the entire temperature range were determined using the above equation. The frequency response of ac conductivity for the BFCN series is presented in the Figure 4.B.11. The data are presented in the group of three temperature regions. It exhibits three different conductivity regions in these samples: (1) low-frequency plateau, (2) mid-frequency dispersion and (3) high-frequency plateau. The low-frequency plateau is related to the dc conductivity originating from the free charge carriers. The observed strong dispersion at mid-frequency and the plateau at the high frequency are related to the ac conductivity.

In order to comprehensively understand the behavior of the conduction process, data were analyzed using the modified power law [14, 21] of the ac conduction, Equation 4.B.14:

$$\sigma' = \sigma_0\omega^{S_0} + \sigma_{ac_1}\omega^{S_1} + \sigma_{ac_2}\omega^{S_2} = \sigma_{dc} + \sigma_{ac_1}\omega^{S_1} + \sigma_{ac_2}\omega^{S_2} \qquad \text{...... (4.B.14)}$$

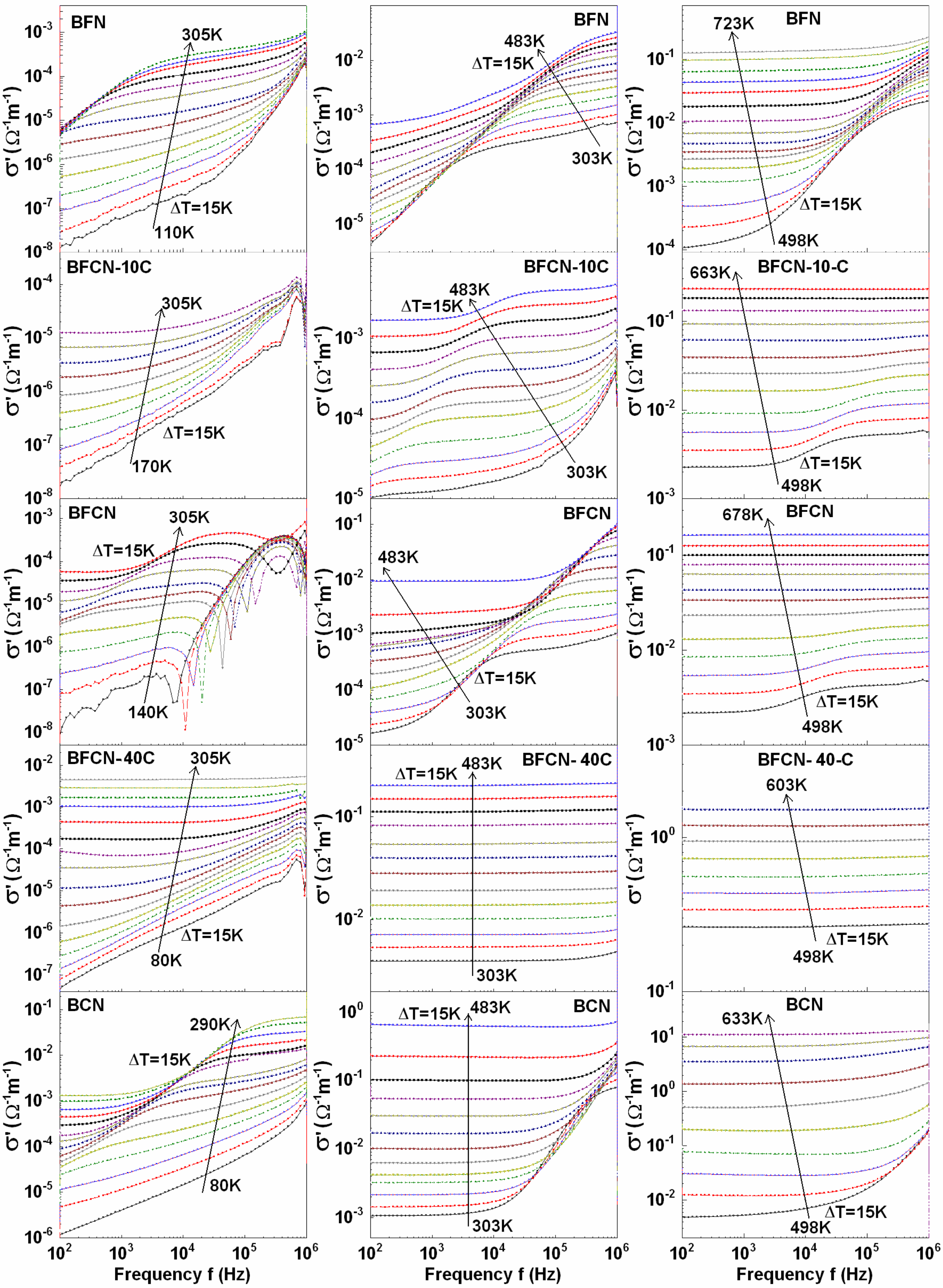

Figure 4.B.11: Ac conductivity data for samples of BFCN series in low temperature, mid temperature and high temperature regions.

The first term on the right-hand-side of Equation 4.B.14 indicates the dc conductivity ($s = s_0 = 0$) as observed in the low-frequency plateau region. The second and third terms represent the mid-frequency 'strong' dispersion ($s = s_1$) and the high-frequency 'weak' dispersion (plateau $s = s_2 \approx 0$), respectively. The values of the s parameter are obtained using the derivative equation:

$$s = \frac{d \ln \sigma'}{d \ln \omega} \qquad \text{...... (4.B.15)}$$

In general the values of the frequency exponent s lies between 0 and 1. It remains close to zero for the observed plateau regions at low frequencies and high frequencies. It makes a peak for the mid frequency dispersion. Different groups have observed such a peak in s parameter vs. $\ln \omega$ curve for various ceramic oxides [22-24].

Now the conduction mechanism involved in the relaxation process can be probed through temperature dependent analysis of the conductivity data. The observed conductivity in the low frequency plateau region is generally considered as dc conductivity values. The dc conductivity values obtained at different temperatures can be analyzed using Arrhenius law given by Equation 4.B.16.

$$\sigma_{dc} = \sigma_{0dc} \exp\left(\frac{-E_a}{k_B T}\right), \text{ Arrhenius law for dc conductivity} \qquad \text{...... (4.B.16)}$$

Where, E_a is the activation energy required by the carriers to overcome the conduction barrier. The activation energy values can be determined using a Arrhenius plot between $\log \sigma_{dc}$ and inverse temperature. The different mechanisms involved in the conduction process can be identified using the activation energy values.

The temperature dependence of the s parameter for the critical mid-frequency region helps in the identification of the carriers responsible for relaxation and conduction as well as focus on the mechanism of conduction. The temperature response of s parameter can be explained using three different models; viz. small polaron tunneling (SPT) [25-26], overlapping large polaron tunneling (OLP) [25-26] and correlated barrier hopping (CBH) [25-26].

It is predicted that in a covalent crystals addition of charge carriers generates a local lattice distortions which forms polarons. Small polarons are generally assumed to be so small and localized that their distortion clouds do not overlap. Therefore, the ac conductivity only in the high temperature limit is expected to be due to tunneling of randomly distributed carriers trapped at structural defects [25]. The frequency exponent s for the small polaron tunneling (SPT) [25-26] model is given by:

$$s = 1 - \frac{4}{\ln\left(1/\omega\tau_0\right) - W_H/kT} \qquad \text{...... (4.B.17)}$$

Here, W_H is the activation energy required for polaron transfer. The above equation suggests that the s parameter depends on both temperature and frequency. According to this model the s parameter increases with temperature in at high temperature end. The frequency exponent s is expected to show downward trend with increase in the frequency at a constant temperature.

On the other hand, overlapping large polaron tunneling (OLP) model [25-26] predicts the larger size of such polarons so that their distortion clouds can easily overlap each other. The frequency exponent for this model is given by:

$$s = 1 - \frac{1}{R'_\omega} \frac{4 + 6W_{H0}r'_0/kT\,R'^2_\omega}{\left(1 + W_{H0}r'_0/kT\,R'^2_\omega\right)^2} \qquad \text{...... (4.B.18)}$$

Here, $R'_\omega = 2\alpha R_\omega$ and $r'_0 = 2\alpha r_0$ are reduced tunneling distance and reduced polaron radius respectively. The parameter W_{H0} is the maximum hopping energy required by the polaron. The above equation suggests that the s parameter not only depends on the temperature and frequency but also depends on the size of polarons. The frequency exponent s decreases from unity with increasing the temperatures for large values of r'_0. In the case of smaller size of OLP (i.e. small r'_0) the s parameter shows a minima and starts increasing with temperature. Further, at a constant temperature the s parameter remains nearly constant for sufficiently large OLP while shows decrement with increase in the frequency for the small size of OLP.

According to the Correlated barrier hopping (CBH) model [25-26], the parameter s has the form:

$$s = 1 - \frac{6kT}{[W_M - kT\ln(1/\omega\tau_0)]} \qquad \text{...... (4.B.19)}$$

Here, W_M is the energy required to cross the barrier height. The above equation suggests that the frequency exponent s depends on temperature as well as frequency. It means that the hopping follows thermally activated process. The model suggests that the s parameter increases for small values of W_M/kT in the low frequency region. The model further predicts downward nature of the s parameter with increase in the temperature.

Thus the complex electric data can be analyzed effectively using above four representations. The contribution of each factor (intrinsic and/or extrinsic) in the observed dielectric relaxation can be distinguished systematically by applying sequential analysis through above four representations. In the next seven sections we will analyze dielectric response our samples in the group of seven series. The data will be evaluated by employing impedance representation, permittivity representation, modulus representation and dc conductivity analysis as tools of investigation. The analysis of frequency exponent s with the variation of frequency as well as temperature is carried out collectively for all the samples and presented after these seven sections.

4.B.2.1 Complex Electrical Analysis of 100% Series: [Ba(X$_{0.5}$Nb$_{0.5}$)O$_3$] (where X=Fe, Co, Mn, Gd, Eu, Y):

The samples of this series are prepared by complete substitution of Fe by 3d transition elements (Co and Mn) and 4f rare earth elements (Gd, Eu and Y) in the BFN ceramic. The effects of substitution on electrical properties of these compounds are investigated in this section. The whole investigation is carried out using above discussed four representations.

Impedance representation: The equivalent circuits modeling of semicircular arcs, obtained in the complex impedance plots, were performed for the entire temperature range. The best fitted parameters i.e. grain resistance (R_g), grain boundary resistance (R_{gb}), grain relaxation time (τ_g), grain boundary relaxation time (τ_{gb}), grain capacitance (C_g) and grain boundary capacitance (C_{gb}) are obtained for the samples of this series at all temperatures. The temperature dependent analyses of R_g, R_{gb}, τ_g and τ_{gb} using Arrhenius law are shown in the Figure 4.B.12 and Figure 4.B.13 respectively for low temperature region and high temperature region. The temperature dependent variations in the C_g and C_{gb} are also presented in the figures. It is to be noted here that this analysis could not be performed for the samples having rare earth elements due to their highly resistive nature. The values of τ_0 obtained from the linear fit of $\ln\tau \rightarrow 1000/T$ (not shown in Figures) are found in the range of 0.04 ns to 0.9 ns, which indicates the presence of non-dipole type relaxation in these compounds.

It is revealed from the non linear nature of the curves that the resistance R and relaxation time τ do not follow the simple Arrhenius law given by Equation 4.B.7. This clearly suggests that the activation energy required for the thermally activated change in R and τ is not a constant value but it depends on the temperature. Therefore we obtained the temperature dependent activation energy values using the following derivative equations.

$$E_a = k\frac{d(\ln R)}{d(1/T)}, \text{ for Resistance} \qquad \ldots\ldots \text{(4.B.20)}$$

$$\text{And, } E_a = k\frac{d(\ln \tau)}{d(1/T)}, \text{ for Relaxation time} \qquad \ldots\ldots \text{(4.B.21)}$$

Here, k is the Boltzmann constant. The variation of the activation energy as a function of temperature is shown in the Figure 4.B.12 and Figure 4.B.13. In the low temperature region the activation energies are found similar for grain as well as for grain boundaries. This indicates similar nature of the spices responsible for the process in side the grain and at the grain boundaries. Further it is also found similar for the process of relaxation and impedance, suggesting that, the mechanism of these processes are also same. The obtained very less values of activation energies (<0.6 eV), in the low temperature region, are very close to the activation energy of the singly ionized oxygen vacancies (0.3 eV) [16]. This clearly suggests that the observed dielectric relaxation in this temperature region is not only related with the dipoles but is also influenced by the interaction of free surface charges with singly ionized oxygen vacancies. In the high temperature region, for BFN sample, the values of activation energy E_a related to grain boundaries shows oscillations with increased values up to 1.5 eV while remains

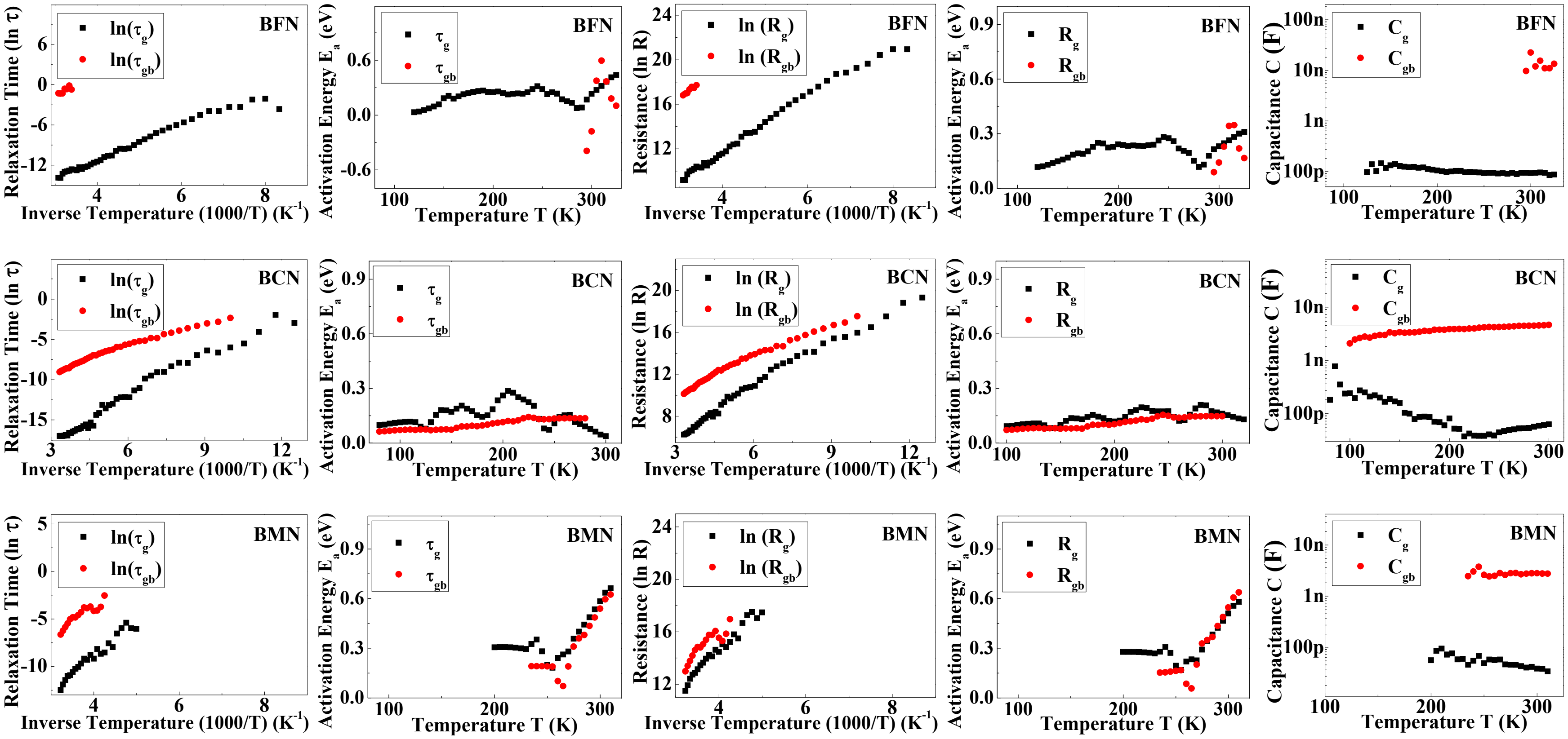

Figure 4.B.12: The impedance Cole-Cole fitting parameters with their Arrhenius plots and temperature dependent activation energies for 100% series for bellow room temperature region.

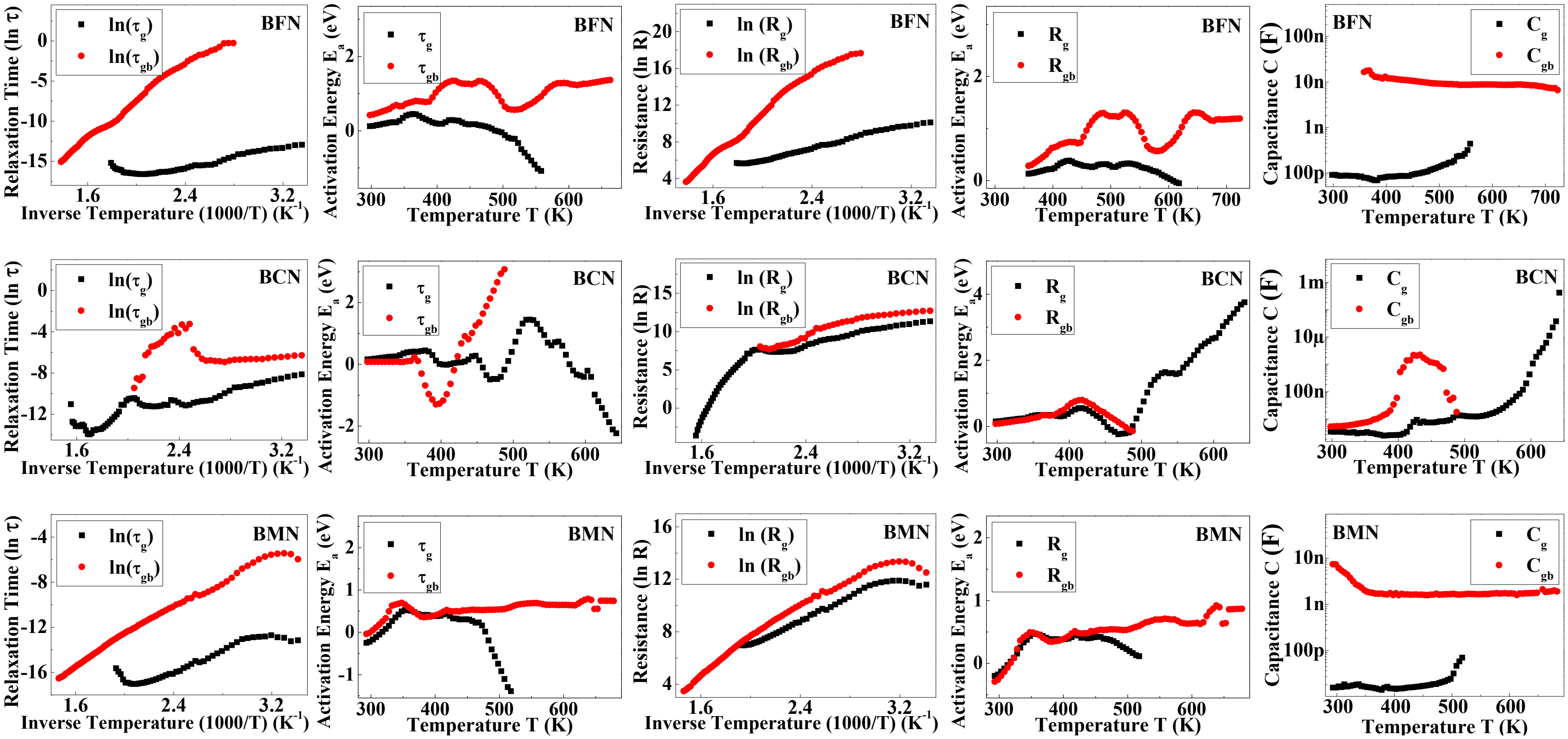

Figure 4.B.13: The impedance Cole-Cole fitting parameters with their Arrhenius plots and temperature dependent activation energies for 100% series for above room temperature region.

constant at 0.6 eV related to the grains for the both process (relaxation and impedance). The observed oscillations represent the NTCR-PTCR transitions in the temperature dependent curves of R and τ [27]. The gradual increase in the activation energy values from 0.5 eV to 1.0 eV up to 450 K suggests the development of doubly ionized oxygen vacancies [16]. The observed higher values of E_a (~1.5eV) at temperatures >450 K, suggests enhanced interaction of relaxing dipoles with the oxygen vacancies. In contrast to BFN, initially for BCN and BMN up to 400 K, the values of activation energy E_a related to grain and grain boundaries are equal and remain constant at 0.6 eV. The observed less activation energy for BCN and BMN in comparison with BFN could be due to the doped electrons and holes through Co^{3+} ($3d^6$) in BCN and Mn^{3+} ($3d^4$) in BMN respectively. The relaxation through free doped charges in BCN or BMN requires less activation energy in comparison with the relaxation through induced dipoles due to oxygen vacancies in BFN. Further for BMN and BCN at elevated temperatures the values of E_a increases for grain boundaries and becomes negative for grain suggests more conducting nature of grain. Here, in comparison to grain the grain boundaries act as a large barrier in the path of conduction. This is reflected through the observed increase in the E_a values of grain boundaries at high temperatures. The values of activation energy for BCN sample shows oscillating nature related to the peaks and transitions in the temperature dependent curves of R and τ at higher tempers.

The values of C_g found constant up to 550 K and then shows sudden increment while the values of C_{gb} found constant in the entire temperature range for BFN and BMN samples. The reason for increase in grain capacitance is related to high conducting nature of grain after 450K due to the interaction of doped electrons with doubly ionized oxygen vacancies. The nearly constant values of grain boundary capacitance suggest that it is not influenced by oxygen vacancies. The observed peak in the values of C_{gb} for BCN sample from 400 K to 500 K suggests possible phase transition in the sample.

Permittivity representation: The samples of this series have shown dominant nature of conductivity over relaxation process. Therefore the relaxation peak in the $\varepsilon''(f)$ curve is completely masked by the conduction. This has resulted in to the absence of clear semi circular arc related to the Cole-Cole curve as well as not so clear relaxation peak in the $\varepsilon''(f)$ curve. In this view we could not perform analysis using the permittivity representation.

Electric modulus representation: The dielectric relaxation analysis for the conducting samples can be done effectively through the electrical modulus representation. The values of mean relaxation time τ are obtained for each sample using the peak of $M''(f)$ curve in the entire temperature range. It should be noted here that the low temperature analysis for rare earth doped samples could not be performed due to highly resistive nature of the samples. The temperature dependent analysis of mean relaxation time τ using Arrhenius law is presented in the Figure 4.B.14. The Arrhenius plot of relaxation time τ obtained for our samples have not shown any linear nature therefore the temperature dependent activation energies were calculated using the Equation 4.B.21. The variation of the activation energy as a function of temperature is presented in the Figure 4.B.14.

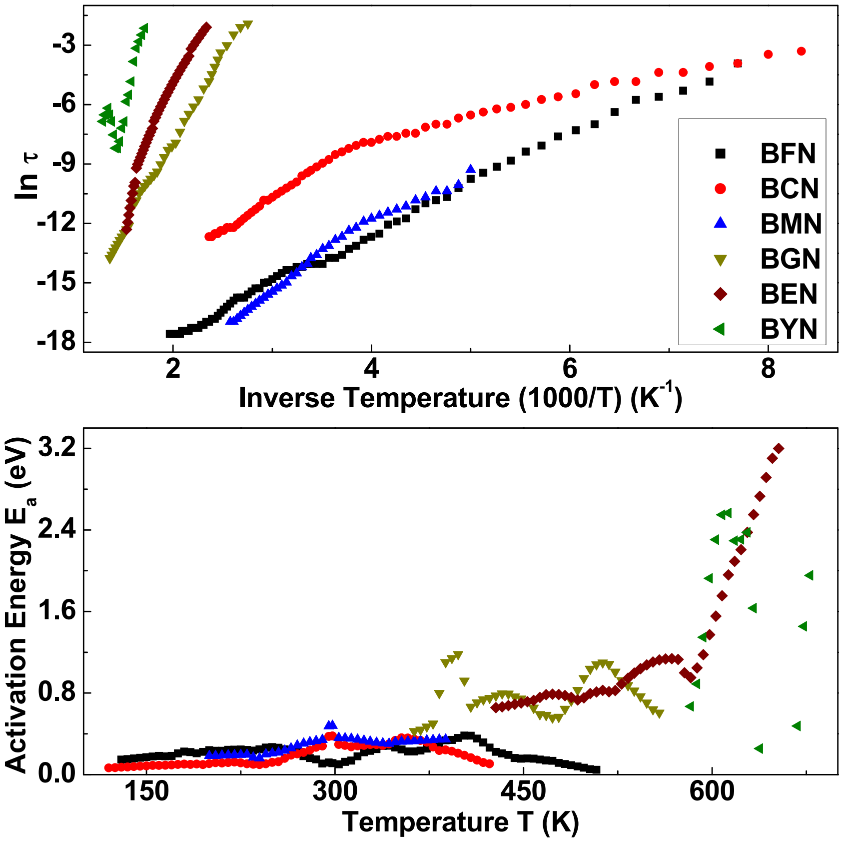

Figure 4.B.14: The Arrhenius plot of relaxation time along with temperature dependent activation energies obtained using electric modulus data for 100% series.

The observed nearly constant values of E_a (<0.6 eV) for all the samples in the low temperature region are in agreement with the impedance analysis. The E_a values increase marginally on increasing the temperatures from 200 K to 300 K. The observed increase in E_a values indicates the increased interaction of space charge with singly ionized oxygen vacancies.

Such an interaction of space charge with the oxygen vacancies was masked by high conduction in the complex permittivity representation. The activation energies for the samples having 3d transition elements (i.e. BFN, BCN and BMN) found nearly constant (~0.6 eV) in the high temperature region (up to 550 K), whereas it is found to increased up to 1.2 eV for the samples having rare earth elements (i.e. BGN, BEN and BYN). A systematic enhancement of the activation energy for the temperatures from 300 K to 550 K, suggests the development of doubly ionized oxygen vacancies in the samples. The enhanced E_a values observed for samples with rare earth elements suggest comparatively rigid nature of ionized oxygen vacancies. The reason for such rigidity could be large ionization potentials for rare earth elements compared to transition elements. Further at elevated temperatures (>550 K) the E_a increases suddenly for BYN and BEN and shows a sharp rise. The observed oscillating nature of activation energy followed by sharp rise for rare earth doped samples suggests possibilities of phase transition at these temperatures. It should be noted here that the activation energy values E_a for the samples BFN, BCN and BMN could not be determined at very high temperatures (> 550 K) due to absence of relaxation peak at such higher temperatures.

Conductivity representation: The analysis of the free charge carriers responsible for the observed high dielectric loss can be done using dc conductivity analysis. The values of dc conductivity are obtained for each sample through extrapolating the low frequency plateau of $\sigma'(f)$ curve at all temperatures. The temperature dependent analysis of dc conductivity σ_{dc} using Arrhenius law is presented in the Figure 4.B.15 and Figure 4.B.16 respectively for low temperature region and high temperature region. The Arrhenius plot of dc conductivity σ_{dc} obtained for our samples have not shown any linear nature therefore the temperature dependent activation energies were calculated using the Equation 4.B.22.

$$E_a = k\frac{d(\ln\sigma_{dc})}{d(1/T)}\text{, for dc conductivity} \qquad \text{…… (4.B.22)}$$

Here, k is the Boltzmann constant. The variation of the activation energy as a function of temperature is presented in the Figure 4.B.15 and Figure 4.B.16 respectively for low temperature region and high temperature region.

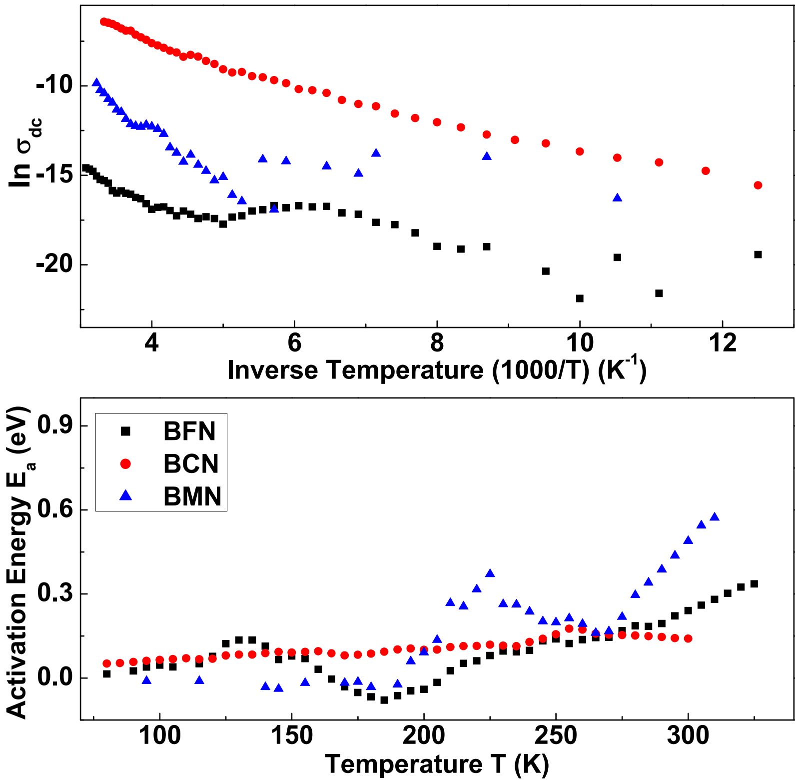

Figure 4.B.15: The Arrhenius plot of dc conductivity along with temperature dependent activation energies for 100% series in bellow room temperature region.

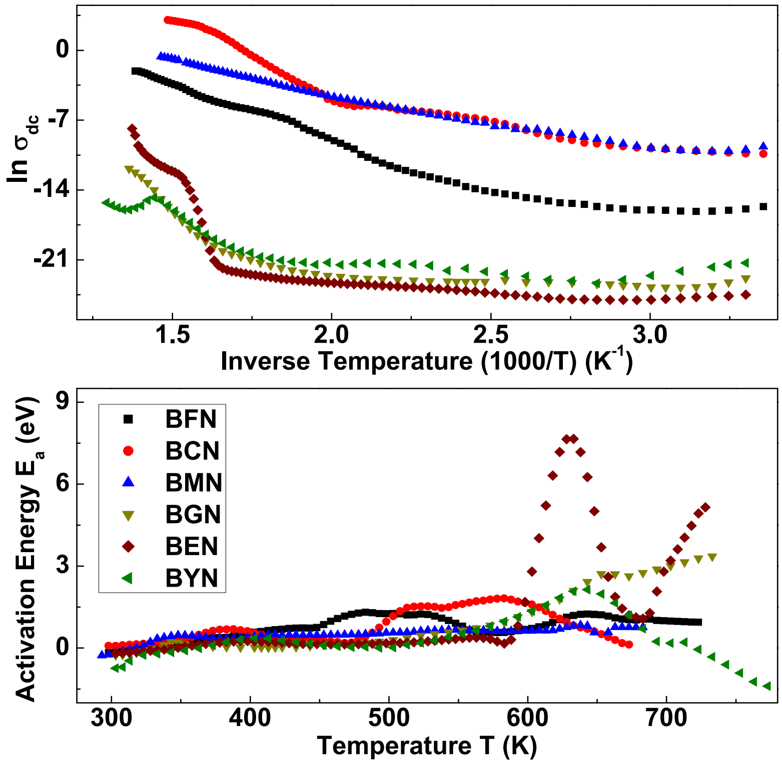

Figure 4.B.16: The Arrhenius plot of dc conductivity along with temperature dependent activation energies for 100% series in above room temperature region.

The activation energy values remains between 0.1 eV to 0.3 eV in the low temperature region for BFN, BCN and BMN. These observed values of E_a (~0.3 eV) suggests that the low temperature conductivity is due to presence of singly ionized oxygen vacancies [14, 16]. The observed steps for BFN and BMN indicate NTCR-PTCR transitions observed in the dc conductivity curves.

The comparison of dc conductivity values, in the above room temperature region (Figure 4.B.16), clearly suggest more conducting nature of the samples having 3d transition elements then the samples containing rare earth elements. The observed conductivity in this temperature region is influenced by the ionization of oxygen vacancies. Here the charge state of B'-site ion fluctuates to balance the positively charged oxygen vacancies [16]. Such an ionization of oxygen vacancies is comparatively easier for the 3d transition atoms in comparison to 4f rare earth atoms. This could be the probable reason of observed high conductivity for the samples having 3d transition elements. The observed gradual increment in the activation energies from 0.3 eV to 0.8 eV suggests development of doubly ionized oxygen vacancies [14, 16]. In addition, the BMN and BCN samples possessing more conductivity than the BFN sample is due to doped free charges like electron and holes respectively for BCN and BMN (as pointed out earlier). It is also in agreement with the fact that the likely concentration of doped charges will always be higher than the developed oxygen vacancies. The interaction of such doped charges with oxygen vacancies further enhances the dielectric constant to a giant values along with high conductivity (see figure 4.B.6). Further, the activation energy E_a increases gradually up to 1.2 eV in the temperature range 450 K to 600 K suggesting enhanced interaction of relaxing dipoles with the oxygen vacancies. At elevated temperatures (> 600 K), the E_a values for rare earth samples show a relatively sharp peak. These peaks are related with the NTCR-PTCR transitions observed in dc conductivity curves. These NTCR-PTCR transitions, with such high E_a values may be linked to a possible structural phase transitions.

4.B.2.2 Complex Electrical Analysis of BFCN Series: [$Ba(Fe_{0.5-X}Co_XNb_{0.5})O_3$] where X=0, 0.10, 0.25, 0.40, 0.50:

The samples of this series are prepared through gradual substitution of Fe by Co in the BFN ceramic. The effects of substitution on electrical properties of these compounds are investigated in this section. The whole investigation is carried out using above discussed four representations.

Impedance representation: The temperature dependent analyses of R_g, τ_g, R_{gb} and τ_{gb} using Arrhenius law are shown in the Figure 4.B.17 and Figure 4.B.18, respectively, for low temperature region and high temperature region. The temperature dependent variations in the C_g and C_{gb} are also presented in the figures. The Arrhenius plots of R and τ obtained for our samples have not shown any linear nature therefore the temperature dependent activation energies were calculated using the Equation 4.B.20 and Equation 4.B.21. The variation of the activation energy as a function of temperature, obtained for R and τ, is presented in the Figure 4.B.17 and Figure 4.B.18. In the low temperature region the activation energies are found similar for grain as well as for grain boundaries. This indicates similar nature of the spices involved in the mechanisms associated with grain and grain boundaries. The values of E_a also found to be similar in the process of relaxation and impedance, suggesting similar mechanisms for these processes. The obtained low values of activation energies (~0.3 eV), suggest singly ionized oxygen vacancies induced dielectric relaxation in this temperature region [14, 16]. In the high temperature region for BFN, the activation energy values increases gradually from 0.5 eV to 1.0 eV along with temperature moving to 450 K suggesting the conversion of singly ionized oxygen vacancies in to doubly ionized oxygen vacancies[14, 16]. In contrast to BFN, the values of activation energy E_a remain constant at 0.6 eV for Co substituted samples pointing to the fact that here relaxation is only due to doped charges. The activation energy values for intermediate samples remains constant at 0.6 eV up to 500 K, which is followed by gradual rise up to 1.2 eV at elevated temperatures. Similar to earlier series this suggests enhanced interaction of relaxing dipoles with the oxygen vacancies. Further the oscillating nature and peak formation at elevated temperatures points to the possible phase transitions.

The values of grain capacitance C_g and grain boundary capacitance C_{gb} are found to be constant in the entire temperature range (except high temperature tails) for the samples BFN, BFCN-10C and BFCN. The observed nature at high temperature end is affiliated with the phase change mechanism. The values of C_g and C_{gb} remains constant at low temperatures and shows gradual rising nature at high temperatures for Co rich samples BFCN-40C and

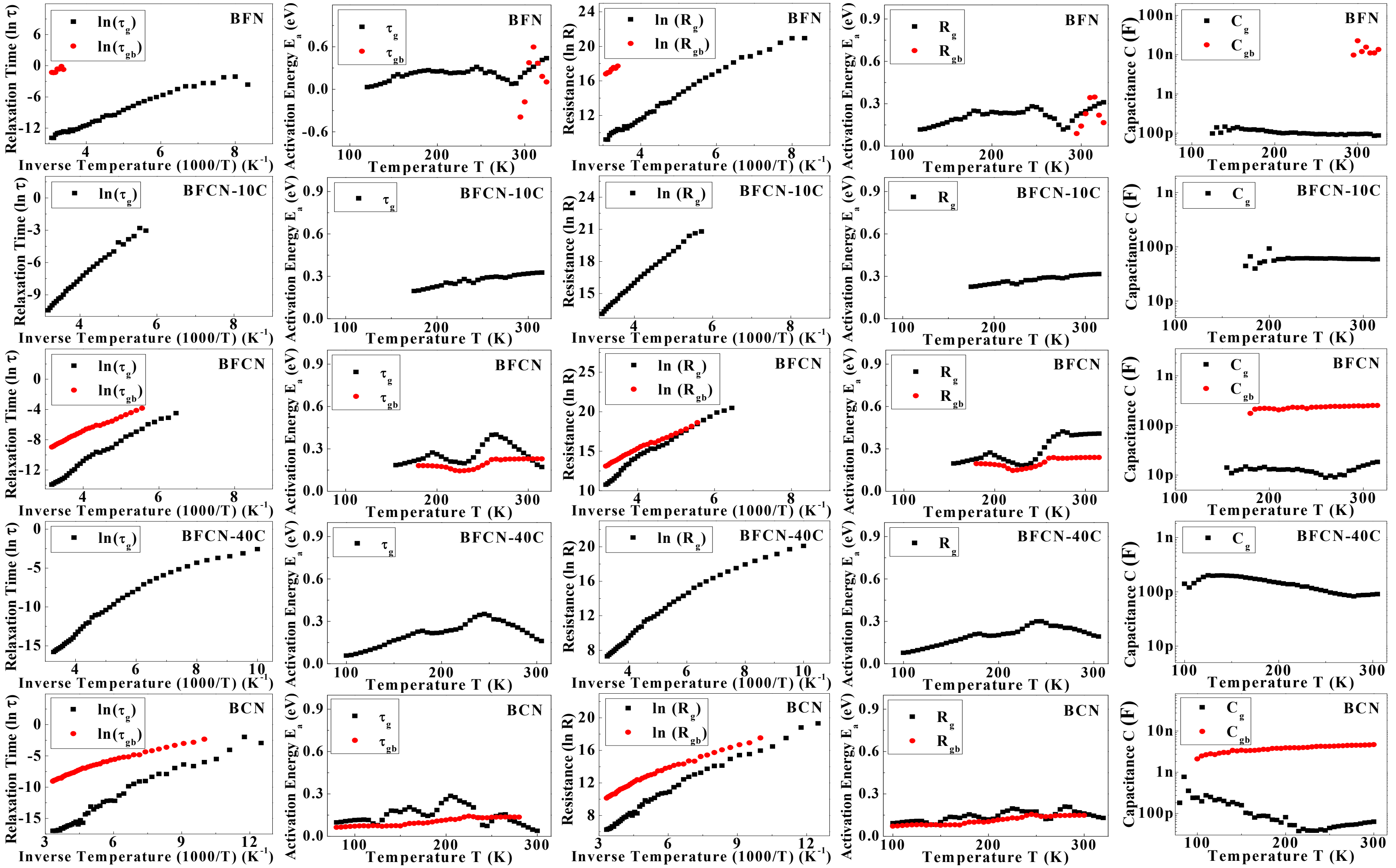

Figure 4.B.17: The impedance Cole-Cole fitting parameters with their Arrhenius plots and activation energies for BFCN series for bellow room temperature region.

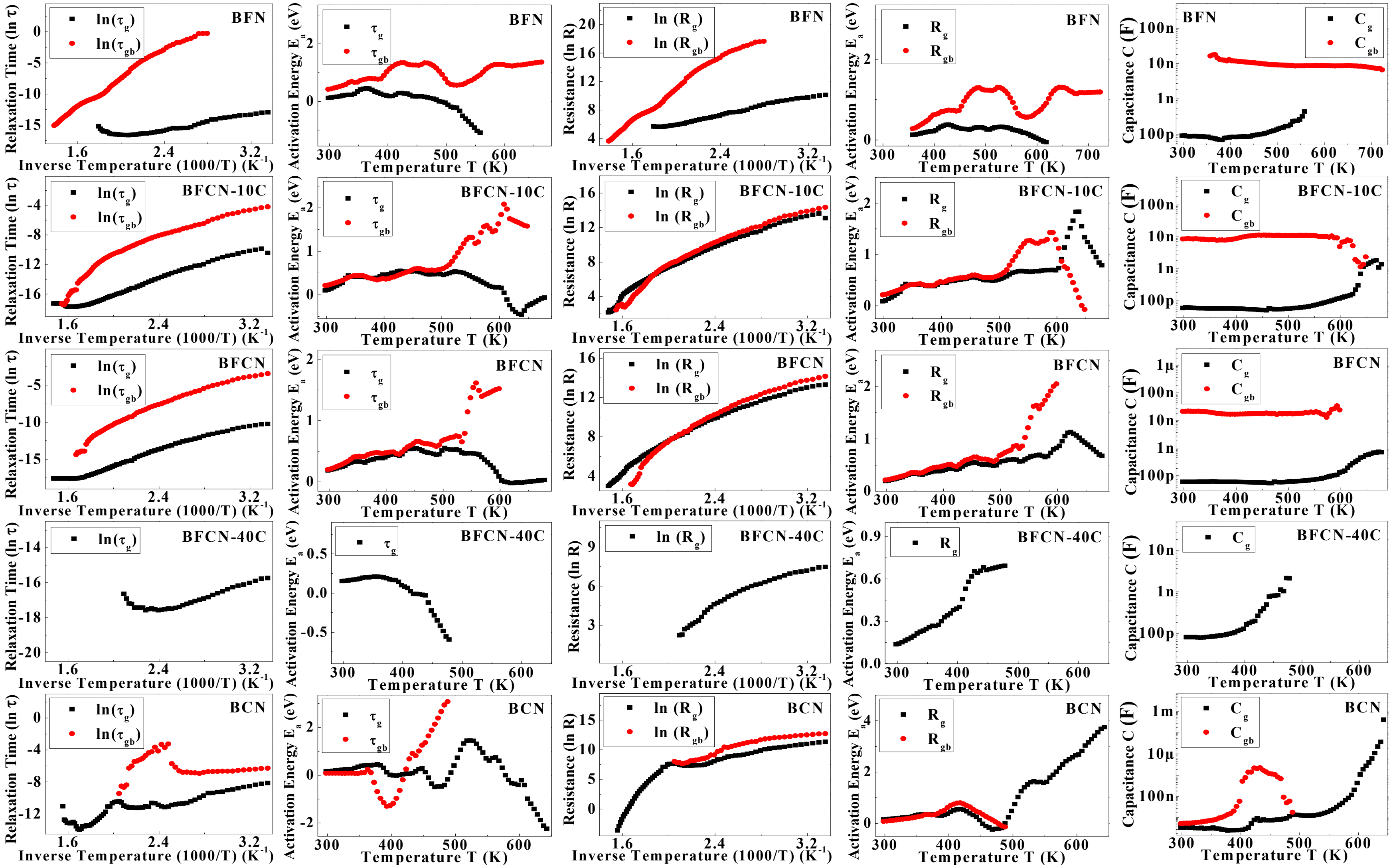

Figure 4.B.18: The impedance Cole-Cole fitting parameters with their Arrhenius plots and activation energies for BFCN series for above room temperature region.

BCN. The observed rise in C_g and C_{gb} for Co rich samples is related to enhanced interaction of doped electrons with doubly ionized oxygen vacancies at elevated temperatures.

Permittivity representation: The complex permittivity data of this series are analyzed using Cole-Cole equation. It should be noted here that the semicircular arc related to the Argand diagram is observed only for three samples; BFN, BFCN and BCN. The other two samples have not shown any semicircular arc due to high conductivity. The fitting parameters of Cole-Cole equation, i.e. Cole-Cole parameter α and mean relaxation time τ, are obtained for this three sample in the entire temperature range. The temperature dependent variation of Cole-Cole parameter α is presented in Figure 4.B.19.

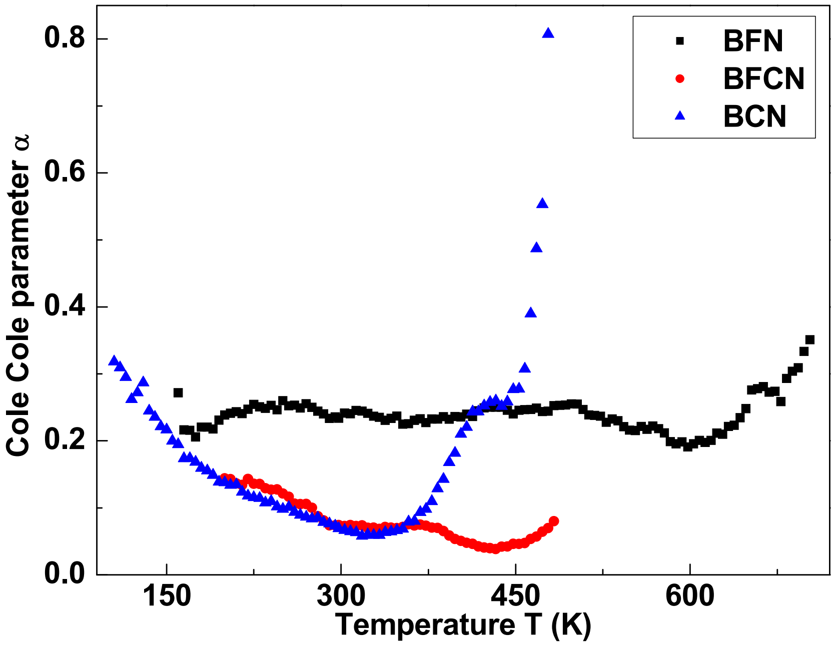

Figure 4.B.19: The variation of Cole-Cole parameter α with temperature for samples of BFCN series.

The observed non-zero values of Cole-Cole parameter α, confirms the non-Debye type poly-dispersive nature of these samples. The nearly constant values of Cole-Cole parameter α for BFN indicate that the distribution of relaxation time is independent of temperature. In contrast to BFN, the α parameter decreases up to 375 K and then show little increment for the BFCN sample. The BCN sample show α parameter to decrease up to 325 K and then increases drastically. The observed initial decrement for both of these samples suggests that the distribution of relaxation time reduces and the system moves towards ideal Debye type relaxation. The observed temperature dependant nature of α parameter for BFCN and BCN samples suggest that the relaxing dipoles are interacting with the free charges doped through replacement of Fe^{3+} ($3d^5$) by Co^{3+} ($3d^6$). The observed sudden increase in the α parameter for BCN sample points at the enhanced interaction of the relaxing dipoles with the doped charges beyond this temperature. The probable reason for the absence of such an interaction in the BFCN, could be due to the enhancement in Co–Co length in –Fe–Nb–Co–Nb–Fe–Nb–Co– like chains in comparison to –Co–Nb–Co–Nb–Co– chains.

The figure 4.B.20 shows variation of mean relaxation time vs. inverse temperature. The observed reduction in the values of mean relaxation time suggests increased flexibility of charge carriers for Co rich samples. The values of τ_0 obtained from the linear fit of $\ln\tau \rightarrow 1000/T$ (not shown in Figure 4.B.20) are found in the range of 0.04 ns to 0.7 ns, which indicates the presence of non-dipole type relaxation in these distorted perovskite samples [14].

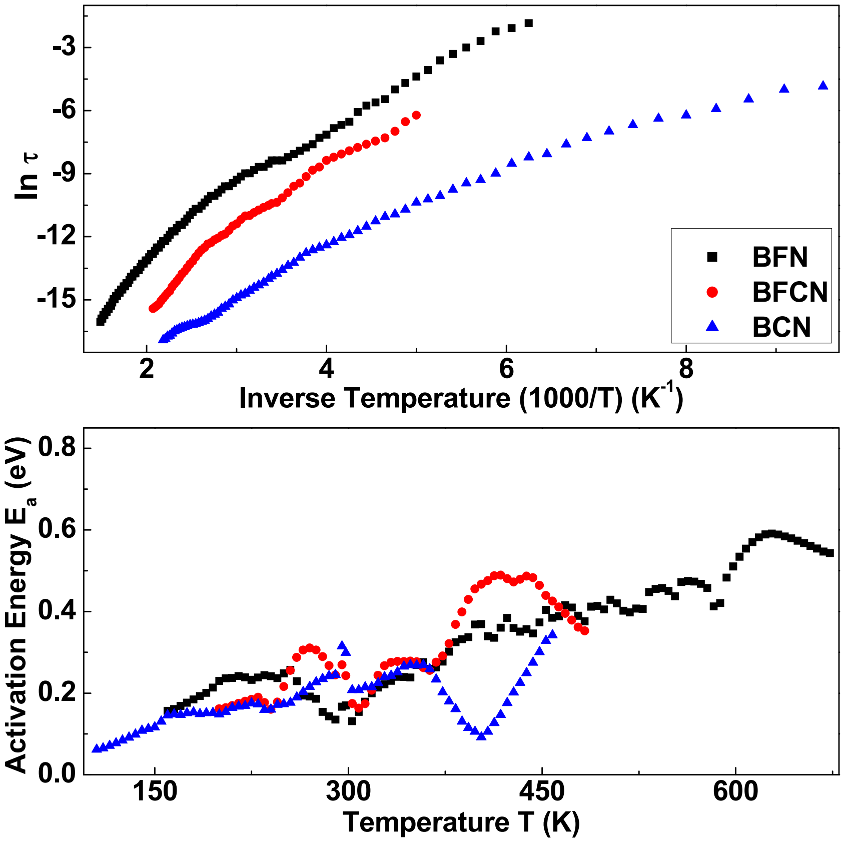

Figure 4.B.20: The Arrhenius plot of relaxation time along with temperature dependent activation energies obtained using permittivity Cole-Cole plots for BFCN series.

The Arrhenius plot of relaxation time τ obtained for our samples have not shown any linear nature therefore the temperature dependent activation energies were calculated using the Equation 4.B.21. The variation of the activation energy as a function of temperature is presented in the Figure 4.B.20. It is clear from the figure that the activation energy gradually increases with temperature. The observed values of E_a (<0.3 eV) in the low temperature region, are very close to the activation energy of the singly ionized oxygen vacancies (0.3 eV) [14, 16]. This clearly suggests that the observed dielectric relaxation is due to the interaction of free surface charges with singly ionized oxygen vacancies. The values of E_a increase gradually up to 0.5 eV for BFN, in the temperature range 300 K to 500 K, suggests development of doubly ionized oxygen vacancies. The observed less activation energy for BCN in comparison with BFN could be due to the doped electrons of Co^{3+} ($3d^6$): relaxation through free doped charges in BCN requires less activation energy in comparison with the relaxation through induced space charge due to oxygen vacancies in BFN. In contrast to this, the observed unusually higher activation energy values in BFCN therefore may be due to co-existence of micro domains of BFN and BCN within the grains. As suggested before, this might result in distortion of long-range order of $-Fe-Nb-Fe-$ or $-Co-Nb-Co-$ chains [14]. The observed gradual increment in E_a at elevated temperatures suggests enhanced interaction of space charge with doubly ionized oxygen vacancies.

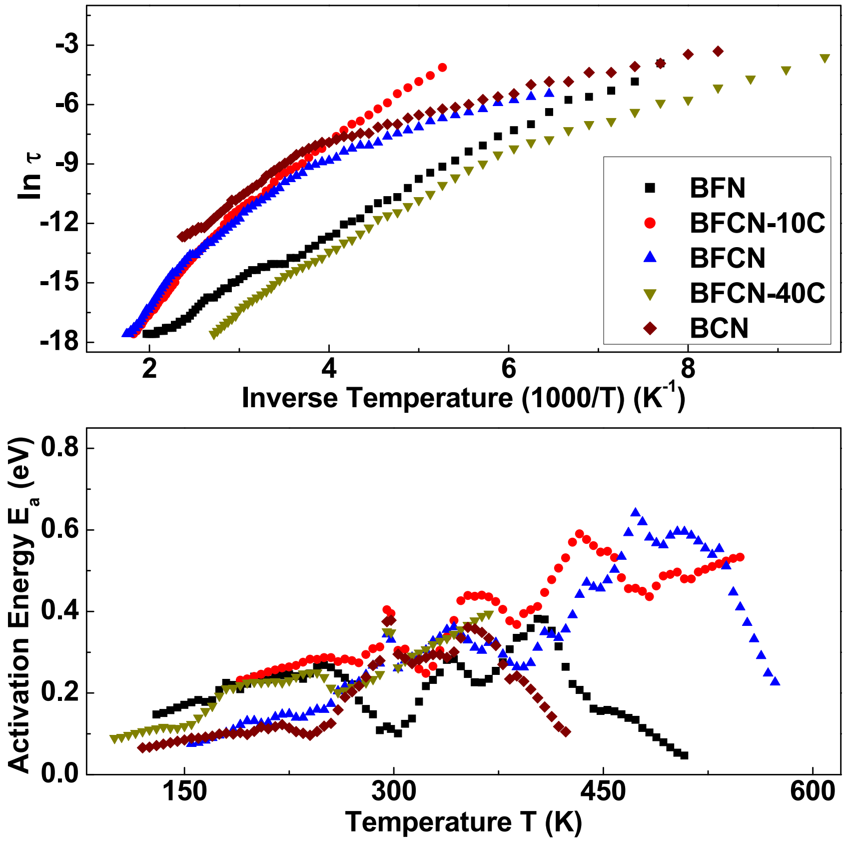

Figure 4.B.21: The Arrhenius plot of relaxation time along with temperature dependent activation energies obtained using electric modulus data for BFCN series.

Electric modulus representation: The dielectric relaxation analysis for the conducting samples can be done effectively through the electrical modulus representation. The values of mean relaxation time τ are obtained for each sample using the peak of $M''(f)$ curve in the entire temperature range. The temperature dependent analysis of mean relaxation time τ using Arrhenius law is presented in the Figure 4.B.21. The Arrhenius plot of relaxation time τ obtained for our samples have not shown any linear nature therefore the temperature dependent activation energies were calculated using the Equation 4.B.21. The variation of the activation energy as a function of temperature is presented in the Figure 4.B.21.

The observed less activation energy values E_a (<0.5 eV) for all the samples in the low temperature region are in agreement with the previous analyses. A systematic enhancement of the activation energy (up to 0.6 eV) for the temperatures from 300 K to 550 K, suggests the development of doubly ionized oxygen vacancies in the samples. The observed oscillating nature of activation energy suggests possibilities of phase transition at these temperatures.

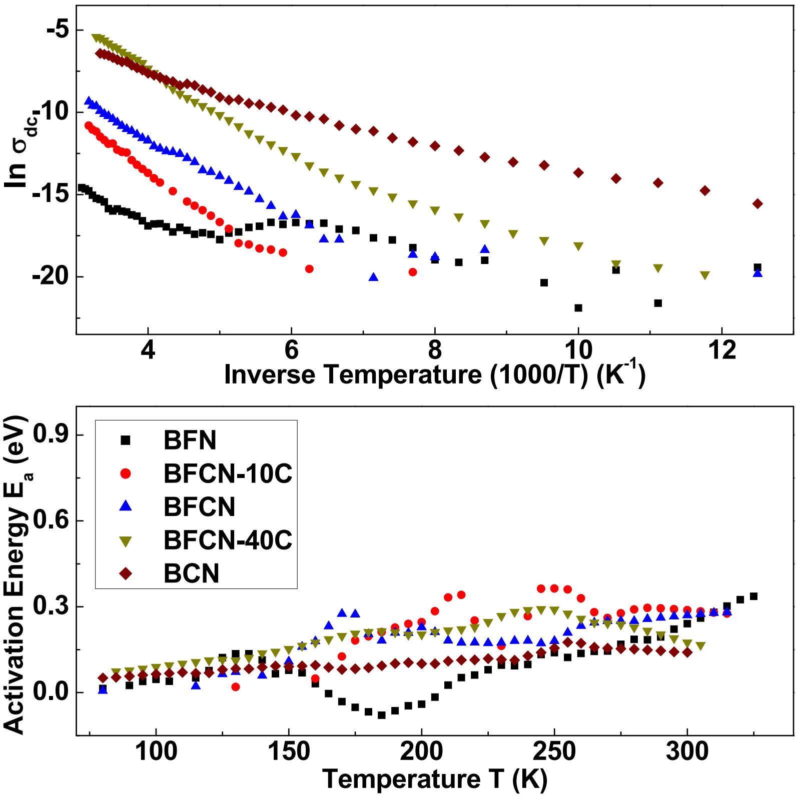

Figure 4.B.22: The Arrhenius plot of dc conductivity along with temperature dependent activation energies for BFCN series in bellow room temperature region.

Conductivity representation: The analysis of the free charge carriers responsible for the observed high dielectric loss can be done using dc conductivity analysis. The values of dc conductivity are obtained for each sample through extrapolating the low frequency plateau of $\sigma'(f)$ curve at all temperatures. The temperature dependent analysis of dc conductivity σ_{dc} using Arrhenius law is presented in the Figure 4.B.22 and Figure 4.B.23 respectively for low temperature region and high temperature region. The Arrhenius plot of dc conductivity σ_{dc} obtained for our samples have not shown any linear nature therefore the temperature dependent activation energies were calculated using the Equation 4.B.22. The variation of the activation energy as a function of temperature is presented in the Figure 4.B.22 and Figure 4.B.23 respectively for low temperature region and high temperature region.

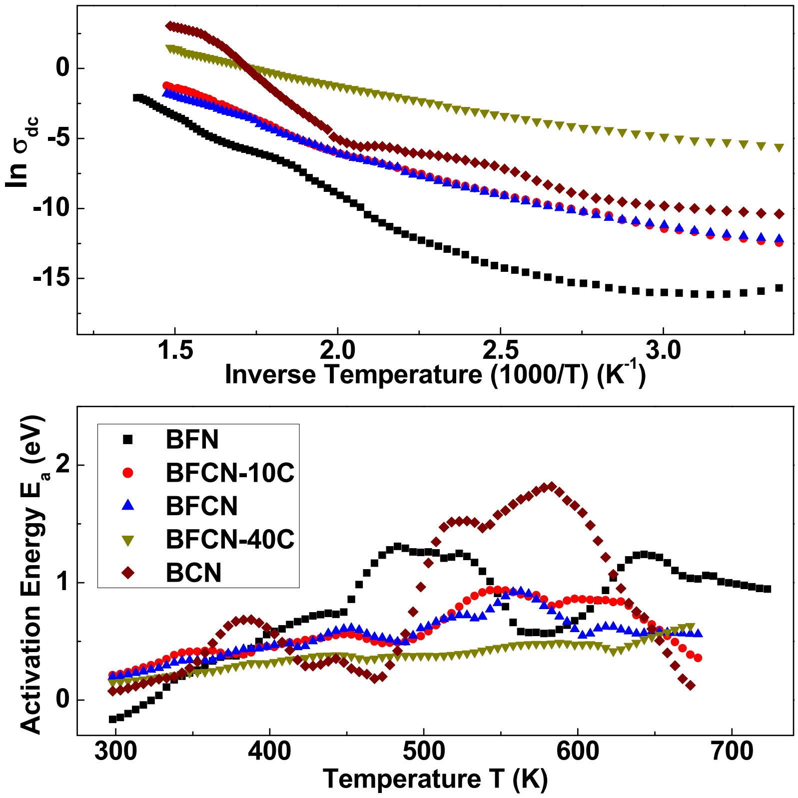

Figure 4.B.23: The Arrhenius plot of dc conductivity along with temperature dependent activation energies for BFCN series in above room temperature region.

The comparison of dc conductivity values clearly suggests increase in conducting nature of the samples with increasing Co concentration. The observed excess conductivity for Co rich samples is due to dominant additional conductivity originating from doped free electrons as pointed out earlier. Further, the activation energy E_a is found to have only small variations (<0.3 eV) in the low temperature region suggesting the presence of singly ionized oxygen vacancies [14, 16]. The E_a values increases gradually up to 0.6 eV in the temperature range of 300 K to 450 K indicating development of doubly ionized oxygen vacancies. The observed subsequent higher values (up to 1.2 eV) indicate enhanced interaction of relaxing dipoles with the oxygen vacancies at elevated temperatures. The observed sharp rise and peak formation in the values of E_a are related with the NTCR-PTCR transitions observed in dc conductivity curves. These NTCR-PTCR transitions may be linked to possible phase transitions.

4.B. 2.3 Complex Electrical Analysis of BFMN Series: [$Ba(Fe_{0.5-X}Mn_XNb_{0.5})O_3$] (where X=0, 0.25, 0.50):

The samples of this series are prepared through gradual substitution of Fe by Mn in the BFN ceramic. The effects of substitution on electrical properties of these compounds are investigated in this section. The whole investigation is carried out using above discussed four representations.

Impedance representation: The temperature dependent analyses of R_g, τ_g, R_{gb} and τ_{gb} using Arrhenius law are shown in the Figure 4.B.24 and Figure 4.B.25 respectively for low temperature region and high temperature region. The temperature dependent variations in the C_g and C_{gb} are also presented in the figures. The Arrhenius plots of R and τ obtained for our samples have not shown any linear nature therefore the temperature dependent activation energies were calculated using the Equation 4.B.20 and Equation 4.B.21. The variation of the activation energy as a function of temperature, obtained for R and τ, is presented in the Figure 4.B.24 and Figure 4.B.25. In the low temperature region the activation energies are found to have little variations (<0.3 eV) suggesting singly ionized oxygen vacancies induced dielectric relaxation in this temperature region [14, 16]. The observed comparatively fast increment in the activation energies for BFMN and BMN, up to 350 K suggests rapid conversion of singly ionized oxygen vacancies in to doubly ionized oxygen vacancies. This process was gradual and lasts up to 450 K for the BFN sample. In contrast to BFN, the values of activation energy E_a remain constant at 0.6 eV for Mn substituted samples indicates that the observed relaxation is due to free charges. The activation energy values rise up to 1.2 eV at elevated temperatures suggests enhanced interaction of relaxing dipoles with the oxygen vacancies. Further the oscillating nature and peak formation at elevated temperatures suggest possible phase transitions.

The values of grain capacitance C_g and grain boundary capacitance C_{gb} found constant in the entire temperature range (except high temperature tails) for all the samples. The observed

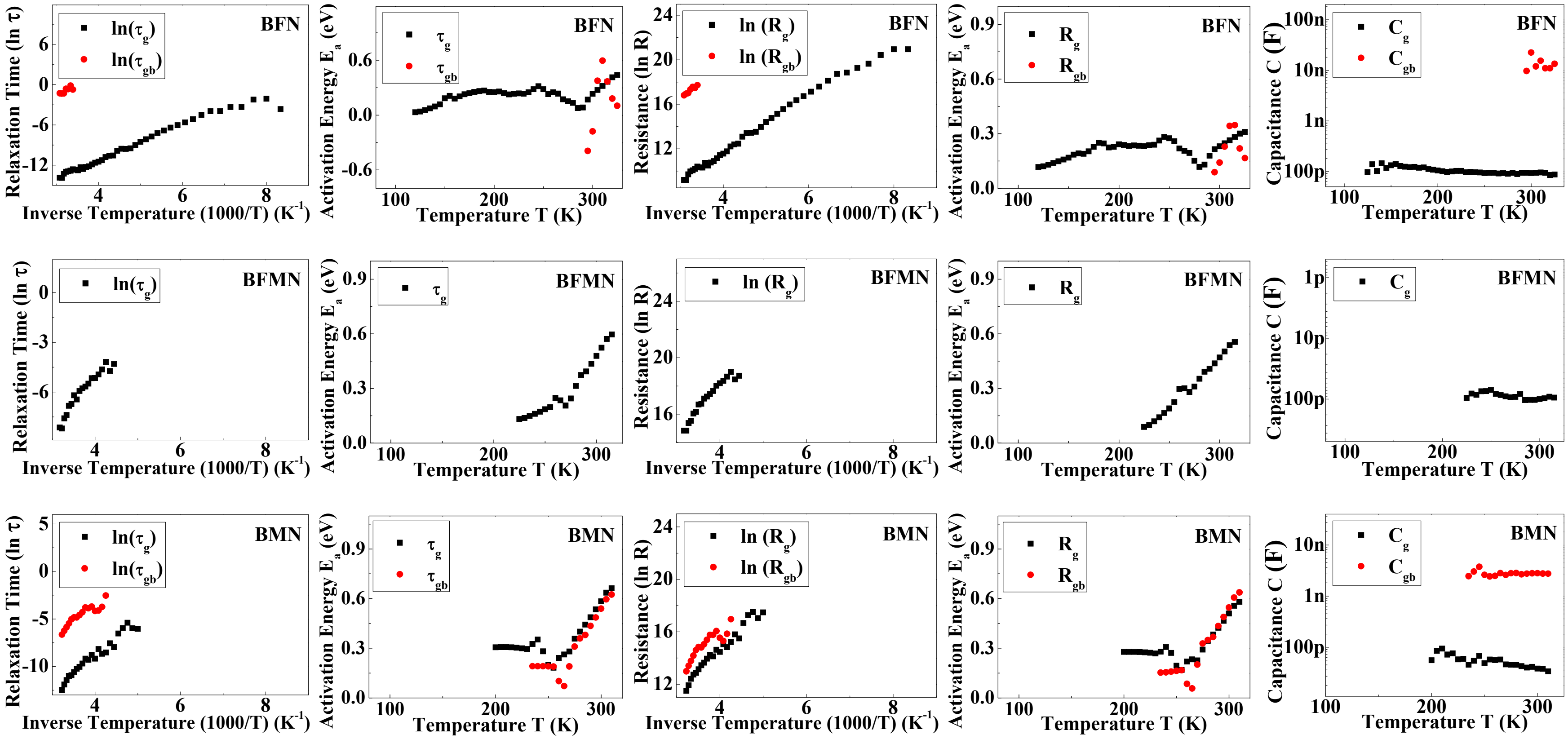

Figure 4.B.24: The impedance Cole-Cole fitting parameters with their Arrhenius plots and temperature dependent activation energies for BFMN series for bellow room temperature region.

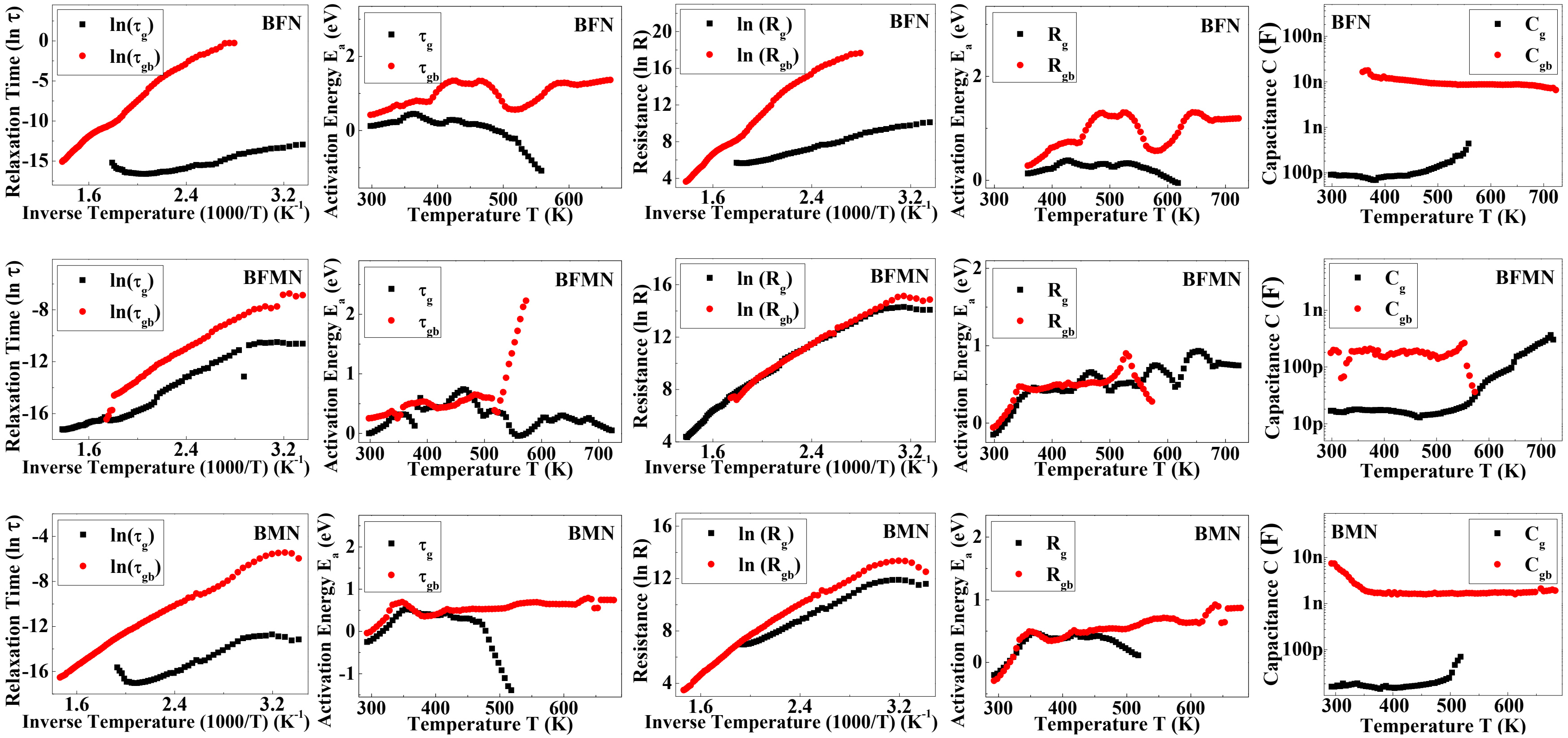

Figure 4.B.25: The impedance Cole-Cole fitting parameters with their Arrhenius plots and temperature dependent activation energies for BFMN series for above room temperature region.

anomalies in C_g and C_{gb} for at elevated temperatures is again related to NTCR – PTCR transition observed in the curves of R_g and R_{gb}. It points at possibilities of phase transitions in this temperature range.

Permittivity representation: The samples of this series have shown dominant nature of conductivity over relaxation process. Therefore the relaxation peak in the $\varepsilon''(f)$ curve is completely masked by the conduction. This has resulted in to the absence of clear semi circular arc related to the Cole-Cole curve as well as not so clear relaxation peak in the $\varepsilon''(f)$ curve. Thus we could not perform analysis using the permittivity representation.

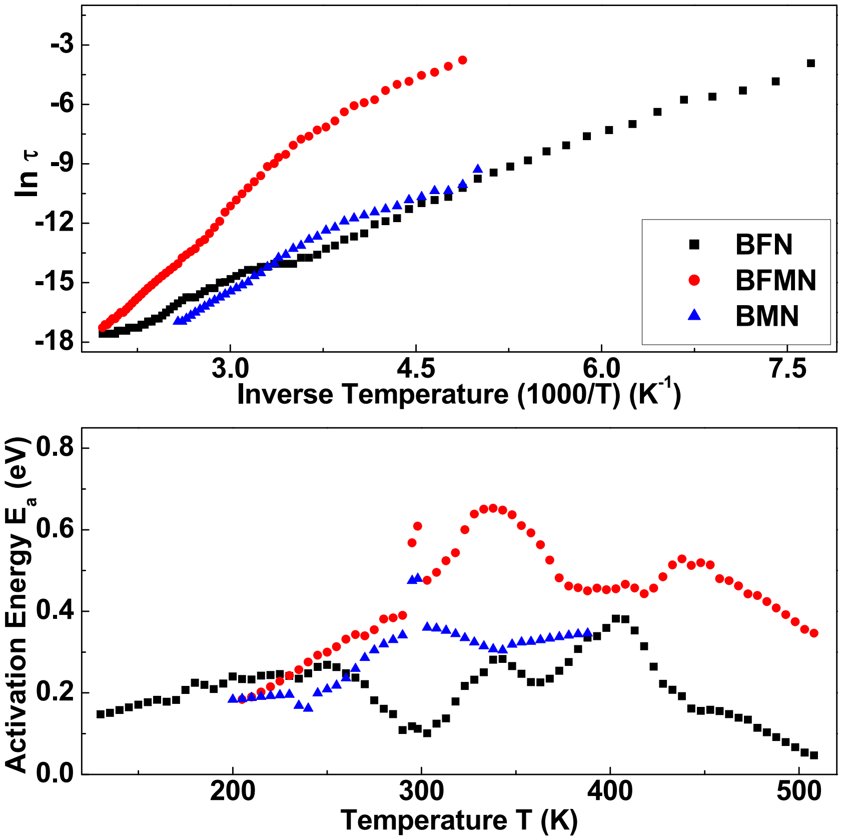

Figure 4.B.26: The Arrhenius plot of relaxation time along with temperature dependent activation energies obtained using electric modulus data BFMN series.

Electric modulus representation: The dielectric relaxation analysis for the conducting samples can be done effectively through the electrical modulus representation. The values of mean relaxation time τ are obtained for each sample using the peak of $M''(f)$ curve in the entire temperature range. The temperature dependent analysis of mean relaxation time τ using Arrhenius law is presented in the Figure 4.B.26. The Arrhenius plot of relaxation time τ obtained for our samples have not shown any linear nature therefore the temperature dependent activation energies were calculated using the Equation 4.B.21. The variation of the activation energy as a function of temperature is presented in the Figure 4.B.26.

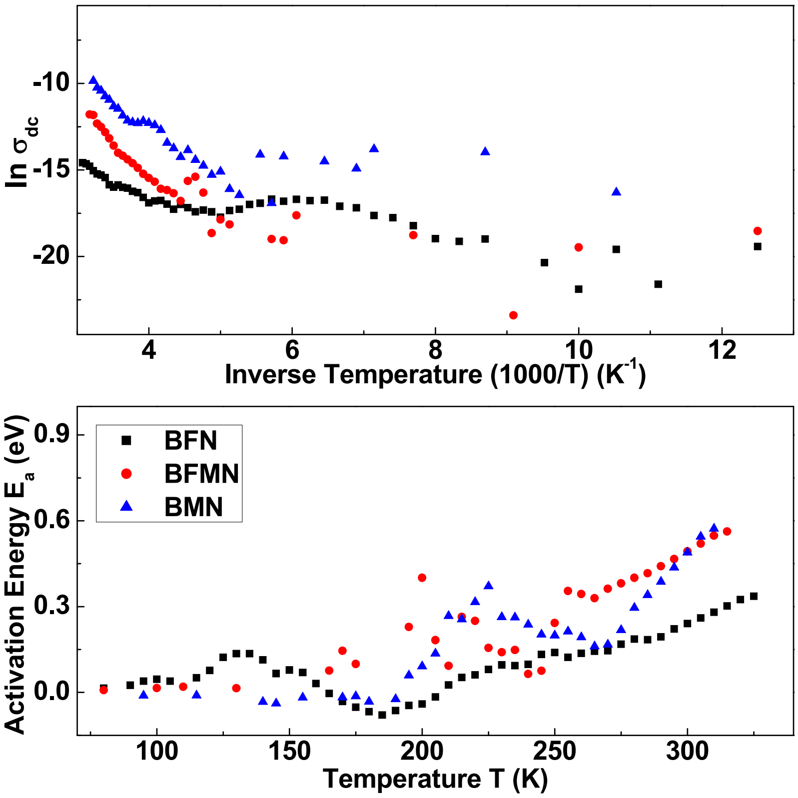

Figure 4.B.27: The Arrhenius plot of dc conductivity along with temperature dependent activation energies for BFMN series in bellow room temperature region.

The observed smaller activation energy values E_a (<0.4 eV) for all the samples in the low temperature region suggests presence of singly ionized oxygen vacancies. A systematic enhancement of the activation energy (up to 0.6 eV) at higher temperatures suggests the development of doubly ionized oxygen vacancies in the samples. The observed unusually higher activation energy values for intermediate BFMN ceramic, unlike BFCN, may be due to co-existence of micro domains of BFN and BMN leading to a distortion of long-range order of $-\mathrm{Fe}-\mathrm{Nb}-\mathrm{Fe}-$ or $-\mathrm{Mn}-\mathrm{Nb}-\mathrm{Mn}-$ chains [14]. The observed broad peaks in the activation energy curve of BFMN suggest possibilities of gradual transition at these temperatures.

Conductivity representation: The analysis of the free charge carriers responsible for the observed high dielectric loss can be done using dc conductivity analysis. The values of dc conductivity are obtained for each sample through extrapolating the low frequency plateau of $\sigma'(f)$ curve at all temperatures. The temperature dependent analysis of dc conductivity σ_{dc} using Arrhenius law is presented in the Figure 4.B.27 and Figure 4.B.28 respectively for low temperature region and high temperature region. The Arrhenius plot of dc conductivity σ_{dc} obtained for our samples have not shown any linear nature therefore the temperature dependent activation energies were calculated using the Equation 4.B.22. The variation of the activation energy as a function of temperature is presented in the Figure 4.B.27 and Figure 4.B.28 respectively for low temperature region and high temperature region.

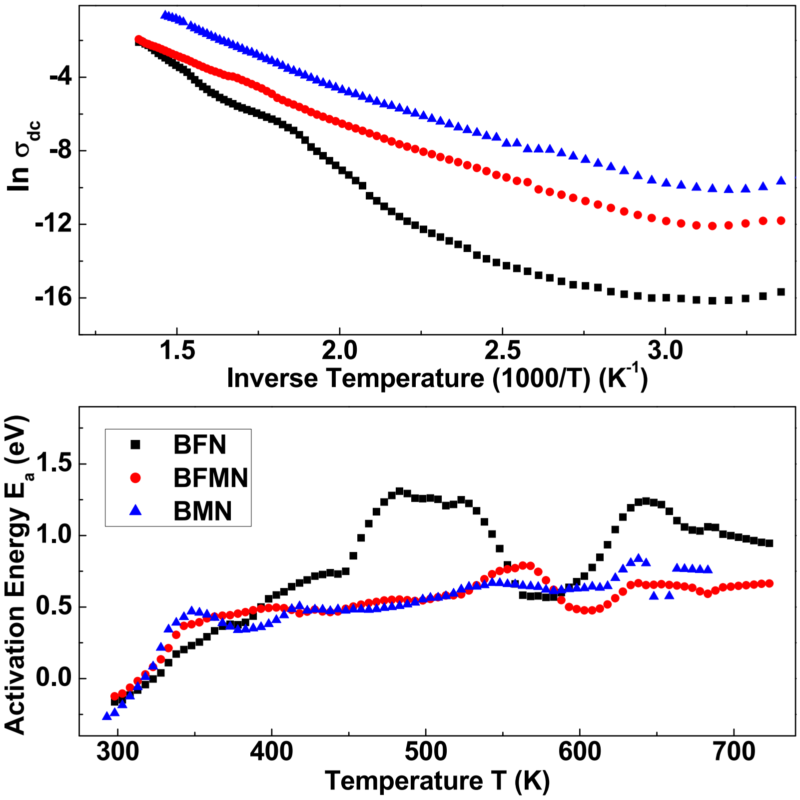

Figure 4.B.28: The Arrhenius plot of dc conductivity along with temperature dependent activation energies for BFMN series in above room temperature region.

The dc conductivity values increases with increasing concentration of Mn. The possible reason for such increment in dc conductivity is doping of holes due to replacement of Fe^{3+} ($3d^5$) by Mn^{3+} ($3d^4$). The activation energy values found to be small (<0.3 eV) in the low temperature region suggests the presence of singly ionized oxygen vacancies [14, 16]. It increases gradually up to 0.5 eV in the temperature range 150 K to 450 K suggest development of doubly ionized oxygen vacancies. The relatively lower activation energy observed for Mn rich samples suggest dominant interaction between oxygen vacancies and doped charges as discussed earlier. The observed oscillations and peak formation in the values of E_a are related with the NTCR-PTCR transitions observed in dc conductivity curves. These NTCR-PTCR transitions may be linked with possible phase transitions. The observed higher values (up to 1.2 eV) for BFN indicates enhanced interaction of relaxing dipoles with the oxygen vacancies at elevated temperatures.

4.B.2.4 Complex Electrical Analysis of BFGN Series: [Ba($Fe_{0.5-X}Gd_XNb_{0.5}$)O_3] (where X=0, 0.25, 0.50):

The samples of this series are prepared through gradual substitution of Fe by Gd in the BFN ceramic. The effects of substitution on electrical properties of these compounds are investigated in this section. The whole investigation is carried out using above discussed four representations.

Impedance representation: The temperature dependent analyses of R_g, τ_g, R_{gb} and τ_{gb} using Arrhenius law are shown in the Figure 4.B.29 for high temperature region only. The temperature dependent variations in the C_g and C_{gb} are also presented in the figure. It is to be noted here that contrary to conducting 3d element substituted BFN samples, impedance analysis could not be performed for the BGN in the entire temperature range and for BFGN in the low temperature region due to their highly resistive nature. The Arrhenius plots of R and τ obtained for BFN and BFGN have not shown any linear nature therefore the temperature dependent activation energies were calculated using the Equation 4.B.20 and Equation 4.B.21. The variation of the activation energy as a function of temperature, obtained for R and τ, is presented in the Figure 4.B.29. The values of activation energy E_a increases up to 0.6 eV as the temperature raise to 350 K for BFGN sample. This suggests development of doubly ionized oxygen vacancies. It remains nearly constant up to 550 K without any broad peak; unlike BFN, suggests absence of NTCR-PTCR transitions in this temperature range [27]. The E_a values show a sharp rise and make a peak in the temperature range of 550 K to 650 K followed by gradual increase at elevated temperatures. The observed sharp peak suggest possible structural phase transition at this temperatures [28]. The observed increase in E_a values at elevated temperatures up to 1.2 eV suggests enhanced interaction of relaxing dipoles with the oxygen vacancies. The observed dip values of grain capacitance C_g near 550 K confirm the possibilities of structural phase transition.

Permittivity representation: The BFGN ceramic has not shown the relaxation peak in the $\varepsilon''(f)$ curve. This has resulted in to the absence of clear semi circular arc related to the Cole-

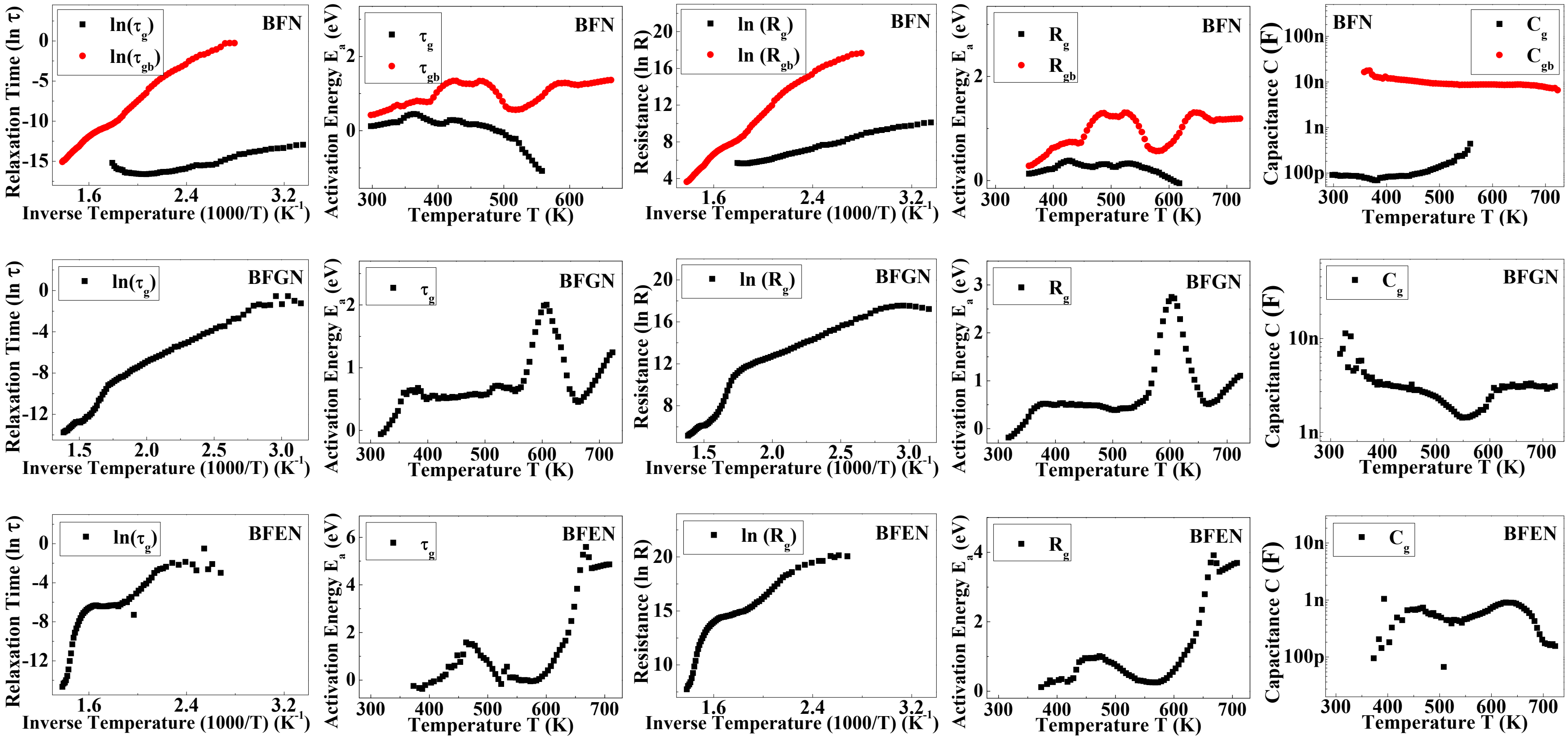

Figure 4.B.29: The impedance Cole-Cole fitting parameters with their Arrhenius plots and temperature dependent activation energies for BFGN and BFEN series for above room temperature region.

Cole curve. Therefore we could not perform analysis using permittivity representation for this series.

Electric modulus representation: The peak in the $M''(f)$ curve is also absent for BFEN ceramic. Therefore it was not possible to identify the relaxation frequency required for analysis using modulus representation. The absence of relaxation peak in permittivity as well as modulus suggests dominant contribution of non dipole type relaxation.

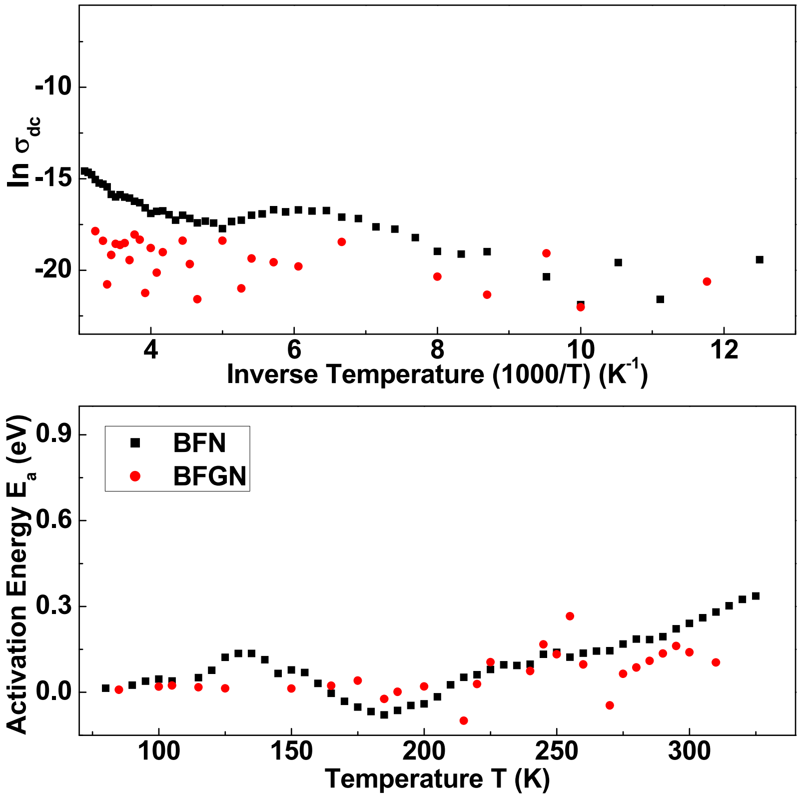

Figure 4.B.30: The Arrhenius plot of dc conductivity along with temperature dependent activation energies for BFGN series in bellow room temperature region.

Conductivity representation: The analysis of the free charge carriers responsible for the observed high dielectric loss can be done using dc conductivity analysis. The values of dc conductivity are obtained for each sample through extrapolating the low frequency plateau of $\sigma'(f)$ curve at all temperatures. The temperature dependent analysis of dc conductivity σ_{dc} using Arrhenius law is presented in the Figure 4.B.30 and Figure 4.B.31 respectively for low temperature region and high temperature region. The Arrhenius plot of dc conductivity σ_{dc} obtained for our samples have not shown any linear nature therefore the temperature dependent activation energies were calculated using the Equation 4.B.22. The variation of the activation energy as a function of temperature is presented in the Figure 4.B.30 and Figure 4.B.31 respectively for low temperature region and high temperature region.

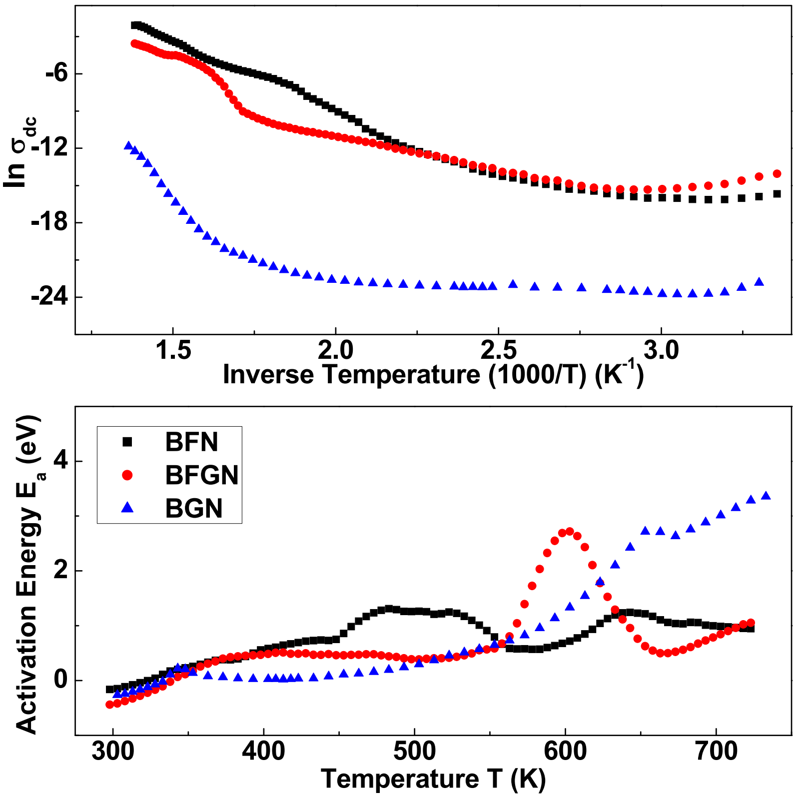

Figure 4.B.31: The Arrhenius plot of dc conductivity along with temperature dependent activation energies for BFGN series in above room temperature region.

The dc conductivity values for BFN and BFGN are comparatively higher than the BGN ceramic. This clearly suggests more insulating nature of BGN ceramic. The observed equivalent conductivity for intermediate BFGN ceramic is due to interaction of oxygen vacancies with the available large BFN crystallites inside the grains of BFGN (see Table 4.A.1). Further, in the low temperature region the values of activation energy E_a found to be ~0.3 eV which corresponds to singly ionized oxygen vacancies. The values of E_a gradually increases up to 0.5 eV in the temperature range 300 K to 400 K suggests development of doubly ionized oxygen vacancies. It remains nearly constant (~0.5 eV) up to 550 K for both BFGN and BGN ceramics. In accordance with the impedance analysis the values of E_a has developed a peak at 600 K followed by gradual rise in E_a up to 1.2 eV. Such a peak is absent in the BGN ceramic and shows gradual increase in the E_a values up to 3.0 eV. This suggests possibilities of change in the mechanism of conduction in BGN at these temperatures.

4.B. 2.5 Complex Electrical Analysis of BFEN Series: [$Ba(Fe_{0.5-X}Eu_XNb_{0.5})O_3$] where X=0, 0.25, 0.50):

The samples of this series are prepared through gradual substitution of Fe by Eu in the BFN ceramic. The effects of substitution on electrical properties of these compounds are investigated in this section. The whole investigation is carried out using above discussed four representations.

Impedance representation: The temperature dependent analyses of R_g, τ_g, R_{gb} and τ_{gb} using Arrhenius law are shown in the Figure 4.B.29 for high temperature region only. The temperature dependent variations in the C_g and C_{gb} are also presented in the figure. It is to be noted here that this analysis could not be performed for the BEN in the entire temperature range and for BFEN in the low temperature region due to highly resistive nature. The Arrhenius plots of R and τ obtained for BFN and BFEN have not shown any linear nature therefore the temperature dependent activation energies were calculated using the Equation 4.B.20 and Equation 4.B.21. The variation of the activation energy as a function of temperature, obtained for R and τ, is presented in the Figure 4.B.29.

The values of activation energy E_a, increases up to 1.5 eV on increasing temperature to 450 K. The E_a gradually decrease up to 0.5 eV in the temperature range of 450 K to 600 K. The observed broad peak (similar to BFN ceramic) at 450 K suggests possibilities of NTCR-PTCR transitions at these temperatures [27]. The E_a values show a sharp rise at 650 K with increased values at elevated temperatures. The observed sharp step suggest possible structural phase transition at this temperature [28]. The observed increased values of E_a at elevated temperatures points at change in the mechanism of relaxation or conduction.

Permittivity representation: The BFEN ceramic has not shown any relaxation peak in the $\varepsilon''(f)$ curve. This has resulted in to the absence of clear semi circular arc related to the Cole-Cole curve. Therefore we could not perform analysis using permittivity representation for this series.

Electric modulus representation: The dielectric relaxation analysis for the conducting samples can be done effectively through the electrical modulus representation. The values of mean relaxation time τ are obtained for each sample using the peak of $M''(f)$ curve in the entire temperature range. The temperature dependent analysis of mean relaxation time τ using Arrhenius law is presented in the Figure 4.B.32. The Arrhenius plot of relaxation time τ

obtained for our samples have not shown any linear nature therefore the temperature dependent activation energies were calculated using the Equation 4.B.21. The variation of the activation energy as a function of temperature is presented in the Figure 4.B.32.

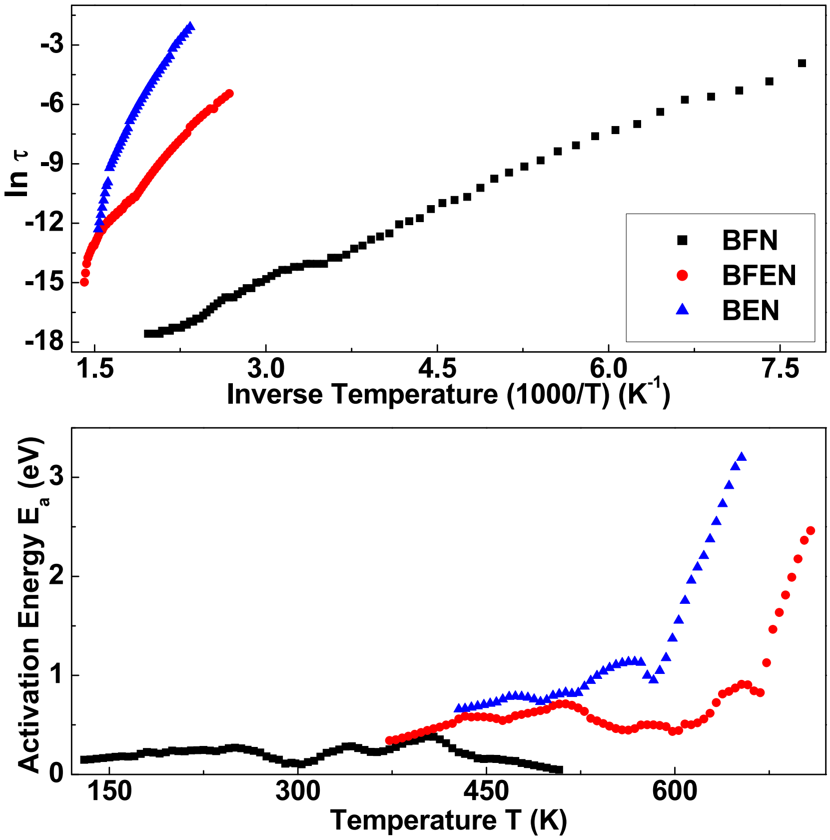

Figure 4.B.32: The Arrhenius plot of relaxation time along with temperature dependent activation energies obtained using electric modulus data for BFEN series.

The peak in activation energy values E_a at 500 K, for BFEN ceramic is similar with the observed peak in BFN ceramic at 400 K. The peak for BFEN is found shifted towards higher temperatures along with higher values of E_a. The enhanced E_a values for BFEN and BEN suggest comparatively rigid nature of ionized oxygen vacancies. The observed broad peak of activation energy suggests possibilities of phase transition at these temperatures. Further, at elevated temperatures (>600 K) the sudden rise in E_a for BFEN and BEN suggests, change in the mechanism of relaxation or conduction.

Conductivity representation: The analysis of the free charge carriers responsible for the observed high dielectric loss can be done using dc conductivity analysis. The values of dc conductivity are obtained for each sample through extrapolating the low frequency plateau of $\sigma'(f)$ curve at all temperatures. The temperature dependent analysis of dc conductivity σ_{dc}

using Arrhenius law is presented in the Figure 4.B.33. The Arrhenius plot of dc conductivity σ_{dc} obtained for our samples have not shown any linear nature therefore the temperature dependent activation energies were calculated using the Equation 4.B.22. The variation of the activation energy as a function of temperature is presented in the Figure 4.B.33.

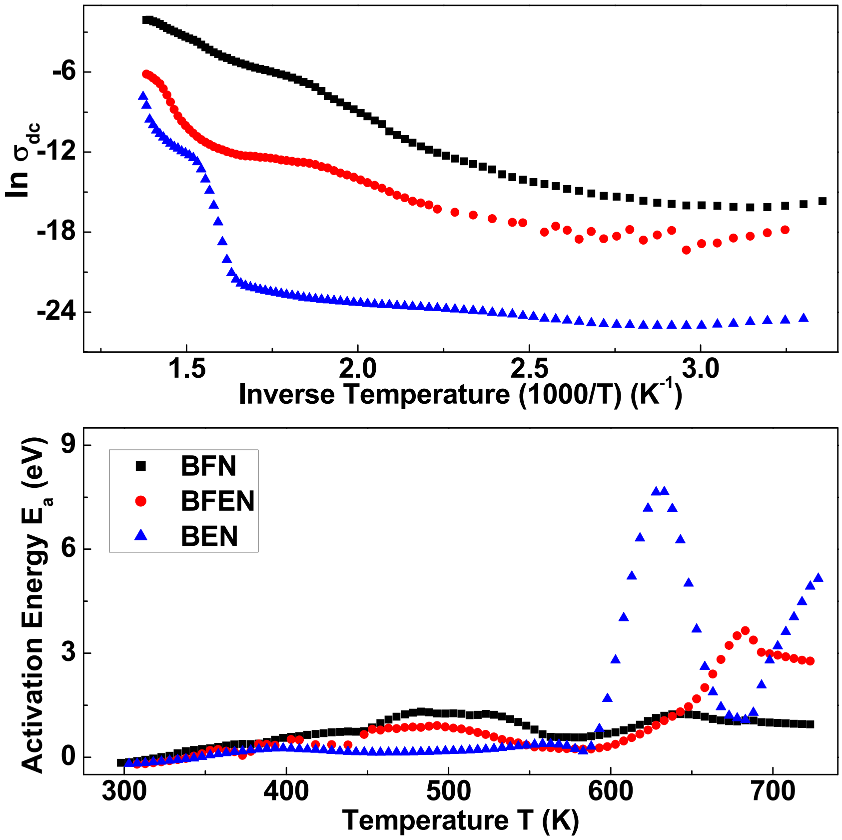

Figure 4.B.33: The Arrhenius plot of dc conductivity along with temperature dependent activation energies for BFEN series in above room temperature region.

The values of activation energy E_a gradually increases up to 0.5 eV in the temperature range 300 K to 400 K suggests development of doubly ionized oxygen vacancies. It remains nearly constant (~0.5 eV) up to 550 K for BEN ceramics while develop a broad peak for BFN and BFEN ceramic. The broad peaks suggest increased interaction of doubly ionized oxygen vacancies. The values of E_a for BEN have developed a peak at 630 K followed by sharp rise in E_a up to 4.5 eV. The observed sharp peak suggest possible structural phase transition at this temperatures [28]. The observed rise in the E_a at higher temperatures suggests possibilities of change in the mechanism of conduction at these temperatures. We observed similar rise for BFEN at increased temperatures.

4.B.2.6 Complex Electrical Analysis of BGCN Series: [$Ba(Gd_{0.5-X}Co_XNb_{0.5})O_3$] (where X=0, 0.10, 0.25, 0.50):

The samples of this series are prepared through gradual substitution of Gd by Co in the BGN ceramic. The effects of substitution on electrical properties of these compounds are investigated in this section. The whole investigation is carried out using above discussed four representations.

Impedance representation: The temperature dependent analyses of R_g, τ_g, R_{gb} and τ_{gb} using Arrhenius law are shown in the Figure 4.B.34 and Figure 4.B.35 respectively for low temperature region and high temperature region. The temperature dependent variations in the C_g and C_{gb} are also presented in the figures. It is to be noted here that this analysis could not be performed for the BGN in the entire temperature range and for BGCN-10C in the low temperature region due to resistive nature of the samples. The Arrhenius plots of R and τ obtained for our samples have not shown any linear nature therefore the temperature dependent activation energies were calculated using the Equation 4.B.20 and Equation 4.B.21. The variation of the activation energy as a function of temperature, obtained for R and τ, is presented in the Figure 4.B.34 and Figure 4.B.35. In the low temperature region the activation energies are found very less (<0.3 eV), suggest singly ionized oxygen vacancies induced dielectric relaxation in this temperature region [14, 16]. The observed broad peak for the activation energy suggests NTCR-PTCR transition. In the high temperature region, the activation energy for BGCN, increases gradually up to 0.6 eV and remains constant in the entire temperature range. The values of E_a for BGCN-10C show broad peak around 600 K suggests enhanced interaction of oxygen vacancies with the free charges. Further, the oscillating nature and peak formation at elevated temperatures suggest possible phase transitions.

The values of grain capacitance C_g found constant up to 400 K and shows gradual rising nature at high temperatures for Co rich samples BGCN and BCN. The observed rise in C_g and C_{gb} for Co rich samples is related to enhanced interaction of doped electrons with doubly ionized oxygen vacancies at increased temperatures.

Permittivity representation: The samples of this series have shown dominant nature of conductivity over relaxation process. Therefore the relaxation peak in the $\varepsilon''(f)$ curve is completely masked by the conduction. This has resulted in to the absence of clear semi circular

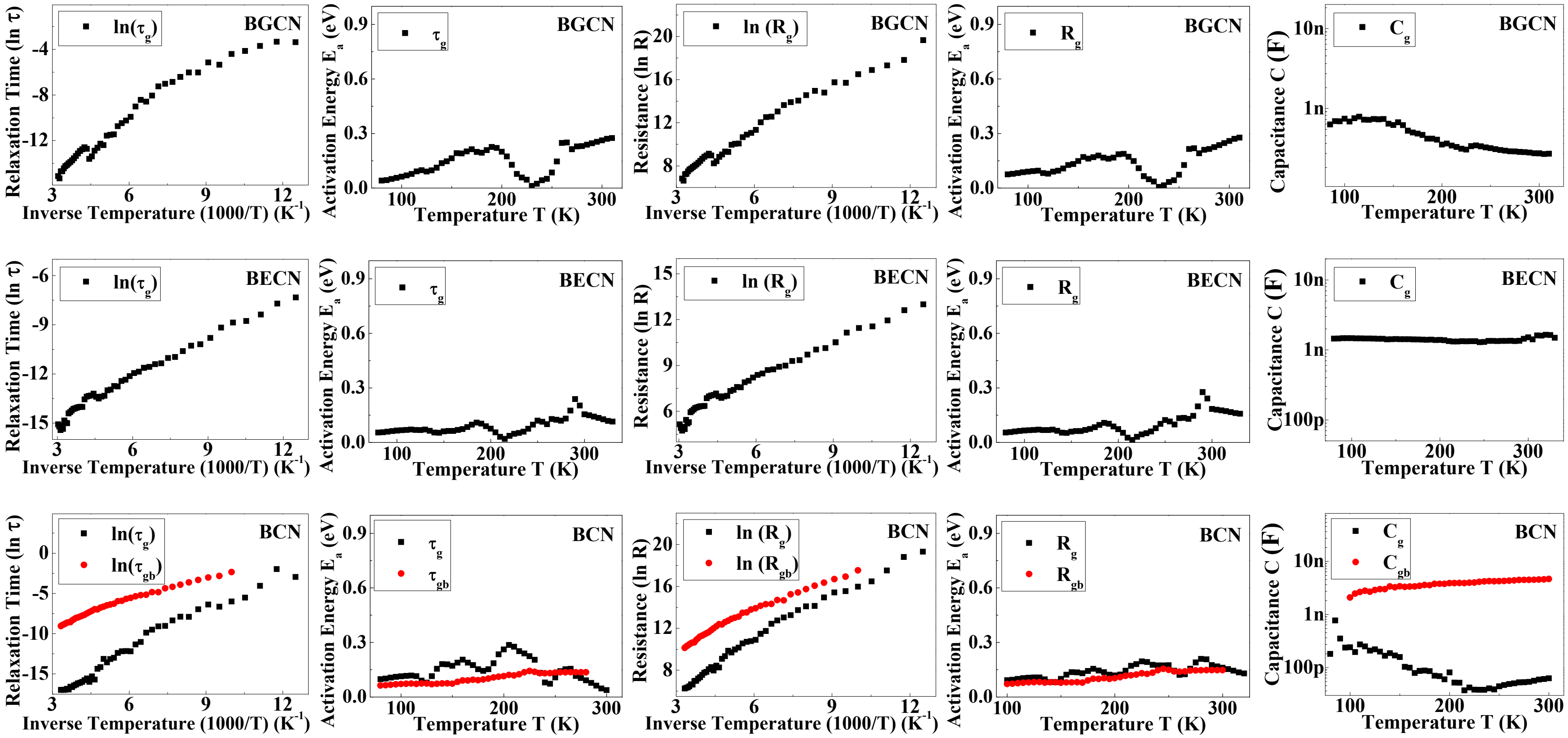

Figure 4.B.34: The impedance Cole-Cole fitting parameters with their Arrhenius plots and temperature dependent activation energies for BGCN and BECN series for bellow room temperature region.

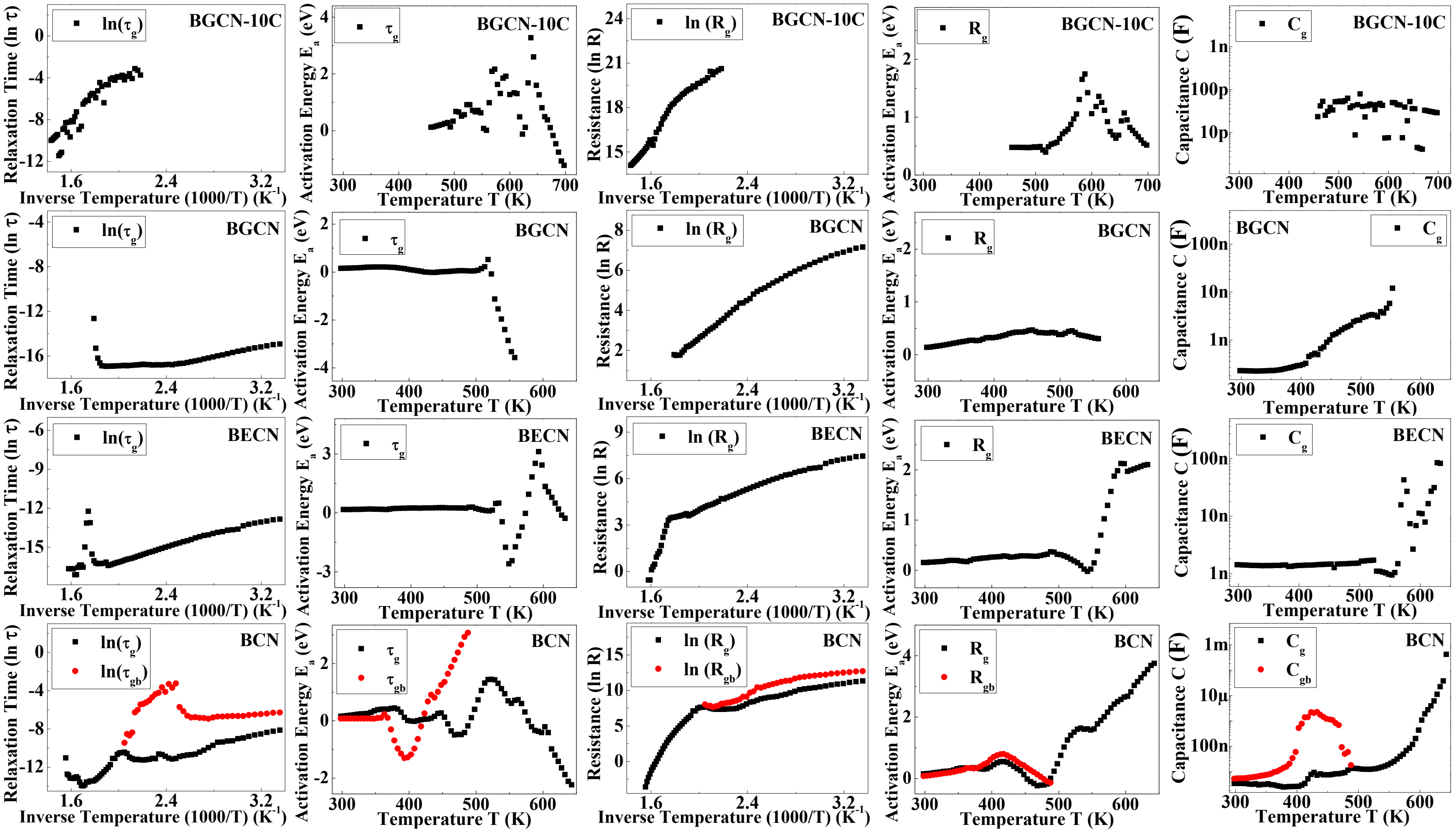

Figure 4.B.35: The impedance Cole-Cole fitting parameters with their Arrhenius plots and temperature dependent activation energies for BGCN and BECN series for above room temperature region.

arc related to the Cole-Cole curve as well as not so clear relaxation peak in the $\varepsilon''(f)$ curve. In this view we could not perform analysis using the permittivity representation.

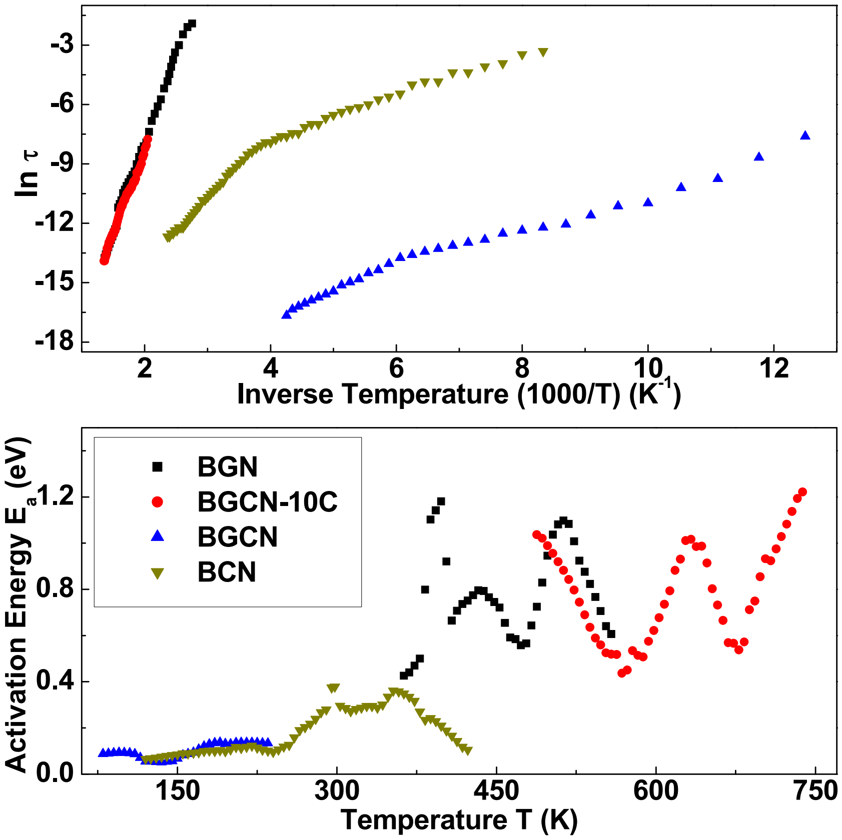

Figure 4.B.36: The Arrhenius plot of relaxation time along with temperature dependent activation energies obtained using electric modulus data for BGCN series.

Electric modulus representation: The dielectric relaxation analysis for the conducting samples can be done effectively through the electrical modulus representation. The values of mean relaxation time τ are obtained for each sample using the peak of $M''(f)$ curve in the entire temperature range. The temperature dependent analysis of mean relaxation time τ using Arrhenius law is presented in the Figure 4.B.36. The Arrhenius plot of relaxation time τ obtained for our samples have not shown any linear nature therefore the temperature dependent activation energies were calculated using the Equation 4.B.21. The variation of the activation energy as a function of temperature is presented in the Figure 4.B.36.

The observed less activation energy values E_a (<0.3 eV) for all the samples in the low temperature region are in agreement with the impedance analyses suggesting presence of singly ionized oxygen vacancies. A systematic enhancement of the activation energy (up to 0.5 eV) for the temperatures from 300 K to 400 K, suggests the development of doubly ionized oxygen vacancies in the samples. The observed higher values (up to 1.2 eV) for Gd rich samples BGN and BGCN suggest comparatively rigid nature of ionized oxygen vacancies. The observed oscillating nature of activation energy suggests possibilities of phase transitions at these temperatures.

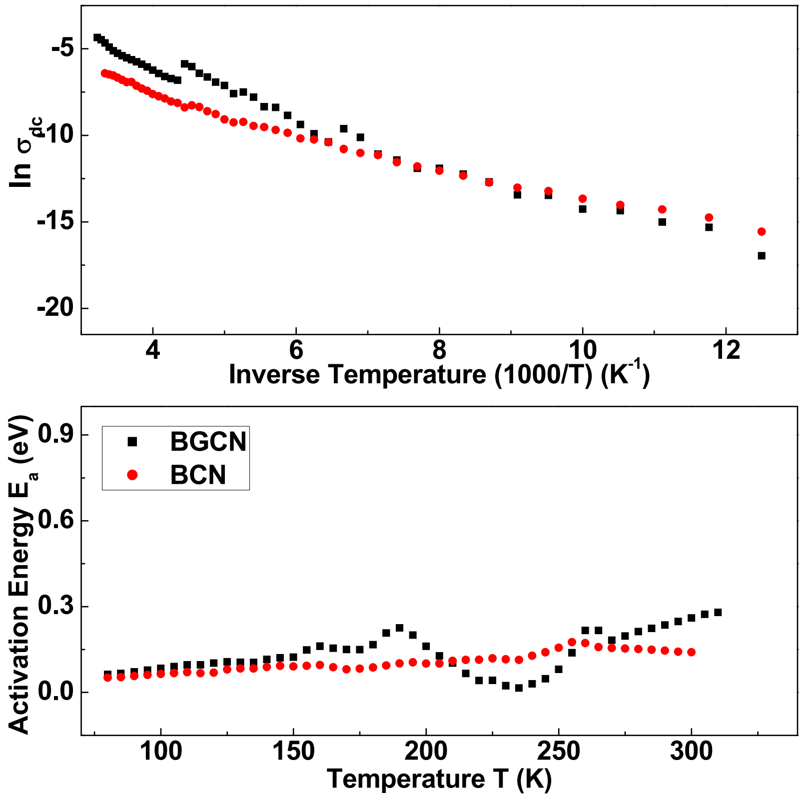

Figure 4.B.37: The Arrhenius plot of dc conductivity along with temperature dependent activation energies for BGCN series in bellow room temperature region.

Conductivity representation: The analysis of the free charge carriers responsible for the observed high dielectric loss can be done using dc conductivity analysis. The values of dc conductivity are obtained for each sample through extrapolating the low frequency plateau of $\sigma'(f)$ curve at all temperatures. The temperature dependent analysis of dc conductivity σ_{dc} using Arrhenius law is presented in the Figure 4.B.37 and Figure 4.B.38 respectively for low temperature region and high temperature region. The Arrhenius plot of dc conductivity σ_{dc} obtained for our samples have not shown any linear nature therefore the temperature dependent activation energies were calculated using the Equation 4.B.22. The variation of the activation energy as a function of temperature is presented in the Figure 4.B.37 and Figure 4.B.38 respectively for low temperature region and high temperature region.

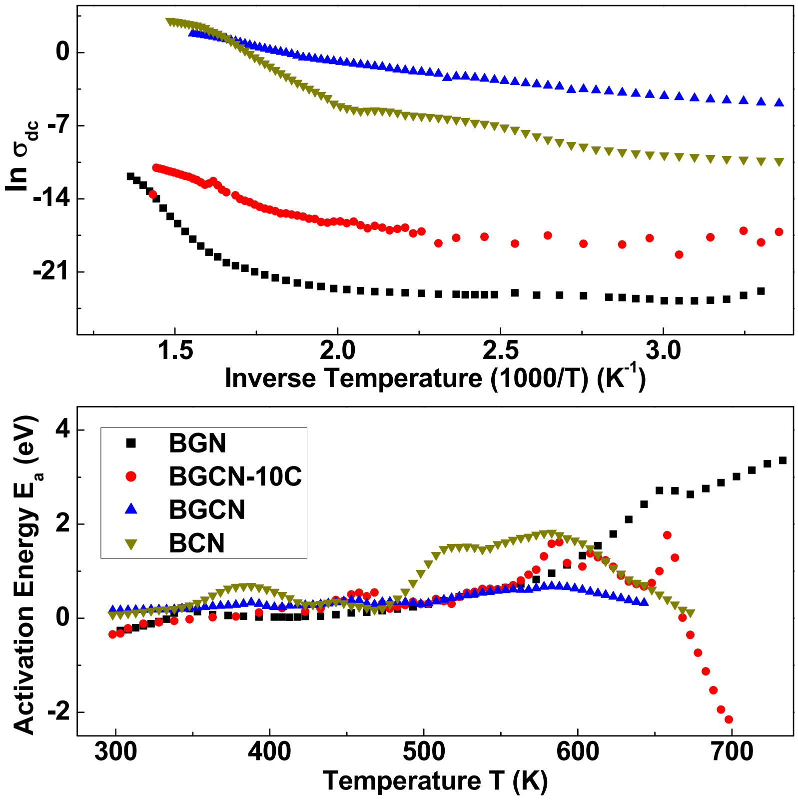

Figure 4.B.38: The Arrhenius plot of dc conductivity along with temperature dependent activation energies for BGCN series in above room temperature region.

The comparison of dc conductivity values clearly suggests increase in conducting nature of the samples with increasing Co concentration. The observed excess conductivity for Co rich samples is due to dominant additional conductivity originating from doped free electrons as pointed out earlier. Further, the activation energy E_a is found very less (<0.3 eV) in the low temperature region suggests the presence of singly ionized oxygen vacancies [16]. The E_a values increases gradually up to 0.6 eV in the temperature range 300 K to 450 K suggesting development of doubly ionized oxygen vacancies. The observed higher values (up to 1.2 eV) indicate enhanced interaction of relaxing dipoles with the oxygen vacancies at elevated temperatures. The observed sharp rise and peak formation in the values of E_a are related with the NTCR-PTCR transitions observed in dc conductivity curves. These NTCR-PTCR transitions may be linked with possible phase transitions.

4.B. 2.7 Complex Electrical Analysis of BECN Series: [$Ba(Eu_{0.5-X}Co_XNb_{0.5})O_3$] (where X=0, 0.25, 0.50):

The samples of this series are prepared through gradual substitution of Eu by Co in the BEN ceramic. The effects of substitution on electrical properties of these compounds are investigated in this section. The whole investigation is carried out using above discussed four representations.

Impedance representation: The temperature dependent analyses of R_g, τ_g, R_{gb} and τ_{gb} using Arrhenius law are shown in the Figure 4.B.34 and Figure 4.B.35 respectively for low temperatures region and high temperature region. The temperature dependent variations in the C_g and C_{gb} are also presented in the figures. The Arrhenius plots of R and τ obtained for our samples have not shown any linear nature therefore the temperature dependent activation energies were calculated using the Equation 4.B.20 and Equation 4.B.21. The variation of the activation energy as a function of temperature, obtained for R and τ, is presented in the Figure 4.B.34 and Figure 4.B.35. In the low temperature region the activation energies are found very less (<0.3 eV), corresponds to singly ionized oxygen vacancies induced dielectric relaxation in this temperature region [14, 16]. In the high temperature region, the activation energy for BECN, increases gradually up to 0.6 eV and remains constant up to 550 K. The sudden rise in E_a for BECN beyond 550 K suggests possibilities of structural phase transition. The higher E_a values at elevated temperatures points at changes in the mechanism of relaxation or conduction. The values of grain capacitance C_g found to be constant up to 550 K and shows sudden step at high temperatures for BECN. The observed increase in C_g is related to the possible structural transition.

Permittivity representation: The samples of this series have shown dominant nature of conductivity over relaxation process. Therefore the relaxation peak in the $\varepsilon''(f)$ curve is completely masked by the conduction. This has resulted in to the absence of clear semi circular arc related to the Cole-Cole curve as well as not so clear relaxation peak in the $\varepsilon''(f)$ curve. In this view we could not perform analysis using the permittivity representation.

Electric modulus representation: The dielectric relaxation analysis for the conducting samples can be done effectively through the electrical modulus representation. The values of mean relaxation time τ are obtained for each sample using the peak of $M''(f)$ curve in the entire temperature range. The temperature dependent analysis of mean relaxation time τ using

Arrhenius law is presented in the Figure 4.B.39. The Arrhenius plot of relaxation time τ obtained for our samples have not shown any linear nature therefore the temperature dependent activation energies were calculated using the Equation 4.B.21. The variation of the activation energy as a function of temperature is presented in the Figure 4.B.39.

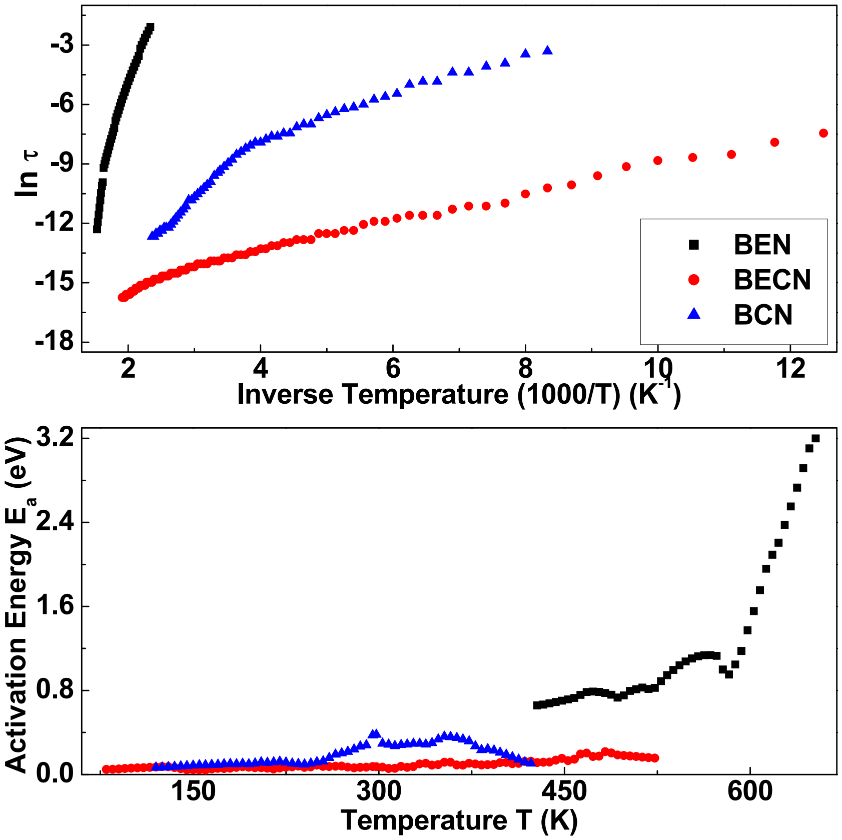

Figure 4.B.39: The Arrhenius plot of relaxation time along with temperature dependent activation energies obtained using electric modulus data for BECN series.

The observed less activation energy values E_a (<0.3 eV) for all the samples in the low temperature region are in agreement with the impedance analyses suggesting presence of singly ionized oxygen vacancies. A systematic enhancement of the activation energy (up to 0.5 eV) for the temperatures from 300 K to 400 K, suggests the development of doubly ionized oxygen vacancies in the samples. The observed higher values (up to 1.2 eV) for BEN suggest comparatively rigid nature of ionized oxygen vacancies. The observed sudden rising nature of activation energy at elevated temperatures suggests possibilities of phase transitions at these temperatures.

Conductivity representation: The analysis of the free charge carriers responsible for the observed high dielectric loss can be done using dc conductivity analysis. The values of dc conductivity are obtained for each sample through extrapolating the low frequency plateau of

$\sigma'(f)$ curve at all temperatures. The temperature dependent analysis of dc conductivity σ_{dc} using Arrhenius law is presented in the Figure 4.B.40 and Figure 4.B.41 respectively for low temperature region and high temperature region. The Arrhenius plot of dc conductivity σ_{dc} obtained for our samples have not shown any linear nature therefore the temperature dependent activation energies were calculated using the Equation 4.B.22. The variation of the activation energy as a function of temperature is presented in the Figure 4.B.40 and Figure 4.B.41 respectively for low temperature region and high temperature region.

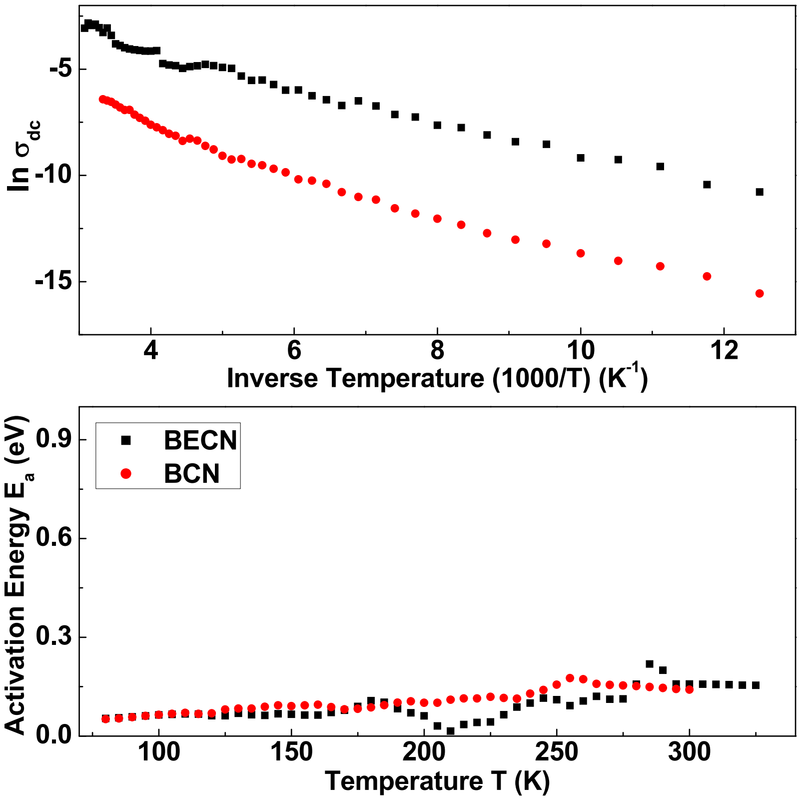

Figure 4.B.40: The Arrhenius plot of dc conductivity along with temperature dependent activation energies for BECN series for bellow room temperature region.

The comparison of dc conductivity values clearly suggests increase in conducting nature of the samples with increasing Co concentration. The observed excess conductivity for Co rich samples is due to dominant additional conductivity originating from doped free electrons as pointed out earlier. Further, the activation energy E_a is found very less (<0.3 eV) in the low temperature region suggests the presence of singly ionized oxygen vacancies [14, 16]. The increased values of E_a up to 0.6 eV suggest development of doubly ionized oxygen vacancies. The observed higher values (up to 1.2 eV) indicate enhanced interaction of relaxing dipoles with the oxygen vacancies at elevated temperatures. The observed peak at 650 K followed by a sharp rise E_a for BEN suggests possibility of structural phase transition.

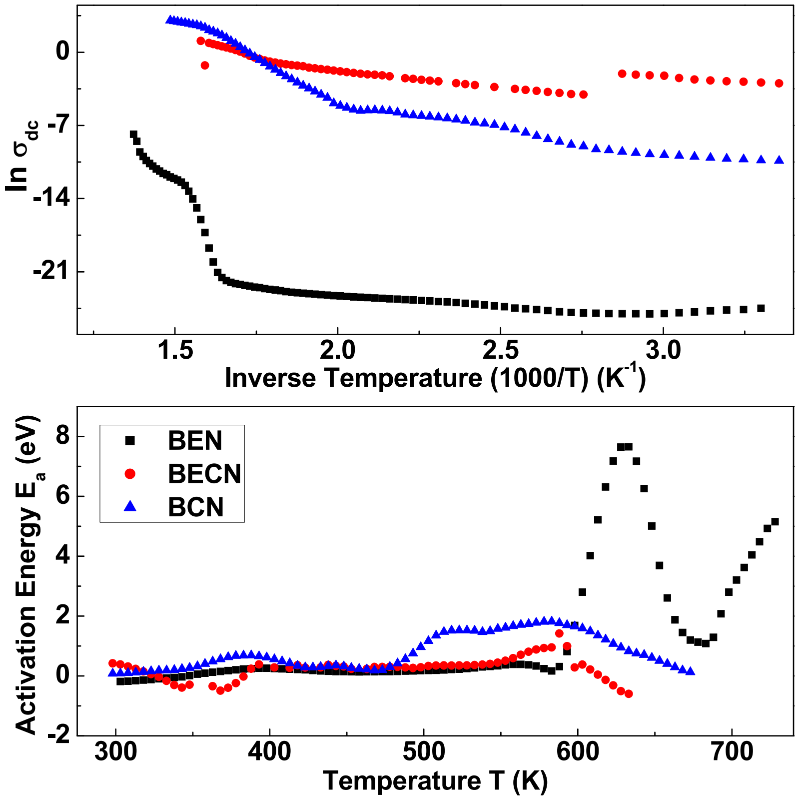

Figure 4.B.41: The Arrhenius plot of dc conductivity along with temperature dependent activation energies for BECN series for above room temperature region.

4.B.2.8 Ac Conductivity Analysis Collectively for All the Samples: ('S' parameter analysis):

The analysis of charge-induced dielectric relaxation can be done effectively using ac conductivity analysis. The detailed analysis of mechanism of conduction is a potential tool to probe the free charge induced giant dielectric constant. In order to analyze the frequency response of conductivity data we applied the modified power law of ac conduction (Equation 4.B.14). The observed three different regions in the ac conductivity data (Figure 4.B.11) viz. (1) low-frequency plateau, (2) mid-frequency dispersion and (3) high-frequency plateau; are explained using modified power law.

The frequency exponent s (obtained using Equation 4.B.15) for the samples with complete substitution of Fe is presented in Figure 4.B.42. The Figure 4.B.43 represents frequency exponent s for the samples of BFCN series. The figures show room temperature values of s parameter with the variation of frequency. The nearly absent or not so distinct dielectric relaxation peak in $\varepsilon''(f)$ curves as well as in $M''(f)$ curves, is now clearly resolved in the form of a peak in s vs. $\ln\omega$ curves (Figures 4.B.42 and 4.B.43). Here the non-zero values of the s_0 parameter (for low frequency plateau region) even at low frequencies observed for BFN and rare earth samples (BGN, BEN and BYN) suggest presence of the low-frequency dispersion (LFD) in the conductivity data (Figure 4.B.11).

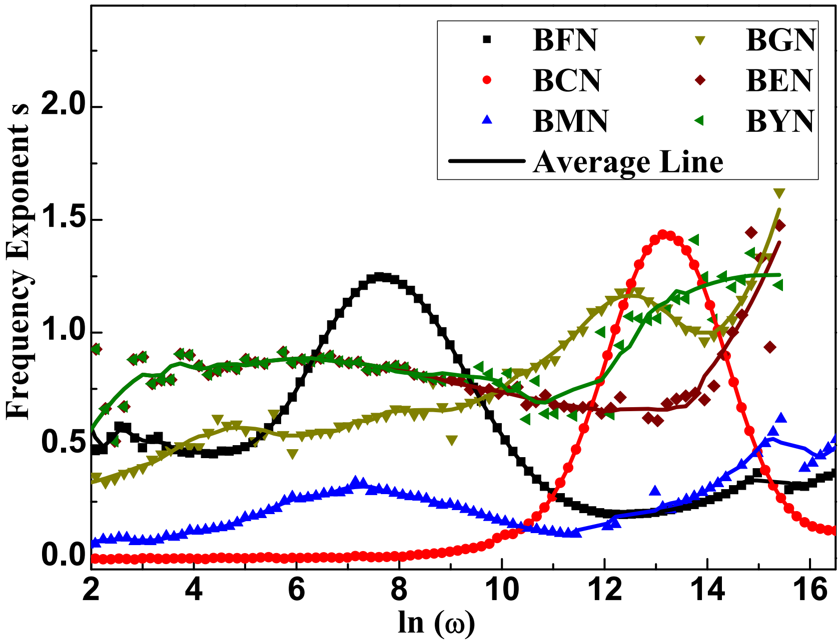

Figure 4.B.42: The room temperature frequency response of frequency exponent s for 100% series.

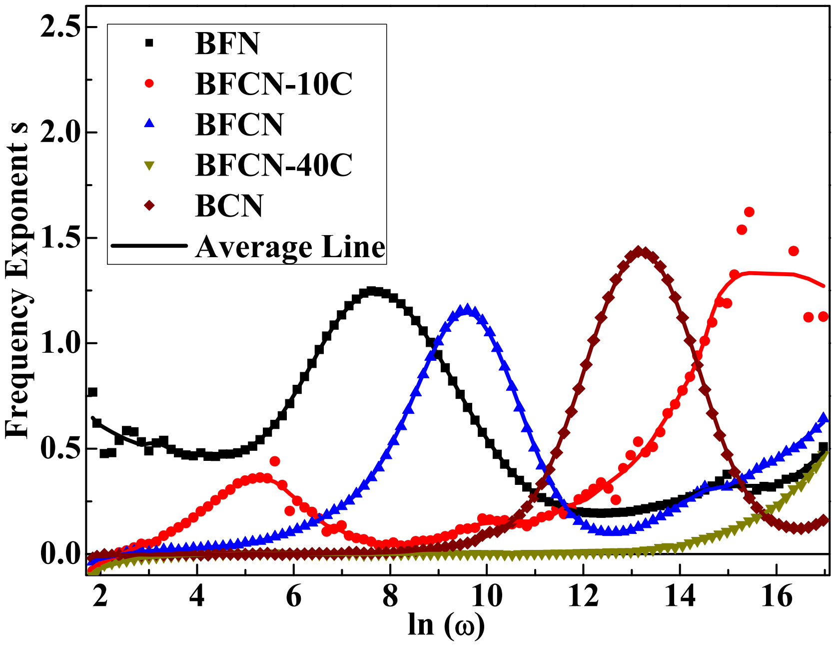

Figure 4.B.43: The room temperature frequency response of frequency exponent s for BFCN series.

This clearly suggests apparent ac conductivity contribution even in the low- frequency region. This low frequency ac conductivity is predominantly due to oxygen vacancy induced electrons. The observed nearly zero values of s_0 parameter at low frequency region for the samples containing Co or Mn suggests that conductivity is independent of frequency. This clearly points at dominant nature of dc conduction over the oxygen vacancies induced ac conduction. Here the additional dc contribution comes from the movement of the doped charges (electrons or holes) originating from the substitution of Fe^{3+} ($3d^5$) by Co^{3+} ($3d^6$) or Mn^{3+} ($3d^4$). Such doped charges produces conductivity due to the back and forth movement between Co/Mn and oxygen vacancy. Thus the observed higher conductivity values for the samples having Co or Mn, is predominantly originating from the charge doping (intrinsic factor) rather than contributions from the oxygen vacancy (extrinsic factor) related conduction. This is further supported by the fact that the likely concentrations of oxygen vacancy will always be less than the concentration of Co^{3+} ($3d^6$) or Mn^{3+} ($3d^4$) in the micro domain.

It is partly reported in our communication [14] that in the mid-frequency region, the s parameter increases rapidly and after showing a peak, it becomes nearly linear at higher frequencies. The observed nature of s in various frequency regions can be explained using the Jump Relaxation Model (JRM) of Funke [29-30], who successfully used it to explain the hopping of ions. In the present case, we have used the same model to explain the hopping of the induced dipoles for the entire s vs. $\ln\omega$ region. It is inferred from the JRM that the constant values of s_0, related to the low-frequency region, results from the long-range translational motion of the conduction carriers (i.e. induced electrons). Here any attempt (by the dipoles) to conduct through the hopping mechanism becomes unsuccessful. As the input ac frequency increases, the rate of successful hopping, indicated by the frequency exponent s, increases. The conductivity in this region corresponds to the short-range translational hopping related to forward-backward jump.

The peak position represents a condition where the number of successful and unsuccessful attempts becomes nearly equal. Beyond this region, the number of carriers (dipoles/oxygen vacancies) available for hopping gradually reaches saturation. This results in a reduction in values of the frequency exponent s. The high-frequency plateau, indicated as s_2, corresponds to a saturation region of charge carriers undergoing relaxational hopping. The shifting of the peak position towards high frequencies in the curves between s vs. $\ln\omega$ is due to the gradual increase of the hopping-length with the gradual increase in cell dimensions resulting from the gradual replacement of Fe by rare earth elements. In this way, through the Jump Relaxation Model we have successfully filtered the contribution of the free doped charges, induced space charges, and the oxygen vacancy induced dipoles in the entire measured frequency range.

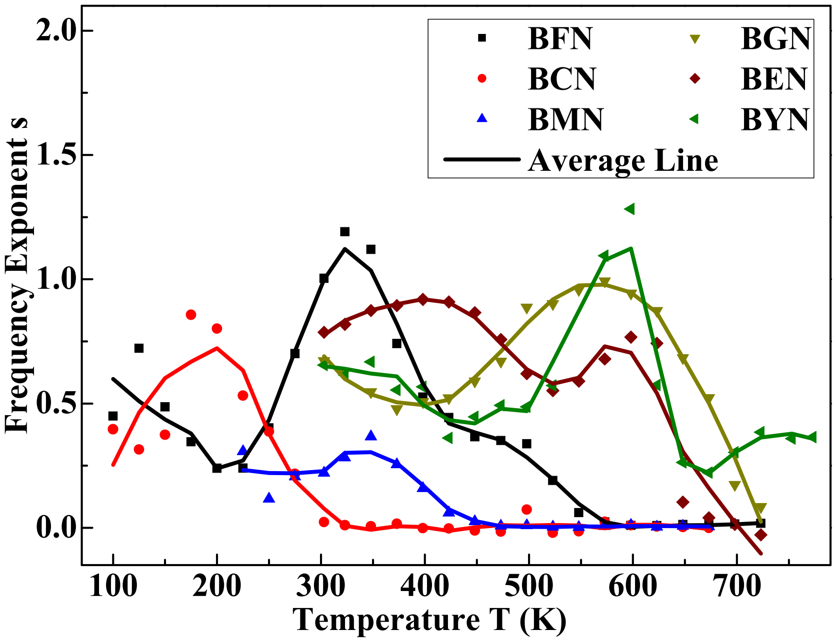

Figure 4.B.44: The temperature dependent values of frequency exponent *s* for 100% series.

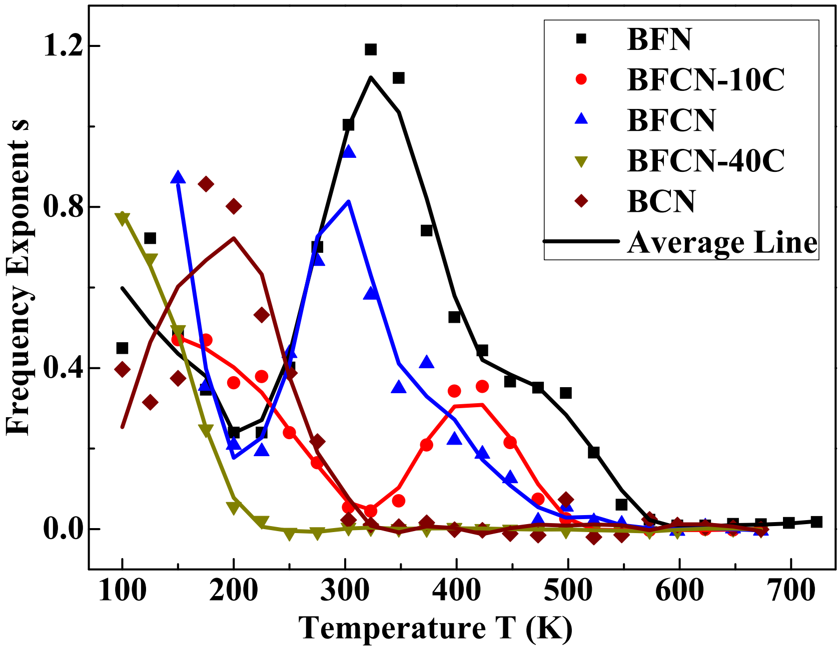

Figure 4.B.45: The temperature dependent values of frequency exponent *s* for BFCN series.

The variations of frequency exponent *s* (at 1 KHz) at different temperatures are presented in Figure 4.B.44 and Figure 4.B.45 respectively for samples of 100% series and BFCN series. The frequency exponent s shows nearly identical downward nature at high temperature region for BFN, BMN and BCN suggest that the conduction process is predominantly due to the correlated barrier hopping (CBH) of electrons. The rare earth doped samples show a dip and then a peak at high temperatures suggests development of polaron in these samples. The observed nature of s parameter in BFCN-10C and BFCN samples suggest polaron tunneling is involved in the conduction process. The sample BFCN-40C is influenced by the hopping of free charges.

4.B. 2. 9 Summary of Dielectric Spectroscopy Analysis:

The observed few values of relaxation time points at the non-dipole type relaxation in these distorted perovskite samples. The values of the activation energy E_a and mean relaxation time indicate that the intrinsic contribution of chemical substitution as well as interaction of free space charges with oxygen vacancies collectively plays a crucial role. The observed high dielectric constant with the dielectric relaxation for the cubic ceramic compounds is predominantly due to the interaction of the oxygen vacancies induced dipoles with the space charges. The suitable iso-valent substitution induced softening of dipolar oscillations as well as charge doping by Co or Mn enhances the above interaction. This, in turn, significantly upgrades the values of the dielectric constant to very high levels (>10^4 times) with a wide operational range of frequency and temperature [14]. Further, the iso-valent substitution of Fe by rare earth elements increases the rigidity of induced dipoles. The interaction of such rigid dipoles along with charge doping enhances the dielectric constant to giant values up to 10^8 (Figure 4.B.6 for BECN and BGCN) with comparatively lower conductivity values.

The crucial conduction mechanism study shows that the dc conductivity contribution originates in different proportions from the oxygen vacancy induced free charges as well as from the introduction of doped electrons owing to the substitution of Fe^{3+} ($3d^5$) by Co^{3+} ($3d^6$). Present analysis of the frequency exponent s based on the Jump Relaxation Model completely bifurcate the conductivity response originating from (1) the free doped charges, (2) the induced space charges, and (3) the oxygen vacancy induced dipoles in the entire measured frequency range. The nonlinear nature of the ac conductivity mainly obeys the hopping mechanism of charge carriers [14]. The rare earth doped samples where the hopping barrier is sufficiently large the conduction carriers follows the quantum mechanical tunneling. Here the large polarons developed near the defect centers are dominant conduction carriers. The conductivity curves for intermediate compositions BFCN-10C and BFCN also demonstrate significant polaron tunneling. The temperature, as well as distortions along the chains of -Nb-Fe/Co-Nb-, decides the percentage contribution of polaron tunneling and/or correlated barrier hopping to the conductivity [25].

4.B.3 Electrical Polarization Studies: P-E loop Analysis :

The P-E loop measurement is one of the necessary characterizations to ensure the ferroelectric nature of the samples. The polarization values for ceramic samples are generally influenced by the conductivity originating from the defects and oxygen vacancies developed during the synthesis of samples [31-32]. The polarization for such ceramic compounds could not attain saturation due to leakage current. In order to analyze the effects of such dc conduction we conducted our measurement at ac bias field. The measurements were done with variation of frequency as well amplitude of the electric bias field. Further, the frequency and field dependent dynamic analysis of PE loop helps to probe the leaky nature of the ferroelectric material [33-35]. The P-E data collected at different frequencies and amplitude of bias field for our few samples are presented in the Figure 4.B.46 and Figure 4.B.47. It is to be noted here that the P-E measurements for the samples containing elements Co or Mn have shown dominant conductivity influence. The P-E loop for conducting BMN sample (Figure 4.B.47) has shown nearly elliptical shape instead of ideal square shape. Further, the samples with substitution of Eu and Y have not shown considerable P-E loop. The P-E loop collected for BEN sample exhibited very narrow loop with significantly small values of polarization (Figure 4.B.47). Therefore, the analysis of P-E loop data was conducted only for the BFN, BGN and BFGN samples. The rest samples are not considered for analysis because of either conducting nature or very narrow and small size of P-E loop.

The effect of frequency and amplitude of the bias field on the P-E data for BFN, BFGN and BGN are presented in the figures. The observed very less values of polarization (<1.2 μC/cm^2) suggest very weak dipolar contribution. It is clear from the shape of the P-E loops that it has not reached to the saturation values of polarization. The conductivity originated from unavoidable defects like oxygen vacancies limit us to apply high field values required to obtain saturation polarization. Further, the observed rounded saturation peaks for BFN suggest comparatively leaky nature of the sample. The observed increment in the size of P-E loop with increase in amplitude of bias field at constant frequency is in agreement with the expected behavior of the samples. The increment in the frequency of bias field at constant amplitude orients the loop towards the bias axis. The loop becomes narrower with reduction in the values

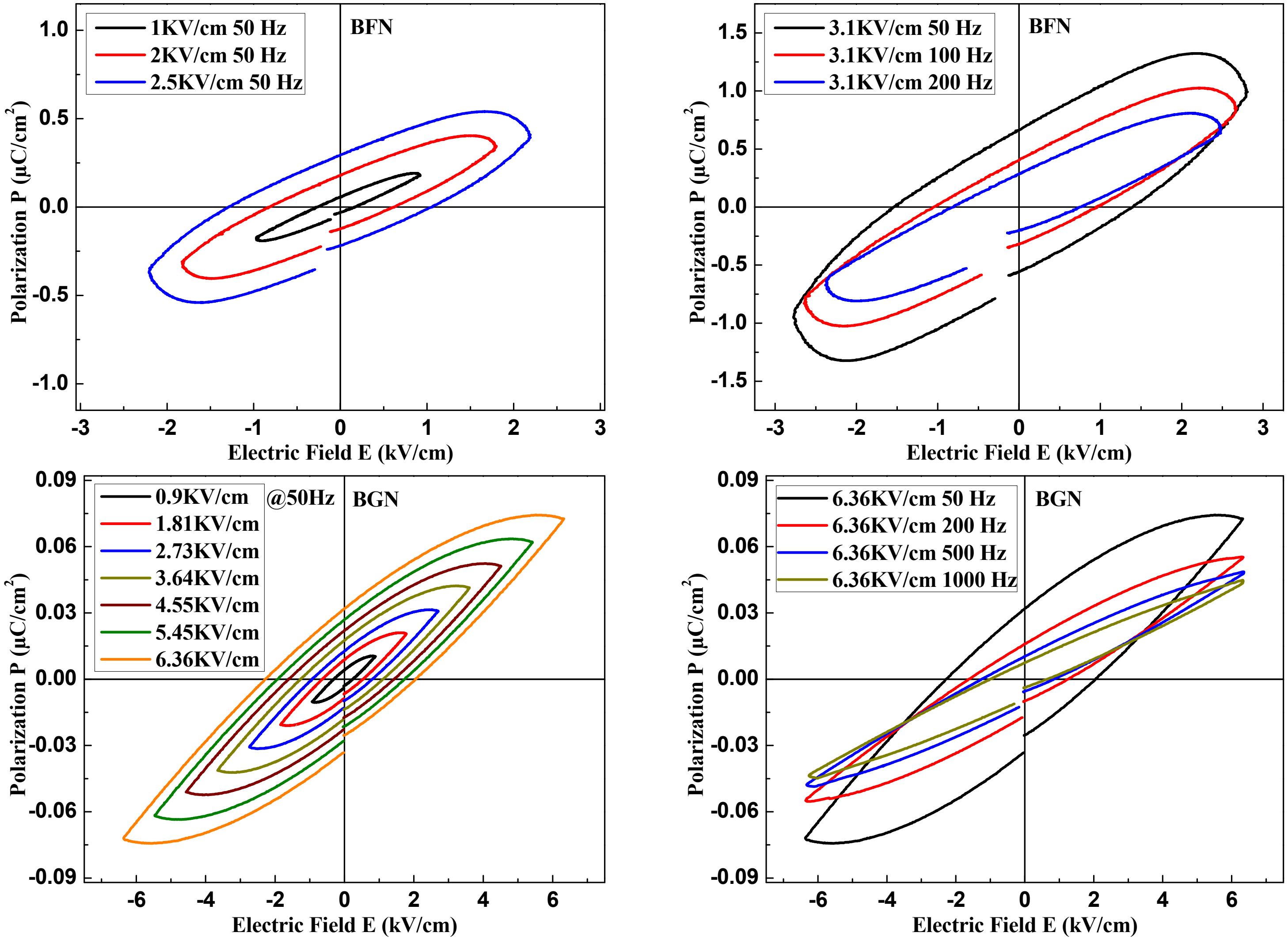

Figure 4.B.46: The P-E data collected at different frequencies and amplitude of bias field for BFN and BGN.

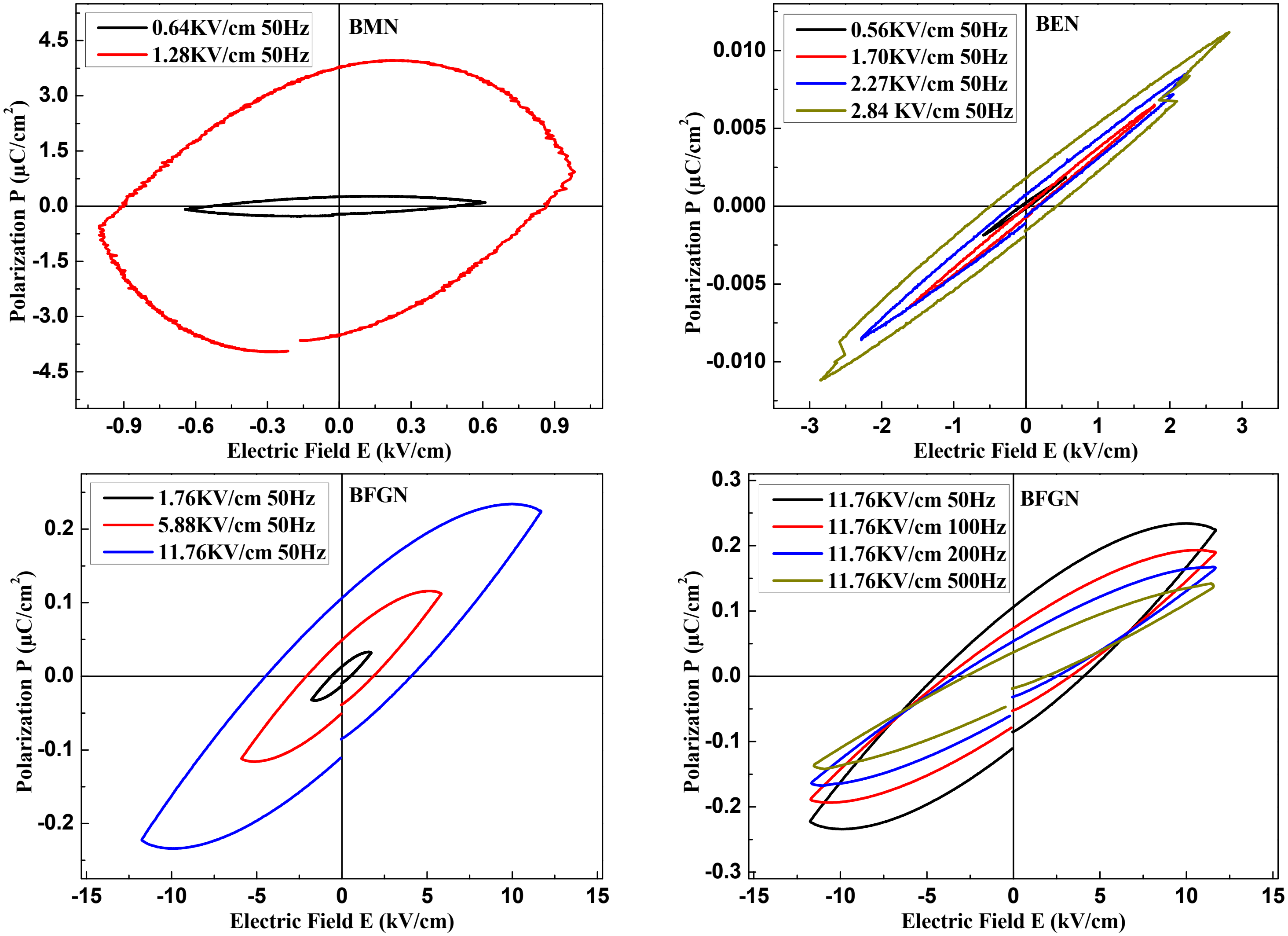

Figure 4.B.47: The leaky loop of BMN and distorted loop of BEN along with the P-E data of BFGN at different frequencies and amplitude of bias field.

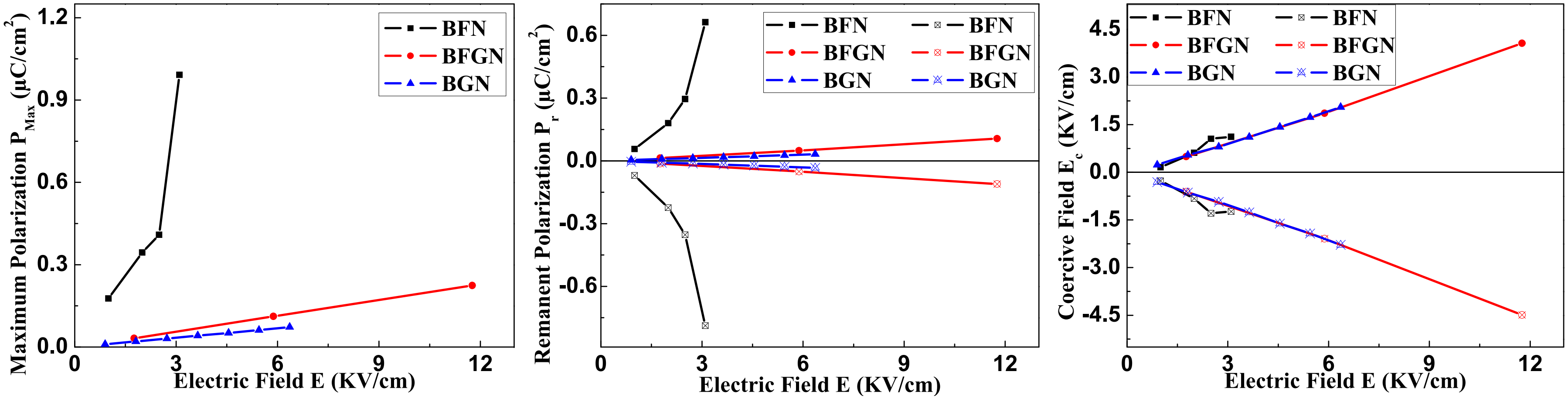

Figure 4.B.48: The maximum polarization $P_{\max}$, Remanent polarization P_r and coercive field E_c with the variation of bias amplitude for BFN, BFGN and BGN. The negative values correspond to the reverse part of the loop.

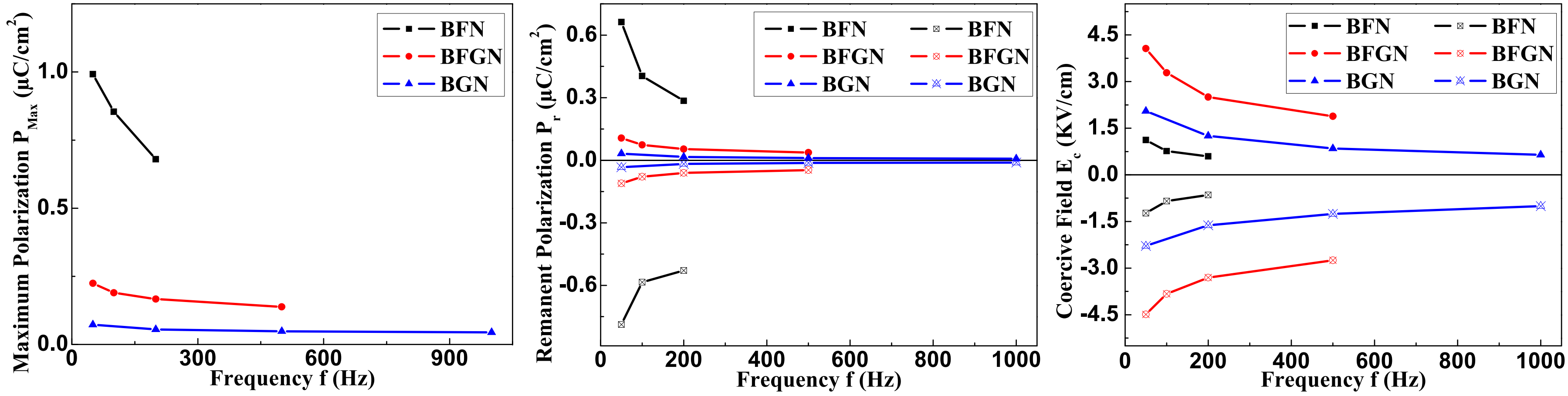

Figure 4.B.49: The maximum polarization $P_{\max}$, Remanent polarization P_r and coercive field E_c with the variation of bias frequency for BFN, BFGN and BGN. The negative values correspond to the reverse part of the loop.

of maximum polarization ($P_{\max}$) and remanent polarization (P_r). The values of maximum polarization ($P_{\max}$), remanent polarization (P_r), reverse remanent polarization ($-P_r$), coercive field (E_c) and reverse coercive field ($-E_c$) with variation of bias amplitude and bias frequency are presented in the Figure 4.B.48 and Figure 4.B.49 respectively. It is evident from both the figures that the overall values of $P_{\max}$ and P_r are higher for the BFN ceramic while lower for the BGN ceramic. The values of $P_{\max}$ and P_r for BFGN ceramic are little higher than the values of BGN. The non-linear variation of $P_{\max}$, P_r and E_c with the bias amplitude observed for the BFN ceramic (Figure 4.B.48) confirm the increased interaction of charge carriers with dipoles. Such an interaction is negligible for BFGN and BGN ceramic. The gradual decrement in the values of $P_{\max}$, P_r and E_c, with increase in the frequency of bias voltage can be noticed from the Figure 4.B.49. The linear increment with bias voltage and gradual decrement with the bias frequency in the values of polarization for BFGN and BGN suggest normal ferroelectric nature of the samples.

4.B. 4 Summary of Optical and Electrical Characterization (Bulk):

The prepared ceramic samples fall under the category of wide band gap semiconductors. In spite of cubic symmetry the samples show high values of dielectric constant. The analysis of the electrical transport suggests the significant contribution of oxygen vacancies induced local lattice distortions in the observed high values of dielectric constant. However, the flexibility or rigidity of the oxygen vacancies along with the doping of free charge carriers plays a crucial role in obtaining the giant level of dielectric constant along with moderate level of conductivity. The leaky nature of P-E loop prevents the possible use of samples in ferroelectric storage applications. At the same time nearly constant values of giant dielectric constant in the wide temperature and frequency range provides an opportunity to use these samples in capacitor industries or sensor devices operating at high frequencies.

References:

1. T. Santhaveesuk, T. Chairuangsri, D. Wongratanaphisan, S. Choopun, J. Micro. Soc. Thailand. **23(1),** 70-74 (2009).
2. E. A. Davis and N. F. Mott, Philos. Mag. **22,** 903 (1970).

3. M. H. Habibi and N. Talebian, Acta Chim. Slov. **52,** 53 (2005).
4. J. Tauc, Mater. Res. Bull. **5,** 721 (1970).
5. F. Zhao, Z. Yue, J. Pei, D. Yang, Z. Gui, and L. Li, Appl. Phys. Lett. **91,** 052903 (2007).
6. I.P. Raevski, S.A. Prosandeev, A.S. Bogatin, M.A. Malitskaya, L. Jastrabik, J. Appl. Phys. **93,** 4130 (2003).
7. Z. Wang, X.M. Chen, L. Ni, and X.Q. Liu, Appl. Phys. Lett. **90,** 022904 (2007).
8. Y.Y. Liu, X.M. Chen, X.Q. Liu, and L. Li, Appl. Phys. Lett. **90,** 192905 (2007).
9. Z. Abdelkafi, N. Abdelmoula, H. Khemakhem, O. Bidault and M. Maglione, J. Appl. Phys. **100,** 114111 (2006).
10. C. Elissalde and J. Ravez, J. Mater. Chem. **11,** 1957 (2001).
11. D.C. Sinclair, T.B. Adams, F.D. Morrison, and A.R. West, Appl. Phys. Lett. **80,** 2153 (2002).
12. M.C. Ferrarelli, T.B. Adams, A. Feteira, D.C. Sinclair, and A.R. West, Appl. Phys. Lett. **89,** 212904 (2006).
13. U. Intatha, S. Eitssayeam, J. Wang and T. Tunkasiri, Curr. Appl. Phys. **10,** 21 (2010).
14. D. D. Shah, P.K. Mehta, M. S. Desai, C. J. Panchal, J. of Alloys and Comp. **509,** 1800 (2011).
15. A. Molak, M. Paluch, S. Pawlus, J. Klimontko, Z. Ujma and I. Gruszka, J. Phys. D: Appl. Phys. **38,** 1450 (2005).
16. C. Ang, Z. Yu and L.E. Cross., Phys. Rev. B. **62,** 228 (2000).
17. S. Bu, E. Shin and G. Park, Appl. Phys. Lett. **73,** 1442 (1998).
18. R.H. Cole, the J. Chem. Phys. **23,** 493 (1955).
19. K.C. Kao, Dielectric phenomena in solids, Elsevier Academic Press, USA, (2004).
20. K.S. Cole and R.H. Cole, J. Chem. Phys. **9,** 341 (1941).
21. J.P. Tiwari, and K. Shahi, Philosophical Magazine. **87:29,** 4475 (2007).
22. S. Mahboob, G. Prasad, G.S. Kumar, J Mater Sci. **42,** 10275 (2007).
23. S. Mollah, K. K. Som, S. Chakraborty, A. K. Bera, S. Chatterjee, S. Banerjee, and B. K. Chaudhuri, Phys. Rev. B. **51,** 17512 (1995).
24. N. Ortega, A. Kumar, P. Bhattacharya, S.B. Majumder, and R.S. Katiyar, Phys. Rev. B. **77,** 14111 (2008).
25. S.R. Elliott, Advances in Physics. **36:2,** 135 (1987).
26. R. Gangopadhyay, A. De, and S. Das, J. Appl. Phys. **87,** 2363 (2000).
27. D. D. Shah and P. K. Mehta, AIP Conf. Proc. **1447,** 1017 (2012).

28. D. D. Shah, N.V. Patel, P. K. Mehta and R. Kumar, The Proceedings of 54th DAE Solid State Physics Symposium, 873 (2009).
29. K. Funke, Prog. Solid St. Chem. **22,** 111 (1993).
30. K. Funke, Journal of Non-Crystalline Solids. **172-174(2),** 1215 (1994).
31. Y. P. Wang, G.L. Yuan, X.Y. Chen, J.-M. Liu, Z.G. Liu, J. Phys. D: Appl. Phys. **39,** 2019 (2006).
32. A. K. Pradhan, K. zhang, D. Hunter, J.B. Dadson, G.B. Loutts, P. Bhattacharya, R. Katiyar, J. Zhang, D. J. Sellmer, U. N. Roy, Y. Cui, A. Burger, J. Appl. Phys. **97,** 093903 (2005).
33. J. M. Liu, L. C. Yu, G. L. Yuan, Y. Yang, H. L. W. Chan, Z.G. Liu, Microele. Engg. **66,** 798 (2003).
34. J.F. Scott, Thin Film Ferroelectric Materials and Devices Edited by R. Ramesh, Kluwer, Boston, 115 (1997).
35. S. Li, W. Cao, L.E. Cross, J. Appl. Phys. **69,** 7219 (1991).

CHAPTER 4C

Results and Discussion (Bulk): Magnetic Characterization

(Magnetic Hysteresis and Magnetization Studies of Bulk Samples)

In order to probe the multiferroic properties of the samples magnetic studies were carried out and analyzed in detail. The results of magnetic hysteresis studies and temperature dependent magnetization studies are discussed here. The theoretical modeling of M-H and M-T data is presented to probe the observed magnetic interaction. The reason for observed behavior is also been discussed.

In recent scenario the compounds exhibiting multiferroic properties have gathered more attention. The co-existence of ferroelectric as well as ferromagnetic properties in a single compound is defined as multiferroic property. The studies of multiferroic compounds are of much more importance due to their wide industrial applications. In the present work, possibilities of magnetic nature of our samples have been investigated using magnetization studies of our samples. The change in the magnetic properties of BFN on substitution of Fe by Co and Gd is presented here. We have carried out the magnetic characterization for five samples; viz., BFN, BFCN, BCN, BFGN and BGN only. The measurement of magnetic moment is done with the variation of magnetizing field as well as with the variation of temperature.

4.C.1 Magnetic Field Dependent Magnetization Studies: Magnetic Hysteresis (M-H Loop):

The measurement of magnetic moment (M) with variation of magnetizing field (H), in both forward (+ve) and reverse (-ve) direction results in a curve, generally known as magnetic hysteresis loop. Such a loop is likely to provide information regarding type of magnetism available in the compound. The shape of M-H loop along with the values of magnetic moment helps in identification of magnetic nature of the sample. Here, the study of magnetic hysteresis loop is carried out in two series of samples:

4.C.1.1 Magnetic Hysteresis Studies of BFCN Series: $[Ba(Fe_{0.5-X}Co_XNb_{0.5})O_3]$ where X=0, 0.25, 0.50:

The samples of this series are prepared by substitution of Fe by Co in the BFN compound. It is known that both Fe and Co show ferromagnetism in the pure metallic form. Though the alloys, oxides and salts of these elements deviates from the ferromagnetism and exhibit either antiferromagnetism or ferrimagnetisms. In the present case the compounds under investigation are complex ceramic oxides containing Fe and/or Co. Therefore the magnetic properties of these compounds are expected to be influenced by the mutual interactions along with the spin of unpaired electrons. The magnetic hysteresis loop of these samples collected at two different temperatures; 5 K and 300 K are presented in the Figure 4.C.1 and Figure 4.C.2 respectively.

It is clearly visible from the Figures 4.C.1 that the BFN, BFCN and BCN compounds exhibit a narrow opening in the M-H loop at 5 K. The inset clearly magnifies such narrow opening of the loops justifying presence of ferromagnetism at this temperature. Persistent narrow opening of the M-H loop is observed even up to 300 K for the BFN ceramic (Figure 4.C.2) suggesting presence of ferromagnetism even at room temperature. Contrary to that BFCN and BCN samples now fail to show such narrow opening of loop at 300 K.

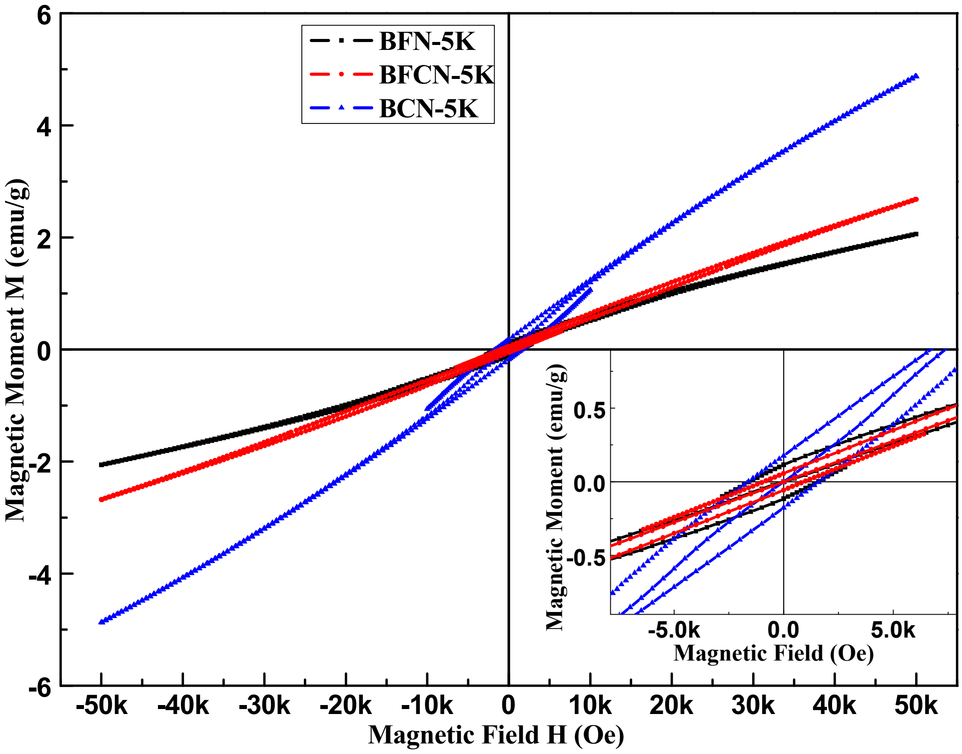

Figure 4.C.1: The magnetic hysteresis loop for BFN, BFCN and BCN at 5 K.

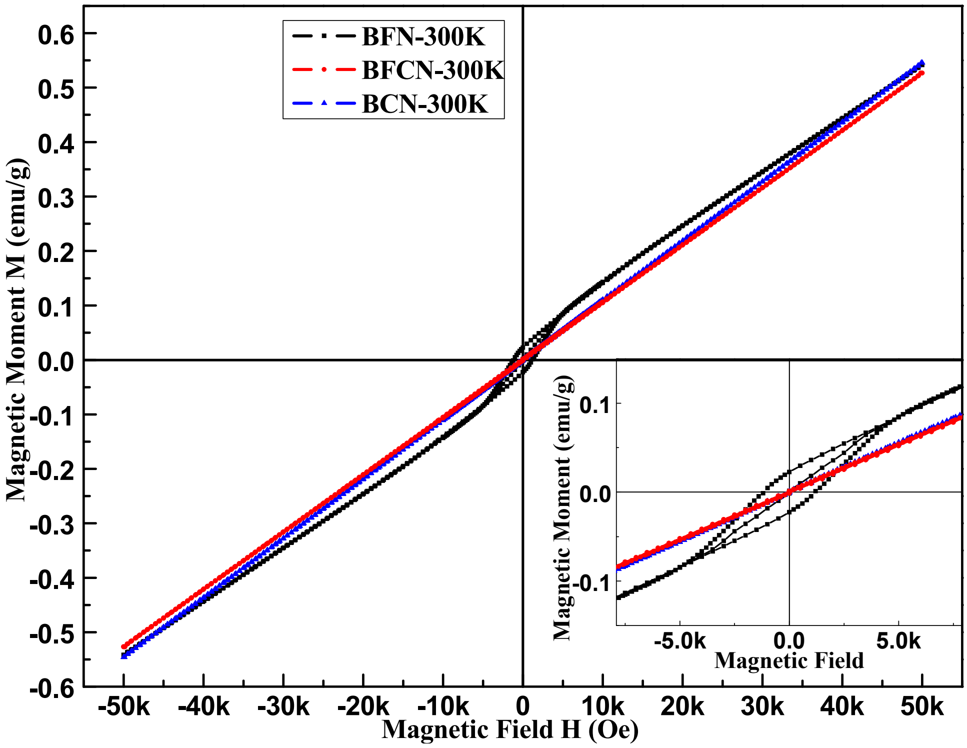

Figure 4.C.2: The magnetic hysteresis loop for BFN, BFCN and BCN at 300 K.

Further, the observed low values of magnetic moments (M in emu/g) for all these samples at both temperatures suggest paramagnetic or antiferromagnetic interactions in the compounds. In order to investigate the observed contradicting magnetic nature of the samples we calculated the magnetic moment of the samples related to the paramagnetic state using the existing theories.

According to the Langevin theory of paramagnetism (Classical theory) the Magnetic moment M of any substance is given by the following equation (Equation 4.C.1.)[1]:

$$M = M_0\left[\coth a - \frac{1}{a}\right] \qquad \text{…… (4.C.1)}$$

Where, $M_0 = N\mu_{eff}$ = Maximum possible moment

$a = \frac{\mu_{eff}H}{kT} = \frac{\text{Magnetic interaction energy}}{\text{Thermal energy}}$

μ_{eff} = Maximum moment of each magnetic atom

H = Magnetizing field

k = Boltzmann constant, T = Absolute temperature

N = Total number of magnetic atoms $= \frac{m \cdot N_A}{M_W}$,

In the present case each formula unit of BFN/BFCN/BCN (i.e. $Ba(Fe_{0.5}Nb_{0.5})O_3$ for BFN) contributes half magnetic atom,

$\therefore N = \frac{m \cdot N_A}{2 \cdot M_W}$

m = Mass of the sample to be measured

N_A = Avogadro number

M_W = Molecular weight

$\mu_{eff} = g\sqrt{J(J+1)}\mu_B$ Here, μ_B = Bohr magneton = 9.27×10^{-21} emu (or erg/Oe).

$\mu_{eff} = g\sqrt{(L+S)\left[(L+S)+1\right]}\mu_B$

The orbital spin contributions for the oxides of transition metals are found generally quenched results in net zero values of orbital quantum number with $g = 2$.

$\therefore \mu_{eff} = 2\sqrt{S(S+1)}\mu_B$

But $S =$ spin number $= n \cdot s = {}^{n}\!/_{2}$ Here, n is number of unpaired electrons and $s = {}^{1}\!/_{2}$ is spin of electron.

$$\therefore \mu_{eff} = \sqrt{n(n+2)}\,\mu_B$$

For the case of BFN, BFCN and BCN the values of n are 5, 4.499 and 4 respectively.

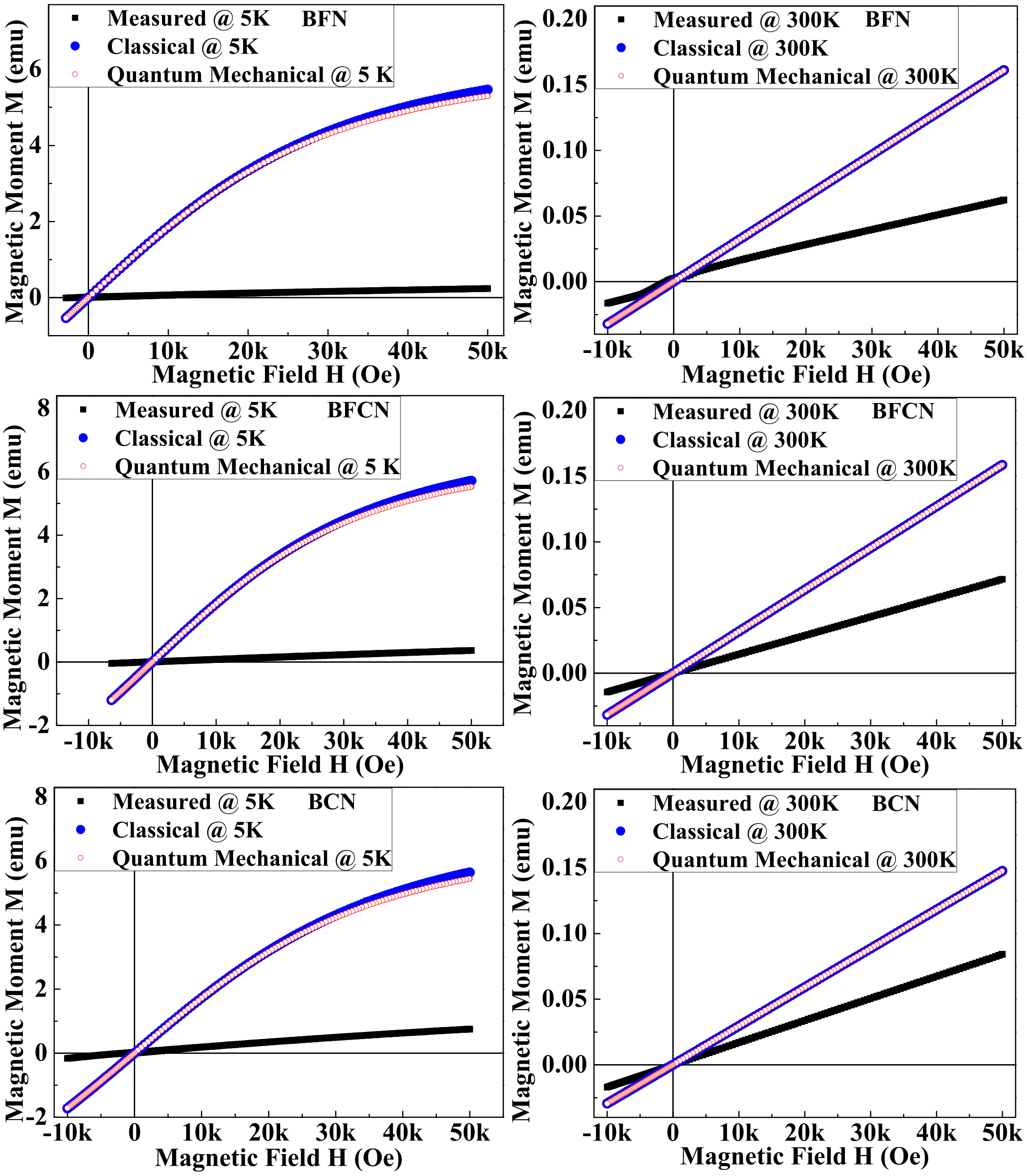

Figure 4.C.3: The measured magnetic moment M for BFN, BFCN and BCN along with theoretically calculated M (paramagnetic state) at 5 K and 300 K.

The quantum mechanical theory of magnetic moment deals with the quantization of spin orientation. The space quantization is applied to the directions of spin resulted in to the modified equation of magnetic moment given by the following equation (Equation 4.C.2)[1]:

$$M = M_0 \left[\frac{2S+1}{2S} \coth \left\{ \left(\frac{2S+1}{2S} \right) a' \right\} - \frac{1}{2S} \coth \left(\frac{a'}{2S} \right) \right] \qquad \text{…… (4.C.2)}$$

Where, $M_0 = N\mu_H = NgJ\mu_B =$ Maximum possible moment

$a' = \frac{\mu_H H}{kT} = \frac{gJ\mu_B H}{kT}$

$\mu_H = gJ\mu_B =$ Component of μ_{eff} in the direction of field

$\mu_B =$ Bohr magneton = 9.27×10^{-21} emu (or erg/Oe).

$N =$ Total number of magnetic atoms $= \frac{m \cdot N_A}{M_W}$, in the present case $N = \frac{m \cdot N_A}{2 \cdot M_W}$ as discussed earlier

$m =$ Mass of the sample to be measured

$N_A =$ Avogadro number

$M_W =$ Molecular weight

$J = L + S = 0 + S = S = s \cdot n = n/2$ and $g = 2$ for spin only contribution

In the present case values of n are 5, 4.499 and 4 for BFN, BFCN and BCN respectively.

The values of magnetic moment (M in emu) calculated using both classical and quantum mechanical theories corresponding to the paramagnetic state of BFN, BFCN and BCN are presented in the Figure 4.C.3 along with the measured experimental data at both the temperatures. The clear deviation of experimental data from the theoretical curves is observed at both temperatures. The observed experimental values of magnetic moment are found quite lower than the calculated moment related to the paramagnetism. The above results clearly suggest that the samples exhibit antiferromagnetic ordering at both the temperatures. The amount of deviation of experimental data from the theoretical values decreases with increasing concentration of Co. This fact points at decreased strength of antiferromagnetic ordering with increment in Co concentration. Further, the graph between the magnetic moment (M) and the temperature normalization of the magnetizing field (H/T) is a quite effective tool to investigate the paramagnetic state of the compounds [1]. These curves (M→H/T) are generally known as isothermal M-H plots. Such isothermal M-H plots obtained at 5 K and 300 K for BFN, BFCN and BCN are presented in the Figure 4.C.4.

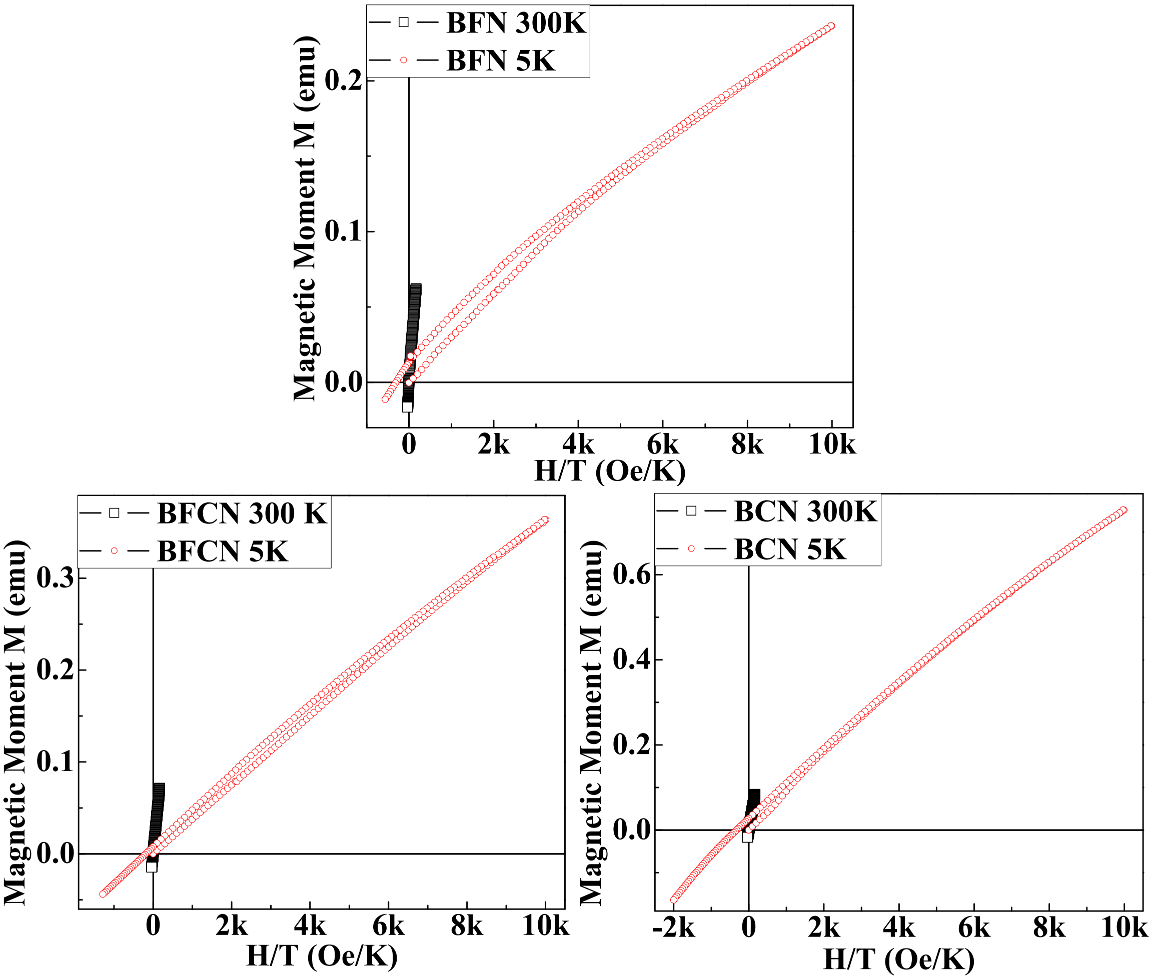

Figure 4.C.4: The isothermal M-H plots for BFN, BFCN and BCN at 5 K and 300 K.

The clear separations between both the curves are observed for all the samples. The values of magnetic moment for low temperature isothermal M-H plots are found to be less than the values of high temperature isothermal M-H plots. They point to the increased antiferromagnetic interaction at lower temperatures.

The observed antiferromagnetism in BFN, BFCN and BCN is originated from the antiparallel alignment of the spin related to the ordered magnetic structure. The BFN is a double perovskite ceramic oxide with Ba occupying corner positions of the cube and Fe/Nb located at the centre of oxygen octahedron placed inside the cube. Here in order to balance the over all charge of the unit cell the strong magnetic ion Fe^{3+} and strong electric ion Nb^{5+} occupy places in ordered manner. The partial negative unit cell of $BaFeO_3$ (containing Fe^{3+} at the centre) is surrounded by the six partially positive unit cells of $BaNbO_3$ (containing Nb^{5+} at the centre) along all the six axial directions in order to neutralize the compound. Such an ordered arrangement represents a –Fe–Nb–Fe– chain. The partial substitution of Fe by Co is also considered to be an ordered system containing chains of –Fe–Nb–Co–Nb–Fe– since the XRD pattern has not distinguished the two different phases related to two different chains of –Fe–Nb–Fe– and –Co–Nb–Co– [2]. As the spin related to each transition metal element represents a lattice point of a magnetic structure. The spin of the nearest neighbor lattice point in the six axial directions are found to align predominantly in the antiparallel direction. This results in observed antiferromagnetism of the compounds. In addition, the observed weak ferromagnetism related to the narrow opening of the M-H loop suggests small amount of ferromagnetic ordering inside a matrix of antiferromagnetic ordered structure. Such a dual property of compounds suggest at the spin glass like behavior of samples [3-5]. This needs further detailed investigation through susceptibility measurements as a function of temperature and field.

4.C.1.2 Magnetic Hysteresis Studies of BFGN Series: $[Ba(Fe_{0.5-X}Gd_XNb_{0.5})O_3]$ where X=0, 0.25, 0.50:

There exists a possibility of samples, where the B-site element Fe is gradually substituted by 4f rare earth element Gd, to show magnetic behavior due to the spin of unpaired electrons available at the 4f orbital [1]. Here the contribution from the orbital spin component could also plays a significant role. The unpaired electrons of inner 4f shell are shielded by the surrounding crystalline field results in unquenched orbital magnetic moment [1]. The nonzero component of orbital magnetic moment interacts with the spin and exhibit high values of magnetic moment for the compounds of these elements. The Gd is exhibiting ferromagnetic behavior just bellow the room temperature ($T_C = 17\,^0C$) [1]. Though, the oxides of the rare earth elements generally exhibit paramagnetism with high values of magnetic moment per atom [1].

The magnetic hysteresis loop of these samples collected at two different temperatures; 5 K and 300 K are presented in the Figure 4.C.5 and Figure 4.C.6 respectively. In contrast to the samples of previous series, the samples of this series (BFGN and BGN) have not shown any opening of M-H loop at both the temperatures. The opening of M-H loop exhibited only by the BFN sample and absence of such opening in BFGN and BGN sample is identified clearly through the magnified view of the low field region presented in the inset of Figure 4.C.5 and Figure 4.C.6. This observed nature of M-H loop points at absence of ferromagnetism in BFGN and BGN samples. In addition the observed less values of magnetic moment (M in emu/g) also support the absence of ferromagnetic interaction and suggest the possibilities of paramagnetic or antiferromagnetic ordering in the compounds.

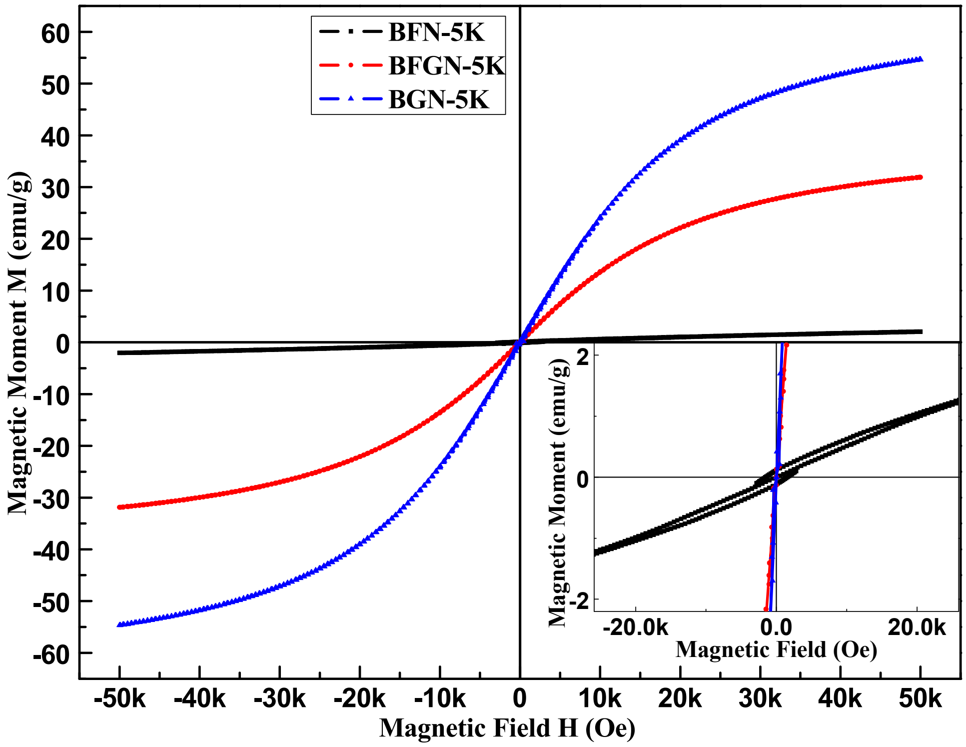

Figure 4.C.5: The magnetic hysteresis loop for BFN, BFGN and BGN at 5 K.

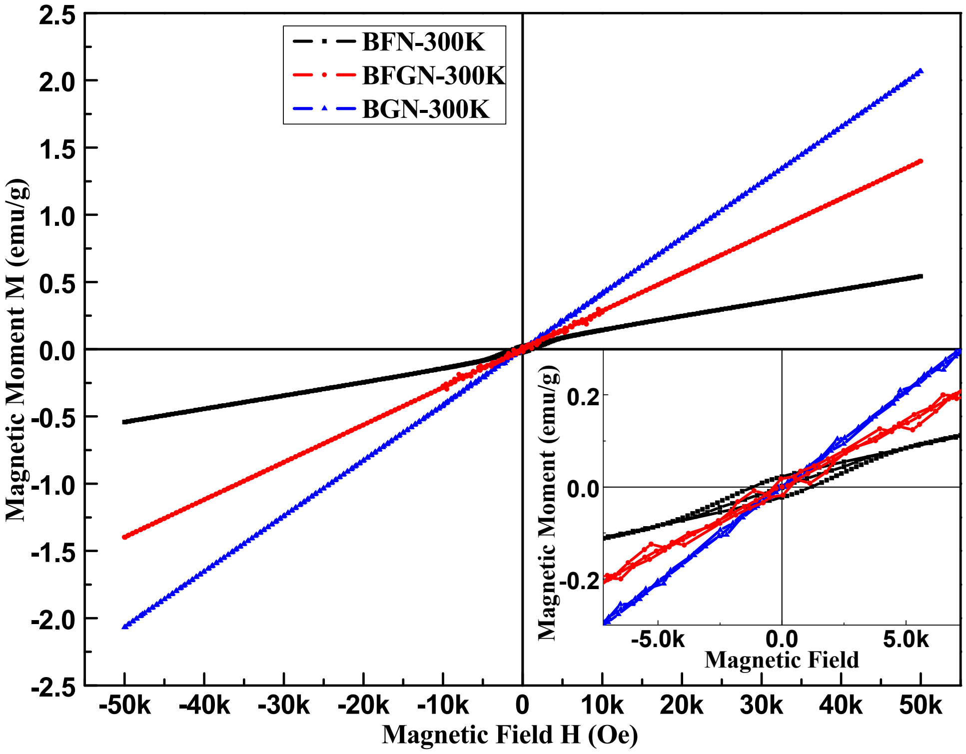

Figure 4.C.6: The magnetic hysteresis loop for BFN, BFGN and BGN at 300 K.

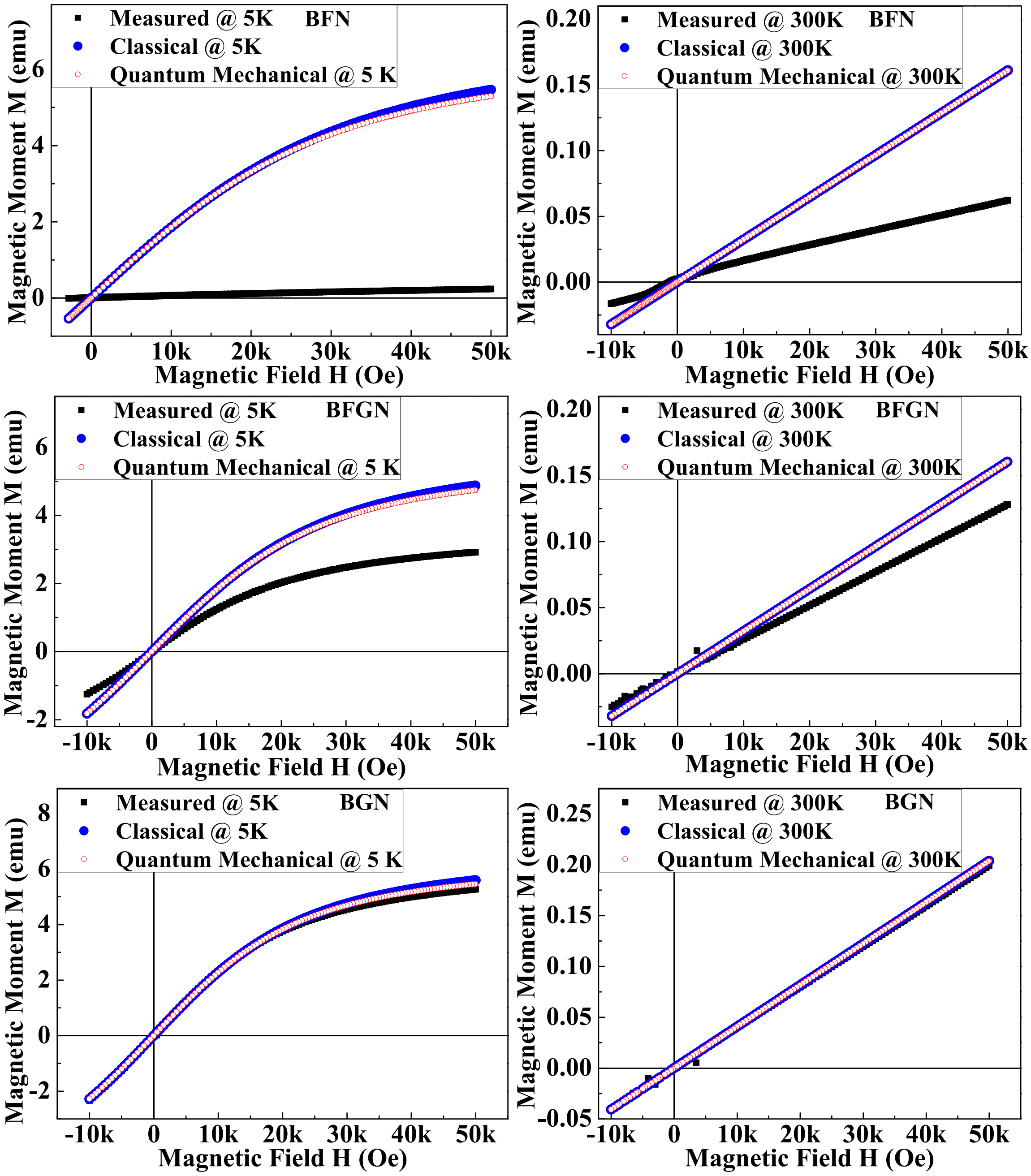

Figure 4.C.7: The measured magnetic moment M for BFN, BFGN and BGN along with theoretically calculated M (paramagnetic state) at 5 K and 300 K.

The further investigation of observed M-H curve of the samples is done by comparing it with the theoretically calculated magnetic moment values. The magnetic moments of the samples are calculated at both the temperatures using the classical theory of paramagnetism (Langevin theory of paramagnetism) presented by Equation 4.C.1 and quantum mechanical theory of paramagnetism presented by Equation 4.C.2. In the present case values of n are 5, 5.998 and 7 for BFN, BFGN and BGN respectively. The calculated values of magnetic moment (M in emu) corresponding to the paramagnetic state of BFN, BFGN and BGN are presented in the Figure 4.C.7 along with the measured experimental data at both the temperatures.

The clear deviation observed for the BFN compound is attributed to the presence of small amount of ferromagnetism as discussed in the earlier section. On the other hand for the compound BGN (complete substitution of Fe by Gd in BFN) the experimental values of magnetic moment are found nearly similar to that of the theoretically obtained curves at both the temperatures. This observed agreement between experimental values and theoretical curves suggests paramagnetic nature of BGN in the entire temperature range. The observed marginal difference in the experimental and theoretical values may be due to consideration of spin only contribution resulted through the quenched orbital moment. The possibilities of unquenched deep orbital moment originated from the screening through surrounding crystalline field can not be neglected for compounds having rare earth elements. The observed deviation of magnetic moment for the BFGN compound from its theoretically calculated values, suggests presence of antiferromagnetic ordering in these compounds. The values of magnetic moment for BFGN compound lie in between the values of BFN and BGN compound. The comparison of M-H curves at both the temperatures suggests that the magnetic moment of BFGN compound represents average sum of the BFN and BGN curves. It clearly suggest co-existence of two different type of magnetic interaction in a single compound, viz., antiferromagnetism related to the BFN ceramic and paramagnetism related to the BGN ceramic. The possibility of such co-existing different magnetic regions is further supported by the observed distinct phases (related to BFN and BGN) in the X-ray diffraction studies of this compound.

Further, the observed paramagnetism can be effectively probed through the M→H/T curves, generally known as the isothermal M-H plots. The isothermal M-H plots obtained at 5 K and 300 K for BFN, BFGN and BGN are presented in the Figure 4.C.8. The both low temperature (5 K) and room temperature (300 K) isothermal curves found superimposed on each other for BFGN and BGN compound. This clearly suggests paramagnetic behavior of these compounds. The observed antiferromagnetism in BFN is originated from the antiparallel alignment of the spin related to the ordered magnetic structure as suggested earlier. On the other hand magnetic interaction is not observed for BGN compound. The paramagnetic nature of BGN compound is supported by the general observation that the oxides of rare earth elements exhibit paramagnetism [1]. The observed weak ferromagnetic ordering inside a matrix of antiferromagnetic ordered structure for the compounds of BFCN series and paramagnetic nature of BGN ceramic needed further detailed investigation through susceptibility measurements carried out with variation of temperature and field.

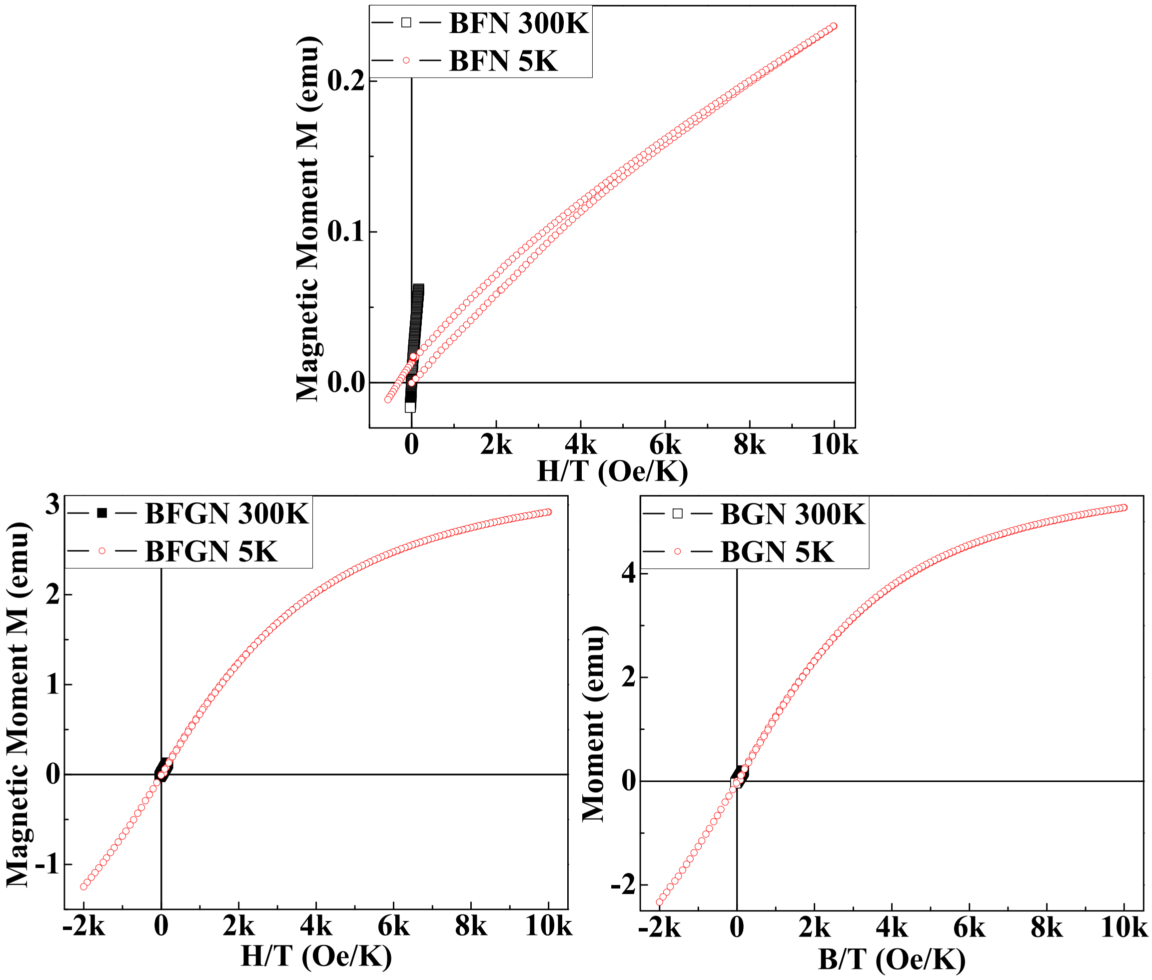

Figure 4.C.8: The isothermal M-H plots for BFN, BFGN and BGN at 5 K and 300 K.

4.C. 2 Temperature Dependent Magnetization Studies: (M-T Curves):

The temperature dependent magnetization data collected with two different modes of measurement; viz., zero field cooled (ZFC) mode and field cooled (FC) mode are likely to provide fruitful information regarding any magnetic transitions. The temperature dependent magnetization curves (M-T curves) of all five samples are collected in the temperature range of 5K to 300 K with ZFC-FC mode. Such M-T curves are measured at two different values of magnetizing field; low field of 500 Oe and high field of 10000 Oe. The Figure 4.C.9, Figure 4.C.10, Figure 4.C.11, Figure 4.C.12 and Figure 4.C.13 show such M-T curves collected for the BFN, BFCN, BCN, BFGN and BGN samples, respectively. The left axis of magnetic moment represents ZFC-FC curves collected at low values of field (500 Oe) while the right axis of magnetic moment represents ZFC-FC curves collected at high values of field (10000 Oe). The observed clear separation between ZFC-FC curves in the entire temperature range collected at 500 Oe for BFN sample suggest the dependence of susceptibility on the thermal history of the sample. The observed separation disappears in the ZFC-FC curves collected at the higher values of magnetizing field up to 10000 Oe.

In general the magnetization data are recorded during warming cycle of the sample, i.e., from low temperatures to high temperatures. But in the present case we have found no deviation in the data even while cooling the sample in field cooled mode (FCC). The observed nature of magnetization data for BFN sample suggests spin-glass like magnetic behavior of the compound [6]. The temperature below which such a separation between ZFC-FC curves be observed, known as freezing temperature T_g. The freezing of magnetic spin bellow this temperature results in spin-glass or cluster glass state. The presence of spin-glass like magnetic structure is further supported by the observed unsaturated M-H curve with narrow opening at low field region which is typical behavior of spin glass [7]. It is to be noted here that other samples of the series have not shown such a separation between ZFC-FC curves suggesting absence of spin glass like behavior in each of them.

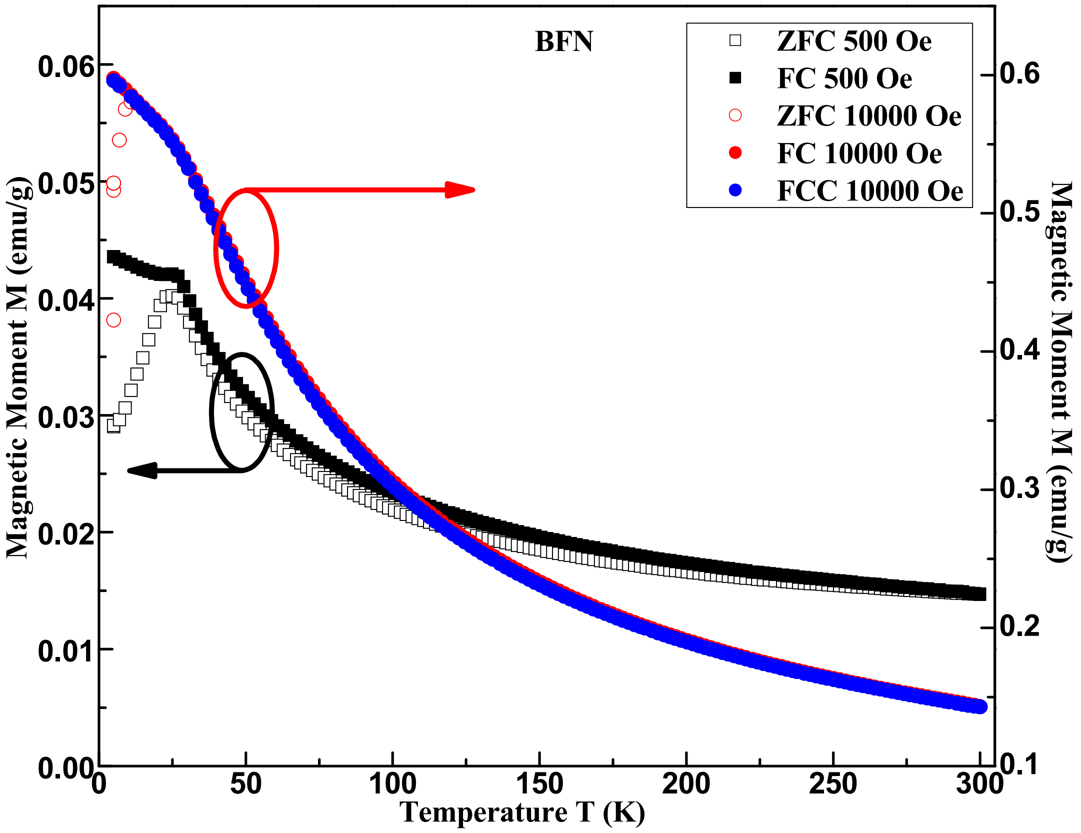

Figure 4.C.9: The temperature dependent magnetization data with ZFC-FC mode for BFN at 500 Oe (left axis) and 10000 Oe (right axis).

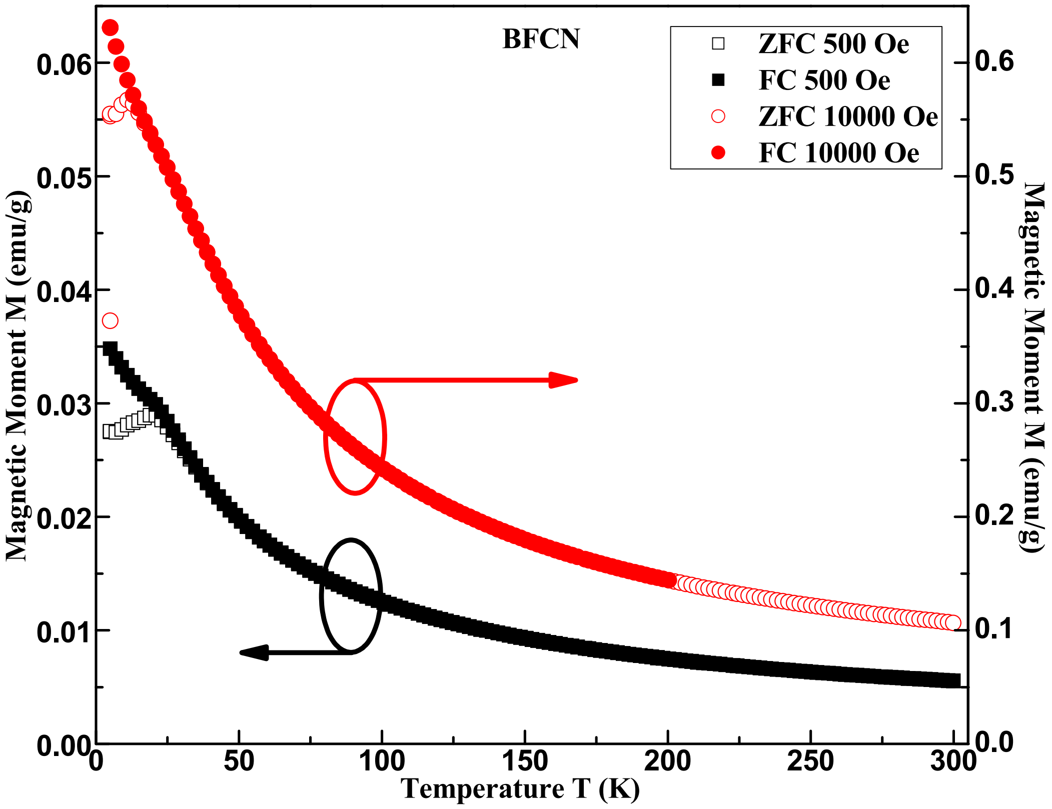

Figure 4.C.10: The temperature dependent magnetization data with ZFC-FC mode for BFCN at 500 Oe (left axis) and 10000 Oe (right axis).

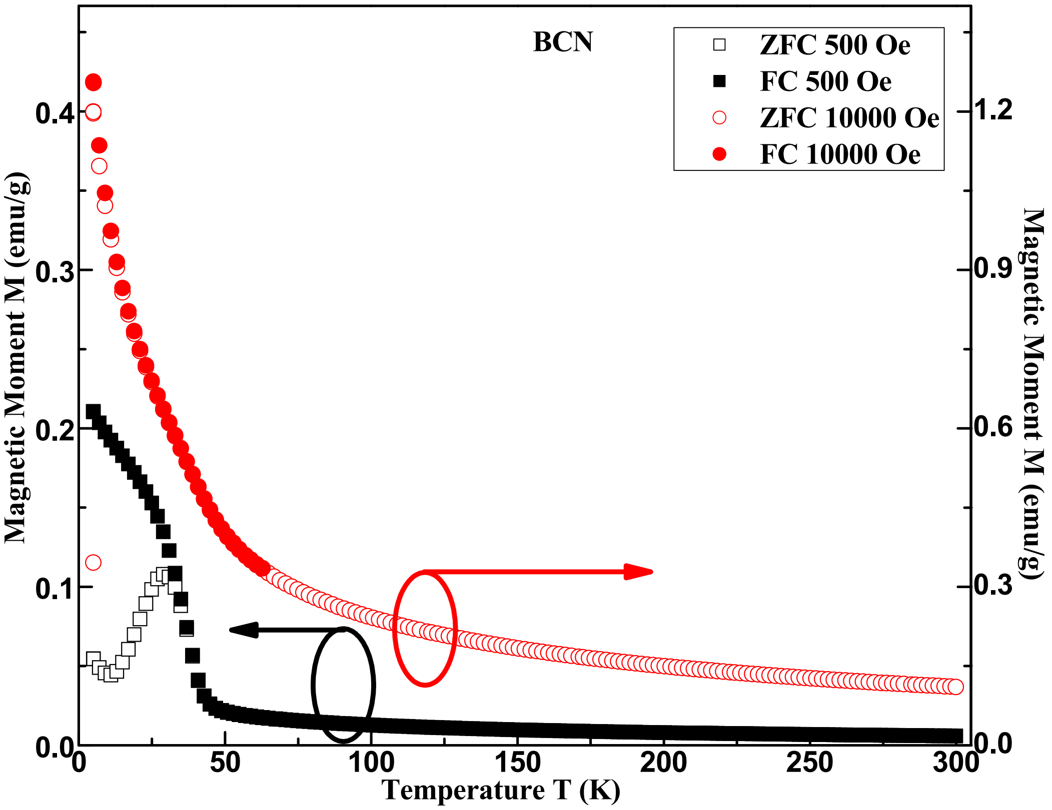

Figure 4.C.11: The temperature dependent magnetization data with ZFC-FC mode for BCN at 500 Oe (left axis) and 10000 Oe (right axis).

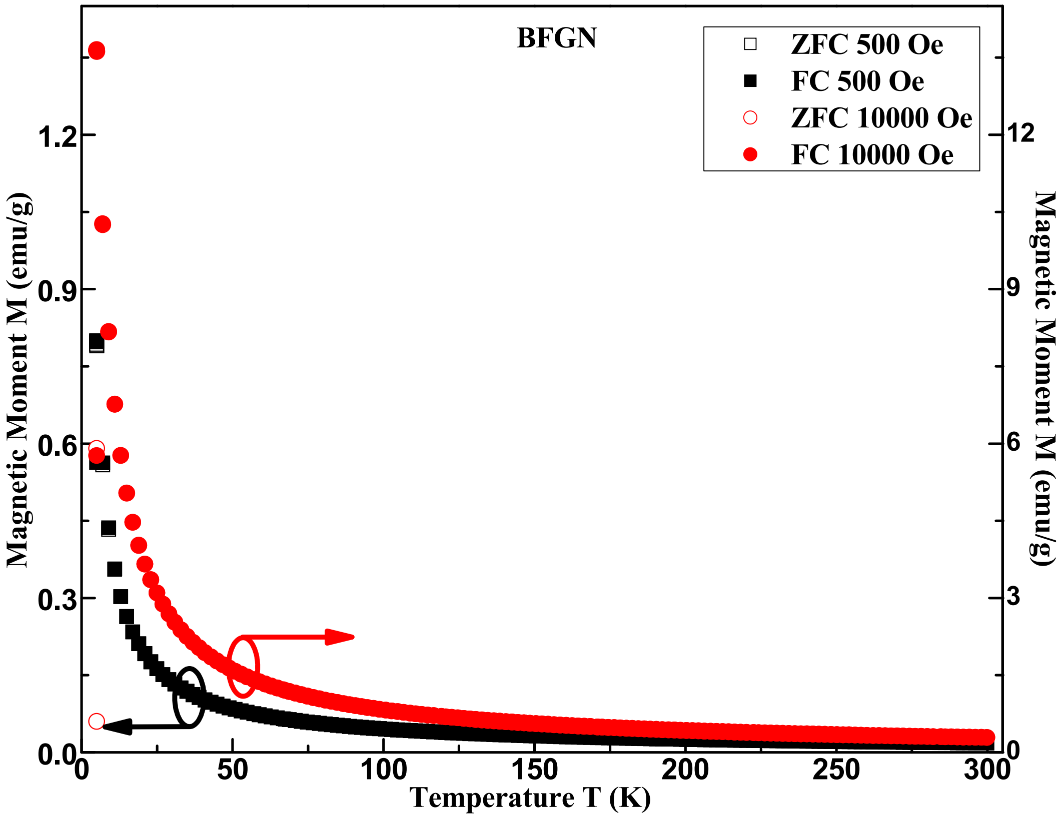

Figure 4.C.12: The temperature dependent magnetization data with ZFC-FC mode for BFGN at 500 Oe (left axis) and 10000 Oe (right axis)

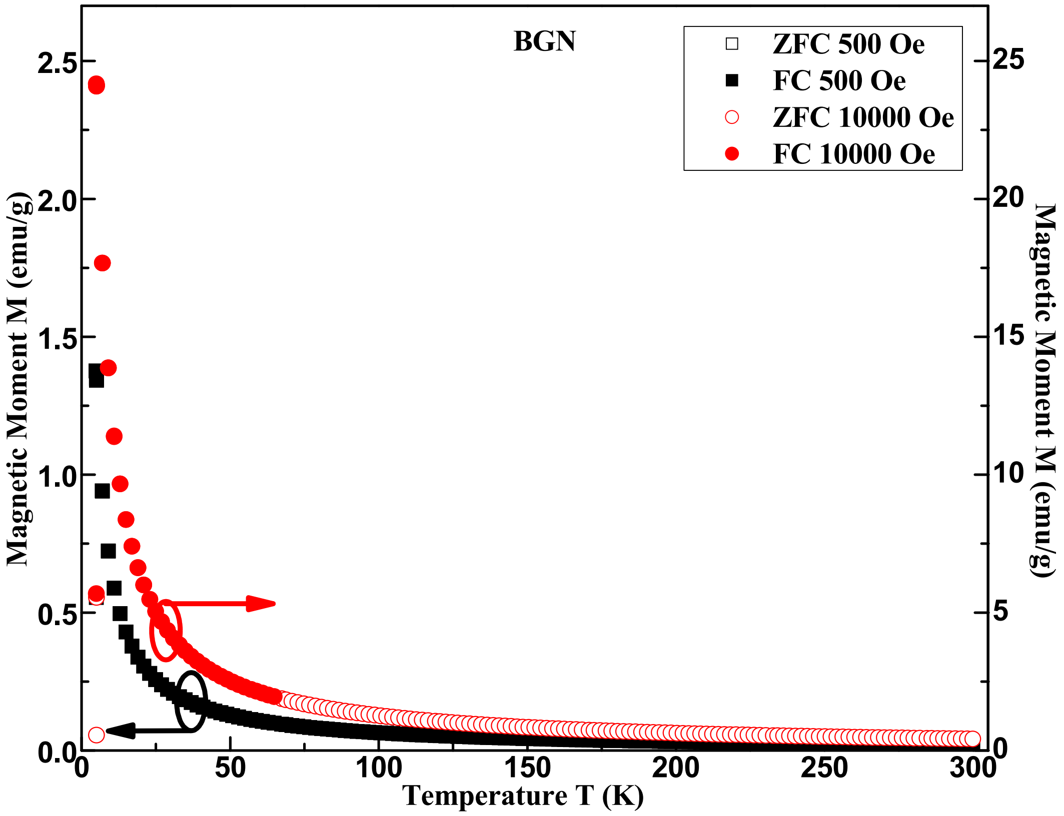

Figure 4.C.13: The temperature dependent magnetization data with ZFC-FC mode for BGN at 500 Oe (left axis) and 10000 Oe (right axis).

In addition to this BFN, BFCN and BCN samples have shown a peak in the magnetization data collected during ZFC mode at 500 Oe in the low temperature region. On the other hand magnetic moment data did not show such a peak in FC mode but exhibited monotones increase in magnetic moment at low temperatures. This typical bifurcation of ZFC-FC data in the low temperature region along with observed peak suggests antiferromagnetic transition in the samples [8]. The temperature values corresponding to peak represents antiferromagnetic transition temperature generally known as Neel temperature T_N. The values of T_N for BFN, BFCN and BCN are 25 K, 19 K and 29 K respectively. The values of T_N shifts to lower temperatures; 11 K, 11 K and <5 K respectively for BFN, BFCN and BCN on increasing the magnetizing field from 500 Oe to 10000 Oe. This nature of antiferromagnetic transition temperature T_N is earlier attributed to the thermodynamic history dependent feature indicating metastable magnetic state at low temperatures [9-10]. This type of metastable magnetic state is observed when a small ferromagnetic cluster is formed in the predominantly antiferromagnetic compound [11]. This is further supported by the observed weak ferromagnetism in the M-H loop of these compounds. The observed weak ferromagnetism is attributed to the super exchange interaction between –Fe–Fe– (or –Co–Co– or –Fe–Co–). Such super exchange interactions are possible only when two magnetic ions occupy the position in the nearby oxygen octahedron. The presence of such super exchange interactions (of nearby magnetic ions) in the antiferromagnetically ordered –Fe–Nb–Fe– (or –Co–Nb–Co– or –Fe–Nb–Co–Nb–Fe–) compound is likely to be related with the defects and distortions. Although the magnetic moment exhibited by the super-exchange interaction should be very high but in the present case the relatively small amount of defects (ferromagnetic clusters) exhibiting super exchange interaction resulted in the observed very less values of magnetic moment. It is already been reported earlier that we have not observed any impurity phase related to the distorted chains in the XRD pattern along with the main phase. Therefore it clearly suggests that the amount of such ferromagnetic regions is much smaller than the typical detection limit of XRD measurement in comparison to the main phase. The samples BFGN and BGN have not shown presence of any antiferromagnetic transition in the M-T curves down to 5 K (Figure 4.C.12 and Figure 4.C.13) suggesting paramagnetic nature of the samples up to this temperature.

The investigation of paramagnetic, ferromagnetic or antiferromagnetic nature of the samples can also be effectively studied through Curie-Weiss law given by Equation 4.C.3.

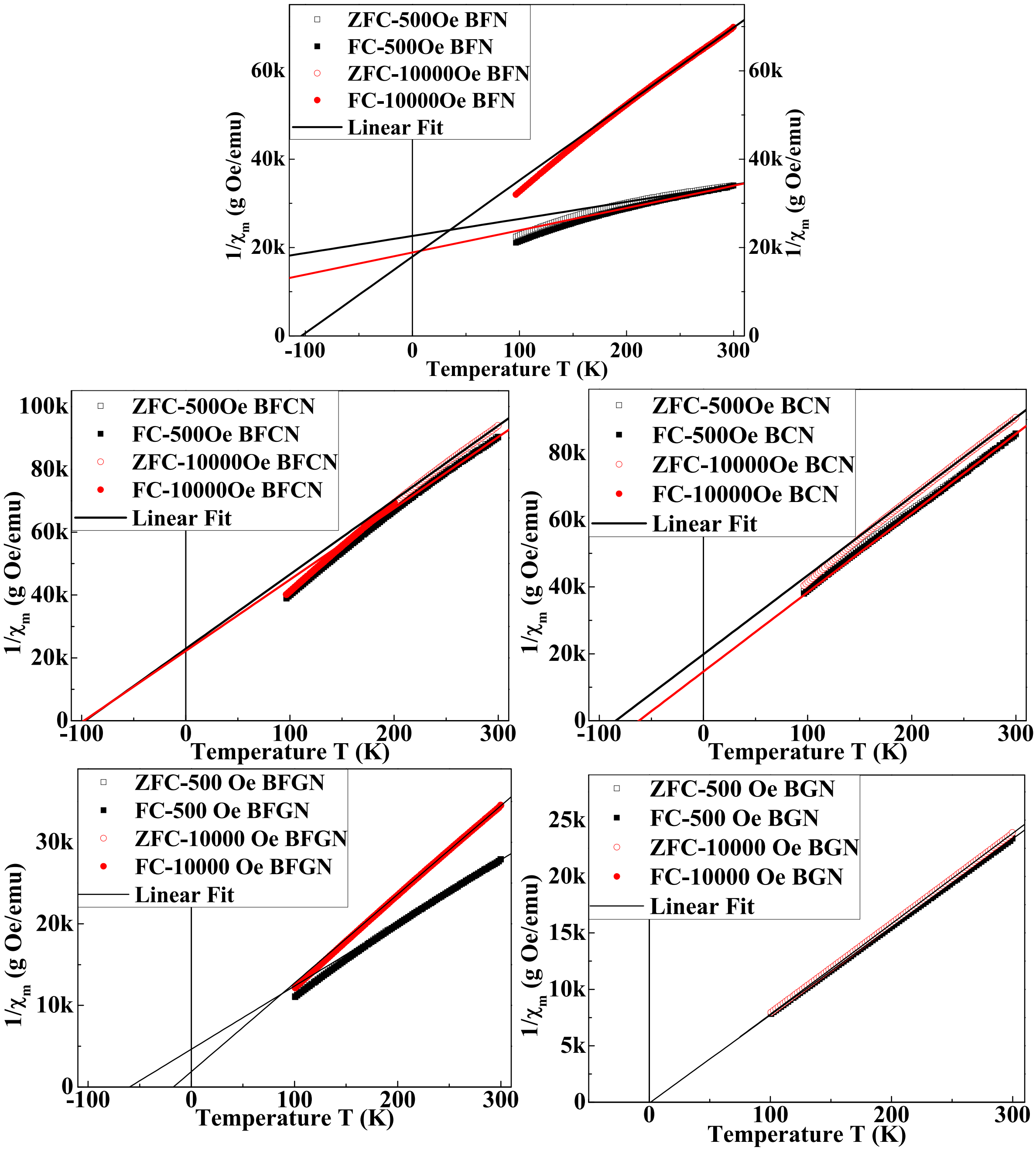

Figure 4.C.14: The curie plot fitting for BFN, BFCN, BCN, BFGN and BGN.

Sr. No	Sample	Neel Temperature T_N K	Curie Constant C erg K g^{-1} Oe^{-2}	θ K
1	BFN	25	0.00585548	-108.52840244
2	BFCN	19	0.00422695	-96.8394737
3	BCN	29	0.00424486	-84.32802204
4	BFGN	-	0.00919933	-17.25504048
5	BGN	-	0.01246962	2.80330782

Table 4.C.1: The fitting parameters of curie plot with Neel temperature.

$$\chi_m = \frac{C}{T-\theta} \qquad \text{…… (4.C.3)}$$

Where, $\chi_m = \frac{M}{H} =$ magnetic susceptibility of the compound

C is Curie constant and θ is a parameter having positive, negative or zero values.

The values of curie constant C and parameter θ can be obtained by fitting a straight line to the $\frac{1}{\chi_m} \rightarrow T$ curve. The slope of the straight line gives values of $1/C$ and its intercept on temperature axis gives values of θ. The zero intercept ($\theta = 0$) represents paramagnetic nature of the sample in the entire temperature region. This type of paramagnetism can be explained using the curie law. The non zero values of parameter θ indicates deviation from the curie law of paramagnetism. The positive values of θ represents ferromagnetism and negative θ values suggest antiferromagnetism. It should be noted here that the Curie-Weiss law is valid only in the paramagnetic region above the transition temperature T_C or T_N corresponding to ferromagnetic or paramagnetic materials respectively. The fitting of curie plot for all five samples are presented in the Figure 4.C.14. The obtained best fitted parameters are listed in the Table 4.C.1. It is evident from the figure that the BGN sample shows pure paramagnetic nature with negligible θ values. The rest four samples viz., BFN, BFCN, BCN and BFGN exhibit antiferromagnetic behavior with negative θ values. Among them the $\frac{1}{\chi_m} \rightarrow T$ curves obtained at low field values (500 Oe) for BFN sample exhibit non linear nature in the entire temperature range. The observed nonlinearity clearly points at apparent contribution of ferromagnetic interaction even up to room temperature.

4.C.3 Summary of Magnetic Characterization (Bulk):

The complex ceramic oxides BFN, BFCN, BCN and BFGN have exhibited antiferromagnetic ordering. The BGN ceramic have shown nearly ideal paramagnetic nature in the entire temperature region. The BFN, BFCN and BCN have shown very weak signal of ferromagnetism at low temperatures. The BFN ceramic has sustained this weak ferromagnetism even up to the room temperature. The observed weak ferromagnetism is attributed to the super exchange interaction between magnetic ions available in the form of ferromagnetic clusters at defects and grain boundaries. Since amount of such super exchange interactions is too small than the predominantly antiferromagnetic ordering, it resulted in to the observed low values of magnetic moments. The thermal history dependent values of magnetic moment/susceptibility for BFN ceramic suggest spin-glass like magnetic behavior of the compound.

References:

1. B. D. Cullity and C. D. Graham, Introduction To Magnetic Materials, second edition, Wiley & Sons, Inc., Hoboken, New Jersey USA. (2009).
2. D. D. Shah, P.K. Mehta, M. S. Desai, C. J. Panchal, J. of Alloys and Comp. **509,** 1800 (2011).
3. A. Falqui, N. Lampis, A. G. Lehmann and G. Pinna, J. Phys. Chem. B. **109,** 22967 (2005).
4. S. A. Larrégola, J. C. Pedregosa, M. Algueró, R. Jiménez, M. G. Hernandez, M. T. F. Díaz and J. A. Alonso, Chem. Mater. **24,** 2664 (2012).
5. R. Havlicek, J. P. Vejpravova and D. Bochenek, Journal of Physics: Conference Series. **200,** 012058 (2010).
6. Spin Glasses and Random Fields, Edited by A. P. Young, World Scientific, Singapore (1997).
7. A. Kumar, R. S. Katiyar, C. Rinaldi, S. G. Lushninkov and T. A. Shaplygina, Appl. Phys. Lett. **93,** 232902 (2008).
8. D. Bochenek, Z. Surowiak, J. P. Vejpravova, J. Alloys. Comp. **487,** 572 (2009).
9. K. Binder and A. P. Young, Rev. Mod. Phys. **58,** 801 (1986).
10. J. A. Mydosh, Spin Glasses: an Experimental Introduction, Taylor and Francis, London. (1993).
11. R. K. Mishra, R. N. P. Choudhary and A. Banerjee, J. Phys.: Condens. Matter **22,** 025901 (2010).

CHAPTER 5

Results and Discussion (Thin Films)

(Structural, Micro structural, Optical and Electrical Characterization of Thin Film Samples)

The characterizations of thin films are presented in this chapter. The structural, optical and electrical studies of the film are presented here. The obtained results were presented collectively for detailed analysis. The results are discussed with respect to different composition as well as with respect to bulk material. Detailed studies on reduction of dimension are presented here. From the application point of view the radiation effects on the films are also been studied and discussed in detail.

5.1 Crystallographic Structural Studies: (X-Ray Diffraction - XRD):

The growth of the desired composition in proper stoichiometry is essential for the successful deposition of thin films. On the other hand an alteration in the stoichiometry of compound results in distorted crystal structure and/or generation of secondary crystallographic phases. The X-ray diffraction analysis is the best tool to study the crystallographic structure of the compound in bulk as well as thin film form. The presence of secondary phases if any can be distinctly separated through comparative studies of XRD patterns. Therefore in order to confirm the single phase formation and to ensure the absence of any impurity phase we have conducted the crystallographic structural studies through X-ray diffraction. The preliminary analyses of the collected data were carried out by comparing the patterns of films with that of respective bulk ceramic. The determinations of crystallite size were done for all the films using Debye scherrer method (Equation 4.A.1) as well as Williamson – Hall equation (Equation 4.A.2) [1-2]. The induced strain was also estimated using Williamson – Hall equation.

The results are presented and discussed in eight different groups. The sections below explain the characterization of various films prepared through PLD technique and discussed in Chapter-3. The induced modifications on irradiating these films by O^{7+} and Ag^{15+} Swift Heavy Ions (SHI) are also discussed here.

5.1.1 X-Ray Diffraction Analysis of BFN-1 Films:

The Figure 5.1 shows XRD patterns of as prepared film (BFN-1), film annealed at 600 °C (BFN-1-An-P), film annealed and irradiated with O^{7+} fluence 5×10^{12} (BFN-1-An-B) as well as film annealed and irradiated with O^{7+} fluence 1×10^{13} (BFN-1-An-C). Figure also include XRD patterns of substrate ITO and bulk target ceramic BFN for comparison. The pattern for as prepared film (BFN-1) clearly indicates the amorphous glassy phase formation along with the small peaks related to substrate ITO. The BFN phase was not developed in the as prepared films. The films were then annealed at 600 °C in air for one hour. The pure single BFN phase was obtained now. The peaks related with the substrate (ITO) are indicated by vertical downward arrow in the figure. The patterns for the irradiated films also sustain the BFN phase. This clearly suggests that the crystallographic structure of BFN-1 films remains unchanged up to the O^{7+} fluence 1×10^{13} ions/cm^2. The elementary analysis of XRD patterns was done using Powder X software. The crystal system, lattice parameter and full width at half maxima (FWHM) of each peak were determined by fitting each of the patterns. The obtained parameters are listed in Table 5.1.

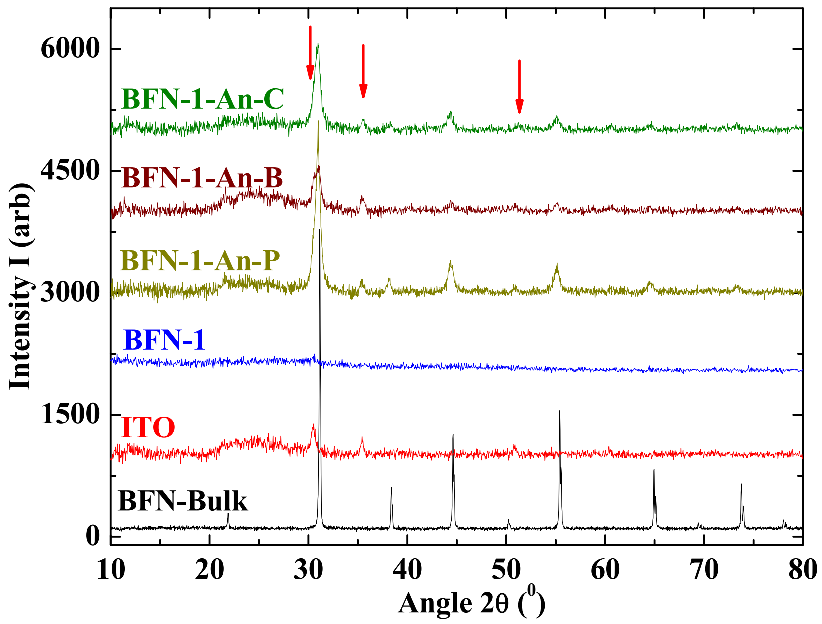

Figure 5.1: The XRD patterns of BFN-1 films with BFN-Bulk and ITO. (All patterns are up lifted by 1000 cps from bellow pattern except BFN-bulk. The peaks indexed with vertical downward aero are related to ITO.)

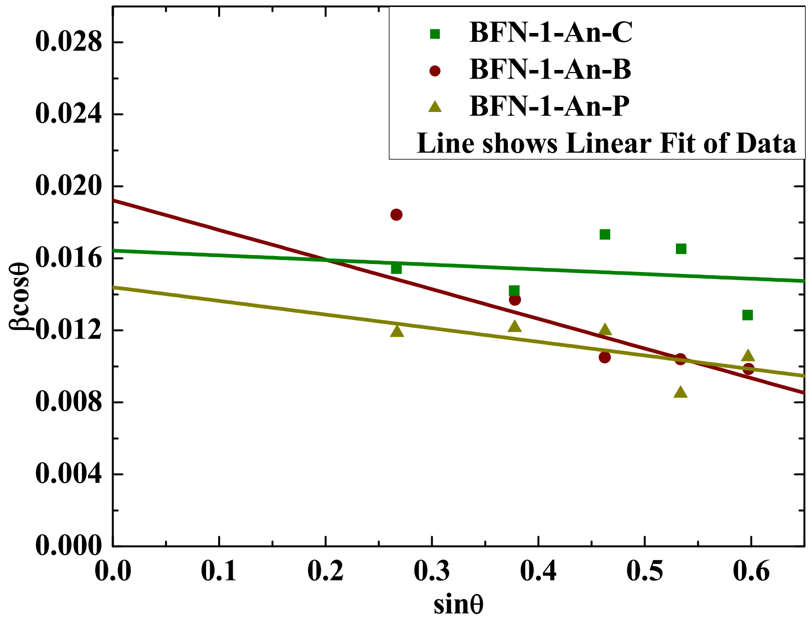

Figure 5.2: The Williamson – Hall plot for BFN-1 films.

In-depth analysis of these patterns was done using Williamson – Hall equation as well as Debye scherrer method. The Figure 5.2 represents fitting of Williamson – Hall equation for all these films. The obtained values of crystallite size and induced strain are presented in the Table 5.1.

The very small and negative values of percentage strain (<0.5) indicates nearly strain less growth of the films [3]. Further, the values of the crystallite size do not show any unidirectional nature. The crystallite size does reduce for the films irradiated with O^{7+} ions.

Sr. No	Sample	Sample Details	Irradiation Fluence	Crystal System	Lattice Parameter a (Å)	Crystallite size (nm)		Percentage Strain
						Debye Scherrer	Williamson – Hall	
1	BFN-1	As Prepared	-	-	-	-	-	-
2	BFN-1-An-P	Annealed	-	Cubic	4.0529	13	10	-0.19
3	BFN-1-An-B	Annealed and irradiated	B	Cubic	4.0529	12	7	-0.41
4	BFN-1-An-C	Annealed and irradiated	C	Cubic	4.0529	9	8	-0.06
5	BFN-2	As Prepared	-	-	-	-	-	-
6	BFN-2-An-P	Annealed	-	Cubic	4.0529	12	13	-0.1
7	BFN-2-An-B	Annealed and irradiated	B	Cubic	4.0529	12	15	0.03
8	BFN-2-An-C	Annealed and irradiated	C	Cubic	4.0529	10	14	0.04
9	BFCN	As Prepared	-	-	-	-	-	-
10	BFCN-An-P	Annealed	-	Cubic	4.0692	11	10	-0.11
11	BFCN-An-B	Annealed and irradiated	B	Cubic	4.0692	11	11	-0.03
12	BFCN-An-C	Annealed and irradiated	C	Cubic	4.0692	12	12	-0.03
13	BCN	As Prepared	-	-	-	-	-	-
14	BCN-An-P	Annealed	-	Cubic	4.0886	8	19	0.55
15	BCN-An-B	Annealed and irradiated	B	Cubic	4.0886	10	10	-0.01
16	BCN-An-C	Annealed and irradiated	C	Cubic	4.0886	6	5	-0.33
17	BMN-1	As Prepared	-	-	-	-	-	-
18	BMN-1-An-P	Annealed	-	Cubic	4.0909	6	7	0.02
19	BMN-1-An-B	Annealed and irradiated	B	Cubic	4.0909	6	5	-0.07
20	BMN-3	As Prepared	-	-	-	-	-	-
21	BMN-3-An-P	Annealed	-	Cubic	4.0909	10	11	0.03
22	BMN-3-An-B	Annealed and irradiated	B	Cubic	4.0909	7	5	-0.4
23	BMN-3-An-C	Annealed and irradiated	C	Cubic	4.0909	6	5	-0.28
24	BGCN-1	As Prepared	-	-	-	-	-	-
25	BGCN-1-An-P	Annealed	-	Cubic	4.2211	10	21	0.45
26	BGCN-1-An-A	Annealed and irradiated	A	Cubic	4.2211	11	13	0.11
27	BGCN-1-An-B	Annealed and irradiated	B	Cubic	4.2211	10	16	0.31
28	BGCN-2	As Prepared	-	-	-	-	-	-
29	BGCN-2-An-P	Annealed	-	Cubic	4.2211	9	23	0.6
30	BGCN-2-An-B	Annealed and irradiated	B	Cubic	4.2211	9	7	-0.25
31	BGCN-2-An-C	Annealed and irradiated	C	-	-	-	-	-

Table 5.1: The crystal structure parameters obtained through XRD analysis along with particle size and lattice strain. (Here A,B,C,D are irradiation fluences respectively, 1×10^{12} ions/cm^2, 5×10^{12} ions/cm^2, 1×10^{13} ions/cm^2, and 5×10^{11} ions/cm^2.

5.1.2 X-Ray Diffraction Analysis of BFN-2 Films:

The BFN-2 films were deposited by keeping the substrate temperature higher than the BFN-1 films at 400 °C. The Figure 5.3 shows XRD patterns of as prepared film (BFN-2), film annealed at 600 °C (BFN-2-An-P), film annealed and irradiated with O^{7+} fluence 5×10^{12} (BFN-2-An-B) and film annealed and irradiated with O^{7+} fluence 1×10^{13} (BFN-2-An-C) along with substrate ITO and bulk target ceramic BFN.

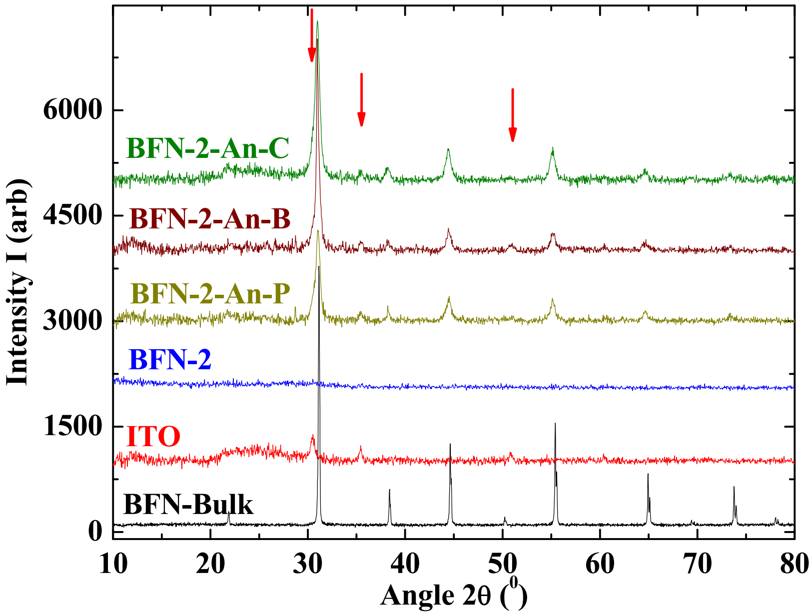

Figure 5.3: The XRD patterns of BFN-2 films with BFN-Bulk and ITO. (All patterns are up lifted by 1000 cps from bellow pattern except BFN-bulk. The peaks indexed with vertical downward aero are related to ITO.)

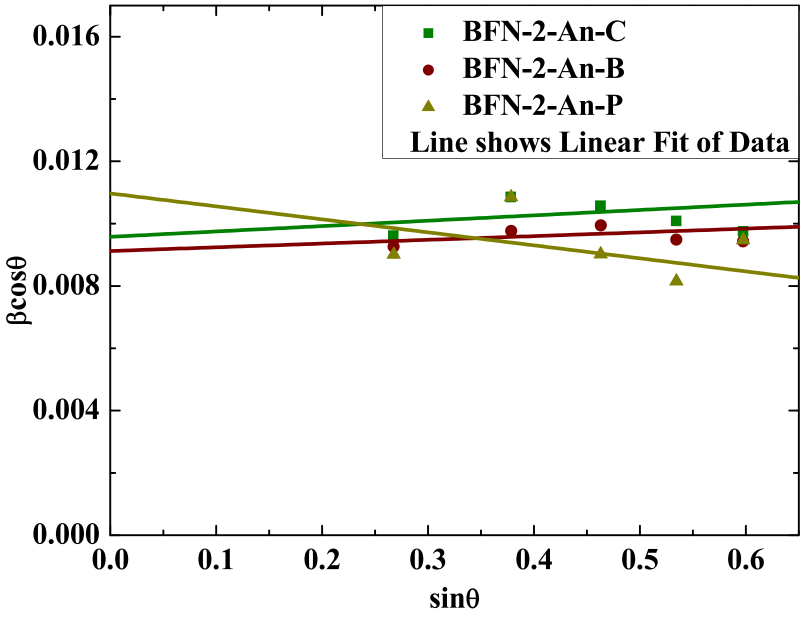

Figure 5.4: The Williamson – Hall plot for BFN-2 films.

The pattern for as prepared film (BFN-2) clearly indicates the amorphous glassy phase formation. The pure single BFN phase was obtained in the films after annealing at 600 °C in air for one hour (see Figure 5.3). The peaks related with the substrate ITO are indicated by vertical downward arrow in the figure. The patterns for the irradiated films also sustain the BFN phase. This clearly suggests that the crystallographic structure of BFN-2 films remains unchanged up to the above mentioned irradiation of O^{7+} ions. The elementary analysis of XRD patterns was done using Powder X software. The crystal system, lattice parameter and full width at half maxima (FWHM) of each peak were determined by fitting each pattern. The obtained parameters are listed in Table 5.1.

In-depth analysis of these patterns was done using Williamson – Hall equation as well as Debye scherrer method. The Figure 5.4 represents fitting of Williamson – Hall equation for all these films. The obtained values of crystallite size and induced strain are presented in the Table 5.1.

The negligible values of percentage strain (<0.1) indicates nearly strain less growth of the films [3]. In contrast to the BFN-1 films the crystallite size increases marginally for the BFN-2 films through irradiation with O^{7+} ions.

5.1.3 X-Ray Diffraction Analysis of BFCN Films:

The BFCN films were deposited by keeping the substrate temperature 400 °C. The Figure 5.5 shows XRD patterns of as prepared film (BFCN), film annealed at 600 °C (BFCN-An-P), film annealed and irradiated with O^{7+} fluence 5×10^{12} (BFCN-An-B) and film annealed and irradiated with O^{7+} fluence 1×10^{13} (BFCN-An-C) along with substrate ITO and bulk target ceramic BFCN. The pattern for as prepared film (BFCN) clearly indicates the amorphous glassy phase formation with small peaks related to the substrate ITO. The pure single BFCN phase was obtained in the films after annealing at 600 °C in air for one hour (see Figure 5.5).

The peaks related with the substrate ITO are indicated by vertical downward arrow in the figure. The patterns for the irradiated films also sustain the BFCN phase. This clearly suggests that the crystallographic structure of BFCN films remains unchanged up to the above mentioned irradiation of O^{7+} ions. The elementary analysis of XRD patterns was done using Powder X software. The crystal system, lattice parameter and full width at half maxima (FWHM) of each peak were determined by fitting each pattern. The obtained parameters are listed in Table 5.1.

In-depth analysis of these patterns was done using Williamson – Hall equation as well as Debye scherrer method. The Figure 5.6 represents fitting of Williamson – Hall equation for all these films. The obtained values of crystallite size and induced strain are presented in the Table 5.1. The negligible values of percentage strain (<0.1) indicates nearly strain less growth of the films [3]. Here also the crystallite size increases for the BFCN films through irradiation with O^{7+} ions. This indicates improvement in crystalline nature of the films with the O^{7+} ion irradiation.

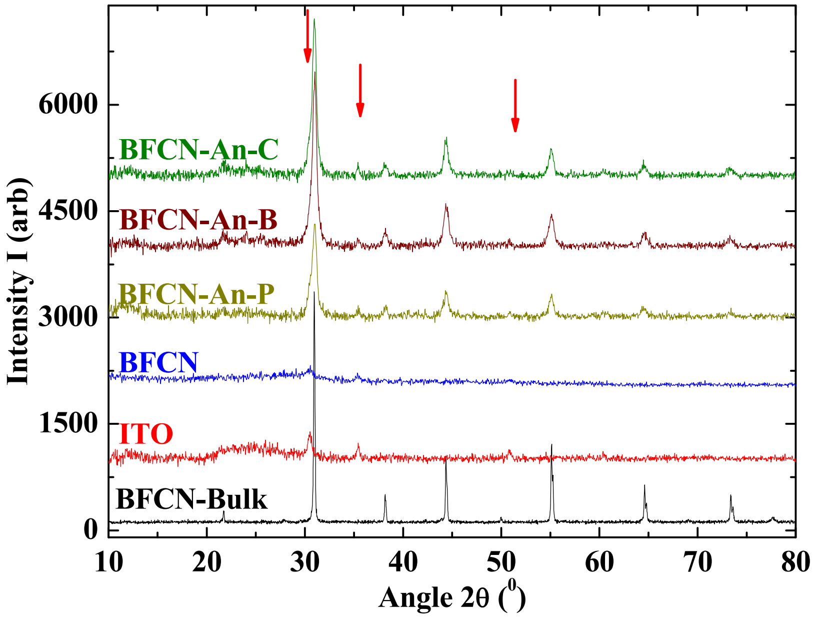

Figure 5.5: The XRD patterns of BFCN films with BFCN-Bulk and ITO. (All patterns are up lifted by 1000 cps from bellow pattern except BFCN-bulk. The peaks indexed with vertical downward aero are related to ITO.)

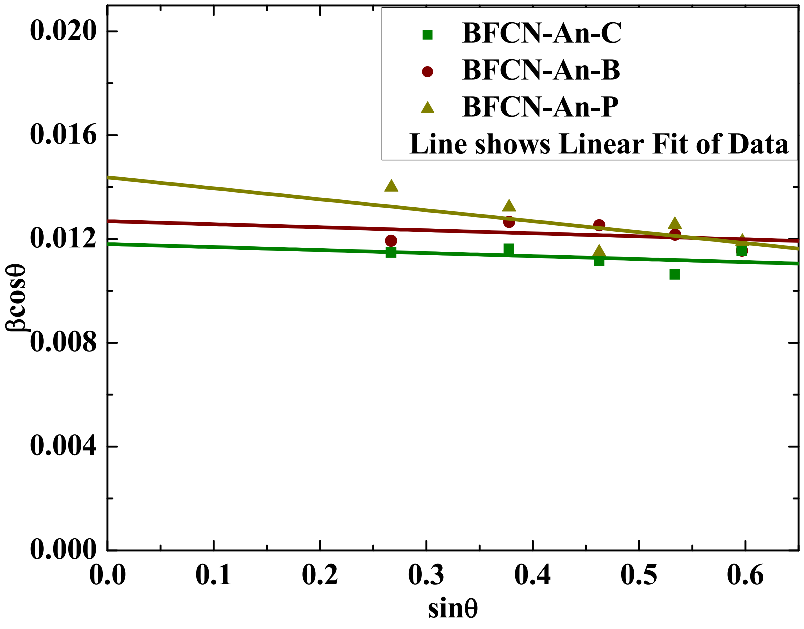

Figure 5.6: The Williamson – Hall plot for BFCN films.

5.1.4 X-Ray Diffraction Analysis of BCN Films:

The BCN films were deposited by keeping the substrate temperature 400 °C. The Figure 5.7 shows XRD patterns of as prepared film (BCN), film annealed at 600 °C (BCN-An-P), film annealed and irradiated with O^{7+} fluence 5×10^{12} (BCN-An-B) and film annealed and irradiated with O^{7+} fluence 1×10^{13} (BCN-An-C) along with substrate ITO and bulk target ceramic BCN. The pattern for as prepared film (BCN) clearly indicates the amorphous glassy phase formation. The pure single BCN phase was obtained in the films after annealing at 600 °C in air for one hour (see Figure 5.7).

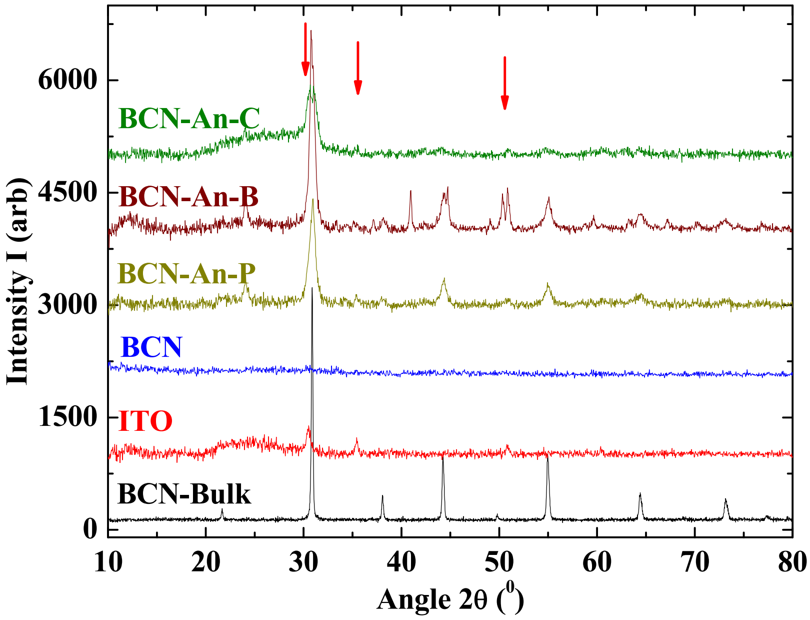

Figure 5.7: The XRD patterns of BCN films with BCN-Bulk and ITO. (All patterns are up lifted by 1000 cps from bellow pattern except BCN-bulk. The peaks indexed with vertical downward aero are related to ITO.)

The peaks related with the substrate ITO are indicated by vertical downward arrow in the figure. Here the crystallographic structure of the films gets distorted on irradiating the films with O^{7+} ions. It is clearly evident from the figure that another impurity phase has been introduced on irradiating the film with O^{7+} fluence 5×10^{12} ions per cm^2 (film BCN-An-B). On irradiating with further higher fluence of 1×10^{13} ions per cm^2 (film BCN-An-C) the large crystallites destroy in to further smaller crystallites. The elementary analysis of XRD patterns was done using Powder X software. The crystal system, lattice parameter and full width at half maxima (FWHM) of each peak were determined by fitting each pattern. The obtained parameters are listed in Table 5.1.

In-depth analysis of these patterns was done using Williamson – Hall equation as well as Debye scherrer method. The Figure 5.8 represents fitting of Williamson – Hall equation for BCN phase of all these films. The obtained values of crystallite size and induced strain are presented in the Table 5.1. The very small values of percentage strain (<0.6) indicates nearly strain less growth of the films [3]. The crystallite size reduces for the BCN films through irradiation with O^{7+} ions.

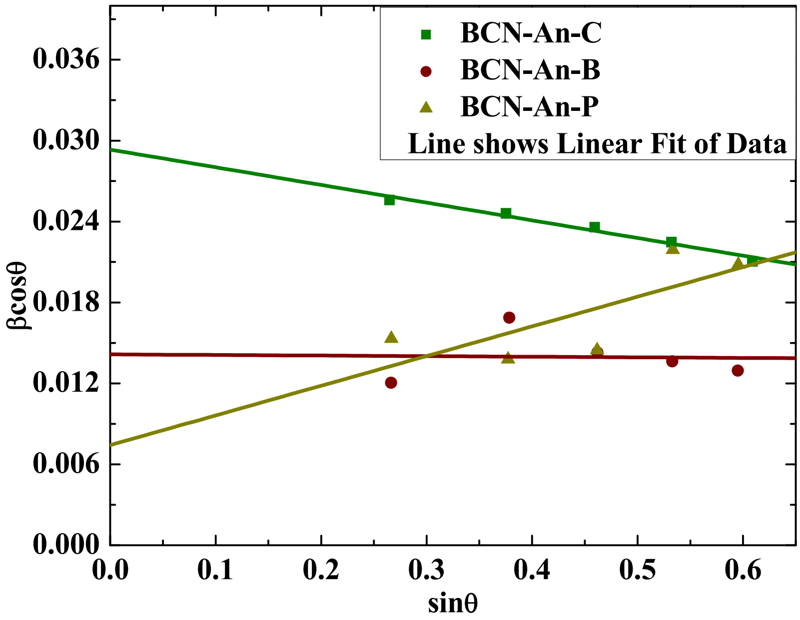

Figure 5.8: The Williamson – Hall plot for BCN films.

5.1.5 X-Ray Diffraction Analysis of BMN-1 Films:

The BMN-1 films were deposited by keeping the substrate temperature 300 °C. The Figure 5.9 shows XRD patterns of as prepared film (BMN-1), film annealed at 600 °C (BMN-1-An-P) and film annealed and irradiated with O^{7+} fluence 5×10^{12} (BMN-1-An-B) along with substrate ITO and bulk target ceramic BMN. The pattern for as prepared film (BMN-1) clearly indicates the amorphous glassy phase formation. The pure single BMN phase was obtained in the films after annealing at 600 °C in air for one hour (see Figure 5.9).

The peaks related with the substrate ITO are indicated by vertical downward arrow in the figure. The pattern for the irradiated film also sustains the BMN phase. This clearly suggests that the crystallographic structure of BMN films remains unchanged up to the above mentioned irradiation of O^{7+} ions. The elementary analysis of XRD patterns was done using Powder X software. The crystal system, lattice parameter and full width at half maxima

(FWHM) of each peak were determined by fitting each pattern. The obtained parameters are listed in Table 5.1.

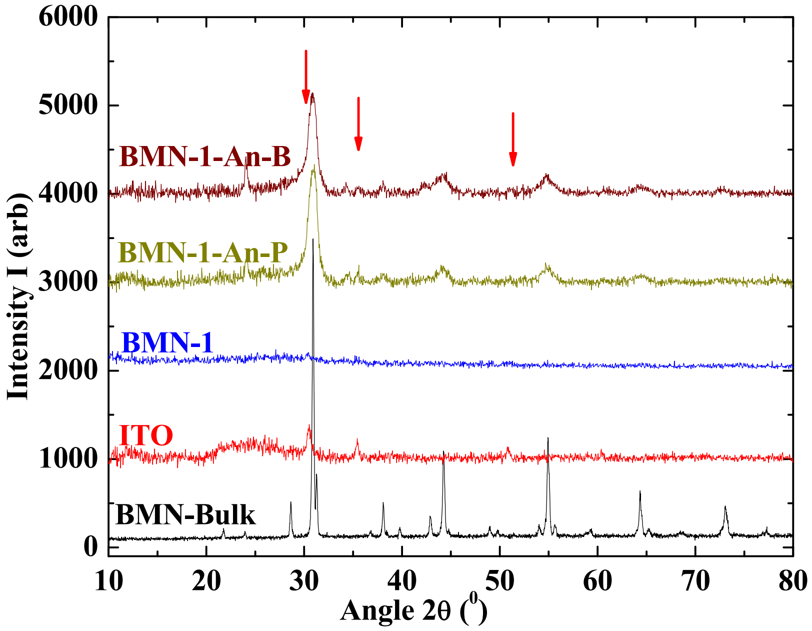

Figure 5.9: The XRD patterns of BMN-1 films with BMN-Bulk and ITO. (All patterns are up lifted by 1000 cps from bellow pattern except BMN-bulk. The peaks indexed with vertical downward aero are related to ITO.)

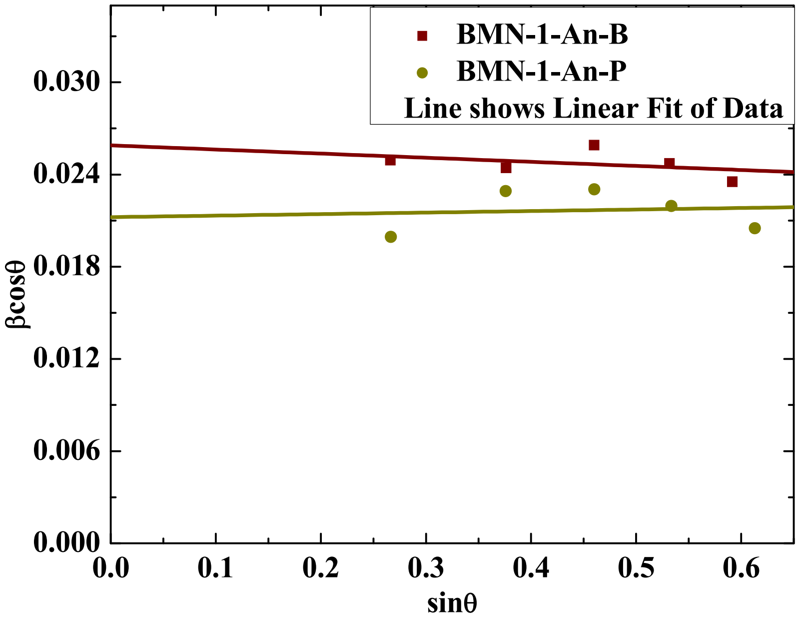

Figure 5.10: The Williamson – Hall plot for BMN-1 films.

In-depth analysis of these patterns was done using Williamson – Hall equation as well as Debye scherrer method. The Figure 5.10 represents fitting of Williamson – Hall equation for all these films. The obtained values of crystallite size and induced strain are presented in the Table 5.1. The negligible values of percentage strain (<0.1) indicates nearly strain less growth of the films [3]. The crystallite size reduces for the BMN-1 films through irradiation with O^{7+} ions.

5.1.6 X-Ray Diffraction Analysis of BMN-3 Films:

The BMN-3 films were deposited by keeping the substrate temperature 400 °C. The Figure 5.11 shows XRD patterns of as prepared film (BMN-3), film annealed at 600 °C (BMN-3-An-P), film annealed and irradiated with O^{7+} fluence 5×10^{12} (BMN-3-An-B) and film annealed and irradiated with O^{7+} fluence 1×10^{13} (BMN-3-An-C) along with substrate ITO and bulk target ceramic BMN. The pattern for as prepared film (BMN-3) clearly indicates the amorphous glassy phase formation. The pure single BMN phase was obtained in the films after annealing at 600 °C in air for one hour (see Figure 5.11).

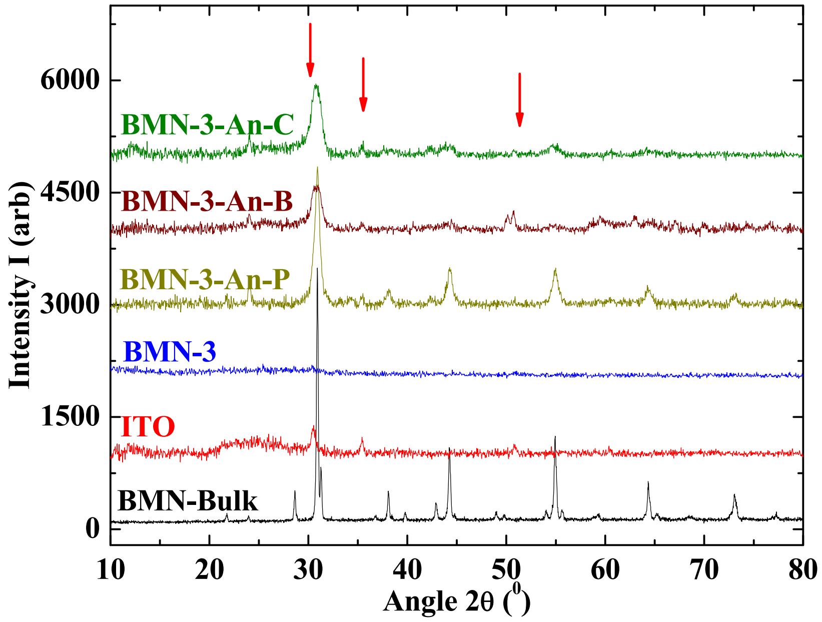

Figure 5.11: The XRD patterns of BMN-2 films with BMN-Bulk and ITO. (All patterns are up lifted by 1000 cps from bellow pattern except BMN-bulk. The peaks indexed with vertical downward aero are related to ITO.)

The peaks related with the substrate ITO are indicated by vertical downward arrow in the figure. Here the crystallographic structure of the films gets distorted on irradiating the films with O^{7+} ions. It is clearly evident from the figure that an impurity phase has been introduced on irradiating the film with O^{7+} fluence 5×10^{12} ions per cm^2 (film BMN-3-An-B). On irradiating with further higher fluence of 1×10^{13} ions per cm^2 (film BMN-3-An-C) not only it re-crystallizes the BMN phase but also splits the larger crystallites in to nano size (5 nm) crystallites. The elementary analysis of XRD patterns was done using Powder X software. The crystal system, lattice parameter and full width at half maxima (FWHM) of each peak were determined by fitting each pattern. The obtained parameters are listed in Table 5.1.

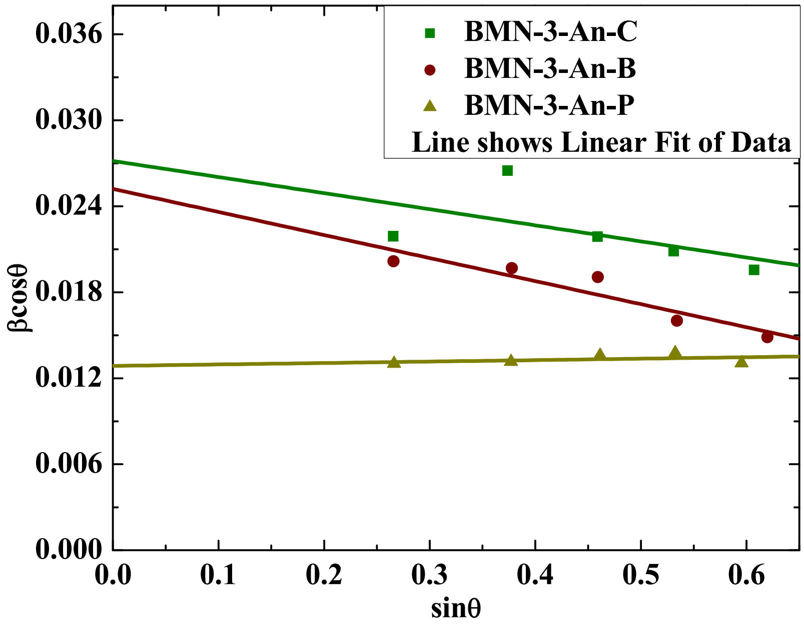

Figure 5.12: The Williamson – Hall plot for BMN-3 films.

In-depth analysis of these patterns was done using Williamson – Hall equation as well as Debye scherrer method. The Figure 5.12 represents fitting of Williamson – Hall equation for BMN phase of all these films. The obtained values of crystallite size and induced strain are presented in the Table 5.1. The very small values of percentage strain (<0.5) indicates nearly strain less growth of the films [3]. The crystallite size reduces for the BCN films through irradiation with O^{7+} ions.

5.1.7 X-Ray Diffraction Analysis of BGCN-1 Films:

The BGCN-1 films were deposited by keeping the substrate temperature 400 °C. The Figure 5.13 shows XRD patterns of as prepared film (BGCN-1), film annealed at 600 °C (BGCN-1-An-P), film annealed and irradiated with Ag^{15+} fluence 1×10^{12} (BGCN-1-An-A) and film annealed and irradiated with Ag^{15+} fluence 5×10^{12} (BGCN-1-An-B) along with substrate ITO and bulk target ceramic BGCN-10C (BGCN). The pattern for as prepared film (BGCN-1) clearly indicates the amorphous glassy phase formation. The pure single BGCN phase was obtained in the films after annealing at 600 °C in air for one hour (see Figure 5.13).

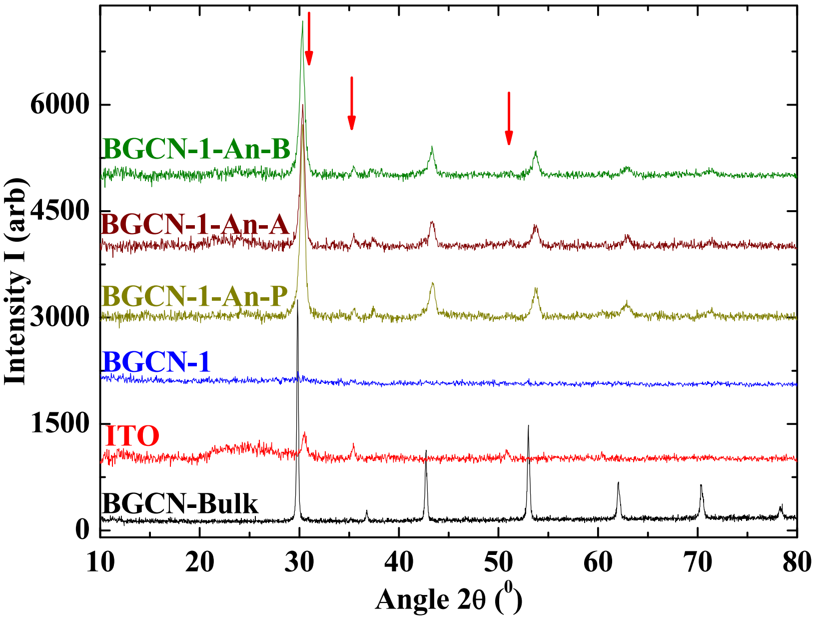

Figure 5.13: The XRD patterns of BGCN-1 films with BGCN-Bulk and ITO. (All patterns are up lifted by 1000 cps from bellow pattern except BGCN-bulk. The peaks indexed with vertical downward aero are related to ITO.)

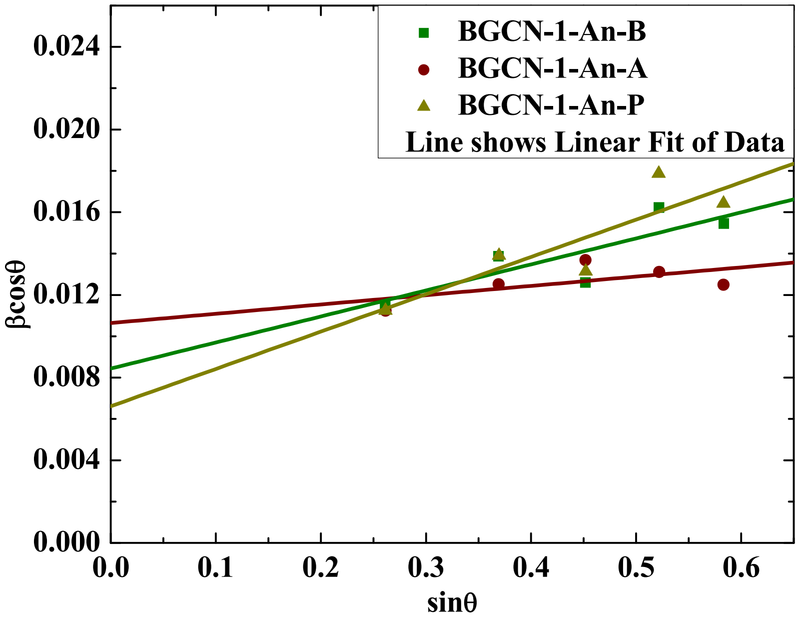

Figure 5.14: The Williamson – Hall plot for BGCN-1 films.

The peaks related with the substrate ITO are indicated by vertical downward arrow in the figure. The patterns for the irradiated films also sustain the BGCN phase. This clearly suggests that the crystallographic structure of BGCN films remains unchanged up to the above mentioned irradiation of Ag^{15+} ions. The elementary analysis of XRD patterns was done using

Powder X software. The crystal system, lattice parameter and full width at half maxima (FWHM) of each peak were determined by fitting each pattern. The obtained parameters are listed in Table 5.1.

In-depth analysis of these patterns was done using Williamson – Hall equation as well as Debye scherrer method. The Figure 5.14 represents fitting of Williamson – Hall equation for all these films. The obtained values of crystallite size and induced strain are presented in the Table 5.1. The very small values of percentage strain (<0.5) indicates nearly strain less growth of the films [3]. The crystallite size reduces for the BGCN-1 films through irradiation with Ag^{15+} ions.

5.1.8 X-Ray Diffraction Analysis of BGCN-2 Films:

The BGCN-2 films were deposited by keeping the substrate temperature 400 °C. The Figure 5.15 shows XRD patterns of as prepared film (BGCN-2), film annealed at 600 °C (BGCN-2-An-P), film annealed and irradiated with O^{7+} fluence 5×10^{12} (BGCN-2-An-B) and film annealed and irradiated with O^{7+} fluence 1×10^{13} (BGCN-2-An-C) along with substrate ITO and bulk target ceramic BGCN-10C (BGCN). The pattern for as prepared film (BCN) clearly indicates the amorphous glassy phase formation. The pure single BGCN phase was obtained in the films after annealing at 600 °C in air for one hour (see Figure 5.15).

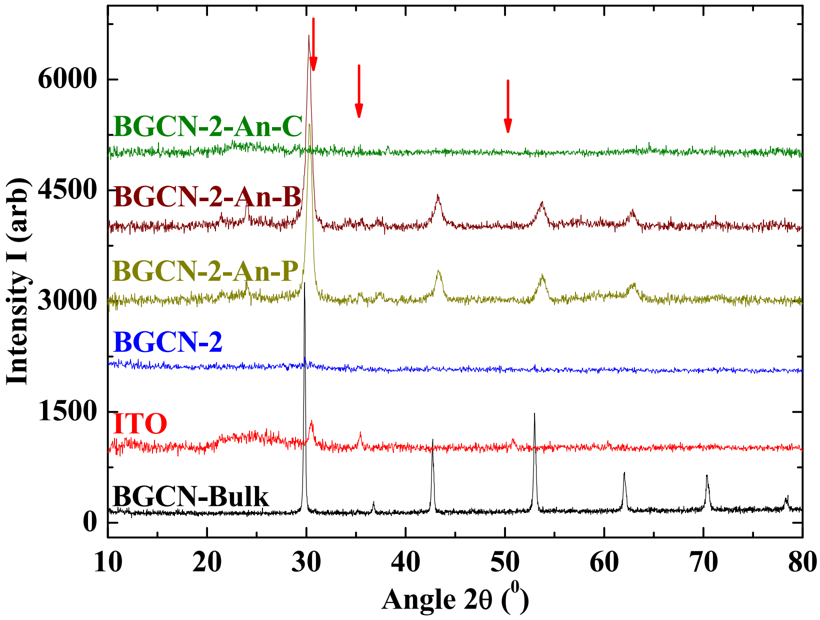

Figure 5.15: The XRD patterns of BGCN-2 films with BGCN-Bulk and ITO. (All patterns are up lifted by 1000 cps from bellow pattern except BGCN-bulk. The peaks indexed with vertical downward aero are related to ITO.)

The peaks related with the substrate ITO are indicated by vertical downward arrow in the figure. Here the crystallographic structure of the films remains unchanged up to the O^{7+} fluence 5×10^{12} ions per cm^2 (film BGCN-2-An-B). On irradiating with further higher fluence of 1×10^{13} ions per cm^2 (film BGCN-2-An-C) the crystalline structure destroys completely in to glassy phase. The elementary analysis of XRD patterns was done using Powder X software. The crystal system, lattice parameter and full width at half maxima (FWHM) of each peak were determined by fitting each pattern. The obtained parameters are listed in Table 5.1.

In-depth analysis of these patterns was done using Williamson – Hall equation as well as Debye scherrer method. The Figure 5.16 represents fitting of Williamson – Hall equation for all these films. The obtained values of crystallite size and induced strain are presented in the Table 5.1.

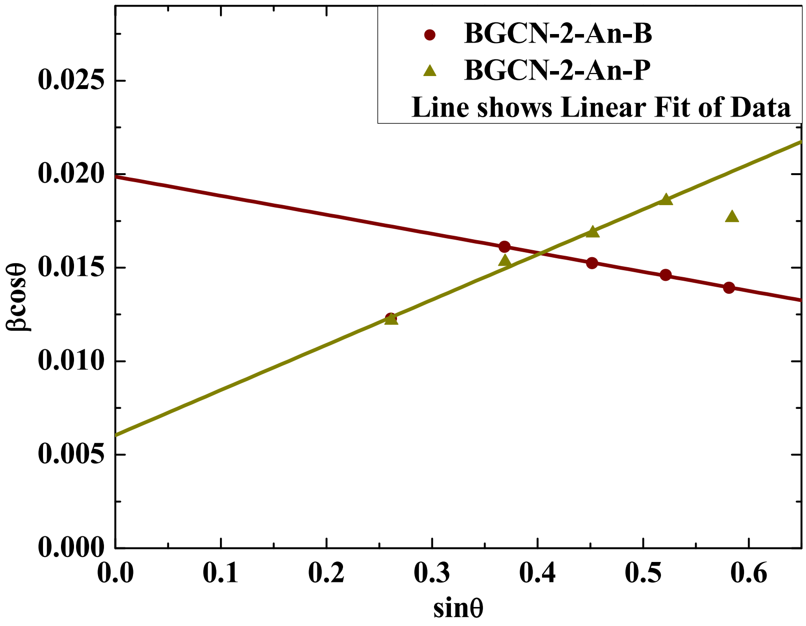

Figure 5.16: The Williamson – Hall plot for BGCN-2 films.

The very small values of percentage strain (<0.6) indicates nearly strain less growth of the films [3]. The crystallite size reduces for the BGCN films through irradiation with O^{7+} ions and then destroys completely into amorphous phase.

5.2 Micro Structural Studies: (Atomic Force Microscopy – AFM):

The microstructure topography of the films is another important feature to confirm the batter quality of the films. The Atomic Force Microscopy (AFM) is useful to collect such 3D images of the films. The surface features like grain growth, cluster formation, defects, micro cracks, roughness, etc, can be determined using AFM.

The micrographs are presented and discussed in eight different groups.

5.2.1 Atomic Force Microscopy of BFN-1 Films:

The Figure 5.17 shows 2D and 3D AFM micrographs of as prepared film (BFN-1), film annealed at 600 °C (BFN-1-An-P), film annealed and irradiated with O^{7+} fluence 5×10^{12} (BFN-1-An-B) and film annealed and irradiated with O^{7+} fluence 1×10^{13} (BFN-1-An-C). It is revealed from the images that the clusters of grains with well defined grain boundaries are developed after annealing the films.

Sr. No.	Sample	Sample Details	RMS Roughness (nm)	Average Roughness (nm)	Height of Maximum Available Peak (nm)	Maximum Valley Depth (nm)	Maximum Peak Height (nm)
1	BFN-1	As Prepared	8.66965	6.96057	11.3905	23.4784	31.174
2	BFN-1-An-P	Annealed	26.7147	20.8361	60.9025	103.061	52.7867
3	BFN-1-An-B	Annealed and irradiated	15.3862	12.0956	25.7655	51.9429	39.8926
4	BFN-1-An-C	Annealed and irradiated	23.0445	17.5617	45.0217	122.279	42.9107
5	BFN-2	As Prepared	5.79113	4.69559	8.14539	16.4231	20.1944
6	BFN-2-An-P	Annealed	20.02	15.75	42.53	74.00	40.70
7	BFN-2-An-B	Annealed and irradiated	17.54	13.58	35.66	70.26	40.26
8	BFN-2-An-C	Annealed and irradiated	16.78	13.34	35.16	64.84	34.28
9	BFCN	As Prepared	10.7746	8.19586	18.1172	43.8935	34.0417
10	BFCN-An-P	Annealed	20.2197	13.7488	47.5765	112.739	40.4266
11	BFCN-An-B	Annealed and irradiated	16.6418	12.8291	29.0333	58.3053	47.4439
12	BFCN-An-C	Annealed and irradiated	16.7043	13.6211	31.568	61.249	39.7282
13	BCN	As Prepared	8.47249	6.91903	12.6576	28.5457	26.3773
14	BCN-An-P	Annealed	18.595	14.8443	35.5978	71.5954	46.0424
15	BCN-An-B	Annealed and irradiated	17.1327	13.9293	29.4145	56.8237	44.4029
16	BCN-An-C	Annealed and irradiated	22.3196	18.6708	36.4714	63.6327	51.5523
17	BMN-1	As Prepared	10.4623	7.73229	21.5031	39.1242	34.8759
18	BMN-1-An-P	Annealed	26.5908	21.8092	50.3605	81.3128	66.51
19	BMN-1-An-C	Annealed and irradiated	25.1759	20.9139	48.9343	87.1479	46.2851
20	BMN-3	As Prepared	12.8983	10.2386	20.3563	43.3222	36.6604
21	BMN-3-An-P	Annealed	18.7538	14.9247	33.758	65.464	66.1395
22	BMN-3-An-B	Annealed and irradiated	22.6714	18.2796	44.9384	71.2024	54.7766
23	BMN-3-An-C	Annealed and irradiated	18.9462	15.0663	35.2864	76.8397	59.6558
24	BGCN-1	As Prepared	16.6718	13.2865	28.0482	59.9093	49.4348
25	BGCN-1-An-P	Annealed	26.7541	21.1531	49.5407	86.0961	76.5408
26	BGCN-1-An-A	Annealed and irradiated	22.8306	16.2821	41.4703	104.071	58.8715
27	BGCN-1-An-B	Annealed and irradiated	52.0487	43.4658	97.3491	161.6	142.008
28	BGCN-2	As Prepared	8.36296	6.79285	13.5955	21.4967	24.654
29	BGCN-2-An-P	Annealed	22.5515	18.0953	43.0103	82.581	52.4009
30	BGCN-2-An-B	Annealed and irradiated	16.1634	13.1622	27.9147	45.266	42.8949
31	BGCN-2-An-C	Annealed and irradiated	24.8858	19.7983	47.9195	87.7102	52.9475

Table 5.2: The roughness parameters of films obtained from surface analyses of AFM micrographs.

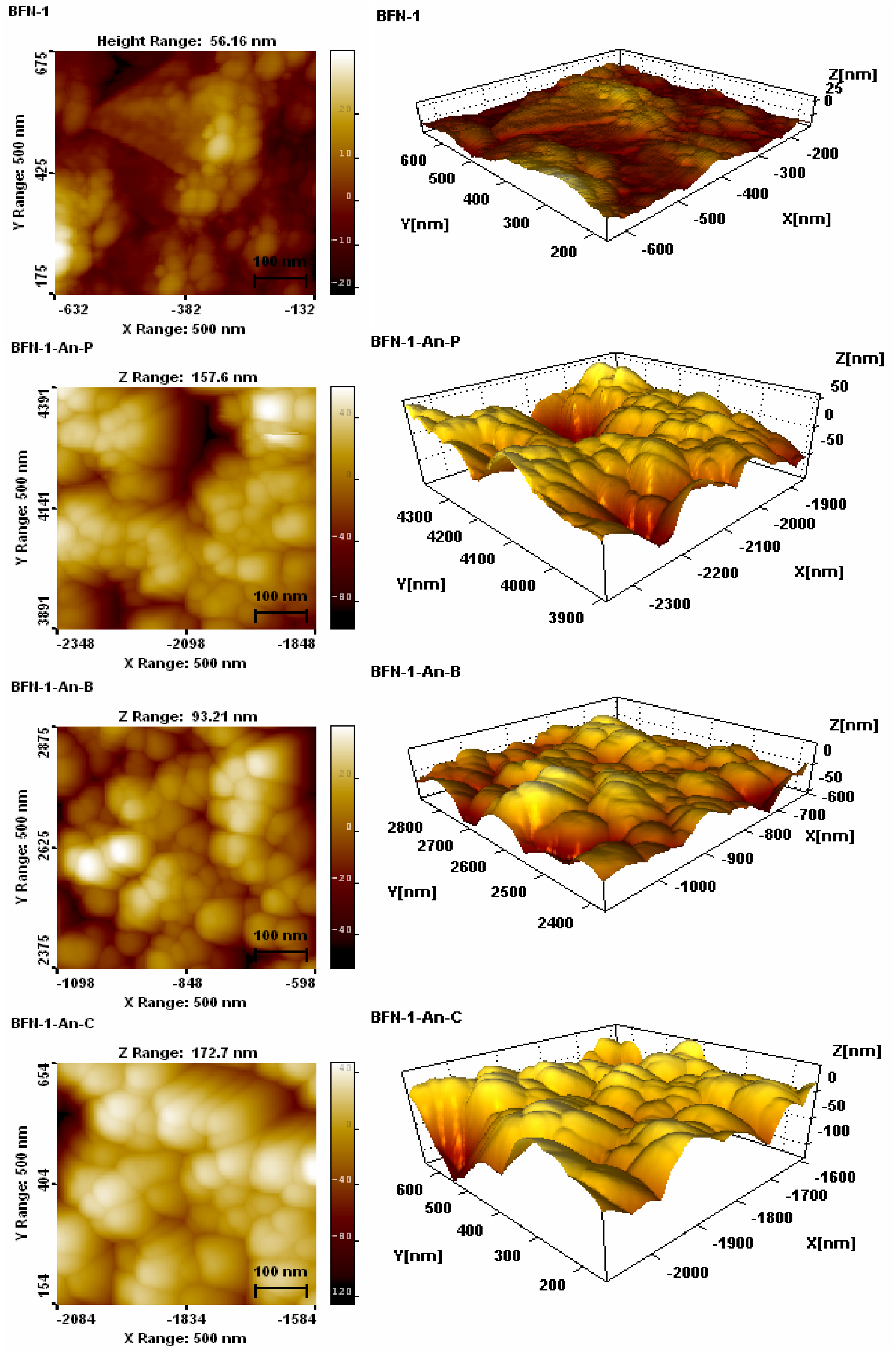

Figure 5.17: The 2D and 3D AFM micrographs for BFN-1 films.

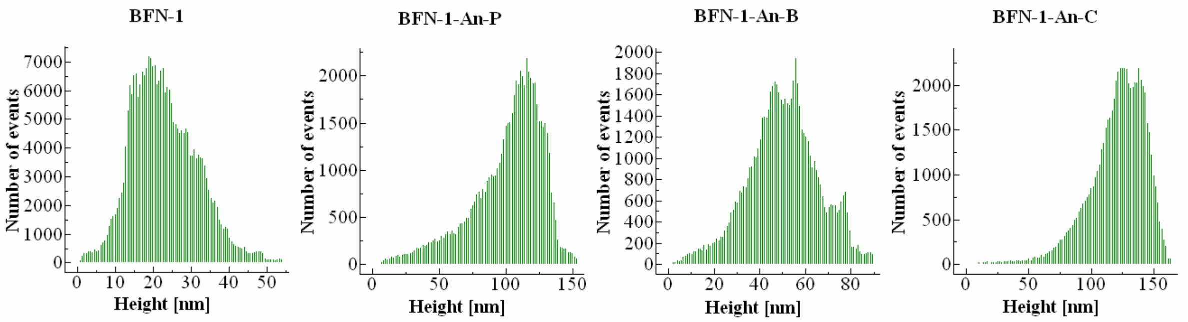

Figure 5.18: The surface roughness histogram obtained for BFN-1 films.

The detailed processing of the images was done in the light of roughness parameters and particle height. The surface roughness histograms collected for all micrographs of BFN-1 films are shown in the Figure 5.18. The obtained different parameters like; rms roughness, average roughness, height of maximum available peak, maximum peak height and maximum valley depth are presented in the Table 5.2. The surface roughness of the BFN-1 films decreases on irradiating the films with O^{7+} ions. The lowest roughness is found for the O^{7+} fluence 5×10^{12} ions per cm^2 (BFN-1-An-B). On irradiating with further higher fluence of 1×10^{13} ions per cm^2 (film BFN-1-An-C) the roughness increases slightly. The height of maximum available peak (maximum available particle size) decreases on irradiating the films with O^{7+} ions. The minimum particle size is obtained for the O^{7+} fluence of 5×10^{12} ions per cm^2 (BFN-1-An-B). These results are in agreement with the variation in the crystallite size from the XRD analysis.

5.2.2 Atomic Force Microscopy of BFN-2 Films:

The Figure 5.19 shows 2D and 3D AFM micrographs of as prepared film (BFN-2), film annealed at 600 °C (BFN-2-An-P), film annealed and irradiated with O^{7+} fluence 5×10^{12} (BFN-2-An-B) and film annealed and irradiated with O^{7+} fluence 1×10^{13} (BFN-2-An-C). It is revealed from the images that the clusters of grains with well defined grain boundaries are developed after annealing the films. The detailed processing of the images was done in the light of roughness parameters and particle height. The surface roughness histograms collected for all micrographs of BFN-2 films are shown in the Figure 5.20.

The obtained different parameters like; rms roughness, average roughness, height of maximum available peak, maximum peak height and maximum valley depth are presented in the Table 5.2.

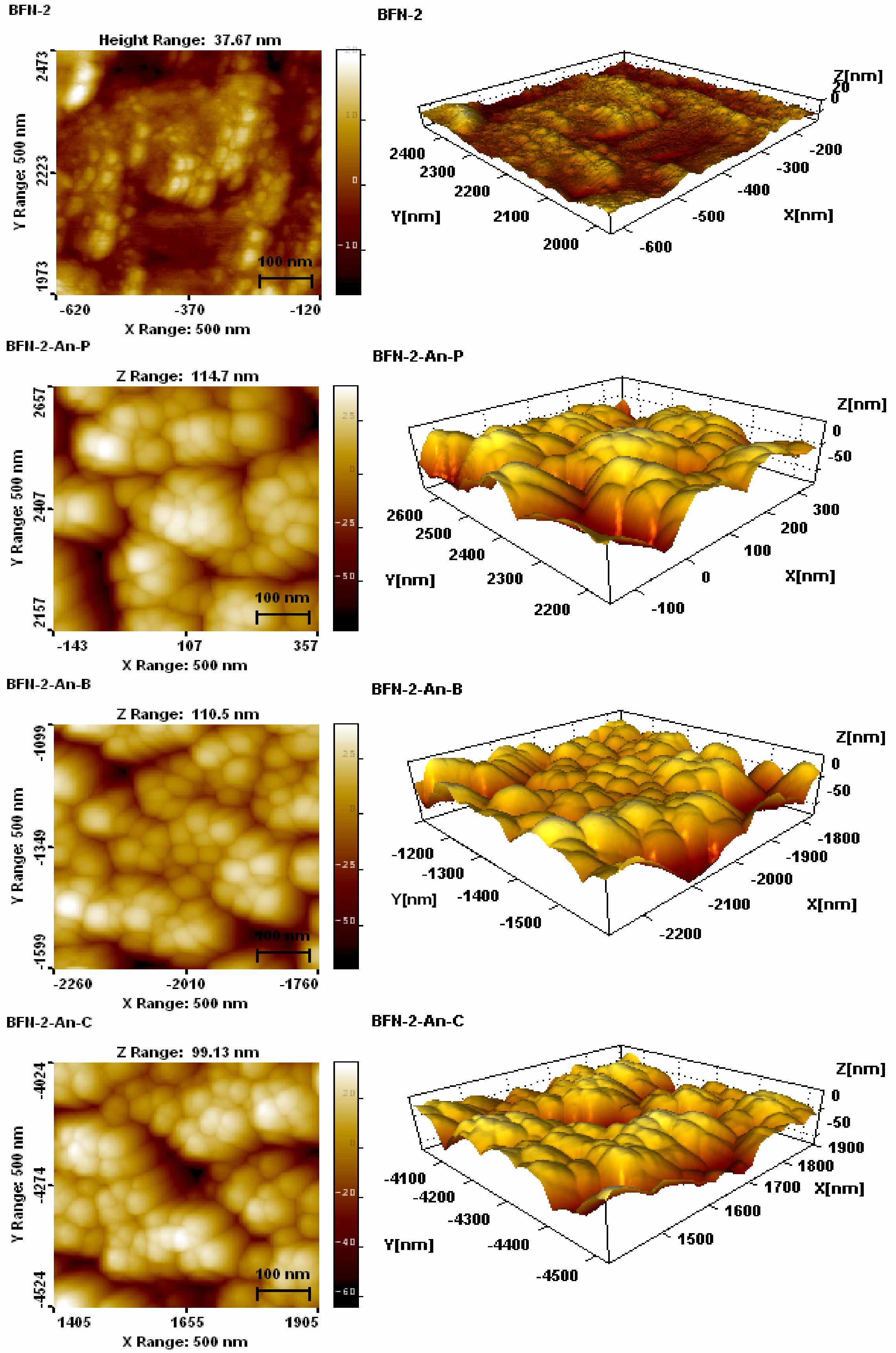

Figure 5.19: The 2D and 3D AFM micrographs for BFN-2 films.

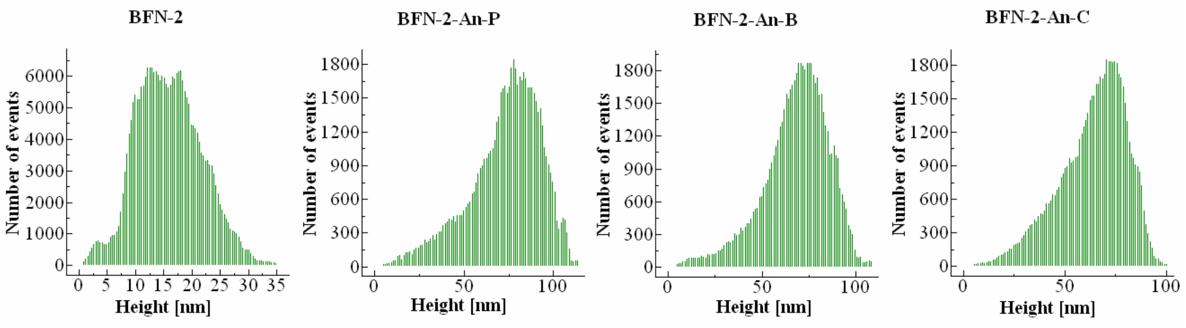

Figure 5.20: The surface roughness histogram obtained for BFN-2 films.

The surface roughness of the BFN-2 films decreases on irradiating the films with O^{7+} ions. The lowest roughness is found for the highest O^{7+} fluence 1×10^{13} ions per cm^2 (BFN-2-An-C). The height of maximum available peak (maximum available particle size) also decreases on increasing the irradiation fluence. These results are not in agreement with the variation in the crystallite size from the XRD analysis. It means that because of irradiation the particle size reduces but the crystallinity improves than that of pristine film. The crystallinity increases up to fluence 5×10^{12} ions per cm^2 and then reduces with higher fluence.

5.2.3 Atomic Force Microscopy of BFCN Films:

The Figure 5.21 shows 2D and 3D AFM micrographs of as prepared film (BFCN), film annealed at 600 °C (BFCN-An-P), film annealed and irradiated with O^{7+} fluence 5×10^{12} (BFCN-An-B) and film annealed and irradiated with O^{7+} fluence 1×10^{13} (BFCN-An-C). It is revealed from the images that the clusters of grains with well defined grain boundaries are developed after annealing the films. The detailed processing of the images was done in the light of roughness parameters and particle height. The surface roughness histograms collected for all micrographs of BFCN films are shown in the Figure 5.22.

The obtained different parameters like; rms roughness, average roughness, height of maximum available peak, maximum peak height and maximum valley depth are presented in the Table 5.2. The surface roughness of the BFCN films decreases on irradiating the films with O^{7+} ions. The lowest roughness is found for the O^{7+} fluence 5×10^{12} ions per cm^2 (BFCN-An-B). On irradiating with further higher fluence of 1×10^{13} ions per cm^2 (film BFCN-An-C) the roughness increases slightly. The height of maximum available peak (maximum available particle size) decreases on irradiating the films with O^{7+} ions.

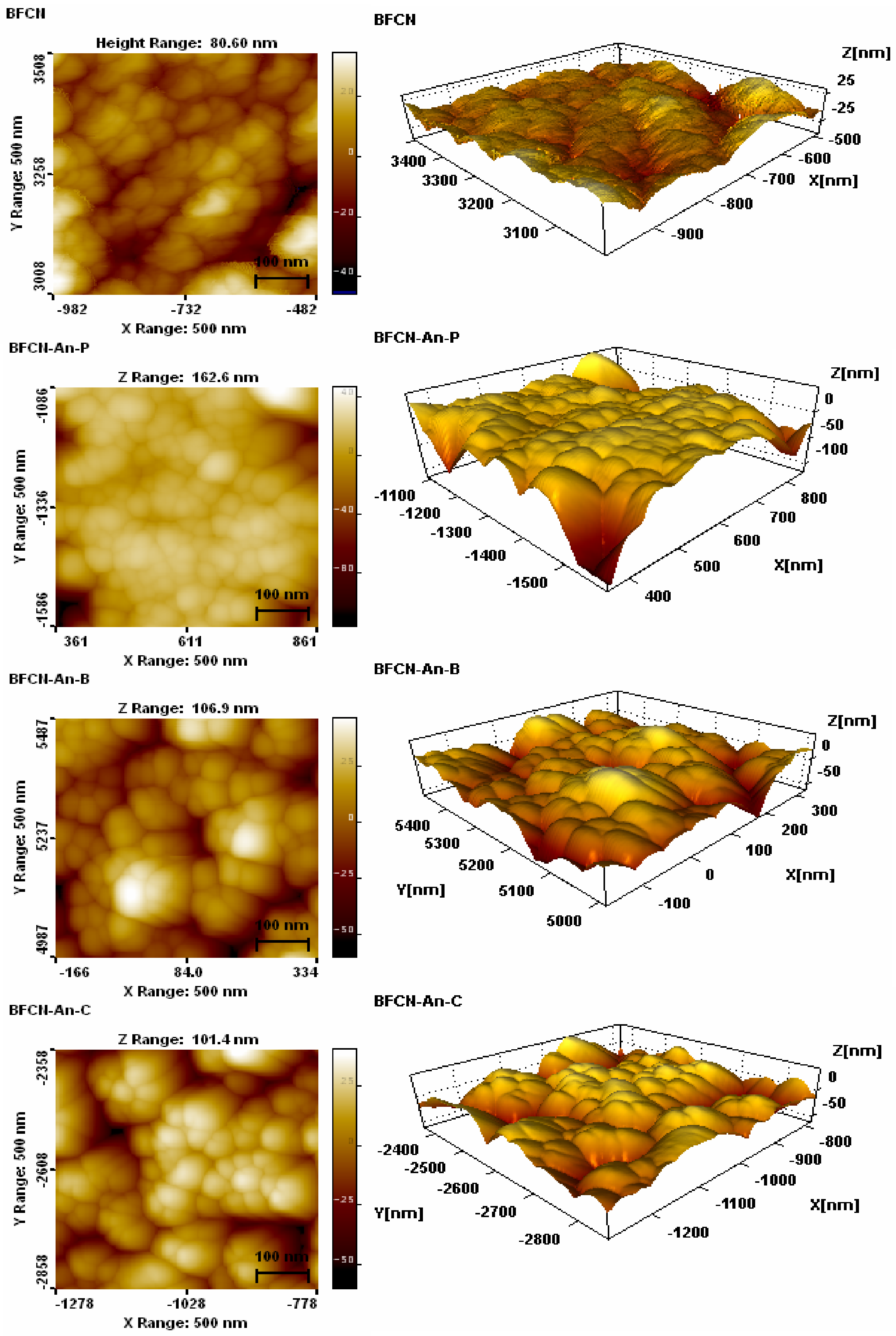

Figure 5.21: The 2D and 3D AFM micrographs for BFCN films.

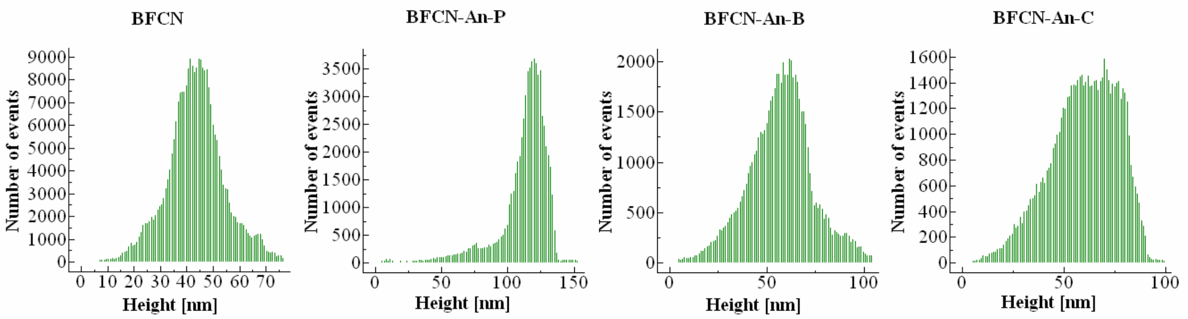

Figure 5.22: The surface roughness histogram obtained for BFCN films.

The minimum particle size is obtained for the O^{7+} fluence of 5×10^{12} ions per cm^2 (BFCN-An-B). These results are not in agreement with the variation in the crystallite size from the XRD analysis. It means that because of irradiation the particle size reduces but the crystallinity improves than that of pristine film.

5.2.4 Atomic Force Microscopy of BCN Films:

The Figure 5.23 shows 2D and 3D AFM micrographs of as prepared film (BCN), film annealed at 600 °C (BCN-An-P), film annealed and irradiated with O^{7+} fluence 5×10^{12} (BCN-An-B) and film annealed and irradiated with O^{7+} fluence 1×10^{13} (BCN-An-C). It is revealed from the images that the clusters of grains with well defined grain boundaries are developed after annealing the films. The detailed processing of the images was done in the light of roughness parameters and particle height. The surface roughness histograms collected for all micrographs of BCN films are shown in the Figure 5.24.

The obtained different parameters like; rms roughness, average roughness, height of maximum available peak, maximum peak height and maximum valley depth are presented in the Table 5.2. The surface roughness of the BCN films decreases on irradiating the films with O^{7+} ions up to fluence 5×10^{12} ions per cm^2 (BCN-An-B). On irradiating with further higher fluence of 1×10^{13} ions per cm^2 (film BCN-An-C) the roughness increases slightly. The height of maximum available peak (maximum available particle size) decreases on irradiating the films with O^{7+} ions. The minimum particle size is obtained for the O^{7+} fluence of 5×10^{12} ions per cm^2 (BCN-An-B). These results are not in agreement with the variation in the crystallite size from the XRD analysis. It means that because of irradiation the crystallinity reduces but the particle size increases for the highest fluence.

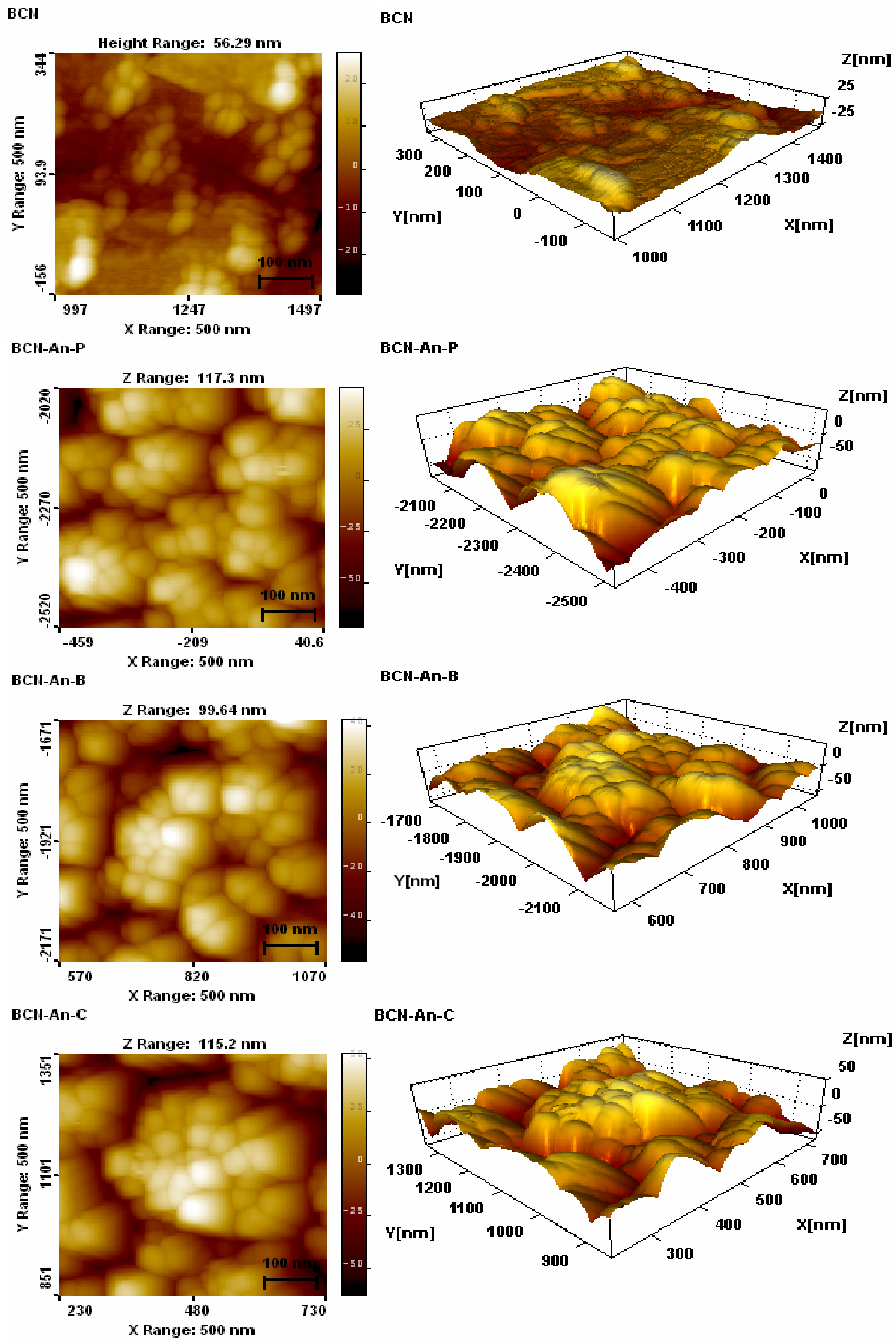

Figure 5.23: The 2D and 3D AFM micrographs for BCN films.

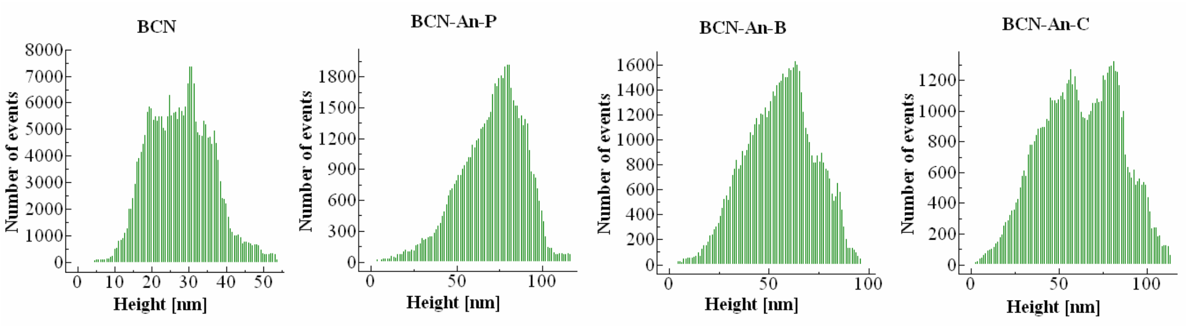

Figure 5.24: The surface roughness histogram obtained for BCN films.

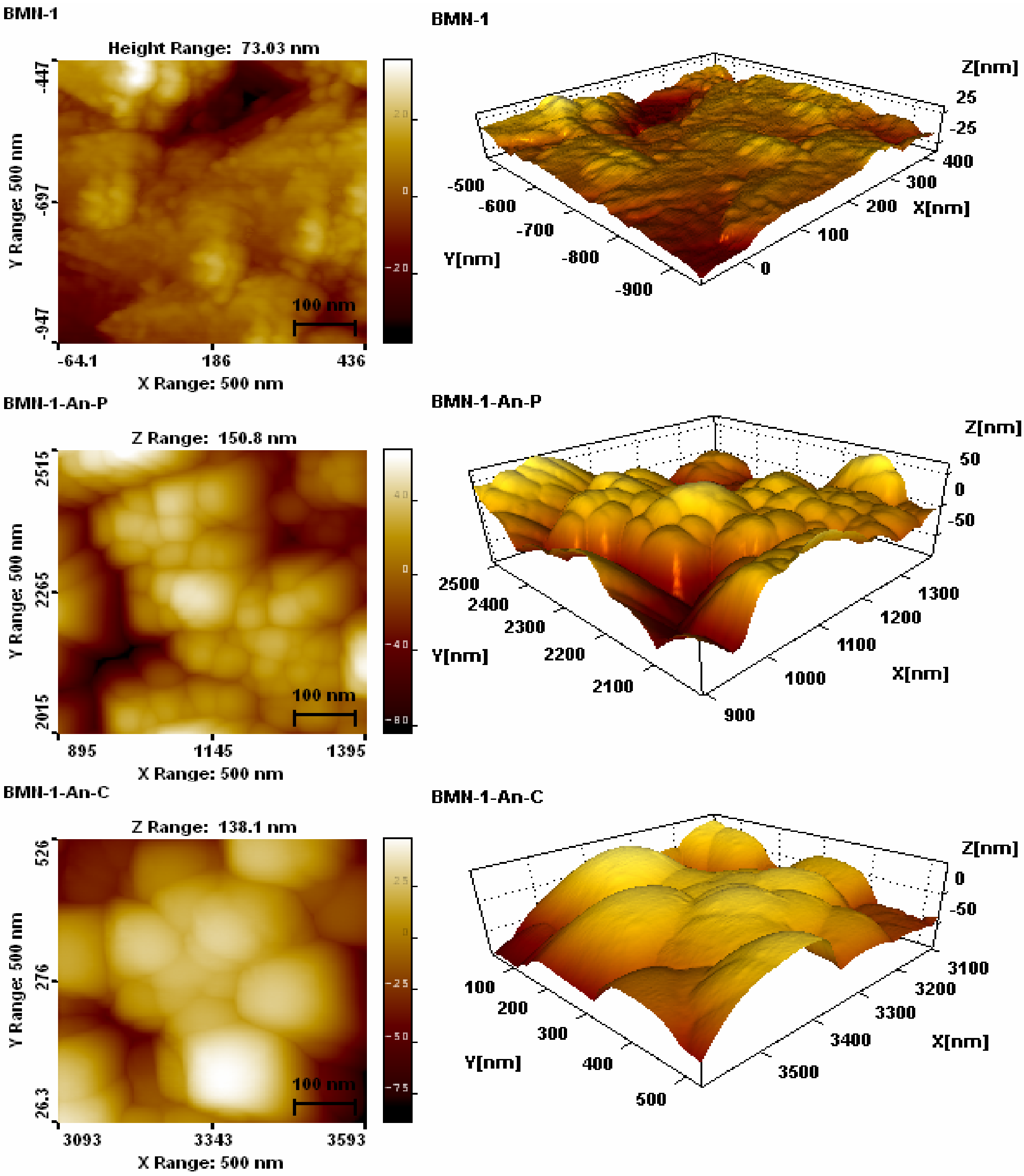

Figure 5.25: The 2D and 3D AFM micrographs for BMN-1 films.

5.2.5 Atomic Force Microscopy of BMN-1 Films:

The Figure 5.25 shows 2D and 3D AFM micrographs of as prepared film (BMN-1), film annealed at 600 °C (BMN-1-An-P) and film annealed and irradiated with O^{7+} fluence 1×10^{13} (BMN-1-An-C).

It is revealed from the images that the clusters of grains with well defined grain boundaries are developed after annealing the films. The detailed processing of the images was done in the light of roughness parameters and particle height. The surface roughness histograms collected for all micrographs of BMN-1 films are shown in the Figure 5.26.

The obtained different parameters like; rms roughness, average roughness, height of maximum available peak, maximum peak height and maximum valley depth are presented in the Table 5.2. The surface roughness of the BMN-1 films decreases on irradiating the films with O^{7+} ions. The height of maximum available peak (maximum available particle size) also decreases on irradiating the films with O^{7+} ions. These results are in agreement with the variation in the crystallite size from the XRD analysis.

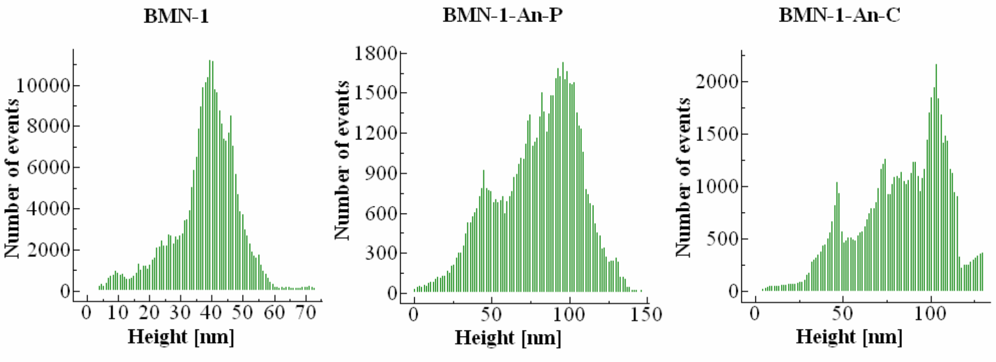

Figure 5.26: The surface roughness histogram obtained for BMN-1 films.

5.2.6 Atomic Force Microscopy of BMN-3 Films:

The Figure 5.27 shows 2D and 3D AFM micrographs of as prepared film (BMN-3), film annealed at 600 °C (BMN-3-An-P), film annealed and irradiated with O^{7+} fluence 5×10^{12} (BMN-3-An-B) and film annealed and irradiated with O^{7+} fluence 1×10^{13} (BMN-3-An-C). It is revealed from the images that the clusters of grains with well defined grain boundaries are developed after annealing the films. The detailed processing of the images was done in the light of roughness parameters and particle height. The surface roughness histograms collected for all micrographs of BMN-3 films are shown in the Figure 5.28.

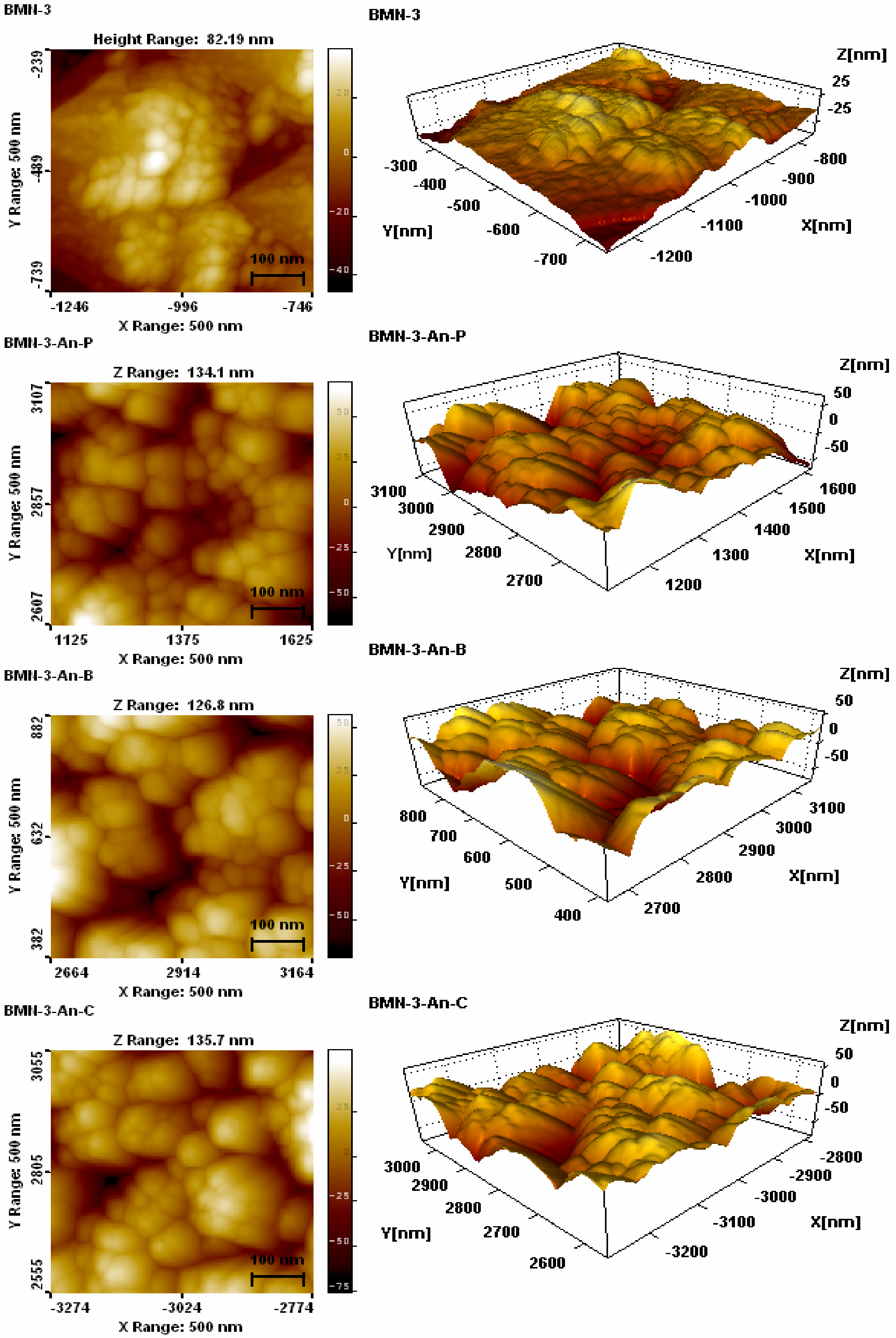

Figure 5.27: The 2D and 3D AFM micrographs for BMN-3 films.

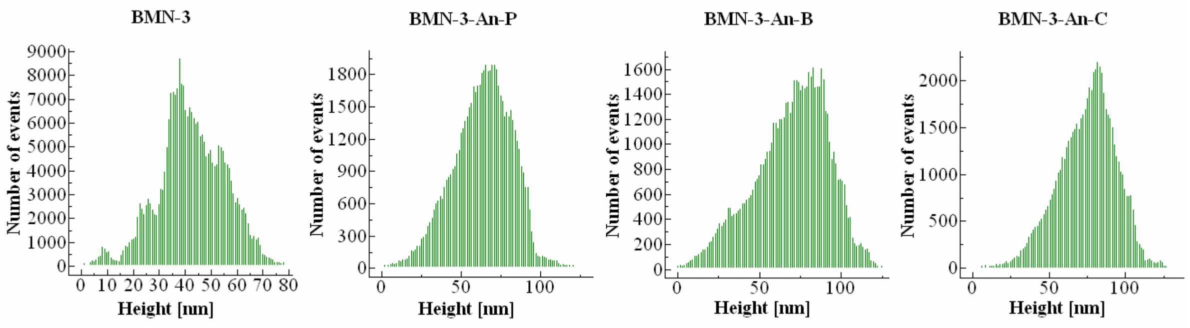

Figure 5.28: The surface roughness histogram obtained for BMN-3 films.

The obtained different parameters like; rms roughness, average roughness, height of maximum available peak, maximum peak height and maximum valley depth are presented in the Table 5.2. The surface roughness of the BMN-3 films increases on irradiating the films up to O^{7+} fluence 5×10^{12} ions per cm^2 (BMN-3-An-C). On irradiating with further higher fluence of 1×10^{13} ions per cm^2 (film BMN-3-An-C) the roughness decreases slightly. The height of maximum available peak (maximum available particle size) also increases on increasing the irradiation fluence. These results are not in agreement with the variation in the crystallite size from the XRD analysis. It means that because of irradiation the crystallinity reduces but the particle size increases.

5.2.7 Atomic Force Microscopy of BGCN-1 Films:

The Figure 5.29 shows 2D and 3D AFM micrographs of as prepared film (BGCN-1), film annealed at 600 °C (BGCN-1-An-P), film annealed and irradiated with Ag^{15+} fluence 1×10^{12} (BGCN-1-An-A) and film annealed and irradiated with Ag^{15+} fluence 5×10^{12} (BGCN-1-An-B). It is revealed from the images that the clusters of grains with well defined grain boundaries are developed after annealing the films. The detailed processing of the images was done in the light of roughness parameters and particle height. The surface roughness histograms collected for all micrographs of BGCN-1 films are shown in the Figure 5.30.

The obtained different parameters like; rms roughness, average roughness, height of maximum available peak, maximum peak height and maximum valley depth are presented in the Table 5.2. The surface roughness of the BGCN-1 films decreases on irradiating the films with Ag^{15+} ions up to fluence 1×10^{12} ions per cm^2 (BGCN-1-An-A). On irradiating with further higher fluence of 5×10^{12} ions per cm^2 (film BGCN-1-An-B) the roughness suddenly increases.

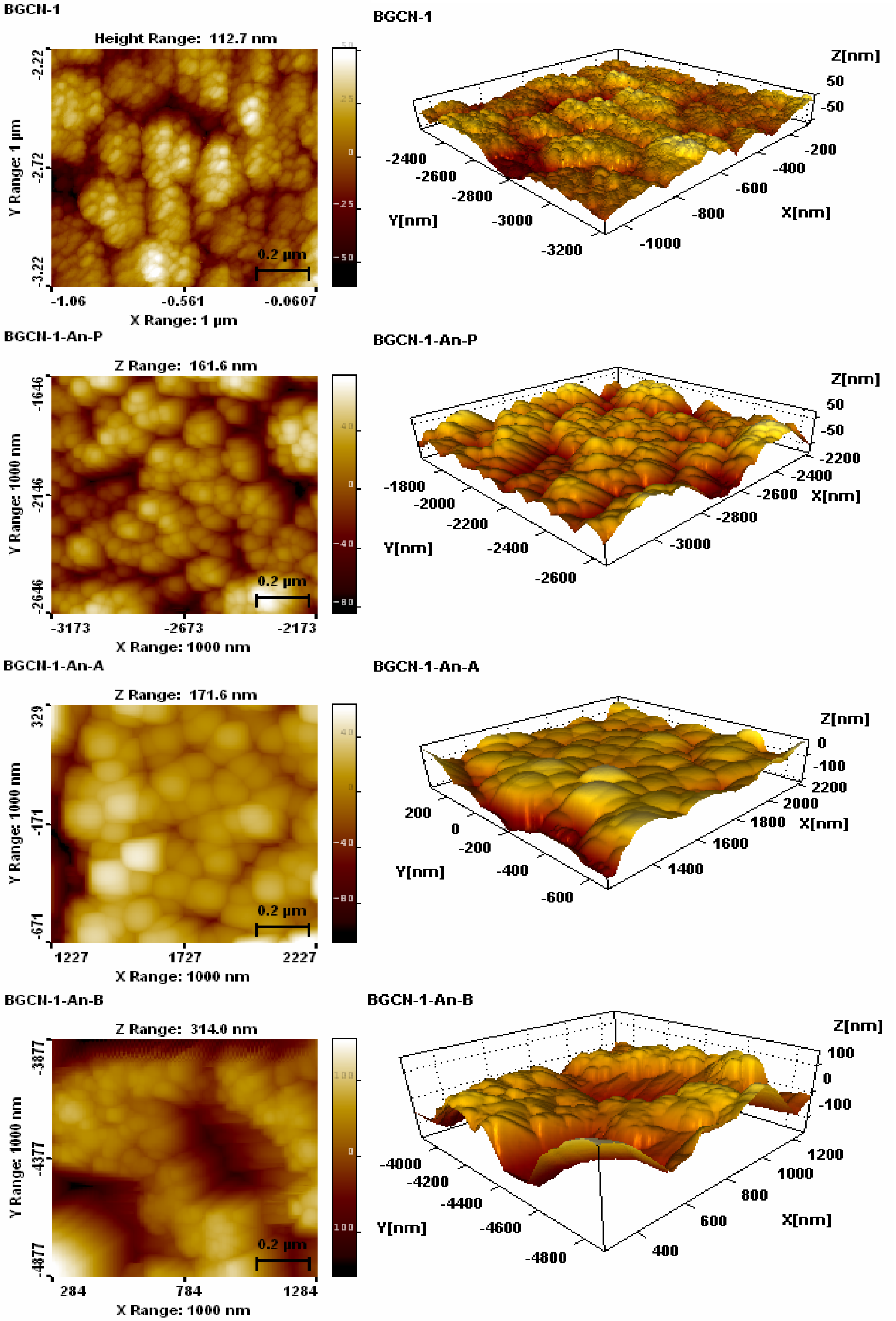

Figure 5.29: The 2D and 3D AFM micrographs for BGCN-1 films.

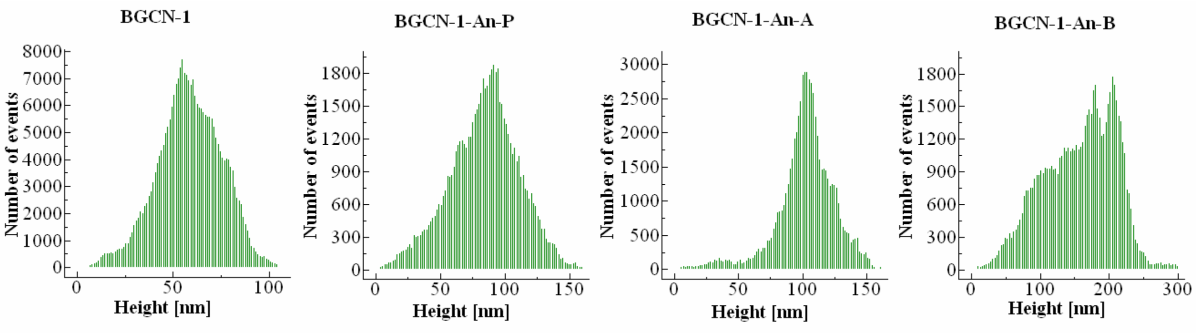

Figure 5.30: The surface roughness histogram obtained for BGCN-1 films.

The height of maximum available peak (maximum available particle size) also shows similar sharp increment with the highest fluence of Ag^{15+} ions. These results are not in agreement with the variation in the crystallite size from the XRD analysis. The observed sudden increase in the roughness may be due to increased fluence of the very high energy of Ag^{15+} ions (200 MeV).

5.2.8 Atomic Force Microscopy of BGCN-10C-2 Films:

The Figure 5.31 shows 2D and 3D AFM micrographs of as prepared film (BGCN-2), film annealed at 600 °C (BGCN-2-An-P), film annealed and irradiated with O^{7+} fluence 5×10^{12} (BGCN-2-An-B) and film annealed and irradiated with O^{7+} fluence 1×10^{13} (BGCN-2-An-C). It is revealed from the images that the clusters of grains with well defined grain boundaries are developed after annealing the films. The detailed processing of the images was done in the light of roughness parameters and particle height. The surface roughness histograms collected for all micrographs of BGCN-2 films are shown in the Figure 5.32.

The obtained different parameters like; rms roughness, average roughness, height of maximum available peak, maximum peak height and maximum valley depth are presented in the Table 5.2. The surface roughness of the BGCN-2 films decreases on irradiating the films with O^{7+} fluence 5×10^{12} ions per cm^2 (BGCN-2-An-B). On irradiating with further higher fluence of 1×10^{13} ions per cm^2 (film BGCN-2-An-C) the roughness increases slightly than the pristine film. The height of maximum available peak (maximum available particle size) decreases on irradiating the films with O^{7+} ions. The smallest particle size is obtained for the O^{7+} fluence of 5×10^{12} ions per cm^2 (BGCN-2-An-B) and is increases suddenly for the O^{7+} fluence of 1×10^{13} ions per cm^2 (BGCN-2-An-C). The similar behavior is observed in the crystallite size analysis from the XRD up to the O^{7+} fluence of 5×10^{12} ions per cm^2 (BGCN-2-An-B).

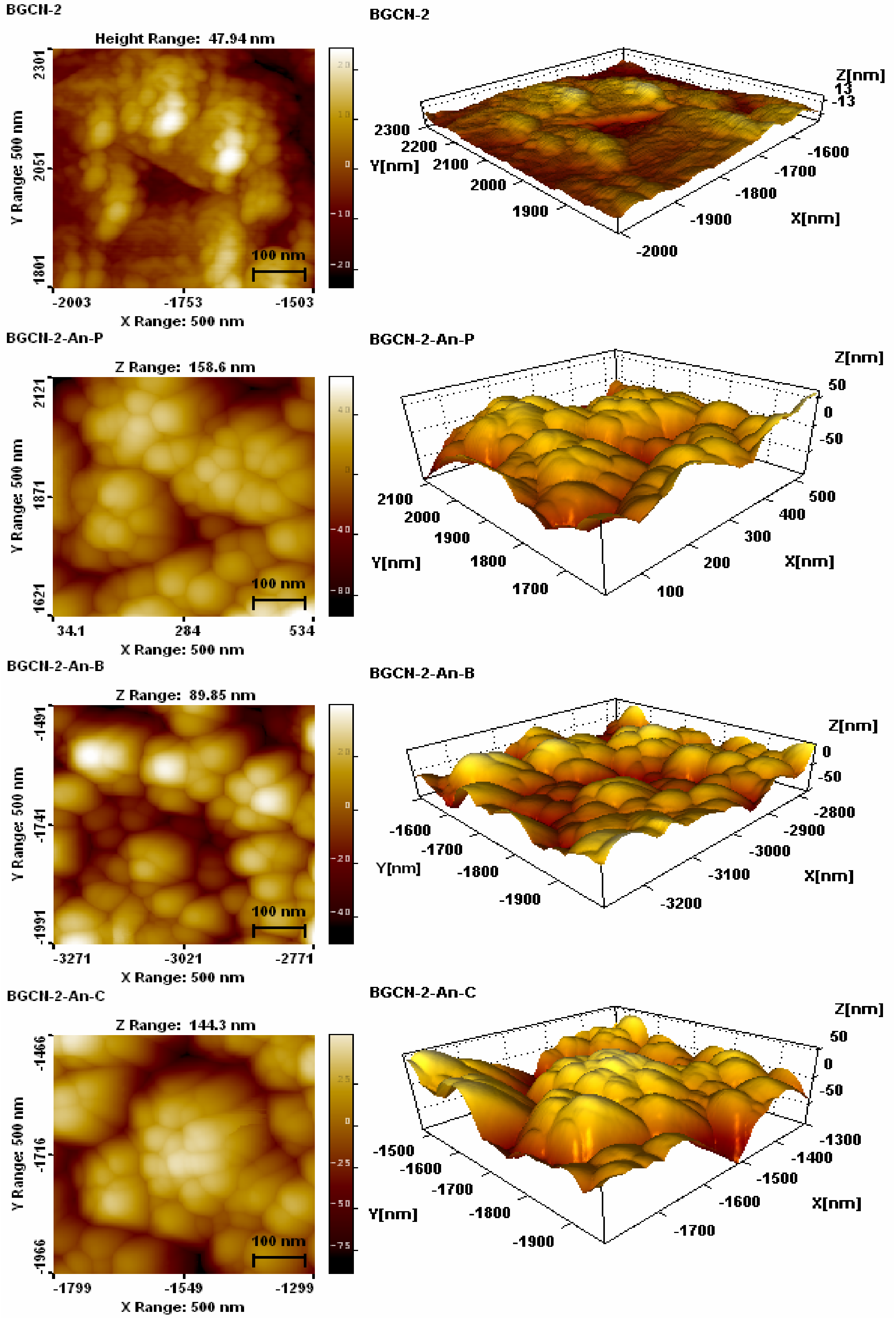

Figure 5.31: The 2D and 3D AFM micrographs for BGCN-2 films.

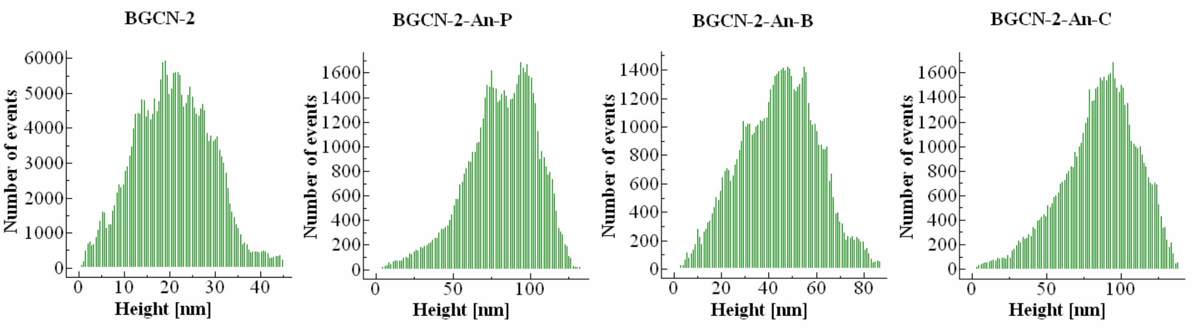

Figure 5.32: The surface roughness histogram obtained for BGCN-2 films.

The structure destroys at further higher fluence of of 1×10^{13} ions per cm^2 (BGCN-2-An-C). These results suggest that the films could not sustain the BGCN phase at such higher fluence of O^{7+} ions.

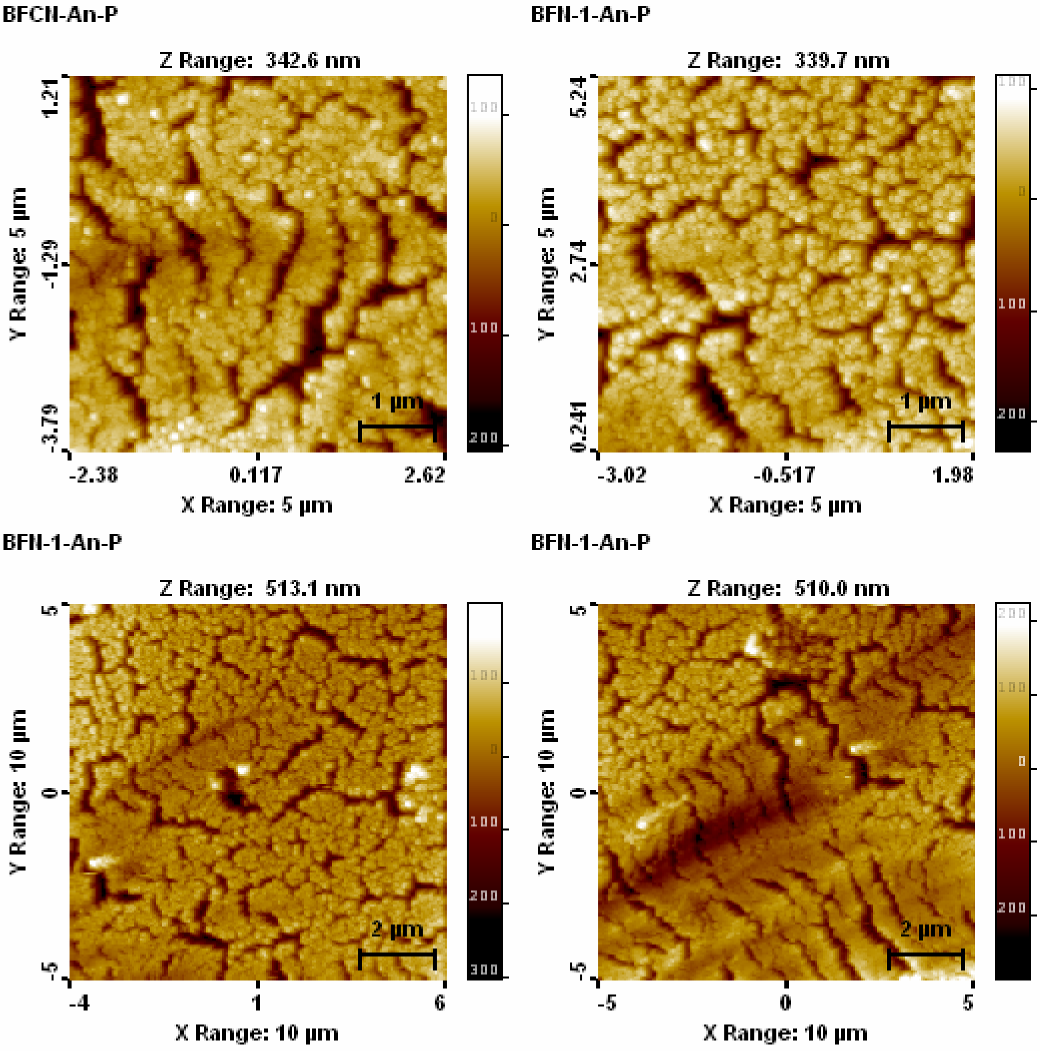

Figure 5.33: The micro cracks observed in AFM micrographs of annealed films.

5.2.9 Observation of the Micro Cracks using Atomic Force Microscopy:

The Figure 5.33 represents micro cracks observed through AFM images. It is clearly evident from the surface features of the films that the micro cracks are developed in the films after annealing the films at 600 °C. The similar micro cracks are observed for majority of the samples. The estimated length of such cracks varies from 1 μm to 7 μm with 0.3 μm width. These typical dimensions of the micro cracks are comparatively larger than the film thickness of ~2000 Å (0.2 μm). Therefore these films can not be utilized for further electrical characterization.

5.3 Optical Spectroscopy: Ultra Violet - Visible (UV-Vis.) Spectroscopic Analysis:

The UV-Vis. spectroscopy is primarily useful to determine the energy band gap of semi-conducting materials. The optical characterization of the prepared thin films was performed by UV–vis transmittance measurements. The inset figures presented in the graphs of Figure 5.34 shows such collected transmittance data plotted against the energy of incident photons for the pristine thin films. The optical absorption coefficient, α; can be calculated from the transmittance data using the formula:

$$\alpha = \frac{1}{d}\ln\left(\frac{1}{T}\right) \qquad \ldots\ldots (5.1)$$

where, d is thickness of the films and T is the transmittance. The relation between incident photon energy $h\nu$ and absorption co-efficient α can be given by well-known Davis and Mott equation [4]:

$$\alpha h\nu = \left[D\left(h\nu - E_g\right)\right]^{\gamma} \qquad \ldots\ldots (5.2)$$

where, constant D is the edge width parameter and E_g represents energy band gap. The parameter γ depends on the type of transition occurs in the material. In the present case we considered $\gamma = 1/2$ corresponding to the direct allowed transition.

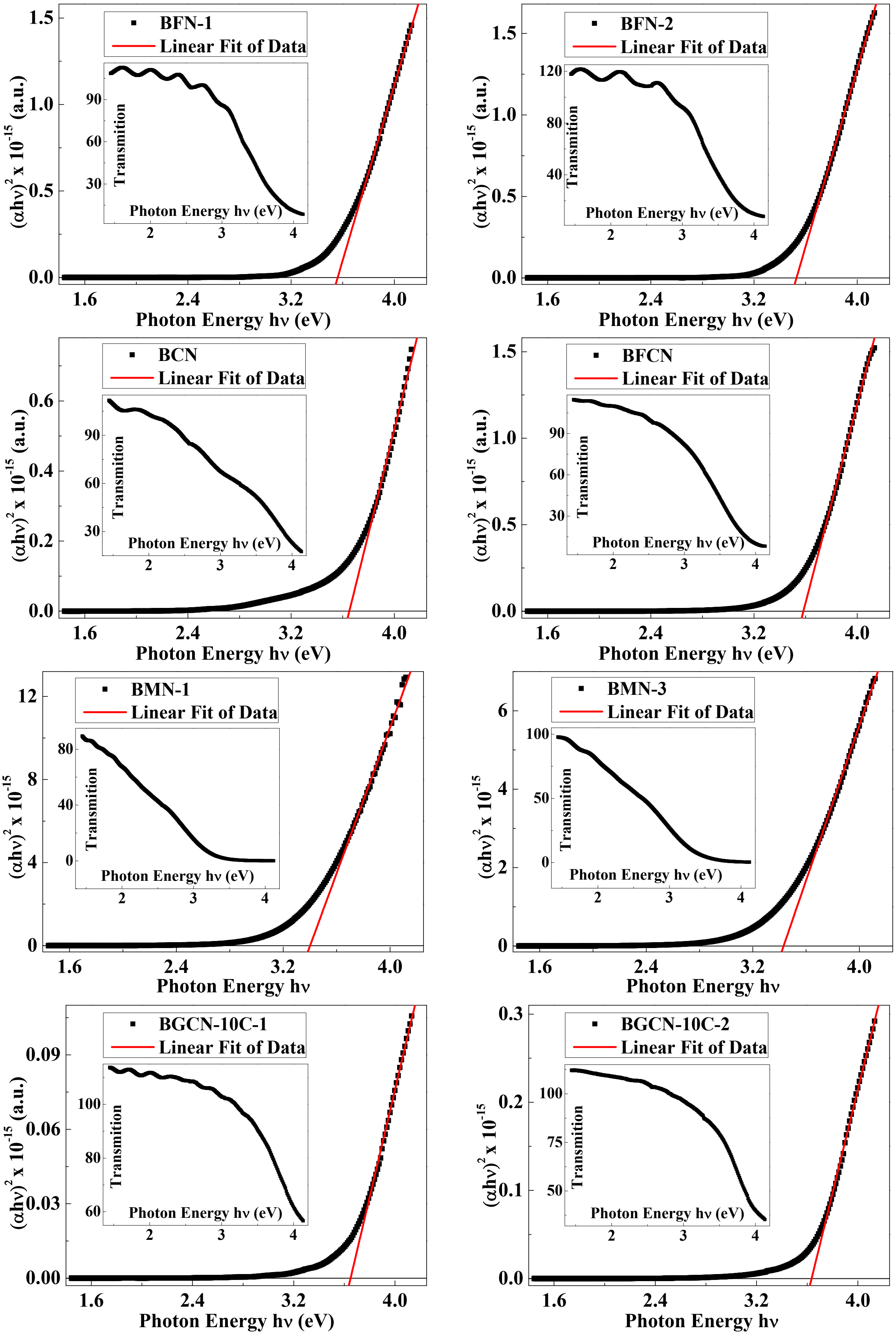

Figure 5.34: The Tauc's plot for pristine thin films obtained from the UV-VIS transmittance data. Inset shows oscillations in transmittance data.

The plot between $(\alpha h\nu)^2$ and $h\nu$, generally known as Tauc's plot [5-6], is developed for all the pristine films to calculate activation energy values. The direct band gap energy E_g can be obtained by extrapolating the linear part of the Tauc's plot.

Sr. No	**Film**	**Formula/Substrate**	**Optical Band Gap Energies Eg (eV)**
1	BFN-1	$Ba(Fe_{0.5}Nb_{0.5})O_3$/ITO/Glass	3.56
2	BFN-2	$Ba(Fe_{0.5}Nb_{0.5})O_3$/ITO/Glass	3.53
3	BFCN	$Ba(Fe_{0.25}Co_{0.25}Nb_{0.5})O_3$/ITO/Glass	3.58
4	BCN	$Ba(Co_{0.5}Nb_{0.5})O_3$/ITO/Glass	3.65
5	BMN-1	$Ba(Mn_{0.5}Nb_{0.5})O_3$/ITO/Glass	3.40
6	BMN-3	$Ba(Mn_{0.5}Nb_{0.5})O_3$/ITO/Glass	3.43
7	BGCN-1	$Ba(Gd_{0.40}Co_{0.10}Nb_{0.5})O_3$/ITO/Glass	3.65
8	BGCN-2	$Ba(Gd_{0.40}Co_{0.10}Nb_{0.5})O_3$/ITO/Glass	3.63

Table 5.3: The optical band gap values obtained from Tauc's plot.

The Figure 5.34 represents such Tauc plots for all pristine films. The obtained values of energy band gap E_g are presented in the Table 5.3. The obtained values of energy band gap E_g (in the range of 1.8 eV to 3.2 eV) suggest that our samples belong to a category of wide band gap semiconductors. The observed oscillating nature of the transmittance data in the inset images of the graphs is likely due to the interference effects. Similar oscillations were reported when transparent thin films are deposited on transparent substrates [7-8].

5.4 Electrical Characterization:

It is mentioned in the section 5.2.9 that the electrode formation on the surface of the film is not possible due to the observed micro cracks in the AFM micrographs. How ever the electrical characterization of BFN-2 films has been performed as it contains negligible micro cracks. The resistivity analysis, capacitance studies and dielectric loss measurements have been performed on these films.

The temperature dependent resistivity of BFN-2 films at 1 kHz frequency is shown in the Figure 5.35. The overall resistivity values decreases with increase in the irradiation fluences of O^{7+} ions. The observed drop off in resistivity values suggests development of defects like oxygen vacancies caused by the columnar defects generated by the fast moving ions. The fast moving ions loose their energy and creates track with local defects during the trajectory through matter. These local defects can trap the charges and enhance the charge asymmetry. This type of defects increases the carrier concentration of electrons and holes.

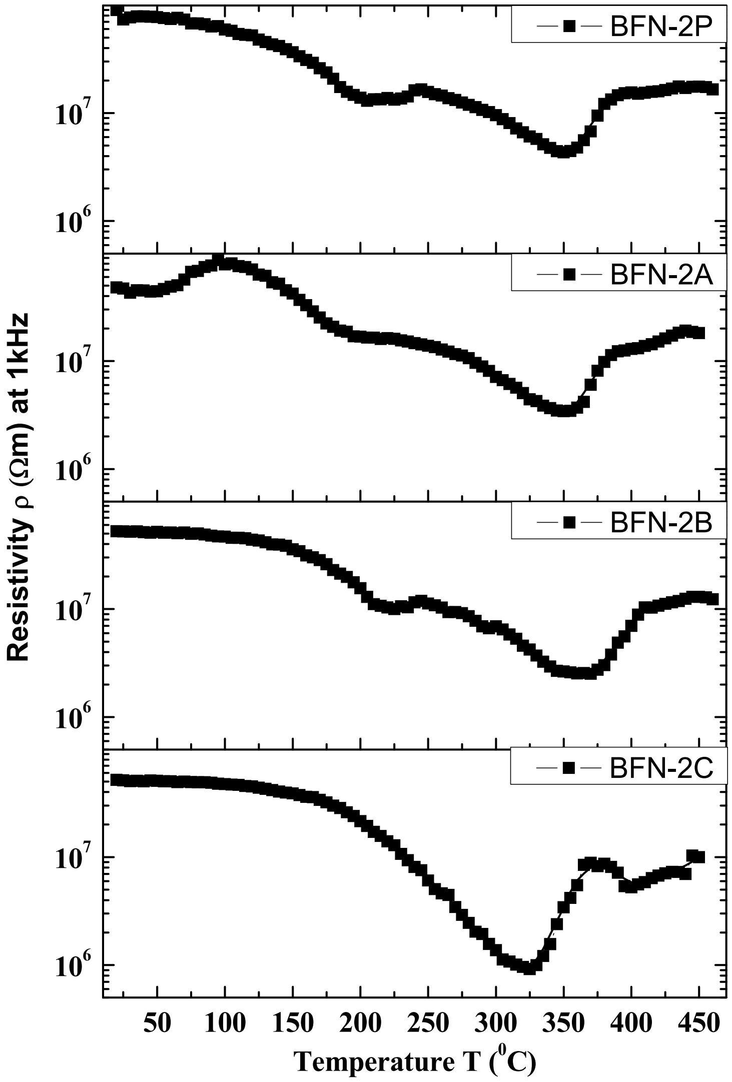

Figure 5.35: The temperature dependent resistivity data of BFN-2 films at 1 KHz frequency.

In general temperature dependent resistivity can be given by Arrhenius equation:

$$\rho = \rho_0 e^{\left(\frac{E_a}{kT}\right)} \qquad \ldots\ldots (5.3)$$

where, ρ_0 is resistivity at infinite temperature, E_a is activation energy, k is Boltzmann constant and T is absolute temperature. This equation suggests monotonic logarithmic variation in the resistivity data. The Figure 5.35 clearly shows that the resistivity of BFN-2 films decreases with increase in temperature up to 350 °C. This suggests normal semi-conducting behavior of the films; following the above Equation 5.3. The resistivity makes a valley and starts increasing with temperature above 350 °C. This typical nature of films indicates metal like conduction in the films. Such change in the nature of resistivity curve points towards presence of a phase transition. It may also be due to possible change in the mechanism of conduction. During such transition the activation energy values do not remain constant. Hence such behavior of resistivity could not be explained by Arrhenius equation. For further analysis of such unanticipated resistivity data we calculated temperature dependent activation energies using derivative Equation 5.4 [9-10]:

$$E_a = k\frac{d\ln\rho}{d\left(1/T\right)} \qquad \text{…… (5.4)}$$

Further, the observed change in the nature of resistivity at 350 °C can be analyzed effectively through the temperature co-efficient of resistance (TCR). It is also a very useful tool for investigation of conduction mechanism along with temperature dependent activation energy analysis. The TCR can be calculated from the resistivity data using following Equation 5.5 [11]:

$$\mathrm{TCR} = \frac{1}{R}\frac{dR}{dT} = \frac{1}{\rho}\frac{d\rho}{dT} \qquad \text{…… (5.5)}$$

The temperature dependent activation energy values and temperature dependent TCR values for the BFN-2 films are presented in the Figure 5.36(a) and Figure 5.36(b) respectively. It is clearly evident from the figure that the activation energy E_a remains constant in the region near to room temperature. The typical low values (~0.1 eV) of E_a suggests that the conduction in this region is dominated by the free charge carriers like electrons trapped at singly ionized oxygen vacancies [12-15]. On increasing the temperature from room temperature to 200 °C, the singly ionized oxygen vacancies makes a transition to doubly ionized oxygen vacancies. This is reflected through increase in activation energy to ~0.5 eV.

A normal behavior of semi conducting thin films is to show negative temperature co-efficient of resistance (NTCR) where as metallic behavior is linked to positive temperature co-efficient of resistance (PTCR). In the present case the BFN-2 films show number of transitions between NTCR-PTCR up to 300 °C. As mentioned in our paper [12] the higher dose of SHI irradiation using O^{7+} on BFN films suppress such NTCR-PTCR transitions. The observed behavior points that the origin of these transitions is purely due to local variation in the defects. But in contrast a strong NTCR-PTCR transition at 350 °C could not be eliminated by means of SHI irradiation of O^{7+} in BFN films. The transition found splitted in to two for highest fluence of O^{7+}. Similar variation is observed for the E_a values also. In addition the activation energy values decreases sharply up to ~ -2.0 eV and again sharply rises to positive values. These results clearly suggest that the transition observed at ~350 °C is not only related with the changes in the conduction mechanism but it is also related with a structural transition linked electrical or magnetic phase transition. The observed sudden transition and its temperature variations with irradiation fluence can be effectively used to prepare electrical/magnetic switching semi-conducting device.

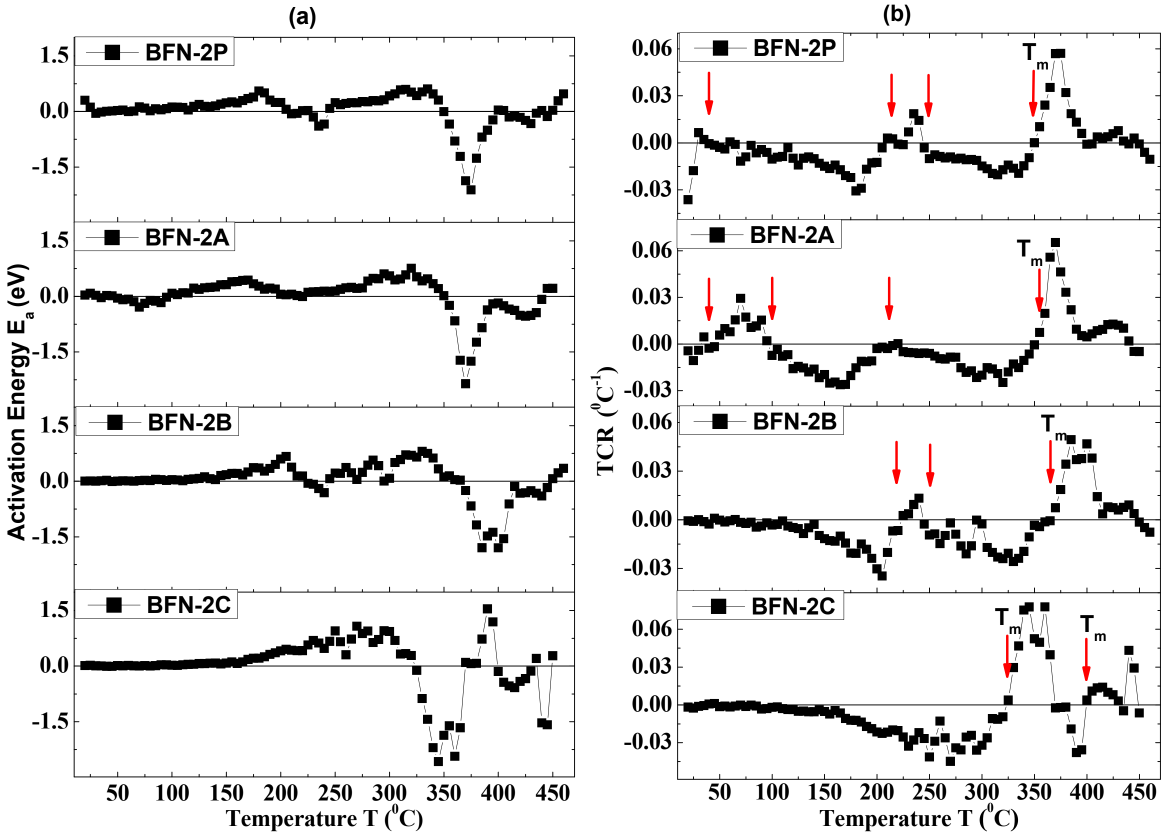

Figure 5.36: The temperature dependent (a) activation energy values and (b) TCR values for BFN-2 films.

The temperature dependent dielectric analysis of the films is shown in the Figure 5.37. The Figure 5.37(a) shows variation of capacitance and dielectric loss at 1 MHz frequency with variation of temperature. The capacitance of the irradiated films improves along with significant decrement in the dielectric loss. The irradiation of film by O^{7+} ion results in improvement of the quality factor. As discussed in our paper [13] the temperature dependent analysis of electrical data shows two dielectric relaxation peaks in the capacitance vs. temperature curves. The overall capacitance also increases with increment in temperature while the dielectric loss remains nearly unaffected.

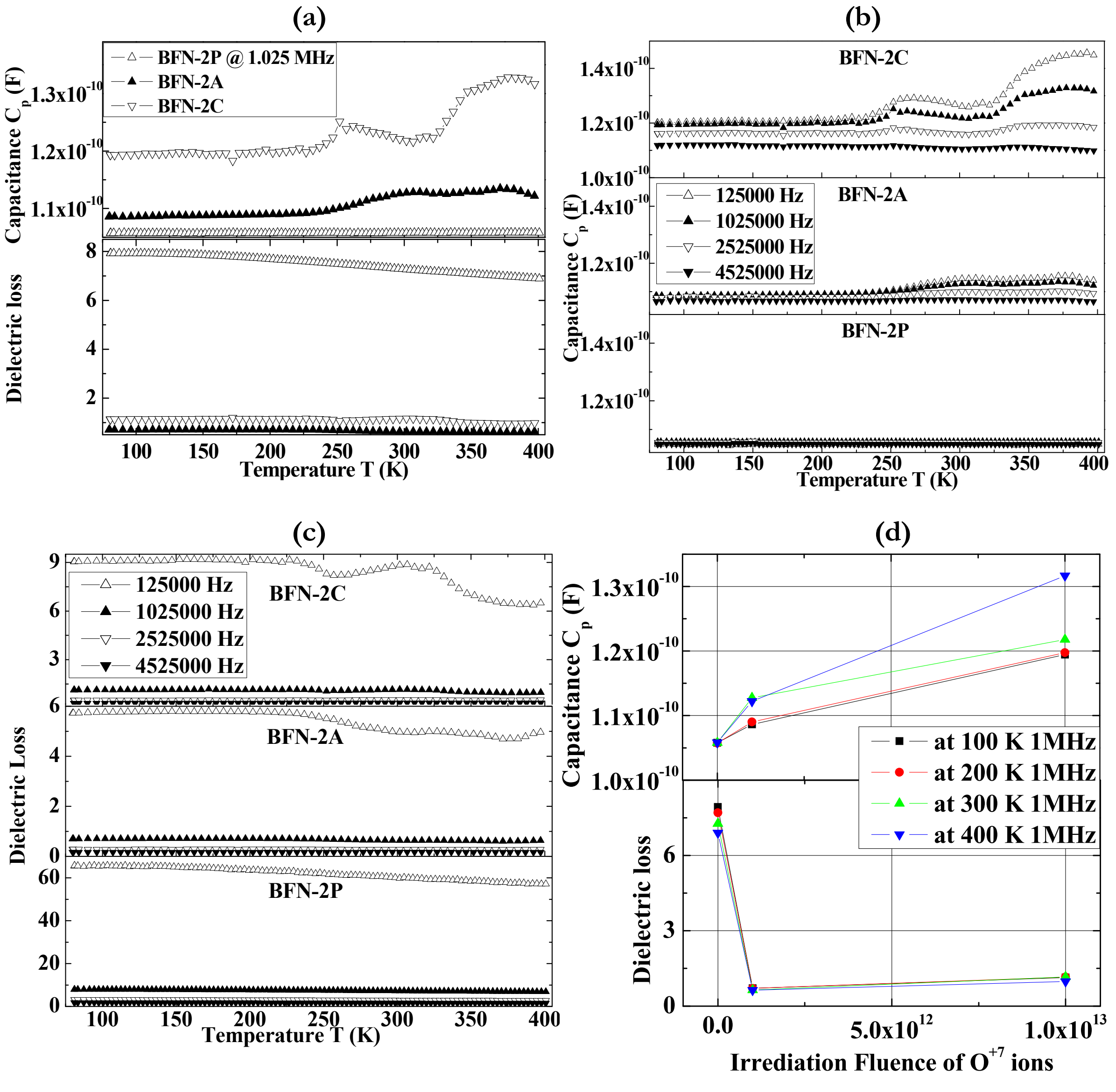

Figure 5.37: (a) The temperature dependent comparison of capacitance and dielectric loss for BFN-2 films. The temperature dependent (b) capacitance and (c) dielectric loss at four different frequencies for BFN-2 films. (d) The variation of capacitance and dielectric loss with different irradiation fluence of O^{7+} ion at four different temperatures measured at 1 MHz frequency.

The in depth analysis of the data is done along with the variation of frequency. The Figure 5.37(b) shows temperature variation of capacitance at four different frequencies. The values of capacitance for pristine film are found to be very small. The frequency or temperature dispersion is not observed for pristine film. On the other hand irradiated films shows increase in dispersion with increment in O^{7+} ion fluences. Further, the dielectric relaxation has also been introduced due to irradiation. For the first fluence of 1×10^{12} ions/cm^2 a very broad relaxation peak is observed. The same peak is enhanced and splitted in two by increasing the fluence up to 1×10^{13} ions/cm^2. The enhancement in capacitance as well as introduction of dielectric relaxations with irradiation is caused by the columnar defects generated by the fast moving ions as pointed out earlier.

The Figure 5.37(c) shows variation of dielectric loss with frequency as well as temperature variation for different thin film samples. The comparison shows very high dielectric losses for the pristine films. Further, variation of dielectric loss does not show any relaxation similar to the capacitance data. We observed that on irradiation, films show reduction in dielectric losses as well as frequency dependency. The reduction in dielectric loss can be explained using the thermal spike model [14-15]. Model suggests that sudden energy loss by fast moving ion causes local heating at the molecular size. Such localized heating induces local annealing resulting in rapid re-crystallization and reduction in imperfections induced by oxygen vacancies [15]. The reduction in oxygen vacancies and/or pinning of charge carrier is the likely reason for the observed reduction in dielectric loss. We do observe marginal increase in dielectric loss for the highest fluence of 1×10^{13} ions/cm^2 (see Figure 5.37(d)). This marginal rise could be due to the observed marginal increase in strain which enhances both the capacitance and the dielectric loss.

5.5 Summary of Thin Film Characterization:

Here, we have successfully synthesized thin films of complex ceramic compounds on ITO/glass substrate using PLD technique. The pure single phase is developed through annealing the films in air at 600 °C. The microstructure photographs of the films have revealed that the grains and clusters are developed on irradiating the films with O^{7+} ions. The O^{7+} ion irradiation also helps to improve the crystallinity of the samples. Over all crystal structure of the films remains nearly unaffected up to the fluence of 1×10^{13} ions per cm^2 SHI irradiation using O^{+7} except for BCN and BGCN films. All these films exhibit band gap in wide band semi-conductor region.

The electrical properties of the BFN-2 films can be suitably modified using the SHI irradiation. The film capacitance increases and the loss decreases significantly with the help of 100 MeV O^{7+} ion irradiation. The SHI irradiation not only modifies the grain boundary strain but also creates local defects. The collective effect of strain reduction and creation of defects can be a valuable tool to tune the dielectric properties of these films. Further, a prominently large NTCR to PTCR transitions is observed at 350 ºC. The origin of this transition is likely to be a temperature dependent structure phase transition rather then a local fluctuating defects. Such a phase transition may be linked with electrical/magnetic phase transition. This makes BFN film a promising candidate as switching device. Further, the switching temperature can also be modified using appropriate SHI irradiation fluence.

References:

1. B. D. Cullity, The Structure of Polycrystalline Aggregates, in Elements of X-ray diffraction, Massachusetts, U.S.A.: Addison-Wesley Publishing Company, Inc., pp. 259-296 (1956).
2. G. K. Williamson and W. H. Hall, Acta Metall. **1,** 22 (1953).
3. S. Pratapa and B. O'Connor, Adva.. X-ray Anal. **45,** 41 (2002).
4. E. A. Davis and N. F. Mott, Philos. Mag. **22,** 903 (1970).
5. M. H. Habibi and N. Talebian, Acta Chim. Slov. **52,** 53 (2005).
6. J. Tauc, Mater. Res. Bull. **5,** 721 (1970).
7. R. Swanepoel, J. Phps. E: Sci. Instrum. **16,** 1214 (1983).
8. C. Mansilla, Solid State Sci. **11,** 1456 (2009).
9. D. D. Shah, P.K. Mehta, M.S. Desai, C.J. Panchal, J. of Alloys and Comp. **509,** 1800 (2011).
10. J. Jadzyn, D. Baumen, J. L. Dejardin, M. Ginovska and G. Czechowski, Acta Phys. Pol. A **108,** 479 (2005).
11. J. L.Wang, Y. S. Lai, S. C. Liou, C. C. Tsai1, B. S. Chiou and H. C. Cheng, J. Phys. D: Appl. Phys. **41,** 085304 (2008).
12. D. D. Shah, P. K. Mehta, M. S. Desai, C. J. Panchal, J. Nano Electron. Phys. **3(1),** 330 (2011).
13. D. D. Shah and P. K. Mehta, to be published in conference proceedings of Solid State Nuclear Track Detector-17 (SSNTD-17) (2012).
14. S. Chandramohan, R. Sathyamoorthy, P. Sudhagar, D. Kanjilal, D. Kabiraj, K. Asokan, V. Ganesan, T. Shripathi, U.P. Deshpande, Appl Phys A. **94,** 703 (2009).
15. R. Kumar, R. J. Choudhary and S. I. Patil, Solid State Commun. **106,** 805 (1998).

CHAPTER 6

Summary of the Work and Future Scope

(Summary of Results, Overall Conclusions, Scope for Future works)

This chapter mainly compiles all the major achievements and concrete conclusions of the work. The over all conclusions of the studies meeting the final requirement of the thesis are presented here. At the end future scope of the above work is discussed in brief.

The major findings, achievements and results are summarized here. The summary is followed by the scopes for future work in this area.

6.1 Summary of Results:

The samples of complex ceramic oxides have been synthesized without the presence of any impurity phase by conventional ceramic synthesis method. These compounds are prepared by gradual substitution of Fe in $Ba(Fe_{0.5}Nb_{0.5})O_3$ by 3d transition elements; Co, Mn and 4f rare earth elements; Gd, Eu and Y. The formation of pure single/double phase of identical matrix is confirmed through fitting the XRD patterns. The compounds BFN, BCN, BMN, BGN, BEN, BYN, BFCN-10C, BFCN, BFCN-40C, BFMN and BGCN-10C have exhibited single phase formation while the compounds BFGN, BFEN, BGCN and BECN have shown double phase formation with identical matrix. The analysis of the XRD patterns revealed that each of these phases has cubic symmetry. The SEM images of the samples have promised the batter densification of the samples with less porosity. The good quality of the samples has been confirmed through values of percentage densification calculated from the structural parameters. The crystallite size as well as induced lattice strain is also determined from the XRD patterns for each phase of the compounds. The thermal analysis of the compounds suggests very broad transition induced by oxygen vacancies for BFN, BFCN and BCN compounds. The BEN compound has shown a weak sharp transition at higher temperature which could be a possible phase transition. Further, the values of band gap energy obtained through optical studies have confirmed the wide band gap semi conducting nature of the samples.

In contradiction to the existing theories of ferroelectricity we observed high values of dielectric constant in spite of having cubic symmetry for the samples containing 3d transition elements. On the other hand the samples not containing 3d transition elements viz.; BGN, BEN and BYN have not shown such high values of dielectric constant with similar cubic symmetry. Additionally the samples containing 3d transition elements have also simultaneously shown very high values of conductivity (dielectric loss) along with high dielectric constant. This resulted in distortion of the P-E loops (leaky nature) for the samples showing high conductivity. In depth analysis of observed high conduction induced dielectric relaxation is carried out through four different representations, viz.; impedance representation, permittivity representation, electric modulus representation and conductivity representation. The Cole-Cole model of dielectric relaxation and Jump relaxation model (JRM) of ac electrical conductivity were utilized to separate out the contribution of intrinsic (doped charges) and extrinsic factors (space charge and oxygen vacancy induced dipoles). In addition, smaller values of activation energy points at the significant contribution of oxygen vacancies. Further, the observed large variations in the electrical response of different samples suggest that the substituted elements at Fe site play a significant role in enhancing or suppressing the dielectric constant values. The studies of conduction mechanism revealed that the process of conduction is either hopping or polaron tunneling. The temperature, as well as distortions along the chains of -Nb-Fe/Co-Nb-, decides the percentage contribution of polaron tunneling and/or correlated barrier hopping to the conductivity

The magnetization studies have shown that the complex ceramic oxides BFN, BFCN, BCN and BFGN have exhibited antiferromagnetic ordering. The BGN ceramic have shown nearly ideal paramagnetic nature in the entire temperature region. On the other hand the BFN, BFCN and BCN have shown very weak signal of ferromagnetism at low temperatures. The BFN ceramic has sustained this weak ferromagnetism up to the room temperature. The observed weak ferromagnetism is attributed to the super exchange interaction between magnetic ions available in the form of ferromagnetic clusters at defects and grain boundaries. Since amount of such super exchange interactions is too small than the predominantly antiferromagnetic ordering, it resulted in to the observed lower values of magnetic moments. The thermal history dependent values of magnetic moment/susceptibility for BFN ceramic suggest spin-glass like magnetic behavior in the compound.

In order to determine the industrial usage of these ceramics we have successfully synthesized thin films of complex ceramic compounds on ITO/glass substrate using PLD technique. The pure single phase is developed through annealing the films in air at 600 °C. The SHI irradiation of the films using O^{7+} ion not only improve the microstructure but also helps to improve the crystallinity of the samples. The electrical properties of the BFN-2 films can be suitably modified using the SHI irradiation. The optical studies exhibit band gap in wide band semi-conductor region for the prepared films.

6.2 Overall Conclusion:

The observed single phase for the compounds with complete substitution of Fe by Co, Mn, Gd, Eu and Y suggests formation of homogeneous chains of unit cells containing B' site element and Nb in ordered manner; i.e. chains of –B'–Nb–B'–Nb–B'–. The charge imbalance originated by the partially negative unit cell of $BaB'O_3$ and partially positive unit cell of $BaNbO_3$ restrict them to be distributed homogeneously in order to neutralize the compound.

The observed antiferromagnetic (or paramagnetic) ordering observed at low temperatures also supports the homogeneous distribution of BaB'O_3 and $BaNbO_3$. Though the observed double phase in the compounds BFGN, BFEN, BGCN and BECN is due to co-existence of separate neutralized chains of –B_1'–Nb–B_1'–Nb–B_1'– and –B_2'–Nb–B_2'–Nb–B_2'–. Here, the difference in the atomic size of B_1' and B_2' elements produce large difference in the length of these individual chains.

Apart from having giant values of dielectric constants the observed leaky nature of P-E loop prevents the possible use of samples in ferroelectric storage applications. On the other hand the nearly constant values of giant dielectric constant in the wide temperature and frequency range shows the possibilities of use of these samples in capacitor industries or sensor devices operating at high frequencies. The in-depth analysis through electrical transport suggests that the local lattice distortions influenced by oxygen vacancies enhances the dielectric constant to such observed higher values. However, the flexibility or rigidity of the oxygen vacancies along with the doping of free charge carriers plays a crucial role in obtaining the giant level of dielectric constant along with moderate level of conductivity.

The SHI irradiation not only modifies the grain boundary strain but also creates local defects in the films of these compounds. The collective effect of strain reduction and creation of defects can be a valuable tool to tune the dielectric properties of these films. Further, the switching temperature of NTCR-PTCR transition can also be modified using appropriate SHI irradiation fluence. This makes BFN film a promising candidate as switching device.

6.3 Scope for Future Works:

The large amount of work has been carried out to obtain high values of dielectric constant in last several years. In the present work we have focused on the origin of such observed giant values of dielectric constant. In order to fulfill the industrial demand we synthesized thin films of these compounds. Apart from having giant values of dielectric constant the observed very high conductivity (dielectric loss) prevent these samples (containing 3d elements) to be utilized for industrial applications on large scale. On the other hand the samples like $BaTiO_3$ (BT) along with the rare earth doped samples BGN, BEN and BYN studied by us exhibit very low loss and comparatively low values of dielectric constant. The development of such a technique is highly desirable through which the property exhibiting giant dielectric constant (of compounds with 3d elements) can be coupled with the property of exhibiting low loss (of compounds with

4f elements). In order to obtain such a technological tuning between giant dielectric constant of BCN and negligible loss of BT we planned to prepare multilayer capacitor of these compounds.

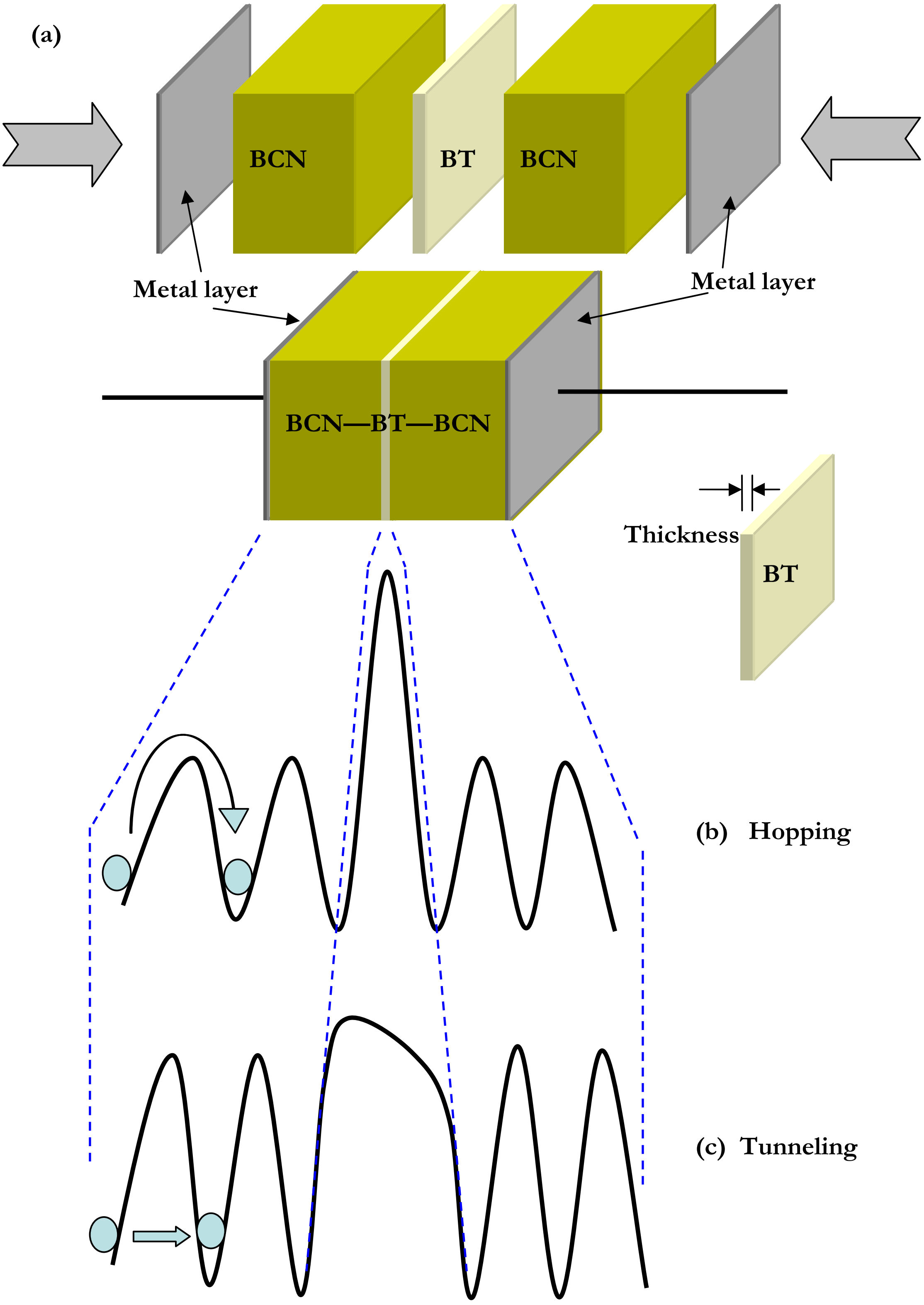

Figure 6.1: (a) A schematic diagram of proposed multilayered capacitor. The (b) and (c) represents corresponding change in hopping and tunneling barrier induced at sandwiched BT layer.

If the layers of BCN exhibiting high loss with giant dielectric constant are separated by thin layer of BT exhibiting very low loss than one can develop a material showing low loss along with high dielectric constant. The Figure 6.1 (a) shows such sandwiched multilayer.

By tuning the thickness of sandwiched BT layer we can obtain desired properties. The tuning can be done by following the two key points:

(1) Thickness of sandwich layer must be higher than Hopping/Tunneling length of the charge carriers.
(2) Thickness must be lesser than the range of ferroelectric interaction between the layers of BCN.

In this way mobility of charge carriers can be restricted satisfying increasing need of high energy storage devices.

Secondly, various types of materials have been synthesized to probe the ferroelectric nature of the materials in recent past but very little attention is given to probe the multiferroic or magneto-electric properties of these compounds. In the present work we have carried out some magnetization experiments to understand the magnetic interaction in the compounds. The observed weak ferromagnetic ordering in BFN ceramic sustains even up to room temperature. This result requires further investigation to probe observed magnetic ordering as either canted antiferromagnetism or ferromagnetism. The neutron diffraction technique is one of the best techniques to probe the local magnetic structure of compound. In addition neutron diffraction analysis can also help in identification of magnetic defect structures which could not be observed through XRD due to their poor contribution in X-ray scattering.

List of Publications in Refereed Journals:

1. "Origin of giant dielectric constant in $Ba[(Fe_{1-x}Co_x)_{1/2}Nb_{1/2}]O_3$ " by **Devang D. Shah**, P. K. Mehta, M. S. Desai and C. J. Panchal, Journal of Alloys and Compounds **509** (2011) 1800–1808
2. "Temperature dependent switching behavior of BFN thin films: a wide band gap semiconductor" by **Devang D. Shah**, P. K. Mehta, M.S. Desai and C.J. Panchal, Proceedings of International Symposium on Semiconductor Materials and Devices (ISSMD-2011) and J. Nano- Electron. Phys. **3** (2011) No1, P. 330-340.

List of Publications in Conference Proceedings:

1. "Dielectric studies of $Ba[(Fe_{1-x}Co_x)_{1/2}Nb_{1/2}]O_3$ Compounds" by **Devang Shah,** Bhagwati Bishnoi and P.K. Mehta, Proceedings of 52nd DAE-SSPS 2007 (P-867).
2. "Structural and dielectric properties of $Ba[(Mg_{1-x}Co_x)_{1/3}Nb_{2/3}]O_3$ (X=0.05)" by Bhagwati Bishnoi, **Devang Shah,** P.K.Mehta, Dinesh Shukla and Ravi Kumar, Proceedings of 52nd DAE-SSPS 2007 (P-861).
3. "Structural and Dielectric properties of $Ba[(Fe_{1-x}Co_x)_{1/2}Nb_{1/2}]O_3$ compounds" by **Devang D. Shah** and P.K. Mehta, in the one day seminar at department of Physics, The M. S. University of baroda, February-2009.
4. "Transport properties of $Ba[(Fe_{1-x}Co_x)_{1/2}Nb_{1/2}]O_3$ compounds" by **Devang D. Shah** and P.K. Mehta, in the one day seminar at Applied Physics department, The M. S. University of baroda, February-2009.
5. "Investigation of Electrical Conduction in $Ba[(Fe_{1-x}Co_x)_{1/2}Nb_{1/2}]O_3$ Compounds" by **Devang D. Shah** and P.K. Mehta, Proceedings of 3rd NSAMS-09, Tirunelveli (P-57). **Won the 1st prize for best oral presentation.**
6. "Effective permittivity analysis for conducting $Ba[(Fe_{0.25}Gd_{0.25})Nb_{0.5}]O_3$" by, **Devang D. Shah,** N. V. Patel P.K.Mehta and Ravi Kumar, Proceedings of 54th DAE-SSPS 2009 (P-873)
7. "Structural Investigations of Relaxor Dielectric Compounds - $Ba[B'_{1/2}Nb_{1/2}]O_3$; where B'=Fe, Co, Y, La, Eu, Gd" by **Devang D. Shah,** Abstract book of National Workshop

on X-Ray Diffraction Techniques and Applications (NWXRD-2010), (P-21) Selected for **oral presentation**.

8. "Tuning of High Energy Storage Materials" by **Devang D. Shah** and P. K. Mehta, Abstract book of 3rd Research Convention (West Zone) – ANVESHAN-2010.
9. "Structural and Impedance Studies of $Ba(Mn_{0.5}Nb_{0.5})O_3$" by **Devang D. Shah** and P. K. Mehta, Proceedings of 55th DAE-SSPS 2010 (P-275), **AIP Conf. Proc. 1349, 1041-1042 (2011).**
10. "SHI Induced Enrichment of the Electrical Properties in BFN Films" by **Devang D. Shah** and P. K. Mehta, Proceedings of Seventeenth National Symposium on Solid State Nuclear Track Detectors and Their Applications (SSNTD-17).
11. "Structural and Electrical Studies of $Ba(Fe_{0.25}Gd_{0.25}Nb_{0.5})O_3$" **Devang D. Shah** and P. K. Mehta, Proceedings of 56th DAE-SSPS 2010, **AIP Conf. Proc. 1447, 1017-1018 (2012). Won the best poster award.**

List of International Recognitions:

1. The XRD Rietveld refinement pattern of $Ba(Fe_{1/2}Nb_{1/2})O_3$ - (BFN), has been **accepted for publication at International Centre for Diffraction Data (ICDD), U.S.A. (Ref ID for pattern IA031F).**
2. The XRD Rietveld refinement pattern of $Ba[Fe_{1/4}Co_{1/4}Nb_{1/2}]O_3$ - (BFCN) has been **accepted for publication at International Centre for Diffraction Data (ICDD), U.S.A. (Ref ID for pattern IA031E).**
3. The XRD Rietveld refinement pattern of $Ba(Co_{1/2}Nb_{1/2})O_3$ - (BCN) has been **accepted for publication at International Centre for Diffraction Data (ICDD), U.S.A. (Ref ID for pattern IA031D).**